SAPIENZA
UNIVERSITÀ DI ROMA

The Nature of Hot Gas in Galaxy Clusters

Exploring the chemical and dynamical properties of the intracluster medium

Department of Physics
Doctor of Philosophy in Astrophysics

Ang Liu

Thesis Advisor
Dr. Paolo Tozzi

October 2019

The Nature of Hot Gas in Galaxy Clusters - Exploring the chemical and dynamical properties of the intracluster medium

This thesis is supported by the National Institute for Astrophysics (INAF), Sapienza University of Rome, and Tor Vergata University of Rome.

Author's email: liuang@arcetri.astro.it; liuang.ou@gmail.com

Abstract

In this Thesis I focus on the chemical enrichment of galaxy clusters by tracing the evolution of iron in the intracluster medium (ICM) through high-angular resolution X-ray observations from the *Chandra* X-ray Observatory. The detailed search and modelization of the emission lines of iron also allow me to perform dynamical studies of the ICM by measuring its velocity through the accurate position of the line centroid in X-ray spectra extracted from different regions. Eventually, the chemical, thermodynamical and dynamical properties of the ICM investigated in this work, can be put together in a unique framework in the context of the cosmological evolution of galaxy clusters. This Thesis is structured as follows.

Chapter 1 gives a general introduction to the scientific background, including the cosmological framework, the fundamental physical properties of galaxy clusters, the current state of the art of chemical and dynamical studies of the ICM, and the past, present, and future X-ray observational instruments.

In Chapter 2, I investigate the spatial distribution of iron in the ICM in a selected sample of relaxed clusters up to redshit $z \sim 1$, measuring the deprojected iron abundance and gas density profiles. First, I confirm the finding that the emission-weighted iron abundance within the cool core (from where most of the measurements of the ICM average abundance reported in the literature come from) is typically higher than the mass-weighted value across the cluster, showing that spatially-resolved analysis is necessary to achieve a quantitative assessment of the chemical enrichment. Thanks to an accurate modelization of the azymuthally-averaged iron distribution as a function of the cluster radius, I also show that the spatial profile extends with time, as a result of the mixing of the highly-enriched central regions with the surrounding ICM, possibly associated with the mechanical-mode feedback from the central Active Galactic Nucleus (AGN).

In Chapter 3, I focus on the distribution of iron in the very center, and study the origin of the 'central abundance drop', i.e. a drop of ICM iron abundance that has been observed in a few cool-core clusters. Thanks to high spatial-resolution spectral analysis of different elements including Fe, Ar, Ne, Si, and S, I find that the iron drop is due to two different physical processes.

The first one is simply the mechanical removal of the mostly enriched ICM from the innermost core regions, due to the creation of bubbles associated with the AGN radio-mode feedback. The second and most interesting process, is the iron depletion into dust grains associated with the intense star-forming regions close to the brightest cluster galaxy (BCG), consistent with the most recent scenario of the baryon cycle in cool-core clusters.

In Chapter 4, I present our main findings on ICM chemical enrichment as a function of cosmic epochs, consisting in a comprehensive study on the chemical evolution of galaxy clusters. This is obtained by measuring the iron mass in the ICM after dissecting different components in the abundance profiles, namely an iron peak in the center associated with the BCG, and an approximately constant baseline across the whole cluster associated with early enrichment. Using *Chandra* archival data of 186 morphologically regular clusters up to redshift 1.1, I compute for each cluster the azimuthally-averaged iron abundance and gas density profiles, the total iron mass, the mass of the iron peak and of the iron plateau, and the mass-weighted iron abundance, out to a typical extraction radius $\sim r_{500}$. I find that the mass-weighted iron abundance within r_{500} does not evolve significantly across cosmic epoch in our sample. Among the two components, the iron plateau shows no evolution with redshift either in the iron mass (scaled by the gas mass), or in the normalization of the distribution. On the other hand, I find marginal ($< 2\sigma$ c.l.) decrease with redshift in both the two quantities associated with the iron peak. While the intrinsic scatter in the mass associated with the iron plateau is consistent with statistical noise, the iron peak mass exhibits an extremely large intrinsic scatter, in line with the fact that the peak is produced after the virialization of the halo and depends on the formation of a cool core and the strength of the feedback. I estimate that the fraction of iron peak mass is only $\sim$1% of the total iron mass within r_{500}. Therefore the evolution of the total amount of iron in the ICM is dominated by the amplitude of the iron plateau, which does not evolve significantly with redshift at least up to $z \sim 1$.

Chapters 5 and 6 are devoted to the dynamical analysis of galaxy clusters. In Chapter 5, I perform a joint analysis combining X-ray, weak lensing, and galaxy spectroscopic data, to investigate the dynamics of the galaxy cluster Abell 2142, a massive supercluster with multiple cold fronts in X-rays probably

induced by core-sloshing. A number of substructures in the galaxy distribution are identified, suggesting the presence of multiple minor mergers, which are responsible for the complex dynamics of Abell 2142. By mapping the X-ray redshift of the ICM, I detect a ring of gas near the two cold fronts, with a velocity significantly higher than the surroundings. This result provides a direct support for the core-sloshing scenario assumed by previous studies, and it constitutes the first detection of line-of-sight effect of core-sloshing in galaxy clusters.

In Chapter 6, I search for a specific dynamic feature, which is usually overlooked when applying the standard hydrostatic equilibrium mass measurements, namely the global rotation of the ICM. We apply our spatially-resolved spectral analysis to the *Chandra* data of the galaxy cluster Abell 2107, where previous studies have reported rotational motion in the member galaxies. I identify the possible rotation axis and the rotation curve. The high maximum rotational velocity of the ICM (> 1000 km/s) creates some tension with the rotational scenario, particularly with the spherical symmetry, and may suggest the presence of an unnoticed, off-centre, ongoing collision between two comparable halos along the line of sight. This result confirms the peculiar dynamical nature of Abell 2107, but is not able to resolve the rotation versus merger scenario, a science case that can be addressed at some level by deeper observations with current facilities, or fully addressed with the next-generation facilities carrying X-ray bolometers on board.

The Thesis ends with an overview of the strategies I intend to use with current X-ray facilities to further progress in these lines of research and, finally, a plan to address the most critical points out of reach of current facilities, with future X-ray missions.

Sommario

Il tema principale di questa Tesi è l'arricchimento chimico nel mezzo intra-cluster (ICM) di ammassi di galassie, basato sulle misure del ferro presente nell'ICM e alla sua evoluzione, ottenute attraverso le osservazioni ad alta risoluzione angolare del satellite a raggi X *Chandra*. Lo studio delle righe di emissione del ferro permette inoltre di eseguire studi sulla dinamica dell'ICM, in particolare attraverso la misura accurata della posizione del centroide delle righe identificate negli spettri X ottenuti da diverse regioni dell'ICM. Infine, le proprietà chimiche, termodinamiche e dinamiche dell'ICM studiate in questo lavoro possono essere sintetizzate in un unico quadro di riferimento nel più ampio contesto dell'evoluzione cosmologica degli ammassi di galassie. La tesi è strutturata come segue.

Il Capitolo 1 fornisce un'introduzione generale al background scientifico, incluso il quadro cosmologico, le proprietà fisiche fondamentali degli ammassi di galassie, lo stato attuale dell'arte degli studi chimici e dinamici dell'ICM e la situazione passata, presente e futura degli strumenti osservativi nella banda X in grado di eseguire analisi spettrale spazialmente risolta come quella necessaria per questi studi.

Nel Capitolo 2, indago la distribuzione spaziale del ferro nell'ICM in un selezionato campione di cluster rilassati fino a redshit $z \sim 1$, misurando i profili deproiettati dell'abbondanza di ferro e della densità di gas. Per prima cosa, trovo la conferma che l'abbondanza di ferro pesata per l'emissività all'interno del cosiddetto 'cool-core' (ovvero il valore che è generalmente usato in letteratura per stimare l'abbondanza media del ferro nell'ICM) è in genere superiore al valore pesato per la densità di massa per l'intero ammasso, dimostrando in modo chiaro che l'analisi spettrale spazialmente risolta è un passo necessario per studiare correttamente l'arricchimento chimico negli ammassi di galassie. Come risultato della modellizzazione della distribuzione spaziale del ferro, mediata in modo azimutale, in funzione del raggio dell'ammasso, riesco a dimostrare che questa distribuzione spaziale evolve col tempo a causa del processo di 'mixing' delle regioni centrali, altamente arricchite, con l'ICM circostante, probabilmente in seguito al 'feedback' di tipo meccanico dovuto al Nucleo Galattico Attivo (AGN) centrale.

Nel Capitolo 3, mi concentro sulla distribuzione del ferro nelle regioni più centrali dell'ammasso, e studio l'origine dell'inattesa diminuzione dell'abbondanza centrale, ovvero una zona di minimo locale nell'abbondanza del ferro che finora è stata osservata nelle regioni centrali di alcuni ammassi con 'cool-core'. Grazie all'alta risoluzione spaziale dell'analisi spettrale di diversi elementi tra cui Fe, Ar, Ne, Si e S, trovo che il calo centrale del ferro è dovuto all'azione combinata di due diversi processi. Il primo è semplicemente la rimozione meccanica dell'ICM più arricchito dal centro dell'ammasso, come risultato della creazione di bolle nell'ICM dovute al feedback meccanico dell'AGN centrale. Il secondo, più interessante dal punto di vista fisico ed inaspettato nel contesto della fisica dell'ICM finora conosciuta, è l'assorbimento del ferro sui grani di polvere associati alle regioni con più intensa formazione stellare nella galassia centrale (Brightest Cluster Galaxy, o BCG). Tale fenomeno può essere compreso all'interno di un più ampio e complesso scenario del ciclo dei barioni negli ammassi di galassie.

Nel Capitolo 4 presento le principali conclusioni sull'arricchimento chimico dell'ICM, ottenute da una misura sistematica delle righe di emissione del gerro. In dettaglio, ho ricostruito la massa di ferro nell'ICM dopo aver identificato spazialmente diverse componenti nella distribuzione del ferro, in particolare un picco centrale di abbondanza associato alla BCG e una distribuzione approssimativamente costante attraverso l'intero ammasso, presumibilmente associata all'arricchimento originario precedente alla formazione dello stesso ammasso. Usando i dati di archivio di *Chandra* di 187 cluster con morfologia regolare e redshift fino a $z \sim 1.1$, ho calcolato per ciascun ammasso la media azimutale dei valori di abbondanza di ferro e densità del gas, la massa totale di ferro, la massa nel picco del ferro e nella componente costante, quindi l'abbondanza media globale pesata per la densità di massa, fino ad un raggio di estrazione tipico $\leq r_{500}$. Trovo che l'abbondanza di ferro pesata in massa entro r_{500} non evolve in modo significativo in funzione dell'epoca cosmica, per lo meno negli oggetti rappresentati dal campione qui utilizzato. Tra le due componenti, il plateau del ferro non mostra alcuna evoluzione col redshift sia nella massa totale (rinormalizzata alla massa del gas), che nella normalizzazione della distribuzione. D'altra parte, siamo in grado di misurare una diminuzione poco significativa ($< 2\sigma$ c.l.) col redshift in entrambe le due quantità associate

al picco di ferro. Mentre la dispersione intrinseca nella massa associata al plateau è consistente con il rumore statistico, la massa del picco di ferro mostra una dispersione intrinseca significativa, in linea con il fatto che il picco viene prodotto dopo la virializzazione dell'alone e dipende dalla formazione del 'cool-core' e dall'intensità e dalla frequenza degli episodi di feedback. Stimiamo che la frazione della massa del picco di ferro sia in media del $\sim$1% rispetto alla massa totale di ferro entro r_{500}. Pertanto l'evoluzione del ferro nell'ICM è dominata dall'altezza del plateau (ovvero della componente spazialmente costante e quindi probabilmente originaria), che non evolve significativamente col redshift almeno fino a $z \sim 1.1$.

I capitoli 5 e 6 sono dedicati all'analisi dinamica degli ammassi di galassie. Nel Capitolo 5, eseguo un'analisi congiunta combinando dati a raggi X, effetto di lente gravitazionale debole e spettroscopia ottica di singole galassie, per indagare le dinamiche dell'ammasso Abell 2142, parte di un massiccio supercluster con più fronti freddi osservati nei raggi X dovuti probabilmente dal fenomeno di 'sloshing' del 'cool-core'. Siamo in grado di dentificare numerose sottostrutture nella distribuzione delle galassie membri dell'ammasso, che interpretiamo come l'effetto di numerosi 'merger' con aloni di piccola massa, responsabili della complessità dell'aspetto dinamico di Abell 2142. Attraverso il confronto con mappe di redshif dell'ICM ottenute grazie all'analisi spettrale spazialmente risolta, sono in grado di rilevare un anello di gas vicino ai due fronti freddi, con una velocità notevolmente superiore rispetto a quella dell'ICM circostante. Questo risultato fornisce un supporto diretto per lo scenario 'core-sloshing' già discusso da studi precedenti, ed è, di fatto, la prima evidenza osservativa nei raggi X del fenomeno di 'core-sloshing' lungo la linea di vista.

Nel Capitolo 6, affronto l'osservazione di un particolare aspetto dinamico che è solitamente ignorato quando si applica l'equilibrio idrostatico per la misura della massa totale degli ammassi: mi riferisco alla rotazione globale dell'ICM. Abbiamo applicato la nostra strategia di analisi spettrale spazialmente risolta all'ammasso di galassie Abell 2107, in cui studi precedenti hanno riportato l'evidenza di rotazione nel moto delle galassie membri. Siamo in grado di identificare un possibile asse di rotazione e misurare la curva di rotazione. La massima velocità di rotazione dell'ICM (> 1000 km/s) tuttavia, è in tensione con l'ipotesi di rotazione, in particolare con la forma sferica dell'ammasso,

e suggerisce, invece, una collisione frontale non rilevata dai dati disponibili, leggermente fuori asse, lungo la linea di vista. Questo risultato conferma la peculiare dinamica di Abell 2107, ma non è in grado di verificare lo scenario di rotazione rispetto all'ipotesi della collisione. Questo è un caso scientifico che può essere affrontato soltanto in parte dai telescopi X tuttora in funzione, e che per essere risolto definitivamente richiede gli strumenti X di prossima generazione, in particolare le missioni con bolometri a raggi X.

LaTesi si conclude con una panoramica delle strategie che intendo utilizzare con gli strumenti a raggi X attualmente disponibili per ottenere ulteriori risultati nelle linee di ricerca affrontate in questa tesi. Infine, presento e discuto brevemente un piano di lavoro per affrontare, con gli strumenti futuri, i punti critici della fisica dell'ICM che sono in questo momento al di là delle capacità degli strumenti disponibili.

Contents

Chapter 1

Introduction

1.1 Background: cosmological framework

The main focus of this thesis is the chemical evolution of the intracluster medium in galaxy clusters in a cosmological context. To reach a comprehensive understanding on this topic, we first need to obtain a basic knowledge of the cosmological framework. Therefore, in this section, we will start from the very beginning of the life of our Universe, namely the Big Bang scenario, to continue with the standard picture of the formation and evolution of the large scale structures in today's Universe, and finally discuss the most advanced theories for the formation and evolution of galaxy clusters. Due to space limitations, I will present the cosmological context in the simplest way. Readers should consult books on cosmology, e.g. Peebles (1993) [269], Peacock (1999) [268], and Liddle (2003) [189], for more details.

1.1.1 The Big Bang scenario

Cosmology is the study of the origin and evolution of the Universe. Despite the long history of humanity's exploration of the origin of the cosmos from a philosophical point of view, physical cosmology is thought to start with the theory of gravity by Isaac Newton. Therefore we will now begin a brief discussion of cosmology based on Newtonian gravity, to reach a general description of the evolution of our Universe.

Before going further, we need to introduce a basic assumption, called the

cosmological principle: the spatial distribution of matter in the Universe is homogeneous and isotropic when observed on a large scale. This principle has actually been proved by many observational facts, such as the apparently isotropic distribution of galaxies, and the homogeneity and isotropy of cosmic microwave background (CMB) when averaged over large scales. Here we do not discuss the scope of application of cosmological principle in details but merely adopt it as a basic assumption to describe the dynamics of the expanding Universe.

We now consider a uniform expanding Universe with density ρ, and a particle with mass m and distance r from the center. Since we assume that the Universe is homogeneous and isotropic, the center can be any point. According to Newton's law of gravity, the particle only feels the force from the mass within radius r, which can be written $M = 4\pi\rho r^3/3$. The force from M is then:

$$F = \frac{GMm}{r^2} = \frac{4\pi G\rho m r}{3}. \tag{1.1}$$

The gravitational potential energy of the particle is therefore:

$$V \equiv \int F dr = -\frac{GMm}{r} = -\frac{4\pi G\rho m r^2}{3}. \tag{1.2}$$

Given the kinetic energy $T = m\dot{r}^2/2$, and the energy conservation $U = T + V$, we can describe the evolution of r:

$$U = \frac{1}{2}m\dot{r}^2 - \frac{4\pi G}{3}\rho m r^2. \tag{1.3}$$

Since the Universe is expanding, i.e., $r = r(t)$, we change to another coordinate system, called the *comoving coordinates*, by adding a time-dependent expansion to the coordinates:

$$\mathbf{r}(t) = a(t) \cdot \mathbf{x}, \tag{1.4}$$

where $\mathbf{x}$ is the coordinate system at $t = t_0$, and $a(t)$ is the *cosmic scale factor* which measures the expansion rate of the Universe: $H(t) \equiv \dot{a}/a$. So the velocity of the particle is:

$$\mathbf{v}(\mathbf{r}, t) = \frac{\mathrm{d}}{\mathrm{dt}}\mathbf{r}(t) = \dot{a}\mathbf{x} = \frac{\dot{a}}{a}\mathbf{r} = H(t)\mathbf{r}. \tag{1.5}$$

Setting $t = t_0$, we have the Hubble law:

$$v = H_0 D, \tag{1.6}$$

where v is the velocity of a source at distance D. Obviously, the velocity v cannot be observed directly, but is calculated from the redshift z, which is defined as $z = (\lambda_{\rm obs} - \lambda_0)/\lambda_0$, where $\lambda_{\rm obs}$ is the wavelength corresponding to an observed feature (e.g. an emission or absorption line in the spectrum), while λ_0 is the rest frame wavelength of this feature. Given the definition of the cosmic scale factor a, we have $\lambda_0 = a\lambda_{\rm obs}$, and therefore the relation between redshift and the cosmic scale factor:

$$1 + z = \frac{1}{a}. \tag{1.7}$$

We stress that the redshift here is the cosmological redshift, caused by the expansion of the Universe itself. Substituting r with a, and let $kc^2 = -2U/mx^2$, we can rewrite Equation (1.3):

$$\dot{a}^2 = \frac{8\pi G}{3}\rho(t)a^2(t) - kc^2, \tag{1.8}$$

in which the sign of k characterizes the qualitative behavior of the cosmic expansion history. By assuming $k = 0$, which implies that the Universe will never re-collapse, we obtain the *critical density* and the dimensionless *density parameter* of the Universe at $t = t_0$:

$$\rho_{\rm cr} = \frac{3H_0^2}{8\pi G}; \quad \Omega_0 = \frac{\rho_0}{\rho_{\rm cr}}. \tag{1.9}$$

Modifying Equation (1.8) with general relativity, we have the final equations of motions of the Universe, also called the Friedmann equations:

$$\left(\frac{\dot{a}}{a}\right)^2 = \frac{8\pi G}{3}\rho - \frac{kc^2}{a^2} + \frac{\Lambda}{3}, \tag{1.10}$$

and

$$\frac{\ddot{a}}{a} = -\frac{4\pi G}{3}\left(\rho + \frac{3p}{c^2}\right) + \frac{\Lambda}{3}, \tag{1.11}$$

where Λ is the cosmological constant introduced by Einstein, and p is the pressure of the matter component. The essential components of matter in the Universe include pressure-free matter with density $\rho_{\rm m}$, radiation with density $\rho_{\rm r}$, and vacuum energy with density ρ_Λ. Obviously, we have $\rho = \rho_{\rm m} + \rho_{\rm r} + \rho_\Lambda$

and $\Omega = \Omega_{\rm m}+\Omega_{\rm r}+\Omega_\Lambda$. Given the fact that $\rho_{\rm m} \propto a^{-3}$, $\rho_{\rm r} \propto a^{-4}$, and $\rho_\Lambda = const$, we can write Equation (1.10) as:

$$\left(\frac{\dot{a}}{a}\right)^2 = H^2(t) = H_0^2(a^{-4}\Omega_{\rm r} + a^{-3}\Omega_{\rm m} - a^{-2}\frac{kc^2}{H_0^2} + \Omega_\Lambda). \tag{1.12}$$

We can obtain the value of k by substituting $H(t)$ and $a(t)$ at the present epoch, and ignore $\Omega_{\rm r}$:

$$k = \left(\frac{H_0}{c}\right)^2 (\Omega_{\rm m} + \Omega_\Lambda - 1). \tag{1.13}$$

Finally the expansion equation can be written as:

$$\left(\frac{\dot{a}}{a}\right)^2 = H^2(t) = H_0^2[a^{-4}\Omega_{\rm r} + a^{-3}\Omega_{\rm m} + a^{-2}(1 - \Omega_{\rm m} - \Omega_\Lambda) + \Omega_\Lambda]. \tag{1.14}$$

We can further obtain the age of the Universe at any given scale factor using the relation $\mathrm{d}t = \mathrm{d}a/aH(t)$:

$$t(a) = \frac{1}{H_0}\int_0^a \mathrm{d}a[a^{-2}\Omega_{\rm r} + a^{-1}\Omega_{\rm m} + (1 - \Omega_{\rm m} - \Omega_\Lambda) + a^2\Omega_\Lambda]^{-1/2}. \tag{1.15}$$

Equation (1.14) shows that the Universe is dominated by different components at different epochs, corresponding, in turns, to different scale factors. For small a, the Universe is dominated by radiation. For slightly larger a, the Universe is dominated by pressure-free matter. For very large a, the Universe is dominated by the cosmological constant, which is a particular case of what is usually called *dark energy*. Furthermore, Equation (1.14) also shows that we can classify cosmological models based on measurements of Ω_Λ and $\Omega_{\rm m}$. Figure 1.1 shows the behaviors of different cosmological models in the ($\Omega_{\rm m}$, Ω_Λ) plane. According to observational evidences collected so far (e.g. the measurement of CMB [270], the observations of supernovae Ia [296, 272]) our Universe originated from the Big Bang ~ 13.7 Gyr ago, and is currently experiencing an accelerated expansion. At the time of writing, the best values for the cosmological parameters are where $\Omega_0 = 0.308 \pm 0.012$ and $\Lambda = 0.692 \pm 0.012$ [282].

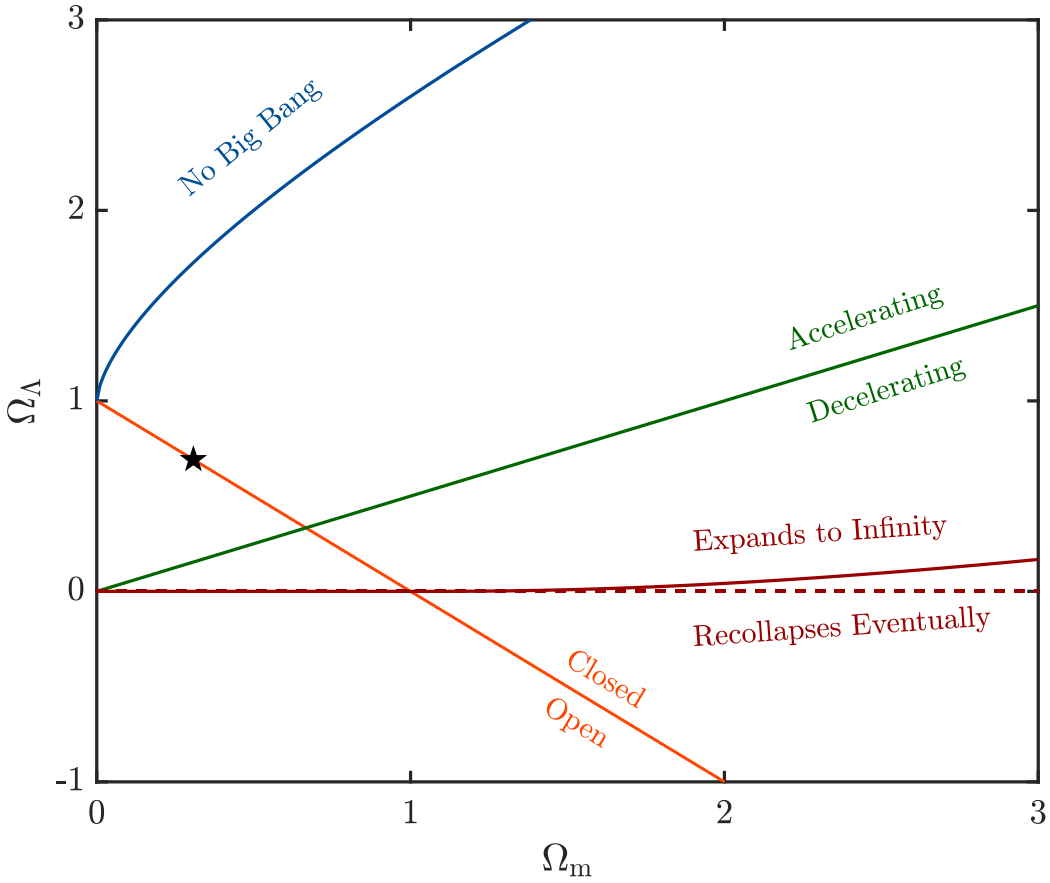

Figure 1.1. Classification of cosmological models in the Ω_m,Ω_Λ plane. The orange line corresponding to a flat Universe ($\Omega_m + \Omega_\Lambda = 1$), and it constitutes the line separating closed and open models. A negative Ω_Λ, as well as positive but sufficiently small Ω_Λ, will result in a recollapse in finite time. Otherwise the Universe will expand forever. Models with $\Omega_\Lambda > \Omega_m/2$, i.e. with the *deceleration factor* $q = \Omega_m/2 - \Omega_\Lambda < 0$, correspond to an accelerating expansion. In the upper left corner, models with an expansion history where a has never been zero, are not consistent with a Big Bang. The black star symbol marks the current measurements of cosmological parameters made by *Planck* [282], where $\Omega_0 = 0.308 \pm 0.012$ and $\Lambda = 0.692 \pm 0.012$. Credit: Ang Liu.

1.1.2 The formation of large scale structure

In this section we will briefly describe the formation and evolution of the large scale structure of the Universe. First, we will review some problems of

the standard Big Bang model that puzzled the scientific community in the 1990s. The theories to solve these problems are pivotal ingredients in the whole evolutionary picture of the Universe.

The *horizon problem* describes the extremely precise uniformity of the CMB. Here the expression 'horizon' represents the farthest distance a signal can travel at the speed of light at a given time. According to the Big Bang scenario, regions at two widely separated directions which are not in causal contact, had no chance to change information, and therefore should never be able to smooth out any difference among themselves. However, observations have found that the average fluctuation of the CMB temperature is only $\sim$0.001%, despite computed among regions at distances much larger then the horizon at the epoch they are observed [346].

The *flatness problem* is based on the fact that the total density parameter Ω_0 has been extremely close to 1 in the past. In fact, an Ω either slightly smaller or larger than 1 at early times, would have resulted in extreme effects, i.e., a Universe that is completely different from it is today. This requires a very precise and sensitive 'fine-tuning' of the Ω parameter.

The inflationary theory is a possible solution for both problems. The *inflation* posits that the Universe underwent an exponential expansion at very early times for a very short period of time:

$$a(t) \propto \exp\left(\sqrt{\frac{\Lambda}{3}} \cdot t\right). \tag{1.16}$$

The horizon problem can therefore be solved because the regions observed to be out of each other horizon were in causal contact before the inflation, and this implies that the homogeneity of the CMB is actually due to causal processes happened within the horizon before inflation. The flatness problem is also solved because the tremendous expansion during the inflationary smooths out any initial curvature, resulting in a Ω_0 very close to 1.

Although the physical details of the inflation model is still unclear, an obvious achievement of the inflationary model, as well as one of the reasons why it has been commonly accepted, is that it provides a natural mechanism also for the origin of the fluctuations in the initial density field, which are the seeds of the future large scale structure of the Universe.

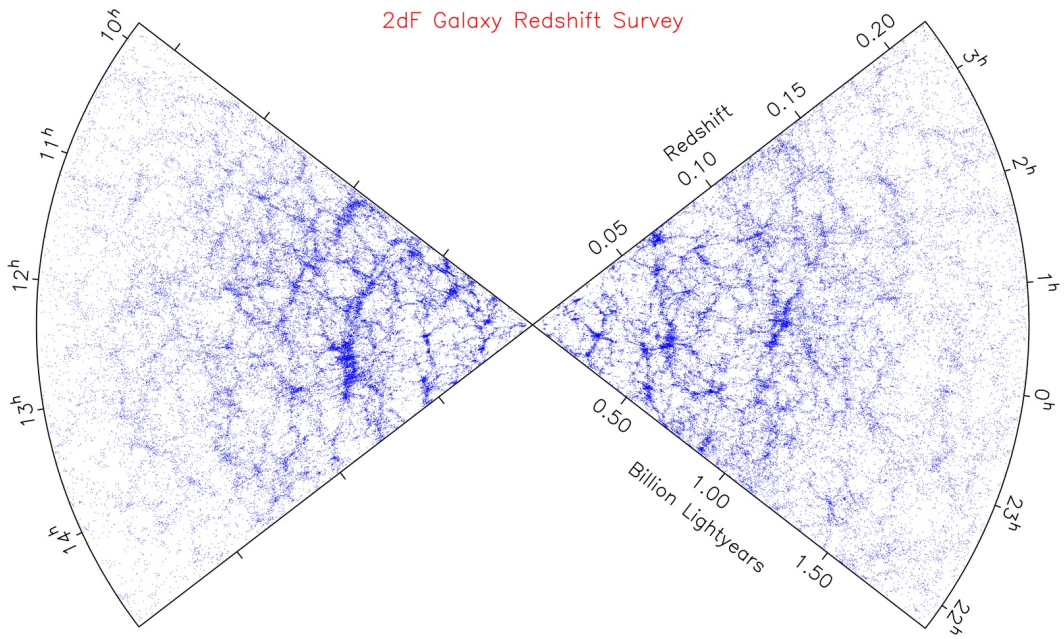

Figure 1.2. The distribution of more than 200,000 galaxies in the 2dFGRS [54].

Despite the homogeneity of the Universe at large scale, even a momentary glimpse at the night sky provides immediate evidence that the Universe is inhomogeneous at small scales. Not only the stars in the Milk Way are not distributed randomly and uniformly, but the galaxies in the Universe also form groups and clusters, and these, in turn, are often organized in more massive superclusters. In Figure 1.2 we show the distribution of galaxies in the sky observed by the 2-degree Field Galaxy Redshift Survey (2dFGRS) [56, 57, 54], where dramatically evident large-scale structures, such as 'filaments', 'walls', and 'voids', can be clearly seen. Cosmological N-body numerical simulations can currently reproduce the formation of these large scale structures. See an example in Figure 1.3, where a simulated dark matter density field at three different redshift is shown (from the Millennium Simulation Project [349]).

The origin of these large scale structures is the growth of the initial density field driven by gravitational instability. As we mentioned before, inflation can generate irregularities in the density field, which will be the seeds that, through gravitational instability, will allow the formation of cosmic structures. Quantum mechanics is a key ingredient in this process: according to Heisenberg's uncertainty principle, spacetime is made of a seething mass of quantum

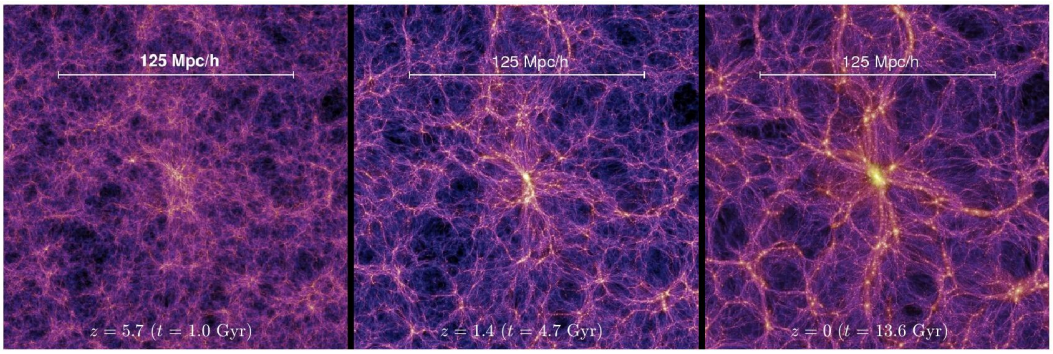

Figure 1.3. Dark matter density field from the Millennium Simulation Project performed with the code GADGET-2 [349], and adapted by Ang Liu. Each slice is 15 Mpc/h thick, and is centered on a massive cluster of galaxies.

fluctuations, where particles are continually popping in and out of existence. Thanks to the inflation mechanism, these quantum fluctuations, which are small at the beginning, are stretched to large scales, and become the seeds that eventually evolve into the structures like galaxies, galaxy clusters, walls, and voids we observe today.

1.2 Galaxy clusters and the ICM

After a very quick introduction to the basic cosmological framework, in this section we will turn to the main topic of this Thesis: galaxy clusters.

1.2.1 Basic physical pictures

As far as we know today, galaxy clusters are the most massive gravitationally–bound systems in the Universe. According to the widely accepted hierarchical structure formation scenario [180, 168, 302, 1, 177], as we mentioned in the last section clusters form and evolve through the gravitational instability-driven growth of the initial density fluctuations [302, 177]. Since galaxy clusters are the youngest large scale structures formed during cosmic evolution, they are located at the crossroads of cosmology and galaxy-scale astrophysics. Being the largest isolated systems, they are also regarded as massive closed boxes which retain the cumulative information of the past history in a given region of

the Universe, corresponding to the comoving volume that eventually collapse to form the cluster.

A typical galaxy cluster has a spatial scale of several Mpc, and a total mass in the range 10^{14}-$10^{15} M_{\odot}$. Despite their name, galaxy clusters are not a simple collection of galaxies, but their total mass budget is instead dominated by the dark matter component, which contributes by 80–90%. While the member galaxies only constitute a minority of the total mass, the remaining 10–20% is dominated by the intracluster medium (ICM), which outweigths the stellar mass in galaxies by a factor of ~ 5. The ICM is a hot and diffuse plasma in collisional ionization equilibrium (CIE) at low densities ($n \sim 10^{-3}\mathrm{cm}^{-3}$), being heated by the deep dark matter potential well to a temperature of 10^{7}–10^{8} K. At such high temperatures, the main mechanism of radiation is thermal bremsstrahlung (free-free radiation) due to the acceleration of electrons in the Coulomb field of positive ions. The electron plasma emits X-rays with total luminosities in the range 10^{43} to 10^{45} erg $\cdot\, s^{-1}$, going from groups to massive clusters. In addition to the strong X-ray emission, ICM can also be detected from its imprints on the background photons of the CMB: high-energy electrons in the hot ICM can distort the spectrum of CMB photons through inverse Compton scattering. This effect, called the Sunyaev-Zel'dolvich (SZ) effect, was first predicted by Rashid Sunyaev and Yakov B. Zel'dovich early in 1970s [359, 360], and observationally confirmed later [350, 385, 294, 279, 280, 281].

In Figure 1.4, upper panels, we show a typically regular, dynamically relaxed cluster (Abell 2029) in the X-ray and optical bands. In the left panel we show the diffuse X-ray emission from the ICM, with some random background AGN appearing as point sources on the X-ray image. In the right panel we show hundreds of galaxies centered around the brightest cluster galaxy (BCG) which is usually an elliptical galaxy with an extended envelope of intracluster light (ICL). In dynamically relaxed clusters, the BCG is often located at the peak of the ICM emission, so that the BCG-X-ray peak offset is often used as a signature of ongoing or recent merger [204, 306, 198]. In this last case, the X-ray morphology will also present several clear signatures originated from the disturbed dynamical status [389, 214, 215, 308] and a visible departure from the spherical symmetry typical of relaxed clusters. We will discuss these aspects

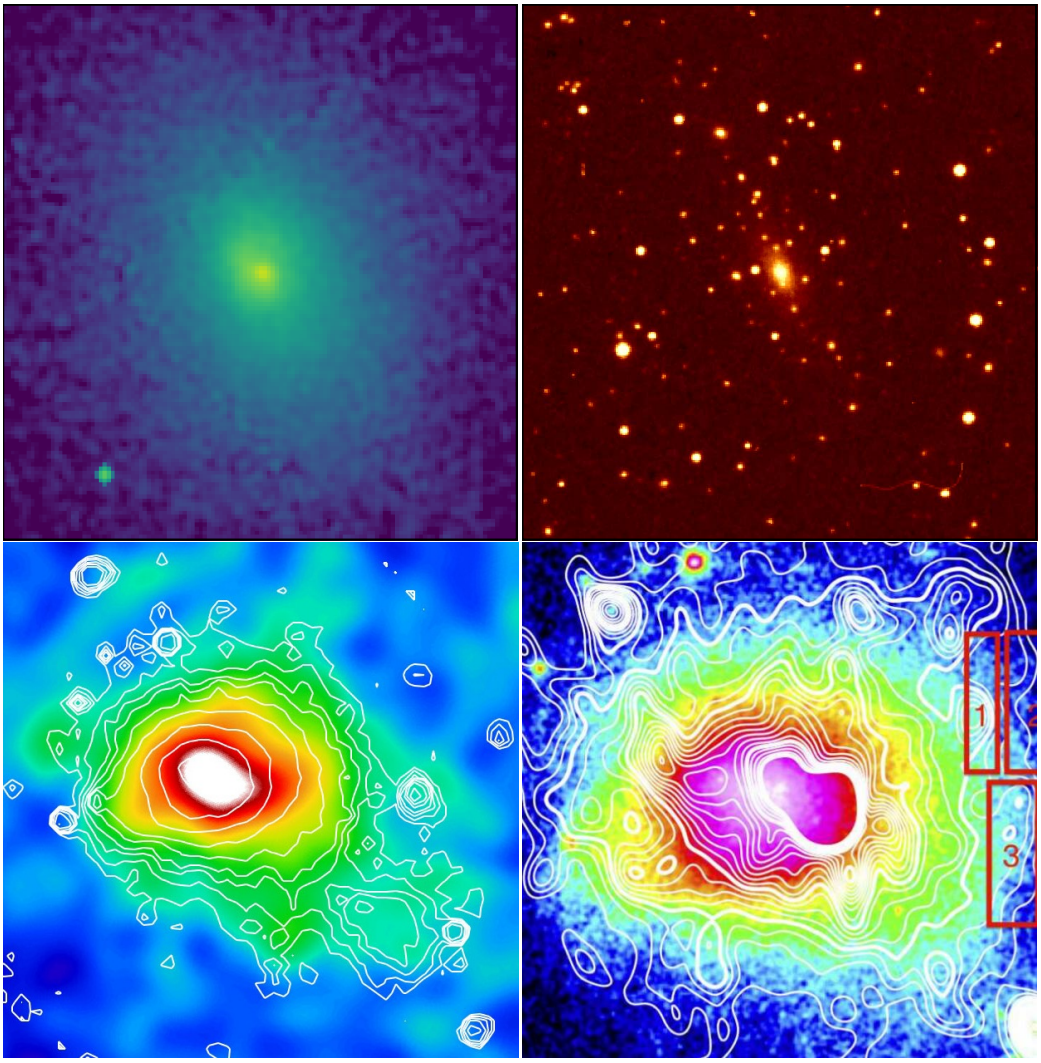

Figure 1.4. *Upper panels*: Images of the galaxy cluster Abell 2029. Left: *Chandra* X-ray image showing the diffuse emission of the ICM. The emission peak in the center of the cluster shows the existence of the 'cool core'. The bright source in the south-east corner is an AGN unrelated to the cluster. Right: optical image of Abell 2029 from the Digitized Sky Survey (DSS). The central elliptical galaxy with an extended envelope is called the 'brightest cluster galaxy' (BCG). In dynamically relaxed clusters like Abell 2029, the BCG is usually loacted at the peak of the ICM X-ray emission. *Lower panels*: Images of the Coma cluster. Left: SZ effect seen by *Planck* (colormap) overlaid by X-ray emission observed by ROSAT/PSPC (white contours). Credit: ESA/LFI and HFI Consortia. Right: Radio emission (white contours) of Coma observed by the Westerbork Synthesis Radio Telescope at 352 MHz [36] superimposed on the ROSAT/PSPC X-ray image (colormap).

seen by *Planck* through SZ effect, and as observed in radio (lower panels).

1.2.2 General properties of the ICM as observed in X-rays

Historical notes

The first detection of X-ray emission from galaxy clusters was made by Byram et al. in 1966 [42], who identified M87, the central galaxy of the Virgo cluster, as a source of X-ray emission. Soon afterwards, X-ray sources were also detected near the position of the Perseus [110] and Coma [231] clusters, and confirmed later by the *Uhuru* X-ray satellite [142, 141, 109]. In fact, confirming that massive galaxy clusters are X-ray sources is one of the most important discoveries of *Uhuru* [129, 368, 143]. With the later X-ray facilities, such as *Einstein*, ROSAT, XMM-Newton, and *Chandra*, X-ray emission has been detected also in lower mass clusters and groups, and even in massive elliptical galaxies. X-ray, therefore, became a new, accessible and optimal window to study the physical properties of galaxy clusters, by observing directly their major baryonic component.

X-ray spectrum of the ICM

As we have mentioned in the last section, the ICM is a hot plasma in collisional ionization equilibrium. The main radiation mechanism of the ICM in the X-ray band is thermal bremsstralung (free-free radiation), which is produced by the acceleration of electrons in the Coulomb field of protons and atomic nuclei. The thermal bremsstrahlung emissivity at a given frequency ν can be described by [137, 327]:

$$\epsilon(\nu) = \frac{32\pi e^6}{3m_{\rm e}c^3} \cdot \sqrt{\frac{2\pi}{3m_{\rm e}}} \cdot \frac{Z^2 n_{\rm e} n_{\rm i} g}{\sqrt{k_{\rm B}T}} \cdot \exp(-h\nu/k_{\rm B}T), \tag{1.17}$$

where e is the electron charge, $m_{\rm e}$ the electron mass, Z the effective charge of the corresponding ion, $n_{\rm e}$ and $n_{\rm i}$ the number density of electrons and ions, T the electron temperature of the ICM. The factor $g \equiv g(T, \nu)$, called the Gaunt factor, is a quantum mechanical correction, and is a slowly varying function of frequency and temperature [167, 170]. The Gaunt factor g is usually close to

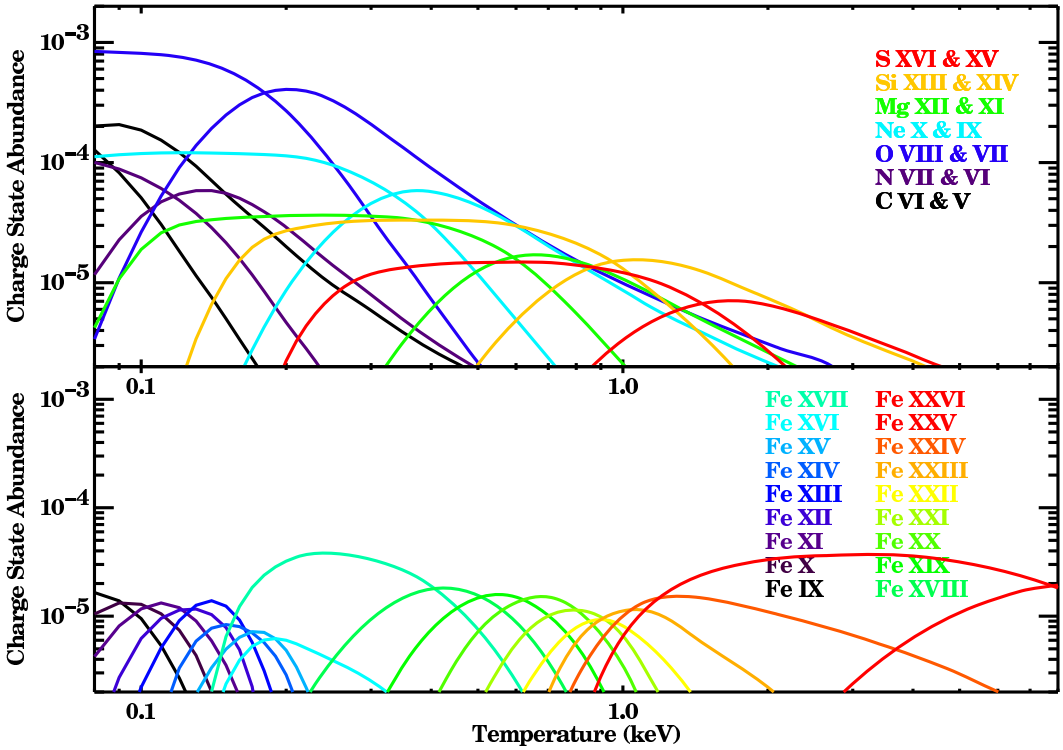

Figure 1.5. The abundance of various ions as a function of the equilibrium temperature (from Peterson & Fabian (2006) [273]). The data are from Arnaud & Raymond (1992) [10]. The top panel shows the cases of low-Z atoms, and the bottom panel shows the iron ions only, with electrons in the K, L, and M shells. We see in the figure that for massive clusters hotter than 4 keV, almost all the elements but iron are fully ionized.

1, and can be approximated by:

$$g(T,\nu) \approx \frac{3}{\sqrt{\pi}} \cdot \ln\left(\frac{9k_{\rm B}T}{4h\nu}\right). \tag{1.18}$$

Note that this equation is only applicable to one of the six regions in the energy-temperature parameter space (see the figure 5.2 of Rybicki & Lightman 1986 [310] for more details). If we eliminate the constants in Equation (1.17), then we have

$$\epsilon(\nu) \propto T^{-1/2} \cdot \exp(-h\nu/k_{\rm B}T), \tag{1.19}$$

where the exponential term with the argument $(-h\nu/k_{\rm B}T)$ indicates that the X-ray spectrum of a single temperature ICM exponentially depends on the

frequency, as confirmed by observations. Moreover, this exponential term also implies a sharp cut-off of the spectrum at high energies, and therefore the position of the cut-off $\nu \propto T$, or $\nu \propto T/(1+z)$ when considering the redshift, can be used as a probe of the ICM temperature, if the cutoff occurs well within the observed energy range. Integrating Equation (1.17) over ν, we can calculate the total emissivity:

$$\epsilon = \frac{\mathrm{d}E}{\mathrm{d}t \cdot \mathrm{d}V} = \int_0^\infty \epsilon_\nu \mathrm{d}\nu \propto n_\mathrm{e}^2 \cdot T^{1/2}, \tag{1.20}$$

which implies that the emission of the ICM is strongly dependent on its electron density, and weakly on its temperature, particularly in the energy band below the ICM temperature scale.

In addition to the bremsstralung continuum, another relevant component of the ICM X-ray spectrum is the line emission from different elements. In 1976, emission lines in ICM spectrum were discovered in Perseus, Coma, and Virgo clusters by Mitchell et al. and Serlemitsos et al. using the *Ariel V* and *OSO-8* satellites [243, 334]. However, the only emission line that could be resolved at that time is the Fe K_α complex at 6.7–6.9 keV, which is originated from the transition of He-like and H-like Fe, i.e. Fe nuclei with two and one electrons, respectively. The Fe K_α complex is also one of the most prominent line features in ICM spectrum, which is of great importance in determining the physical properties of the ICM, like metallicity, redshift, bulk and turbulent velocity, as we will discuss thoroughly in this Thesis.

Detection of emission lines from other elements became possible only after the launch of *ASCA* in 1993, in particular for line emission from O, Ne, Mg, Si, S, Ar, Ca, Fe, and Ni [107, 106]. Today, with high resolution spectroscopic observations, abundance of different elements in the ICM can be measured accurately, although the measurement of elements other than Fe usually requires higher signal to noise ratio (S/N), and relatively low temperature. At high temperatures, the other elements tend to be highly or fully ionized, as can be seen in Figure 1.5, which shows the abundance of ions as a function of temperature for a plasma in collisional ionizaton equilibrium. A set of theoretical spectra for ICM with different temperatures is shown in Figure 1.6, where we can see that the contribution of line emission to the spectrum decreases with temperature because of the decreasing population of

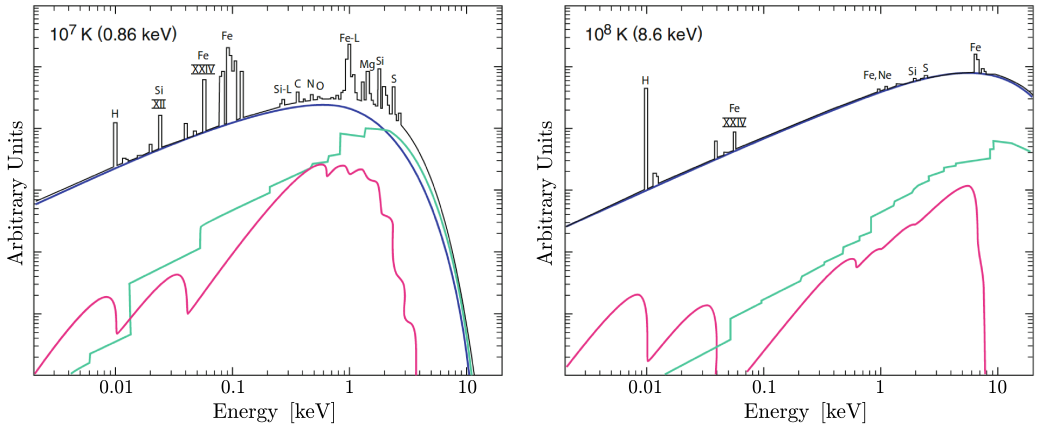

Figure 1.6. Theoretical X-ray spectra of ICM at different temperature, and with solar abundance. Blue, green, and red lines show the contributions from thermal bremsstralung, recombination radiation, and two-photon transition, respectively. Clearly, the spectrum for high temperature ICM is dominated by bremsstralung radiation at any energy. The figure is adapted from Böhringer et al. (2010) [32].

the corresponding ions.

Fitting the spectrum with appropriate models can be used to directly constrain the physical properties of the ICM, such as temperature, metallicity, and electron density. Since the first X-ray observation on galaxy clusters, many models have been developed to describe the ICM spectrum [62, 61, 292, 237, 238, 361, 164]. For example, a vastly used, reference description is provided by the `apec` model [345]. For high temperature clusters ($kT > 2.5$ keV), the determination of temperature is dominated by the global shape of the spectrum and, given a sufficiently high S/N, the position of the exponential cut-off. At low temperatures, where line contribution becomes relevant, temperature can also be constrained by the strength ratios of different lines from the same element, thanks to the accurate prediction of the CIE. Metal abundance can be measured directly from the equivalent width of the emission line, which is defined as:

$$EW \equiv \int_{\nu_-}^{\nu_+} \left(\frac{I_\nu - I_\nu^{\rm con}}{I_\nu^{\rm con}} \right) h \mathrm{d}\nu, \tag{1.21}$$

where I_ν is the total spectrum, $I_\nu^{\rm con}$ is the continuum component, and the

integral is over a restricted energy range $[\nu_-, \nu_+]$ in the vicinity of the line. The electron density can be estimated from the fit of the spectrum using the normalization parameter:

$$\mathrm{norm} = \frac{10^{14}}{4\pi[D_\mathrm{A}(1+z)]^2} \cdot \int n_\mathrm{e} n_\mathrm{p} \mathrm{d}V, \tag{1.22}$$

where D_A is the angular diameter distance to the cluster, z is the redshift, n_e and n_p are the number densities of electron and proton (hydrogen), respectively.

An example of ICM X-ray spectrum from *Chandra* ACIS observations of the Centaurus cluster, fitted with Xspec [8], is shown in Figure 1.7. The best-fit model is a double `vapec`, which is the same as `apec`, but allows the abundance of He, C, N, O, Ne, Mg, Al, Si, S, Ar, Ca, Fe, Ni to vary separately.

The spatial distribution of ICM X-ray emission.

X-ray emission from the ICM of regular galaxy clusters is extended, and usually centered on the position of the BCG or on the center of mass of the distribution of member galaxies. To describe the distribution of gas density ρ_g, we start from the hydrostatic equilibrium equation:

$$\frac{1}{\rho_\mathrm{g}} \frac{\mathrm{d}P}{\mathrm{d}r} = -\frac{\mathrm{d}\Phi}{\mathrm{d}r} = -\frac{GM(r)}{r^2}, \tag{1.23}$$

where Φ denotes the gravitational potential produced by the total mass, and $M(r)$ is the total mass enclosed within r. Inserting $P = nk_\mathrm{B}T = \rho_\mathrm{g} k_\mathrm{B} T/\mu m_\mathrm{p}$, where $\mu \sim 0.63$ is the mean molecular weight (weakly depending on metallicity if not for the share of H and He). Assuming, for simplicity, an isothermal distribution of gas, we have:

$$\frac{\mathrm{d}\ln\rho_\mathrm{g}}{\mathrm{d}r} = -\frac{\mu m_\mathrm{p}}{k_\mathrm{B}T} \cdot \frac{GM(r)}{r^2}. \tag{1.24}$$

The isothermal distribution of the total mass density can be obtained from the dynamical equilibrium of the member galaxies:

$$\frac{\mathrm{d}\ln\rho}{\mathrm{d}r} = -\frac{1}{\sigma^2} \cdot \frac{GM(r)}{r^2}, \tag{1.25}$$

in which σ denotes the line-of-sight velocity dispersion of the member galaxies. We see immediately that the gas density ρ_g follows the total density ρ to some power: $\rho_\mathrm{g} \propto \rho^\beta$. Since the isothermal distribution of ρ can be described with

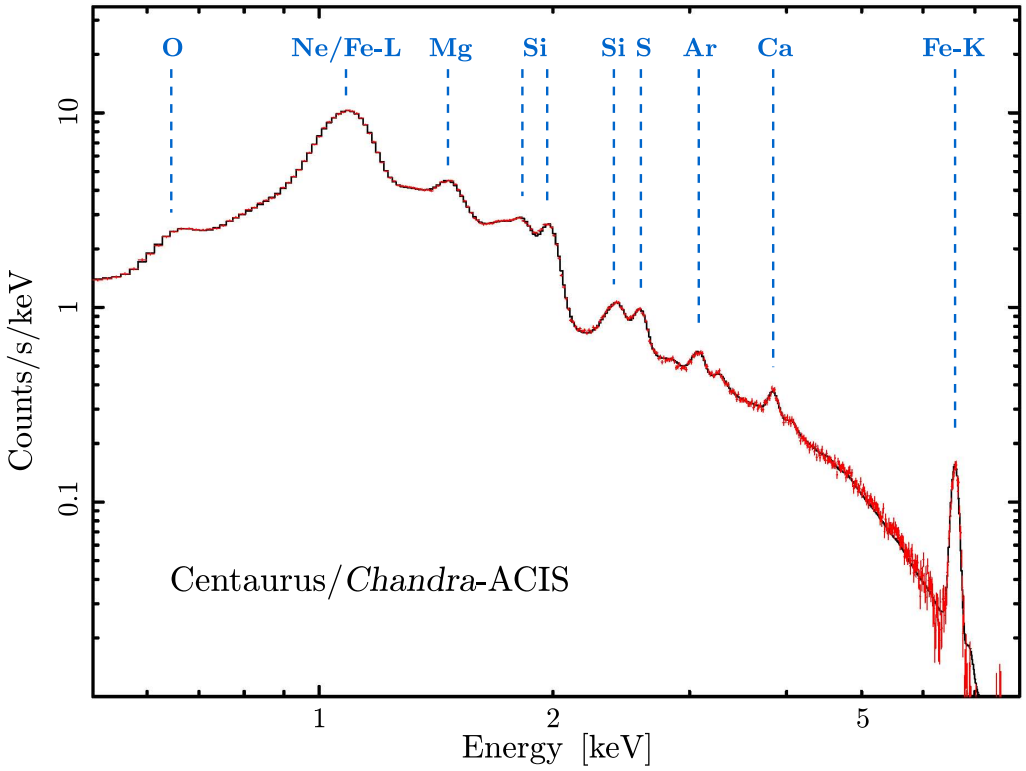

Figure 1.7. X-ray spectrum of the Centaurus cluster observed by *Chandra* ACIS. The data with a total clean exposure of ~ 660 ks are taken from the *Chandra* data archive. The black solid line shows the best-fit double-`vapec` model in Xspec. Emission lines with high S/N have been marked. Note the iron K_α line complex at 6.7–6.9 keV. Credit: Ang Liu.

the so-called King model [171, 172]:

$$\rho(r) \propto \left[1 + \left(\frac{r}{r_\mathrm{c}}\right)^2\right]^{-3/2}, \tag{1.26}$$

$\rho_\mathrm{g}(r)$ is therefore:

$$\rho_\mathrm{g}(r) = \rho_0 \left[1 + \left(\frac{r}{r_\mathrm{c}}\right)^2\right]^{-3\beta/2}. \tag{1.27}$$

Equation (1.27) is called the β-model [47, 48, 147, 327]. The surface brightness distribution $I(R)$ at a projected radius R can be described as [132]:

$$I(R) = 2 \cdot \int_R^\infty \frac{\epsilon(r) \cdot r}{\sqrt{r^2 - R^2}} \mathrm{d}r \propto \left[1 + \left(\frac{R}{r_\mathrm{c}}\right)^2\right]^{(-3\beta+1)/2}, \tag{1.28}$$

where the emissivity should be measured from spectral analysis. Therefore, the β-model has been used to fit both the density and surface brightness profiles since the era of *Einstein*. More recent observations of e.g. ROSAT, *Chandra*, and XMM with high-spatial resolution have detected a surface brightness excess (see the discussion of 'cooling flow' later in this section) in the center of a number of clusters [98, 95], and now a double-β model is adopted more frequently. On the other hand, some more complex models [388, 63] are also introduced for cases where a β-model cannot fully fit the surface brightness distribution, such as the steeper slopes in the core and the outskirts. These modified models are particularly critical for an accurate measure of the mass distribution in galaxy clusters, e.g. the dark matter concentration, and the total hydrostatic mass, etc.

Mass of galaxy clusters

It is not difficult to find that Equation (1.23) provides a practical way to measure the total mass of a cluster within a given radius:

$$M(r) = -\frac{k_{\rm B}Tr}{G\mu m_{\rm p}}\left(\frac{{\rm d}\ln\rho_{\rm g}}{{\rm d}\ln r} + \frac{{\rm d}\ln T}{{\rm d}\ln r}\right), \tag{1.29}$$

where $\rho_{\rm g}$ is the gas density, and can be computed from the electron density: $\rho_{\rm g} = n_{\rm e} m_{\rm p} A/Z$, where $A \sim 1.4$ and $Z \sim 1.2$ are the average nuclear charge and mass for ICM with 0.3 solar abundance [226]. Mass measured using this method is called the hydrostatic mass. Clearly, accurate measurements of the hydrostatic mass require highly resolved temperature and density profiles. Therefore, this method was not applied widely until the launch of high resolution X-ray facilities. The traditional way to measure the mass of a cluster is using the velocity dispersion of the member galaxies based on the virial theorem [53, 408], and the mass measured in this way is referred as the 'virial mass'. Let T be the kinetic energy of the galaxies, and V the gravitational potential energy, we have:

$$2T + V = 0, \tag{1.30}$$

and

$$T = \frac{1}{2}\sum_i m_i v_i^2,\ V = -\frac{1}{2}\sum_{i\neq j}\frac{G m_i m_j}{r_{ij}}, \tag{1.31}$$

where i, j denote the i-th and j-th galaxies in the cluster. The total mass of the cluster can be defined as $M_{\rm tot} = \sum m_i$. Note here $\sum m_i$ is not the total

mass of the galaxies, because we are only regarding galaxies as test particles. Then we can define the mass-weighted velocity dispersion:

$$\langle v^2 \rangle \equiv \frac{1}{M_{\rm tot}} \sum_i m_i v_i^2, \tag{1.32}$$

and the gravitational radius:

$$r_G \equiv 2M_{\rm tot}^2 \left(\sum_{i \neq j} \frac{m_i m_j}{r_{ij}} \right)^{-1}. \tag{1.33}$$

Then, applying the virial theorem we have:

$$M_{\rm tot} = \frac{r_G \langle v^2 \rangle}{G}. \tag{1.34}$$

Provided that the positions of the galaxies and the directions of their velocity vectors are uncorrelated, we have $\langle v^2 \rangle = 3\sigma^2$, where σ is the line of sight velocity dispersion, and $r_G = \frac{\pi}{2} R_G$, where

$$R_G = 2M_{\rm tot}^2 \left(\sum_{i \neq j} \frac{m_i m_j}{R_{ij}} \right)^{-1}, \tag{1.35}$$

and R_{ij} is the projected separation between the galaxies i and j. Finally we can write the total mass as:

$$M_{\rm tot} = \frac{3\pi R_G \sigma^2}{2G} = 1.1 \times 10^{15} M_\odot \left(\frac{\sigma}{1000 \text{ km s}^{-1}} \right)^2 \left(\frac{R_G}{1 \text{ Mpc}} \right). \tag{1.36}$$

From Equation (1.36), we can estimate that rich clusters with typical values of $\sigma \sim 1000$km s^{-1} and $R_G \sim 1$ Mpc has a total mass of $\sim 10^{15} M_\odot$. However, this value is surprisingly high compared to the total optical luminosity of member galaxies of a cluster $L \sim 10^{13} L_\odot$. The typical mass-to-light ratio of clusters $(M_{\rm tot}/L_{\rm tot})/(M_\odot/L_\odot)$ are found to be at least a magnitude higher than the typical values for early type galaxies. Therefore, galaxy clusters must contain a significant fraction of matter not accounted for the visible stellar mass in galaxies (including the small amount of cold gas and dust present in cluster member galaxies). First discovered in the Coma cluster by Zwicky in 1933 [408, 409], this finding paved the way to the dark matter hypothesis. As we already discussed, including the contribution of the ICM mass, which is anyway of the order of 5 times the stellar mass, is not sufficient to explain the dynamical

cluster mass. Today, we assume that dark matter constitutes ∼85% of the total mass in a cluster, and the ICM constitutes 10–15%, while only several percent of the mass is in the form of stars residing in the galaxies. This is the standard picture we will assume throughout the paper when describing the dynamical structure of galaxy clusters. The dark matter hypothesis clearly requires the existence of one or more particles beyond the standard model, motivating a large number of complex experiment aiming at the direct detection of the dark matter particles [103, 286]. Other line of research may provide the solution to the dark matter riddle by eliminating the need for this additional mass component through a modified gravitational theory [321], but this treatment is generally in tension with the X-ray appearance of X-ray clusters [320, 284].

Cooling flows

Equation (1.20) indicates that the bremsstralung emission of the ICM is strongly dependent on its density, and weakly on its temperature. From the density and temperature, we can compute the cooling time of the gas $t_{\rm cool}$, defined as the gas enthalpy divided by the energy loss per unit volume:

$$t_{\rm cool} = \frac{\frac{5}{2} n_{\rm e} k_{\rm B} T}{n_{\rm e}^2 \Lambda(T, Z)}, \tag{1.37}$$

where $\Lambda(T, Z)$ is the cooling function associated with the energy density emitted by a radiative cooling ICM with a given temperature and metallicity [29, 361]. As the gas loses its internal energy, it rapidly cools down. When the density is so high that $t_{\rm cool}$ is shorter than the life time of the system, a so-called 'cooling flow' should naturally form [185, 97, 98, 95]. A 'cooling flow' is characterized by the total amount of baryonic mass completely cooling from the ICM temperature down to 10^4 K, the mass deposition rate $\dot{M}$.

The early evidence for potential cooling flow was first discovered in the Perseus cluster, where the X-ray surface brightness in 0.5–1.5 keV was found to be sharply peaked in a small region around the central galaxy NGC 1275 [101]. Follow-up observations confirmed that the gas density in the center of the Perseus cluster was extremely high, forming a prominent peak in the X-ray image [146, 35]. The discovery of cooling gas, then, extended from the case of Perseus to larger samples of clusters. Cooling flows were identified in the center of half of the *Einstein* clusters [352, 7]. More than 70% of 55 ROSAT clusters

were found to host a cooling flow, and the cooling gas was estimated to have existed for billions of years [271]. Later studies based on higher-quality data and larger samples also presented similar conclusions [276, 390, 323, 387, 155]. Although recent results based on SZ-selected clusters have proved that X-ray selected sample is biased toward cooling-flow clusters, their fraction is still >30% after removing the bias [305], showing that cooling flows are a common structure in clusters.

However, a direct prediction of a cooling flow is the presence of gas at any temperature in order to have a roughly constant and continuous mass flow across the entire temperature range. The predicted amount of gas mass at a given temperature in a cooling flow will be rapidly decreasing with decreasing temperature, simply because the cooling is faster and faster at lower temperature and, therefore, if at a constant pressure, higher density. This can be easily quantified in the isobaric cooling flow model. Therefore, assuming the cooling proceeded isobarically, the ICM would be doomed to cool rapidly, forming a cooling flow with a mass deposition rate $\dot{M}$ that can easily reach 100–1000 $M_{\odot}$/yr, as directly derived from the total X-ray luminosity of the core region. Among the unavoidable consequences, one would expect a large amount of cold gas falling on to the BCG, doomed to form stars due to its low temprature and high density, and, therefore, a star formation rate (SFR) comparable to the predicted $\dot{M}$. However, the observed SFRs in BCGs are modest, of the order of few $M_{\odot}$/yr, consistent with being entirely fueled by the stellar mass loss from the BCG itself [392]. In addition, the amount of cold gas has been known since long time to be much lower than that expected from the high cooling-flow rates, thanks to the measurements of CO emission from molecular gas and other observables [230, 83, 355, 89]. This observational evidence created significant tension with the isobaric cooling-flow model since the very beginning, and received no explanation for more than a decade, stimulating the developements of more complex scenarios.

The final blow to the isobaric cooling-flow paradigm was given by the observations with the reflection grating spectrometer (RGS) onboard XMM-Newton, whose high-resolution spectra of cluster cores showed the absence of the metal emission lines associated to gas cooler than 1/3 of the virial temperature [274, 273]. These findings imply that the bulk of the gas in the

core must be prevented from cooling by some heating mechanisms, leaving only a minority of the ICM, if any, available for complete cooling. Therefore, the 'cooling flow' model was then superseded by the 'cool core' picture [245], and a reheating process (or sum of processes) generally termed 'feedback' became a key ingredient for the thermodynamic of the ICM, as well as of galaxy formation in general.

Clusters with or without a cool-core differ a lot not only in morphology, but also in thermodynamic and chemical properties. The most prominent feature of a cool-core cluster is a central peaked X-ray surface brightness distribution (see Figure 1.4 for example). In particular, the strength of the peak can be quantified with some characteristic parameters. Among them, the most commonly used is the surface brightness concentration ($c_{\rm SB}$) [324], defined as the ratio of the total flux within two different apertures:

$$c_{\rm SB} \equiv \frac{S(r < r_{\rm in})}{S(r < r_{\rm out})}. \tag{1.38}$$

The parameter $c_{\rm SB}$, despite its simplicity turns out to be effective to classify clusters morphologically [45, 200]. When used as an indicator of cool core, $r_{\rm in}$ and $r_{\rm out}$ are usually set to 40 kpc and 400 kpc. Obviously, the radii 40 kpc and 400 kpc are merely empirical estimates of the size of the cool core, and the cluster bulk radius. Nevertheless, observations have verified that $c_{\rm SB}$ is a good probe of cool core in both low- and high- redshift clusters. In addition to the sharp peak in surface brightness, cool-core clusters present many other observational features, including a central drop of the temperature profile, which is just what the name 'cool core' denotes, and a central peak in metal distribution. We will discuss the metal distribution in cool-core clusters in detail in the next sections.

Feedback

The heating mechanisms (or feedback) of cool core has been under debate for many years. Many candidates have been proposed as contributors of the heating process, such as cosmic rays [31], supernovae explosions [76, 188], dissipation of gas turbulence induced either by buoyancy of bubbles inflated by the central AGN or by minor and major mergers [229, 96, 178, 145, 117, 115, 118], or a combination of mixing and heating associated to vortices formed during the inflation of the bubbles [149]. The large amount of mechanical energy stored in

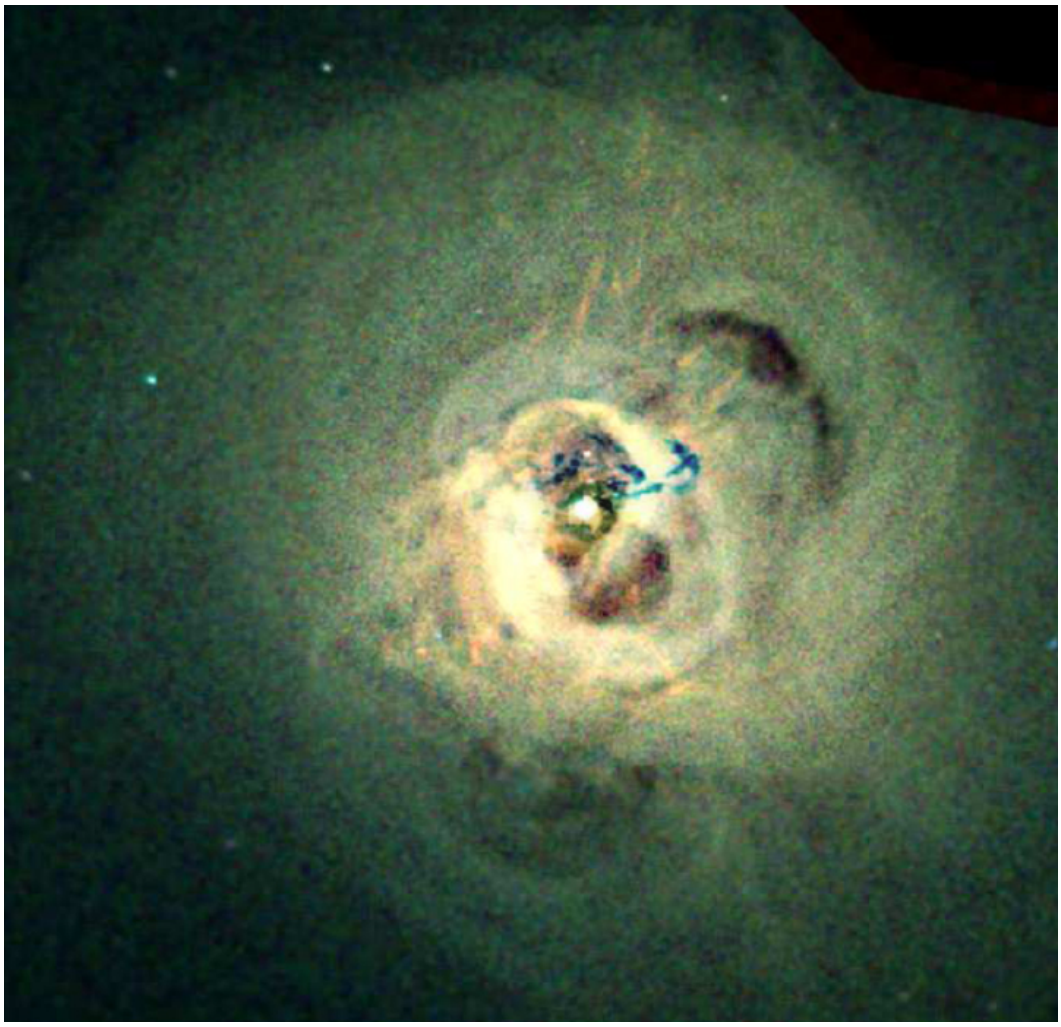

Figure 1.8. *Chandra*-ACIS X-ray image of the core of Perseus cluster [100]. The total exposure time of the 13 pointings used to produce this image is ∼1 Ms. Color code: 0.3–1.2 keV (red), 1.2–2 keV (green) and 2–7 keV (blue) bands. Note the cavities and ripples presented on the image. The blue structure near the center is caused by absorption of an infalling high-velocity foreground system.

the bubbles carved in the ICM by radio jets, makes AGN feedback the strongest candidate as the main heating source. Thanks to the unprecedented angular resolution of *Chandra*, the detailed X-ray image of the Perseus cluster (see Figure 1.8) presented for the first time a clear view of the complex structures arising in the ICM due to AGN feedback, such as cavities and ripples [99, 100]. Recently, the observations of the Perseus cluster with *Hitomi* provided a

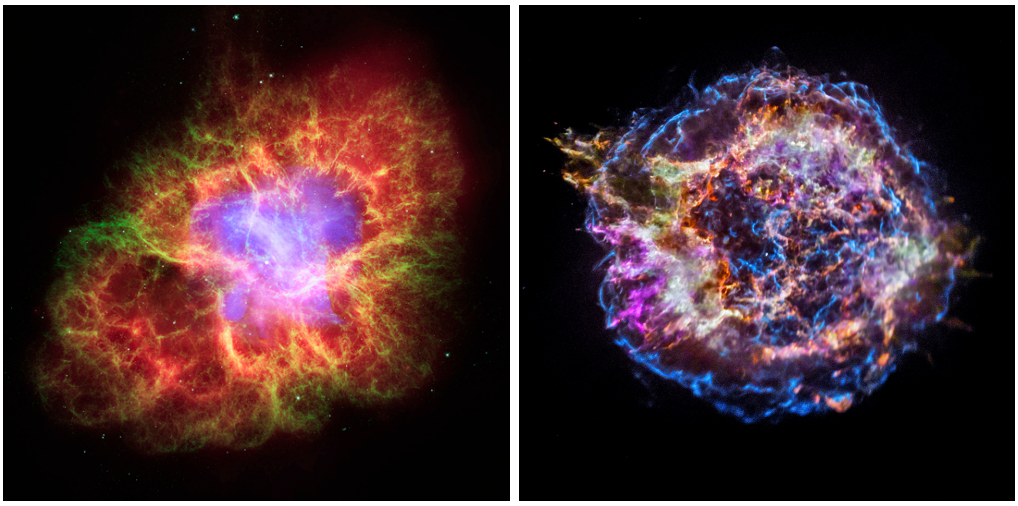

Figure 1.9. Left: Composite image of the Crab Nebula, remnant of a type Ia supernova exploded ∼1000 years ago. The X-ray image of *Chandra* is shown in light blue, the optical images observed by the Hubble Space Telescope are in green and dark blue, and the infrared image by Spitzer Space Telescope is in red. Credit: X-ray: NASA/CXC/ASU/J.Hester et al.; Optical: NASA/ESA/ASU/J.Hester and A.Loll; Infrared: NASA/JPL-Caltech/Univ. Minn./R.Gehrz. Right: X-ray image of the Cassiopeia A (Cas A), remnant of a core-collapse supernova. Color codes denote different elements ejected by the supernova. Credit: NASA/CXC/SAO.

unique measurement of the ICM dynamics associated to the feedback process [150]. This increasing amount of evidence clearly shows that the dynamics and thermodynamics of the ICM are strongly affected by AGN feedback, although the discussion on the heating process is still open, and we are far from having a coherent picture of the cycle of baryons in cool cores. In this framework, the study of the chemical properties of the ICM in different conditions can provide a key ingredients in term of tracking the chemical enrichment patters associated direcly or indirectly to the feedback processes.

1.2.3 Enrichment study of the ICM with X-ray data

Studying the chemical enrichment of galaxy clusters and their ICM is of great importance in many aspects. The cosmic evolution of the global metal abundance of the ICM is crucial in understanding its cumulative enrichment history, and hence the star formation in cluster galaxies. Metallicity measurements

in cluster outskirts also provide important constraints on the cosmic star formation history at early epochs ($z \sim 2$) even before the formation of the cluster itself. Additionally, tracing the evolution of ICM metallicity can help in constraining the SNe explosion rates in cluster galaxies [234, 342]. The ratio of the abundances of various ions provides important clues on the nucleosynthesis products of type Ia supernovae (SNIa) and core-collapse supernovae (SNcc), which eject different sorts of heavy elements [395, 202, 210].

Regarding to the spatial distribution of metals, the forming of the metallicity peak in the center of clusters are strongly associated with the assembling of the BCG which is the main producer of metals near cluster center [68]. The large-scale spatial distribution of metals is a complex effect of a number of processes working on a variety of physical scales: gas motions driven by outflows of the central AGN [338, 299, 96], the sloshing of cool cores [217], stochastic gas motions [293], sinking of highly enriched low-entropy gas [59, 60], galactic winds [372, 300], etc. Therefore, investigating the spatial distribution of metals in the ICM and determining the concrete role and amount of contribution of each process will deepen our understanding on their physics.

The origin of iron in the ICM

Iron is the only element that has been detected in all clusters from $z \sim 0$ to $z > 1.5$ [303, 377, 378], up to $z \sim 2$ but with only 2.6σ confidence level [208], whereas the significant detection of other metals requires either lower temperature ($kT < 3$ keV) or high S/N spectra. Therefore, precise measurements of the abundance of other metals are often confined in low-temperature or low-redshift clusters [67, 366, 315, 235], and the enrichment study of galaxy clusters has mostly focused on iron.

Iron (and iron group elements, Co and Ni) in the ICM are produced by supernovae explosion, including SNIa and SNcc (see Figure 1.9). Despite the highly successful application of SNIa as standard candles in cosmology, the explosion mechanism of SNe has not been fully understood [154, 211, 212]. According to a widely accepted model so far [148, 224, 344, 212], the progenitor of a SNIa is a white dwarf of carbon-oxygen (C/O) composition, who is accreting mass from a companion star in a binary system. When the mass of the white dwarf reaches the Chandrasekhar limit ($\sim 1.44 M_{\odot}$), high temperature causes

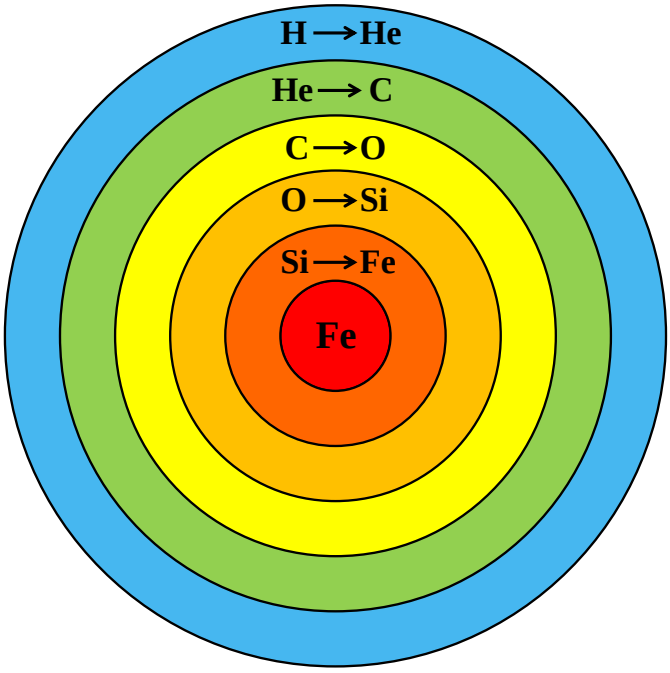

Figure 1.10. A sketch diagram showing the onion-like structure of a massive star before core-collapse, with shells of successively lighter elements burning around an Fe core. Credit: Ang Liu.

the ignition of carbon in the central region, which then leads to a thermonuclear explosion. In this event, iron is produced by explosive fusion and the white dwarf is disintegrated, releasing Fe and all the other products in the surrounding medium. However, the precise nature of the progenitors and the explosion mechanism of SNIa is still under debate. For example, the companion star of the C/O white dwarf can be either a main-sequence star (namely the single-degenerate scenario), or another white dwarf (the double-degenerate scenario) [250]. These different models [161, 203, 333, 105] provide different yields of elements. For a comprehensive introduction on these aspects, see the recent reviews [212, 251].

SNcc originate from the rapid core-collapse and violent explosion of massive stars with mass higher than $\sim 8 M_{\odot}$. To support the self-gravity of the star, elements like helium, carbon, oxygen, silicon are eventually synthesized and ignited in the core, forming concentric layers of elements from lighter to heavier

(see Figure 1.10 for a sketchy diagram of a SNcc progenitor). This evolutionary path comes to an end when an iron core is formed so that further nuclear fusion is not sufficient to provide thermal pressure to support the self gravity of the star. The iron core keeps growing as the nuclear fusion in the outer layers continues, and when its mass finally reaches the Chandrasekhar limit, the core then collapses and the outer layers fall inward. When the core stops collapsing due to neutron degeneracy, the outer layers crash into the core rapidly, and then are violently pushed back by the shock wave, ending with a violent explosion. In this scenario, the iron-peak elements are mostly compressed into the neutron star or black hole formed during the supernova explosion event, and the explosion mainly ejects the lighter elements in the outer layers, such as oxygen, neon, magnesium, silicon, and sulfur, into the surrounding medium. There are a number of SNcc yield models in the literature, with some of them commonly adopted in the literature to interpret the observed abundance patterns [49, 252, 250, 356].

Clearly, the yields of SNIa and SNcc depend not only on the models, but also the initial property of the progenitor star, such as its metallicity, and mass. Therefore, the yields should be calculated by integrating the yield model over the initial mass function (IMF) of a stellar population. The most widely used IMSs are 'Salpeter', or 'bottom-heavy' [311], which is a power-law with a slope of -1.35 or steeper, and 'top-heavy', with a shallower slope (e.g. [6, 64]).

In Figure 1.11 we show an example of yields of SNIa and SNcc calculated from models in the literature. It is possible to see the difference between the yields of the two types of supernovae: while SNcc are likely to be the major producer of lighter elements such as oxygen, neon, magnesium, aluminum, silicon, and sulfur (α-elements), heavier elements like iron, nickel, and calcium are mostly ejected by SNIa (see also [69]). This is considered a general trend, despite the accurate ratios differ in different yield models. Therefore, the abundance ratios between α-elements and iron can also be used to constrain the relative contribution of SNIa and SNcc to the enrichment of the ICM [395]. However, despite early works reported increasing SNIa contribution towards the center [106, 291], recent results are consistent with a constant ratio [365, 329, 240, 222]. Therefore the accurate ratio of the contributions of SNIa and SNcc to ICM enrichment is still under debate.

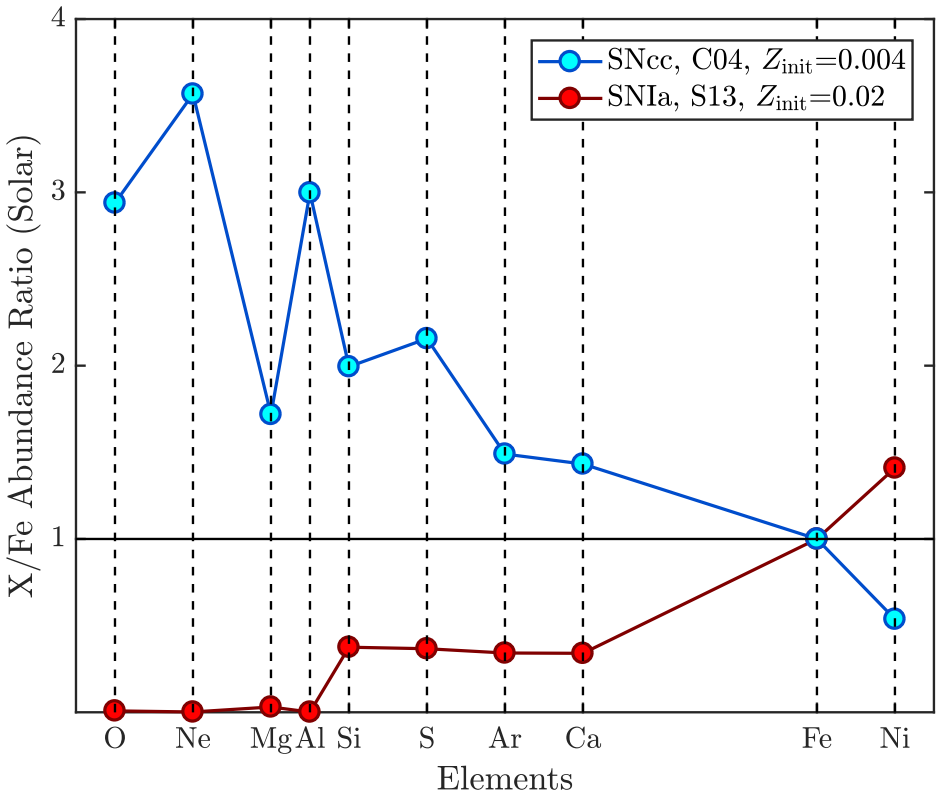

Figure 1.11. Yields of elements relative to iron for SNIa and SNcc calculated from models in the literature. For SNIa, the yield model is from Seitenzahl et al. (2013) [333], with $Z_{\rm init} = 0.02$. For SNcc, the yield model is from Chieffi & Limongi (2004) [49], with $Z_{\rm init} = 0.004$, integrated over a Salpeter IMF from 10 to 50 $M_{\odot}$. The Solar abundances are from Asplund et al. (2009) [12]. Credit: Ang Liu.

Cosmic evolution of ICM iron abundance

The chemical enrichment history of galaxy clusters is a fundamental and complex problem and it has been debated for a long time. The main problem is the great difficulty in the observation of high redshift clusters in X-rays. Despite the early attempt made in 1997 by Mushotzky et al. [248] with *ASCA*, systematic studies was made possible only after the launching of XMM–Newton and *Chandra*. In 2003, with the combined data of *Chandra* and XMM–Newton for 18 clusters, Tozzi et al. [376] measured for the first time the global iron abundance in the ICM of clusters out to redshift larger than 1. Using a

combined spectral fit of cluster subsamples in different redshift bins, Tozzi et al. investigated the evolution of the mean abundance with cosmic epoch. As a result, they found that the mean iron abundances at $z \sim 0.8$ and $z \sim 1.2$ were $Z_{\rm Fe} = 0.25^{+0.04}_{-0.06} Z_{\odot}$ and $Z_{\rm Fe} = 0.21^{+0.10}_{-0.05} Z_{\odot}$, respectively. Given the local value of $Z \sim 0.3 Z_{\odot}$ [295, 66], the results suggested no significant evolution of the mean iron abundance since $z \sim 1.2$.

In a follow-up work in 2007, Balestra et al. [17] extended the sample to 56 clusters, covering a temperature range of 3keV $\leq kT \leq$ 15keV and a redshift range of $0.3 \leq z \leq 1.3$, which was further divided into five redshift bins. They found that the average iron abundance within $(0.15–0.3) R_{\rm vir}$ remained constant at $Z_{\rm Fe} \sim 0.25 Z_{\odot}$ for clusters at redshift $z > 0.5$, but significantly increased to $Z_{\rm Fe} \sim 0.4 Z_{\odot}$ in the redshift range $0.3 < z < 0.5$. The decrease in $Z_{\rm Fe}$ with redshift can be parameterized by a power law of the form $Z_{\rm Fe,0}(1+z)^{-1.25}$. However, either Balestra et al. (2007) or earlier works seem to suffer from the low S/N of the data, and limited by the volume of cluster sample. For example, in Balestra's sample, $\sim 1/3$ of the 56 clusters, and almost all the clusters at $z > 1$, provide less than 1000 net photons in the data, which makes the measurement of the abundance extremely challenging. Given the above caveats, the results of these works must be verified by larger sample and deeper observations.

Nevertheless, the evolutionary signal detected in Balestra et al. (2007) was soon confirmed in 2008 by Maughan et al. [223] who assembled a sample of 115 clusters covering the redshift range $0.1 < z < 1.3$ with the archived *Chandra* ACIS–I observations, which was the largest X-ray selected cluster sample at that time. The abundances of the clusters presented a significant evolution with redshift, increasing by a factor of 2 from $z \sim 1$ to $z = 0.1$ (see Figure 1.12). Although their sample suffered an apparent absence of relaxed clusters at $z > 0.5$, which may bias the result, the evolution was still present (although less significant) when the cluster cores were excluded from the abundance measurements, indicating that the evolution is not solely due to this selection effect. A spatially resolved analysis is made by Ettori et al. (2015) [92]. With a sample of 83 clusters in the redshift range [0.09–1.39], Ettori et al. measure the metallicity of the ICM in three radial bins (0–0.15, 0.15–0.4, > 0.4) r_{500}. They also make a comparison between cool-core and non-cool-core clusters

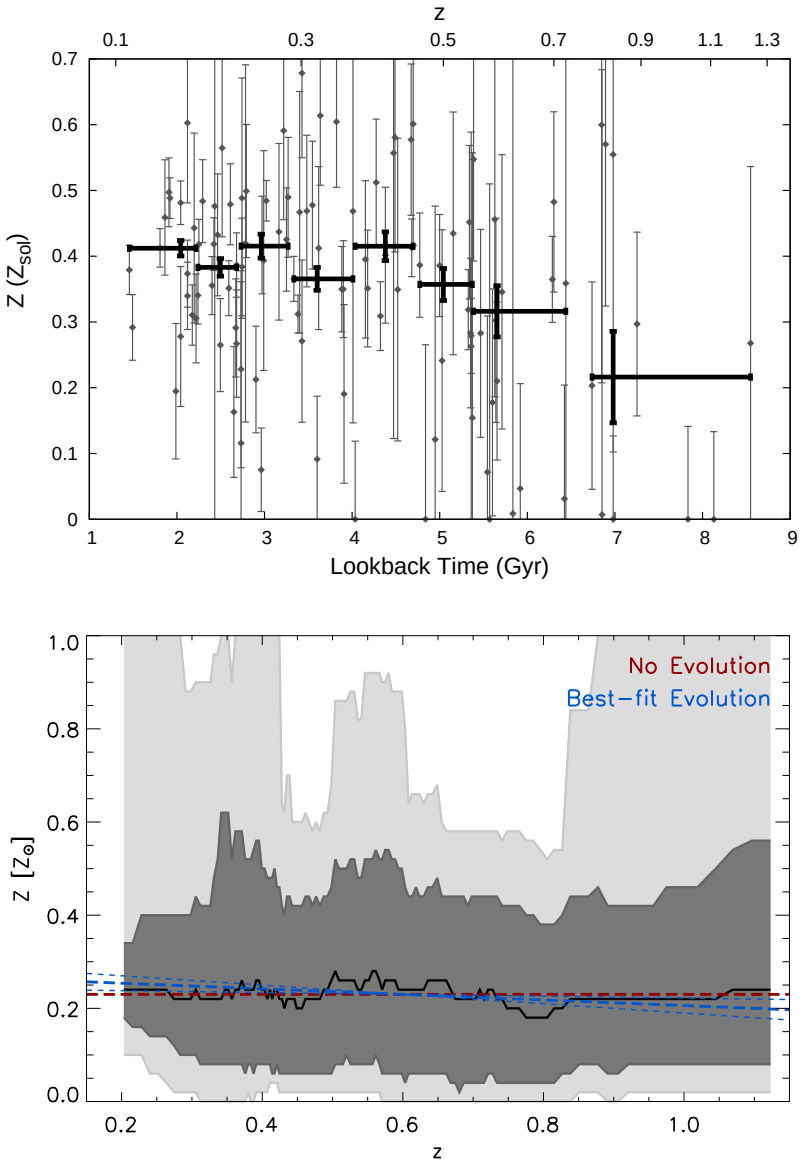

Figure 1.12. Upper panel: ICM abundance within r_{500} as a function of redshift presented by Maughan et al. (2008) [223] based on a sample of 115 *Chandra* clusters. All emission within r_{500} was used when measuring the abundance, despite that the total emission were in fact strongly dominated by the photons within $0.5r_{500}$. Lower panel: ICM abundance (within r_{500}) as a function of redshift based on 153 SPT-SZ clusters [227]. Each redshift bin contains the nearest 21 clusters in redshift space. Black solid line shows the median value of that bin. Dark and light grey show the 1σ (68%) and 2σ (95%) confidence regions, respectively. The horizontal red line shows a non-evolving abundance, while the blue lines show the best-fit model in the form of $Z \propto (1+z)^{\gamma}$. This figure shows that both the scatter and median values are well-fit by a non-evolving model.

in the sample. They find a significan evolution of the ICM metallicity in the inner bin only for cool-core clusters, while no evolution is observed for regions above the core ($r > 0.15r_{500}$).

In recent years, the redshift-independent SZ cluster samples also play an important role in the study of chemical evolution of the ICM. The first attempt of seeking ICM metallicity evolution in a SZ selected sample was made by McDonald et al. [227] in 2016. Their sample contains 153 clusters observed with the *Chandra*, XMM-Newton, and *Suzaku*. These clusters, which span a redshift range [0–1.5], were drawn from a larger, mass-selected sample of clusters discovered in the 2500 square degree South Pole Telescope Sunyaev Zel'dovich (SPT-SZ) survey. McDonald et al. found that the global ($r < r_{500}$) ICM abundance presented no strong evolution ($dZ_{\rm Fe}/dz = -0.06 \pm 0.04 Z_{\odot}$), with a mean $Z_{\rm Fe}$ of $0.23 \pm 0.01 Z_{\odot}$ at $z = 0.6$ (see Figure 1.12). This result is consistent with an early enrichment picture, implying that the bulk of iron in the ICM is produced before redshift $z \sim 1$, with the comulative contribution of late enrichment being almost irrelevant with respect to the current observational uncertainties.

More recently, the early enrichment-only picture gets other supports from Mantz et al. (2017) [207] who doubles the size of the previous samples reaching a total of 245 SZ and X-ray selected clusters, which is the largest sample to date. Mantz et al. performed a spatially resolved measurement of the ICM metallicity. They find that the data at large radii ($0.5–1r_{500}$) are consistent with a constant metallicity, while the data at intermediate radii ($0.1–0.5r_{500}$) suggest a late–time but weak ($< 20\%$) enrichment, consistent with the expected production and mixing of metals in cluster cores. In the center of the clusters, the metallicity shows larger scatter, with no evidence of global evolution. As we will see later, the spatial distribution of the iron will play a crucial role in the measurement of the evolution.

In addition to the studies discussed so far, there are further works on the chemical evolution of the ICM that we are not able to present in detail in this section [3, 5, 14]. To summarize all the contributions to this topic to date, we collect in Table 1.1 the constraints on the evolution of ICM abundance from the literature, both from X-ray and SZ selected samples which are based on ICM signatures. In summary, the evolution of the global abundance of ICM

Table 1.1. Summary of constraints of cosmic evolution of ICM abundance from the literature. [1] Reference; [2] Sample size and selection method; [3] Redshift range of the cluster sample; [4] Radial range used to measure the abundance in units of r_{500}; [5] Main claim on whether the ICM abundance evolves with redshift.

Reference	Sample	z	r	Claim
Tozzi et al. (2003) [376]	18 X-ray	0.3–1.3	0.15–0.30	Unclear
Balestra et al. (2007) [17]	56 X-ray	0.3–1.3	0.15–0.30	Yes
Maughan et al. (2008) [223]	115 X-ray	0.1–1.3	0.0–1.0	Yes
Baldi et al. (2012) [14]	39 X-ray	0.4–1.4	0.0–0.4	Unclear
Ettori et al. (2015) [92]	70 X-ray	0.1–1.4	0.00–0.15	Yes
Ettori et al. (2015) [92]	83 X-ray	0.1–1.4	> 0.15	No
McDonald et al. (2016) [227]	153 SZ	0–1.5	0.0–1.0	No
Mantz et al. (2017) [207]	245 SZ+X-ray	0–1.2	0.0–1.0	No

is still unclear, due to the poor constraints at large radii and high redshifts. In the redshift range of $0 < z < \sim 1$ that can be effectively investigated by the present data, the existence of evolutionary signal of ICM abundance seems to be associated to cluster samples selected via X-rays, while larger and more recent SZ-selected samples basically suggest a negligible evolution since $z \sim 1$. This would imply that the bulk of the iron would be dominated by early enrichment.

The origin of this discrepancy among data sets is reflecting the complex physics of the ICM and the details of the cluster selections. Except for the problem that the measurements of the properties of high redshift clusters have large uncertainties, a common shortcoming for X-ray selected samples is the selection bias toward cool-core clusters in low-z, and non-cool-core clusters in high-z [305], which is called the 'cool core bias'. A lot of evidence has been found that the average global abundance in cool-core clusters is significantly higher than that in non-cool-core clusters at comparable redshifts [66, 65, 186, 67]. Therefore, if the two types of clusters are mixed in the sample, the final results will be highly sensitive to the ratio of cool cores and

non-cool cores (CC/NCC). This effect is even worse in practice, due to the dearth of high redshift clusters in X-ray selected samples. Since the gradients of abundance profiles for cool-core and non-cool-core clusters are significantly different as well, a simple extraction of the inner core will not help much in the result. Furthermore, since the distributions of metals are not uniform in both cool-core and non-cool-core clusters, the results of the global abundance vary a lot with the radial range used for the measurement of abundance.

Some of the claimed evolution of 'global' abundance were, in fact, mimicked by the evolution of the broadening of metal distribution. Despite the very few studies on the evolution of abundance profiles from high- to low- redshifts, evidence has been found in some high redshift clusters that their abundance profiles are significantly less extended than those of low redshift clusters [68]. This effect may at least bias the results measured within a small radial range. To summarize, a general lesson from these complex results from the state of the art studies is that establishing a complete physical model of chemical enrichment of galaxy clusters requires a robust characterization of the spatial distribution of metals, not only the abundance, but also the total mass, as a function of redshift, halo mass, and thermodynamical properties of the ICM.

Spatial distribution of iron in the ICM

Both observations and simulations have confirmed an almost uniform abundance distribution in the outskirts ($r > 0.25r_{200}$ or $0.4r_{500}$) of galaxy clusters [66, 65, 339, 383, 341, 27, 199]. This is not surprising, because all the clusters observable in X-ray band so far form after the cosmic star formation peak at $z \sim 2$ [202]. The ICM in their outskirts have already been enriched before the formation of the clusters, thus we should observe a large-scale flat component in the outskirts of ICM abundance profiles.

In the center of galaxy clusters, especially in cool-core clusters, a prominent peak of iron abundance is ubiquitously found (see Figure 1.13, and [66, 65, 13, 186]). The total mass of iron in the ICM within a given radius r can be calculated by:

$$M_{\rm Fe}(<r) = 4\pi A_{\rm Fe} m_{\rm H} \int_0^r Z_\odot Z_{\rm Fe}(r) n_{\rm H}(r) r^2 {\rm d}r, \tag{1.39}$$

where $A_{\rm Fe}$ is the atomic weight of iron, $m_{\rm H}$ is the atomic unit mass, and

$$Z_{\rm Fe} = \frac{n_{\rm Fe}/n_{\rm H}}{n_{\rm Fe,\odot}/n_{\rm H,\odot}} \tag{1.40}$$

is the abundance of iron with respect to solar value. Therefore we can define an 'excess' in the iron mass by subtracting the mass of iron included in the flat profile from the total mass of iron iron. In the same way we can define an iron mass excess profile as follows:

$$Z_{\rm Fe}^{\rm exc}(r) = Z_{\rm Fe}(r) - Z_{\rm Fe}(r > R), \tag{1.41}$$

where we have set the radius R as the end of the iron peak. The iron peak in the center of cool-core clusters is often associated with the BCG, except in some case when the cluster is not dynamically relaxed. The frequent association of BCG and the iron peak makes the BCG the most likely candidate of the source of iron in cluster center [65, 113, 186]. Based on a sample of 22 nearby clusters observed with *BeppoSAX*, De Grandi et al. (2004) [65] found that the iron mass excess can be entirely produced by their BCGs, and that the iron excess, the optical magnitude of the BCG, and the temperature of the ICM are highly correlated, indicating a strong link between the BCG and the chemical enrichment of its host cluster. However, in some nearby clusters which have been well studied, the iron excess profiles are found to be more extended than the stellar light profiles of the BCGs [66, 221, 50], thus one or more processes must be taking place in diluting the iron from the BCG to the outer regions.

There are several possible mechanisms that are relevant to the diffusion of iron. The series of processes caused by the central AGN are undoubtedly the most likely candidates. These processes include the stochastic gas motions [293], and the formation of buoyant bubbles [338, 299, 96]. Kirkpatrick et al. (2011) [174] presented an analysis of the spatial distribution of metal-rich ICM in 10 clusters using deep observations from *Chandra*. The 2-D abundance maps in Figure 1.14 show that the high abundance ICM are closely aligned with the radio and cavity systems, consistently with being transported outward into the surrounding ICM by the AGN outflow driven by the radio jets. Simulations of AGN feedback also support this picture by showing that AGN outflows were able to transport the surrounding enriched gas at radii as large as hundreds of kpc [116, 283].

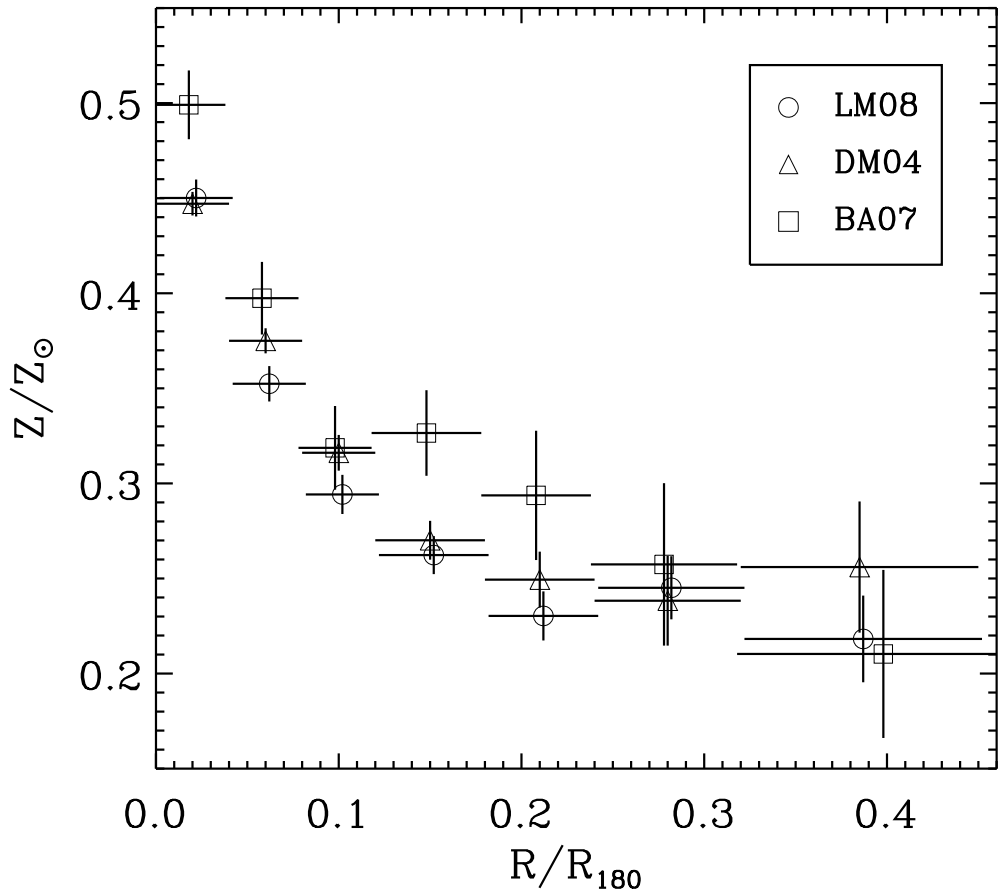

Figure 1.13. Average abundance profiles of galaxy clusters measured in three different works based on different sample and data: De Grandi et al. (2004) [65], 22 clusters observed by *BeppoSAX*; Baldi et al. (2007) [13], 12 clusters observed by *Chandra*; Leccardi & Molendi (2008) [186], 50 clusters observed by XMM-Newton. The figure is from Leccardi & Molendi (2008). Abundances are expressed in Anders & Grevesse (1989) [2] solar values, and are typically $\sim 30\%$ lower than the more recent measurements, e.g. in Asplund et al. (2009) [12].

In addition to the processes originated from the central AGN, larger scale ICM bulk motions, especially the sloshing of cool cores, may also play a relevant role in broadening the iron distribution. First observed by Markevitch et al. (2001) [218] in cluster A1795, cold fronts associated to sloshing are now commonly reproduced in simulations [50, 111, 371], and observed in several systems [217, 128, 340]. Simulations indicate that sloshing can be induced by

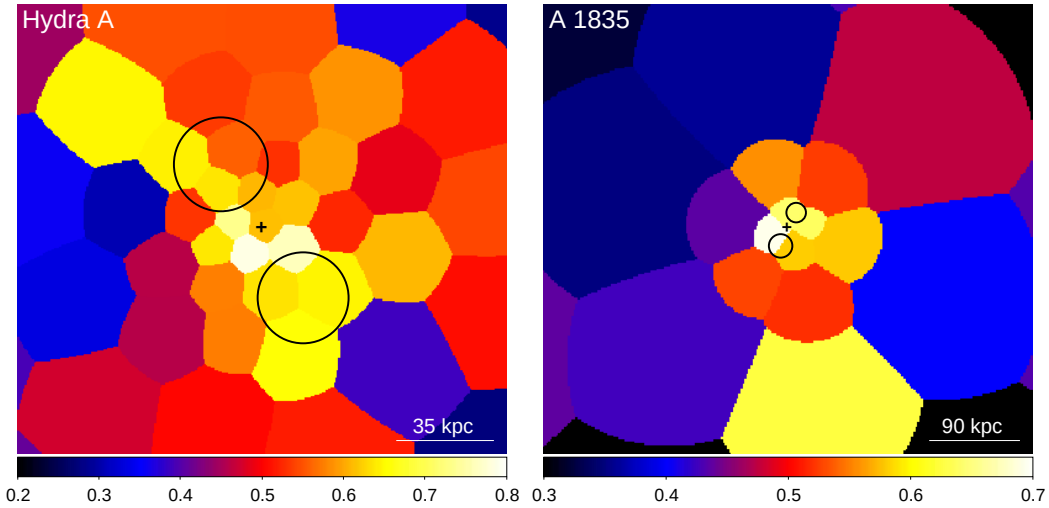

Figure 1.14. The abundance maps of galaxy clusters Hydra A and Abell 1835, adapted from Kirkpatrick et al. (2011) [174]. The black crosses indicate the approximate cluster centers. In both of the two clusters, the ICM with high abundance (colored in yellow and white) extended outwards approximately along the same axis of the cavities, whose estimated sizes and locations are shown by the black circles. This figure indicates that the dilution of iron in the ICM is highly linked to the AGN outflow.

any minor merger in cool core clusters, and can persist for several Gyrs [11], which makes it a promising candidate for the broadening of iron distribution. Evidence that shows gas-sloshing pushing highly enriched ICM out from the BCG to the ICM has also been found in A496 [126] and NGC 5044 [260].

Quantifying the broadening of iron distribution in the ICM and tracing its cosmic evolution are extremely challenging given the quality of current X-ray data, thus only a few attempts have been made so far. Baldi et al. (2012) [14] presented a spatially resolved analysis of the XMM-Newton X-ray spectra of 39 clusters at redshift $0.4 < z < 1.4$ to study how the abundance evolves with redshift not only by means of a single, global measurement, but also by spatially resolving the cluster emission. However, being limited by the angular resolution of XMM-Newton (HEW $\sim$ 15 arcsec), each cluster in the sample is divided into only two or three bins. The results confirm a significant negative trend of $Z_{\rm Fe}$ with radius, but no conclusive results on the evolution with redshift. Due to the sample size and the low statistics, no significant

conclusion about the broadening of iron distribution is possible.

More recently, De Grandi et al. (2014) [68] presented a detailed study of the iron distribution in the high-redshift cluster WARPJ1415.1+3612 at $z = 1.03$ based on *Chandra* observations. As a comparison sample, they also measure the iron profiles of six strong cool-core clusters at low redshift ($z < 0.09$) with the archived data of XMM-Newton. From the ICM iron abundance profiles of WARPJ1415.1+3612, they found that the iron abundance excess produced by the BCG was already in place at redshift $z \sim 1$, suggesting an enrichment epoch earlier than $z \sim 1$. Furthermore, combining the observed iron abundance profiles with those estimated based on the near-infrared (NIR) observations on the stellar emission, including the intracluster light (ICL), they found in WARPJ1415.1+3612 a good agreement between the iron distribution in the ICM and the light distribution of the BCG. On the contrary, when the same analysis is applied to the low-z cluster sample, the distribution of iron is found to be significantly broader than that of the NIR light of the BCGs, indicating that the processes responsible of the broadening the iron distribution in low–z clusters had not significantly shaped the iron distribution in WARPJ1415.1+3612 yet.

Recently, a structure named 'central iron drop' has been observed in a number of galaxy clusters and groups. This is a small-scale (of the order of 10 kpc) decrement of iron (and also other elements like silicon and sulfur) abundance at the center of the abundance peak. Interestingly, the central iron drop is observed usually in association with X-ray cavities [264], implying that the formation of this structure is probably associated with feedback processes in cool cores. One explanation is that the central iron drop is due to some mechanical processes, such as the direct removal of the metal-rich ICM from the core to outer regions, driven by the AGN outflows which create the cavities. Another explanation is the chemical scenario, in which the iron abundance drop is caused by the depletion of iron into dust grains in the central, high density regions [264]. Additionally, some other interpretations are also proposed [235], such as the inappropriate fitting of the non-thermal emission of the central AGN and its surroundings [316], and the underestimate of the helium content in cluster core [94], etc. In particular, the dust depletion scenario can be tested by comparing the abundance profiles of reactive elements, such as iron, silicon,

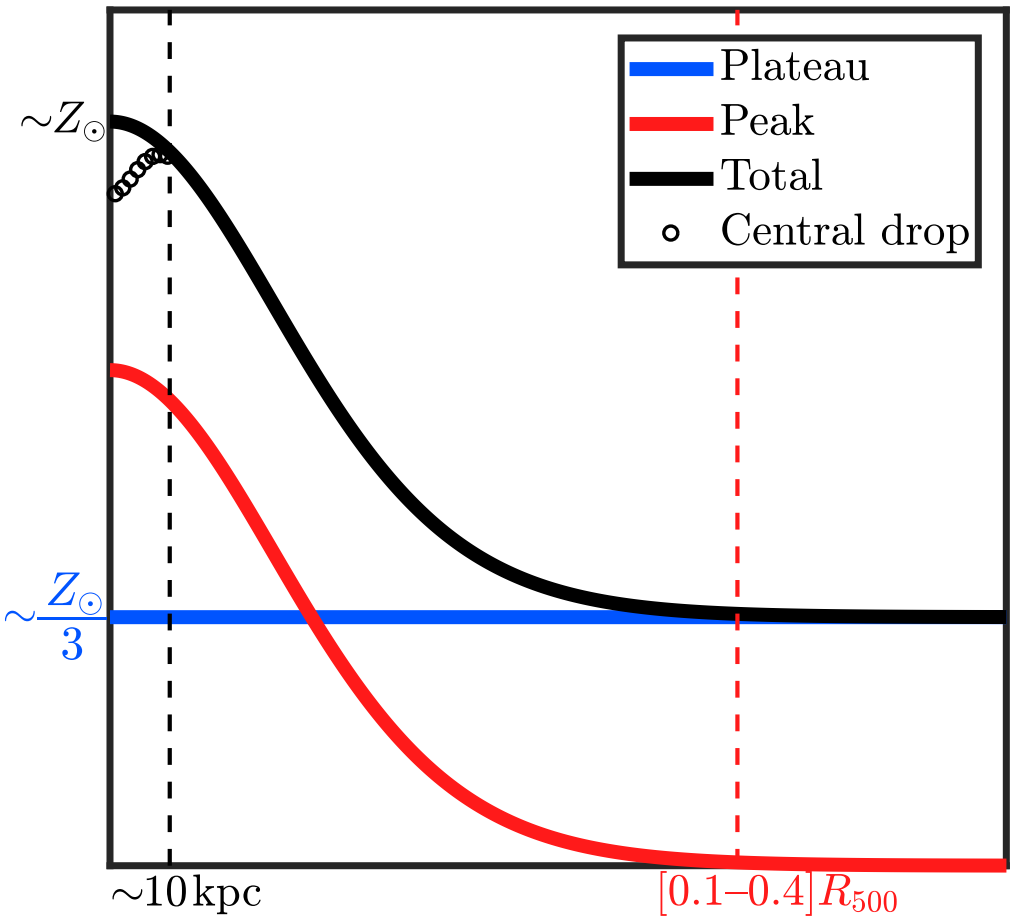

Figure 1.15. A toy-model showing the distribution of iron in the intracluster medium. An iron plateau across the whole cluster with a typical abundance of $\sim$1/3 solar value, and an iron peak on top of it, usually with an extent less than $0.4R_{500}$. In the very center ($\sim$10 kpc), an abundance drop may occur in a number of clusters (see Chapter 3 for more details in this aspect). However, the central abundance drop is not relevant to the measurement of the global iron abundance due to its small spatial scale. Credit: Ang Liu.

and sulfur, to noble elements which cannot be depleted into dust grains. If the dust depletion is really taking place, we should observe the usual central peak in the profiles of noble elements, instead of the central drop for reactive elements. There are two noble elements, argon and neon, that are detectable in the X-ray spectra of ICM. However, the emission line of neon is blended

with the dominant emission from the Fe L-shell complex in CCD spectra, therefore its abundance measured from low-spectral resolution CCD spectra is not reliable. On the other hand, argon can be firmly detected thanks to the isolated emission lines at ∼3 keV, thus the key point of the test is to compare the abundance profiles of iron and argon. We will make this test in Chapter 3 of this thesis.

We summarize our current knowledge about the spatial distribution of iron in the ICM using a simplified model which consists of two main components, as shown in Figure 1.15. One component in this model is the iron plateau, which is approximately a constant across the global cluster, with a typical value of about 1/3 of the solar abundance. This iron plateau is associated with early star formations, probably formed before or shortly after the formation of the cluster itself. On top of this iron plateau is an iron peak centered at the BCG, probably formed more recently due to the star formation activities in and around the BCG. Several processes, such as the gas turbulence and the AGN feedback activities, work continuously to transport the iron produced in the BCG to the outer regions. In the very center, a 'central iron drop' can be observed in a number of clusters, which is likely associated with feedback of cool cores, but has little impact on the global abundance of a cluster due to its very small scale.

1.2.4 Dynamics of the ICM

Mergers and infalling subhalos

According to the hierarchical structure formation picture, galaxy clusters form from a primordial density perturbation field, and evolve through a sequence of mergers and continuous mass accretion [177]. In particular, merging between halos frequently happens at early epochs and still occurs today. Such merging processes strongly affect the dynamics of clusters, often producing bulk motions in the hot ICM. The most prominent observational features of merging events between clusters are shocks, which indicate supersonic relative motions of ICM regions. Shocks in the ICM often creates sharp edges in the X-ray surface brightness, as well as discontinuities in pressure, and entropy (see Figure 1.16 for example). So far, violent merger shocks have been clearly ob-

served in a small number of clusters, such as the Bullet cluster [214], Abell 520 [215], and Abell 2146 [308, 309]. A much more frequently observed structure is the so-called cold fronts [389, 217, 128, 397], which are generated by subsonic motions of the ICM. Although both cold fronts and shock fronts appear as surface brightness edges, cold fronts show an approximately continuous pressure profile, in contrast to the large pressure jump of shock fronts.

Cold fronts have been observed not only in clusters with distinct signatures of mergers, but also in some regular cool-core clusters which is apparently relaxed. In these cases, cold fronts are produced by the 'sloshing' of the cool core, rather than the remnant of a major merger. The sloshing of the core is probably triggered by past minor mergers, where perturbers like infalling subhaloes perturbed the potential well and induced the sloshing of the gas. This scenario is supported by numerical simulations [371, 11]. In particular, Ascasibar et al. (2006) [11] found that sloshing can be induced by minor mergers and can persist for Gyrs, producing concentric cold fronts, but leaving no visible disturbance elsewhere, just as observed in many core-sloshing clusters, such as Abell 2142 [219], Abell 2204 [317], Abell 496 [37], and RXJ1720+26 [225].

Global rotation

Another possible source of motions of the ICM is global rotation. Clusters grow through continuous accretion of smaller halos following the filaments and walls in the large scale structure. Since the initial density field is isotropic and homogeneous, the halos should infall from random directions. Therefore, statistically, global rotation should not be widespread in galaxy clusters. However, in some special cases we can have some residual angular momentum left from the accretion, and this initial tidal torque can induce rotational motions. Additionally, a cluster might also be rotating if it experienced one or more off-axis major mergers during its lifetime. Simulations have shown that the total fraction of rotating clusters should be a few percent [16]. Dynamical analysis of cluster member galaxies also reports the evidence of rotation in a few clusters [157, 373, 205, 347], indicating that global rotation may give a small but non-negligible contribution when accounting for the dynamics of the ICM.

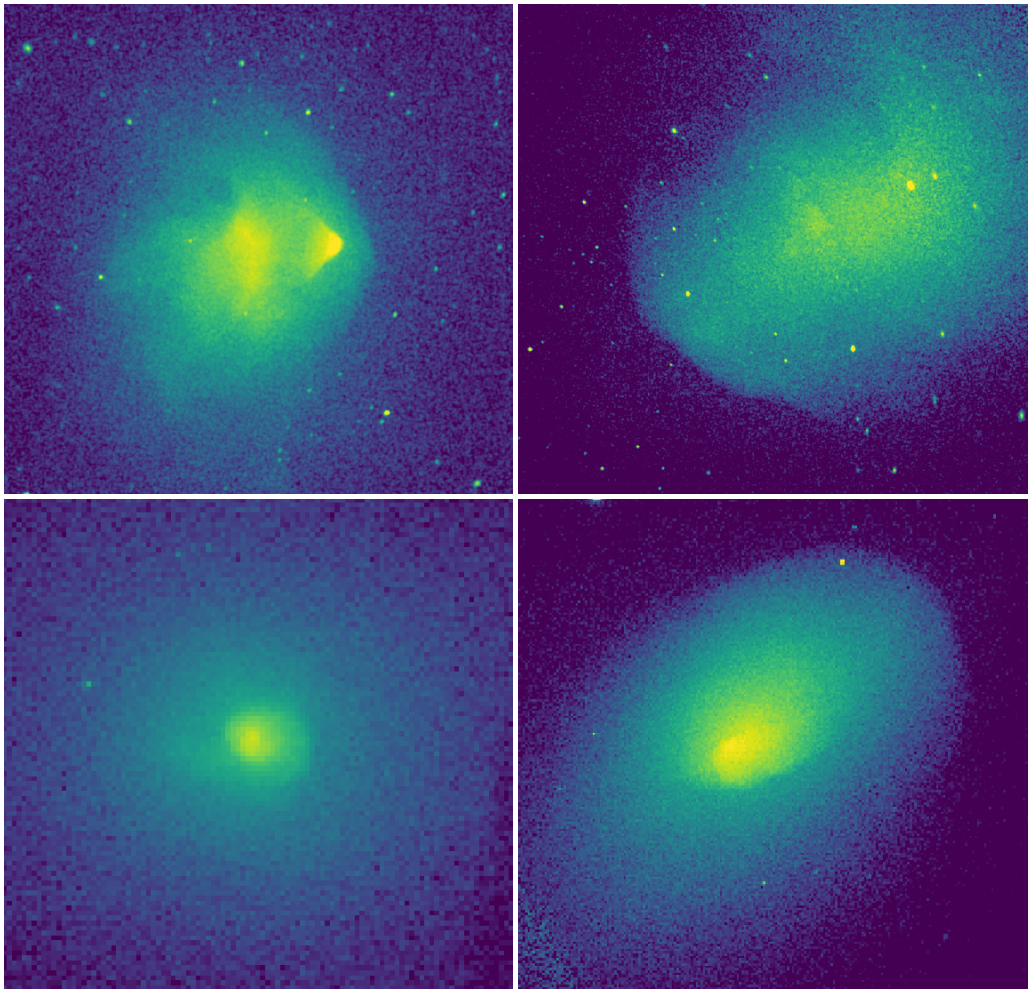

Figure 1.16. Surface brightness distributions of the Bullet cluster (upper left), Abell 3667 (upper right), Abell 2204 (lower left), and Abell 2142 (lower right). The sharp edges in this four clusters represent different cases: a supersonic merger shock in the Bullet cluster, a subsonic cold front in Abell 3667 produced by a major merger; a cold front generated by core sloshing in Abell 2204 and Abell 2142. However the case of Abell 2142 is still unclear, and is probably the result of the combined effects of multiple processes. This cluster will be treated in Chapter 5. Credit: Ang Liu.

Measuring the velocity of the ICM

The velocity of shocks or cold fronts on the plane of the sky can be determined thanks to the Rankine-Hugoniot relations [201] and from the

variations in density, pressure, and temperature of the gas across the edge. The shock velocity can be calculated from [183, 216]:

$$\Delta v_{\rm s} = \left[\frac{kT_0}{\mu m_{\rm p}}(1-C)\left(\frac{1}{C}\frac{T_2}{T_1}\right)\right]^{1/2}, \tag{1.42}$$

where indices 1 and 2 denote quantities of the pre-shock and post-shock gas, μ is the mean molecular weight, and $C \equiv \rho_2/\rho_1$ is the shock compression factor. From the conservation of mass, we have $\rho_1 v_1 = \rho_2 v_2$, thus $C = v_1/v_2$. C can be written as:

$$\frac{1}{C} = \left[\frac{1}{4}\left(\frac{\gamma+1}{\gamma-1}\right)^2\left(\frac{T_2}{T_1}-1\right)^2 + \frac{T_2}{T_1}\right]^{1/2} - \frac{1}{2}\frac{\gamma+1}{\gamma-1}\left(\frac{T_2}{T_1}-1\right), \tag{1.43}$$

where γ is the ratio of specific heats, which is $\gamma = 5/3$ for fully ionized plasma. C can also be measured from the X-ray surface brightness distribution at the shock. Using the compression C alone, we can also calculate the Mach number $\mathcal{M}$ of the shock:

$$\frac{1}{C} = \frac{2}{\gamma+1}\frac{1}{\mathcal{M}^2} + \frac{\gamma-1}{\gamma+1}. \tag{1.44}$$

Analogously, the velocity of a subsonic cold front can be calculated from the ratio of the pressures at the stagnation point (where the velocity of the ICM is zero) to that in the far upstream:

$$\frac{P_{\rm st}}{P_1} = \left(1 + \frac{\gamma-1}{2}\mathcal{M}\right)^{\gamma/(\gamma-1)}, \quad \mathcal{M} \leq 1. \tag{1.45}$$

Since the pressure is continuous across the cold front, the stagnation pressure can be determined inside the cold front, where the S/N is high. Alternatively, the Mach number of bow shocks and cold fronts can also be estimated from the 'standoff' distance, defined as the distance between the stagnation point and the closest point on the bow shock [389, 406], despite the relatively complexity in approximating the standoff distance.

The line of sight velocity of the ICM can be measured with a more straightforward approach, that is measuring the Doppler shift of the emission lines in its spectrum. The prominent iron K_α line at 6.7–6.9 keV which is detectable in all clusters provides an ideal probe for this strategy. However, applying this method to the measurement of ICM bulk motions is extremely challenging.

A velocity of 1000 km s^{-1} only corresponds to a ∼20 eV shift of the iron K_α line, which is below the CCD energy resolution of XMM-Newton/EPIC, *Chandra*/ACIS, and *Suzaku*/XIS (∼100 eV). This constitutes a major obstacle to the direct measurement of the line-of-sight ICM velocity field. Despite these difficulties, there are quite a few works which successfully measured bulk motions in massive clusters using spatially resolved spectral analysis of CCD data [78, 79, 80, 81, 82, 328, 354, 330, 367, 195, 196, 262, 380]. For example, with *Chandra* CCD data, we detected in the Bullet cluster a velocity gradient of $\sim 46\pm13$ km/s/kpc along the line of sight on a scale of 260 kpc along the path of the 'bullet', which can be interpreted as the possible signature of a significant mass of ICM pushed away along a direction perpendicular to the merging (Liu et al. 2015 [195]). As a follow-up of this work, we also performed a systematic search for line-of-sight bulk motions in a sample of galaxy clusters showing evidence of ongoing or recent merger in the plane of the sky, and find evidence of line-of-sight bulk motions in 4 out of 6 clusters (Liu et al. 2016 [196]). This also confirms that cluster mergers can create ICM motions both along the merger direction and also perpendicularly to it, which are detectable with high-spatial resolution CCD data.

More recently, the *Hitomi*/SXS with an energy resolution of ~ 5 eV successfully measured the line of sight velocity field in the center of the Perseus cluster with a precision of ∼50 km s^{-1} [150], which opened a new window for the direct measurement of ICM motions in the future, and stressed the relevance of advanced, high-spectral resolution X-ray instruments. In next section, we will briefly review the next-future development of X-ray observational instruments.

1.3 A brief introduction to X-ray observations

The history of X-ray astronomy is relatively short comparing to other energy bands such as optical and radio. An important reason is that X-ray radiation from space is absorbed by the atmosphere of the Earth, so X-ray observational instruments has to be taken to high altitude by balloons, rockets, or satellites.

Since the energy of X-ray photons is so high, they have a strong tendency to go through materials, and cannot be focused in the same way as optical photons. X-rays will only bounce off a surface with a very shallow incident

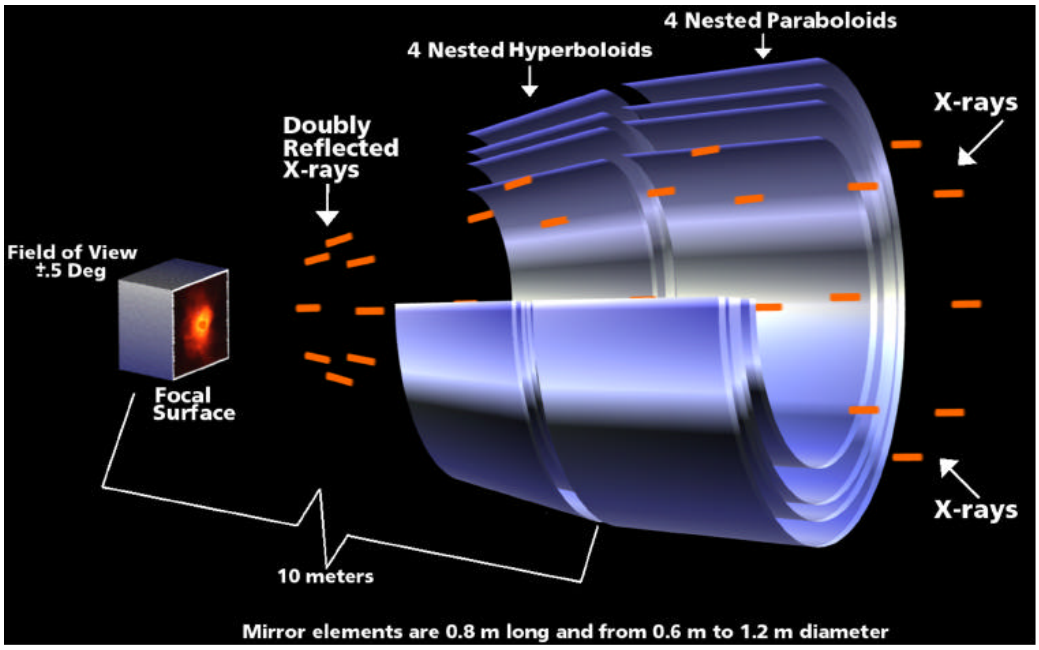

Figure 1.17. Schematic of the grazing incidence X-Ray mirror of *Chandra*. Credit: NASA/CXC/D.Berry/.

angle, and covered by heavy elements like gold and iridium. Therefore, X-ray telescopes are usually composed of one parabolic and one hyperbolic mirrors aligned almost parallel to the incident photon direction. This is known as grazing incidence optics, and telescopes with such an optical design are called Wolter type telescopes [400]. As the incident angle of each single mirror is so small, usually many mirrors are nested inside one-another in order to increase the collecting area of the telescope (see Figure1.17 for an example of Wolter type I telescope).

There have been various types of X-ray detectors during the past half century. The earliest detector used in X-ray observations is a device named 'proportional counter', which is a type of gaseous ionization detector used to measure the energy of incident radiation by producing an output that is proportional to the radiation energy. Proportional counters can provide a high energy resolution and a large field of view (degrees), but have no or extremelly coarse angular resolution. Another detector, named 'Micro-channel plates' (MCP) is a slab of typically 2 mm thickness with a regular array of tiny tubes or slots (micro-channels), and has high angular resolution but no

energy resolution. Today, widely used detectors are e.g. Charge-Coupled Devices (CCD) and calorimeters. While the former works as electrons change energy levels in semi-conductors after being hit by an X-ray photon, the latter measures the temperature increase of the detector, and converts it to the corresponding energy of X-ray photons. CCDs have both good spatial spectral resolution, and are the primary detectors on most of the current X-ray telescopes (e.g. *Chandra* Advanced CCD Imaging Spectrometer[114], and XMM-Newton European Photon Imaging Camera [379, 353]). Calorimeters have much higher spectral resolution than CCDs (e.g. *Hitomi* Soft X-Ray Spectrometer [169]), and can provide superb spectra of X-ray sources. Higher energy resolution (few eV) requires grating spectrometers, such as RGS on XMM-Newton and HETGS/LETGS onboard Chandra. Grating spectrometers clearly have no spatial resolution and require very bright sources to be efficient, and therefore had a limited use in cluster astrophysics, with the noticeable exception of the spectral analysis of bright cool cores [274].

Table 1.2. Properties of some representative X-ray space observatories. Only the energy range and energy resolution of the main detector are presented. Clearly, the parameters such as effective area and energy resolution change with wavelength and time, and cannot be fully listed in this table. Therefore, those listed here are just approximate values. Units: bandpass (keV), effective area (cm^2), energy resolution (eV), angular resolution ($''$), focal length (m).

Name (detector)	ROSAT (PSPC)	ASCA (SIS)	*Chandra* (ACIS)	XMM (EPIC)	*Suzaku* (XIS)	*Hitomi* (SXS)
Launch year	1990	1993	1999	1999	2005	2016
Bandpass	0.1–2.5	0.4–12	0.1–10	0.1–15	0.2–12	0.3–12
Eff. area	240 @1 keV	1300 @1 keV	600 @1.5 keV	4000 @1.5 keV	440 @1.5 keV	200 @1 keV
FOV	$2^\circ \times 2^\circ$	$22' \times 22'$	$17' \times 17'$	$33' \times 33'$	$18' \times 18'$	$3' \times 3'$
$R_{\rm energy}$	∼400	∼100	∼100	∼100	∼100	∼5
$R_{\rm angular}$	25	30	0.5	15	120	80
Focal length	2.4	3.5	10	7.5	4.75	5.6

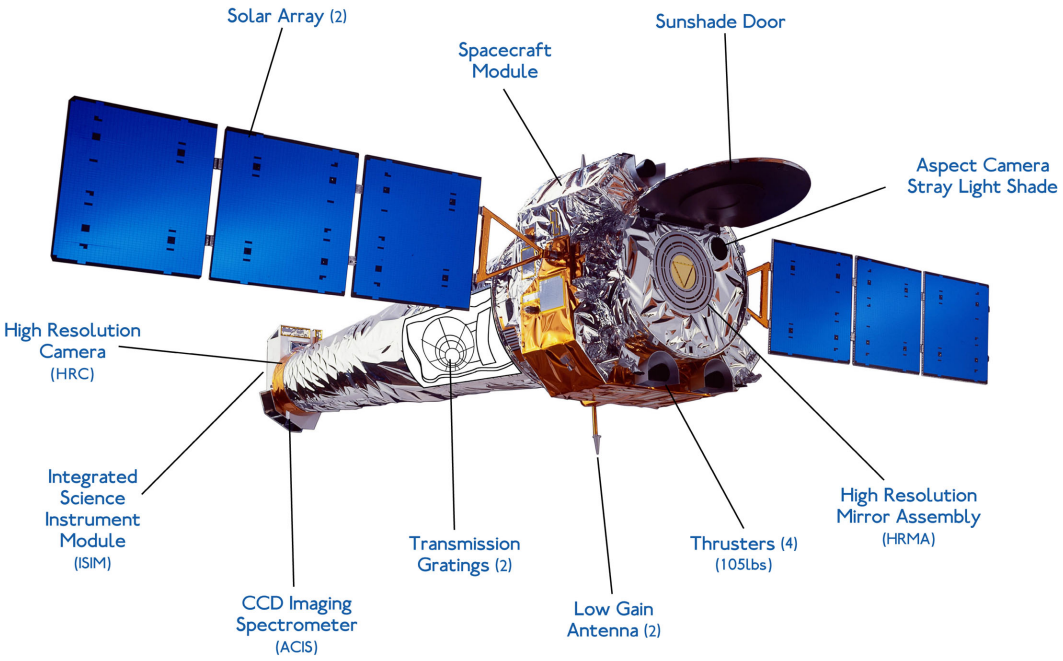

Figure 1.18. Labeled illustration of the *Chandra* X-ray Observatory. Credit: NGST & NASA/CXC.

During the past half century, tens of X-ray satellites have been launched in space, and some of them are still operating. In Table 1.2, we list the major past and present X-ray missions. Among them, we will describe in detail the *Chandra* X-ray observatory and the X-ray Multi-Mirror Mission (XMM-Newton).

1.3.1 The Chandra X-ray Observatory

Chandra, formerly known as AXAF, the Advanced X-ray Astrophysics Facility, was launched on July 23, 1999, and reached its final orbit of $\sim 140,000 \times 10,000$ km on 7 August. Figure 1.18 shows an illustration of *Chandra* and its main components. The principle components of the telescope are the High Resolution Mirror Assembly (HRMA), which consists of four pairs of nested reflecting surfaces with grazing angles $27'$–$51'$ (see Figure 1.17) and covered with iridium. The diameter of the outer most surface is 1.2 m. The mirror has an effective area of 800, 400, and 100 cm^2 at 0.25, 5.0, and 8.0 keV, respectively. Thanks to the delicate design of the optical structure and advanced mirror technology

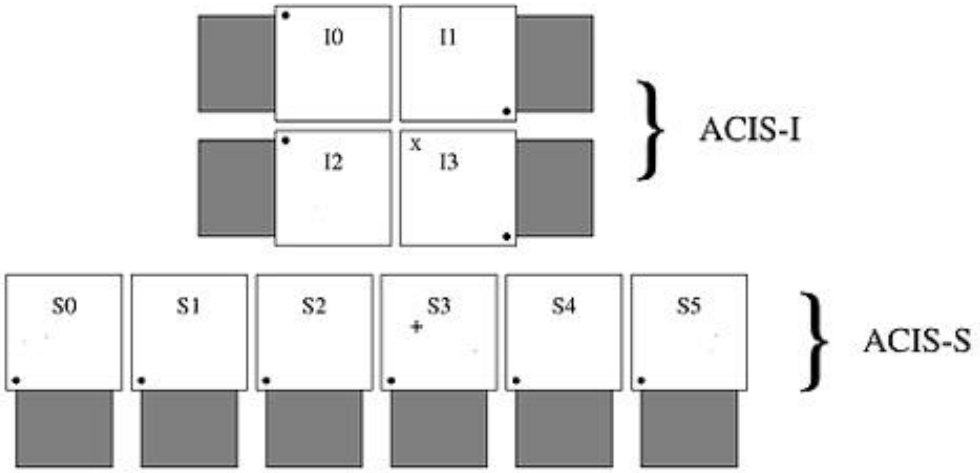

Figure 1.19. ACIS schematic layout to illustrate the location of the imaging (ACIS-I) and spectroscopic (ACIS-S) arrays. Chips S1 and S3 are back-illuminated chips, and all the other eight chips are front-illuminated. Credit: NASA/CXC.

in grinding, polishing and alignment, the angular resolution of the mirror achieved $0.5''$, which makes *Chandra* the most powerful facility in producing high-resolution X-ray images.

The focal plane science instruments include the High Resolution Camera (HRC) and the Advanced CCD Imaging Spectrometer (ACIS). The HRC is a microchannel plate instrument, and is used for high resolution imaging and fast timing measurements. The ACIS is the primary detector of *Chandra*. It consists of 10 (1024×1024) pixels CCD with 24μm pixel size. The 10 chips are configured as a 2×2 imaging array, named ACIS-I, and a 1×6 spectroscopic array, named ACIS-S (see Figure 1.19), which is often used for imaging too, given its higher sensitivity below 2 keV. Two chips in ACIS-S are back illuminated, and the other eight are front illuminated.

Additionally, there are two movable grating spectrometers, the High Energy Transmission Grating (HETG) and the Low Energy Transmission Grating (LETG), which can be inserted into the optical path to disperse spectra across HRC or ACIS-S. The energy resolution of HETG and LETG can be as high as ~ 0.01Å and ~ 0.04Å.

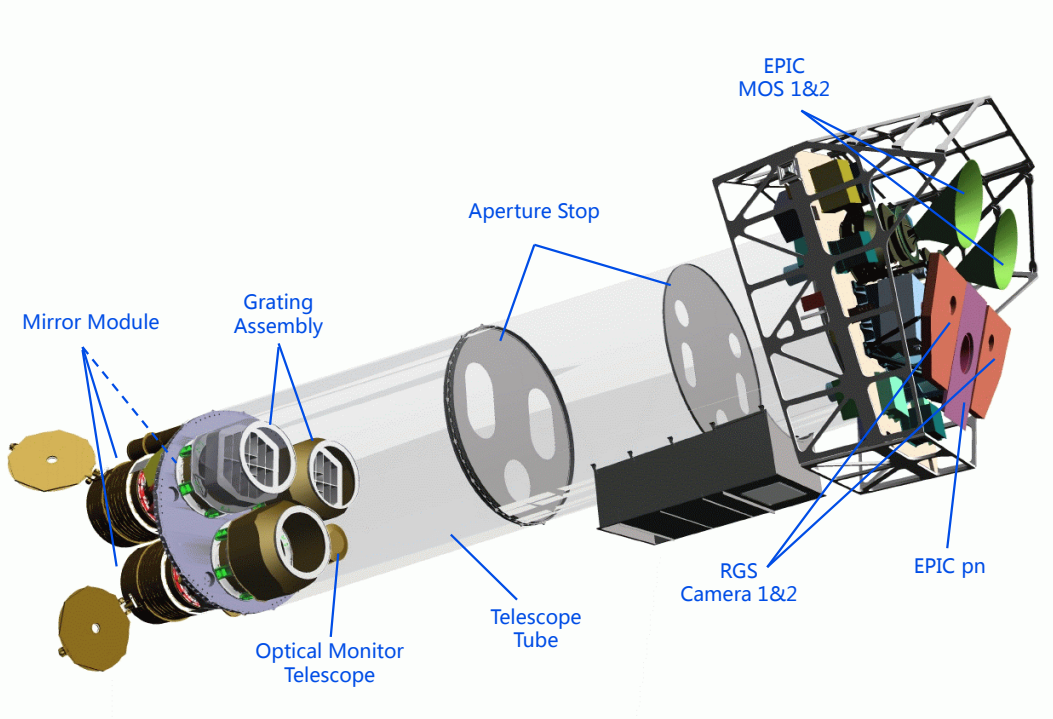

Figure 1.20. XMM-Newton payload. Credit: ESA/XMM-Newton - CC BY-SA IGO 3.0. Adapted by A. Liu.

1.3.2 X-ray Multi-Mirror Mission

The X-ray Multi-Mirror Mission (XMM-Newton) was launched in December 1999 and started scientific operations in July 2000. The orbit of XMM has a high eccentricity ($e \sim 0.82$, while the eccentricity of *Chandra* orbit is ∼0.74), so that it can make long continuous observations of X-ray sources for >200 ks. The effective collecting area of XMM can achieve 1900 cm^2 at 150 eV, 1500 cm^2 at 2 keV, 900 cm^2 at 7 keV, and 350 cm^2 at 10 keV, 4–5 times higher than *Chandra*. The large effective area covering a large energy range makes XMM the most powerful facility so far to collect the photons from faint X-ray sources for spectral analysis. On the other hand, the angular resolution of XMM is $\sim 15''$, thus allowing spatially resolved analysis with moderate resolution.

The telescope of XMM consists of three mirror modules, with each mirror consisting of 58 nested gold-coated nickel surfaces (see Figure 1.20). The primary detector aboard XMM is a system comprising the European Photon Imaging Cameras (EPIC), which is composed of two MOS-CCD cameras and

one pn-CCD camera, with a total FOV of $33' \times 33'$, and an energy range [0.1–15] keV. Besides imaging observations, the MOS cameras also offer the possibility to perform spectroscopy with moderate resolution ($E/\Delta E \sim 20$–50). The two MOS cameras are equipped with the gratings of the Reflection Grating Spectrometers (RGS), which divert ∼40% of the original incoming flux that reaches the MOS cameras, and allow spectral observation of high resolution. Another instrument is the EPIC Radiation Monitor (ERM), whose main task is detecting the radiation belts and solar flares to supply particle environment information to ensure the correct operation of the EPIC system.

1.3.3 Next-Generation X-ray Missions

Hitomi

Despite its very short lifetime, the successful launch and operation of *Hitomi* marks the beginning of the 'next-generation' X-ray astronomy. *Hitomi* (formerly known as ASTRO-H) was launched on February, 17 2016, but the contact was lost on March 26, 2016. It was found out later that multiple incidents with the attitude control system caused an uncontrolled spinning of the satellite, and finally resulted in a breakup of structurally weak elements. The mission was officially aborted on April 28, 2016.

Hitomi is equipped with four science instruments covering an energy range from 0.3 to 600 keV: the Soft X-ray Spectrometer (SXS), the Soft X-ray Imager (SXI), the Hard X-ray Imager, and the non-imaging Soft Gamma-ray Detector (SGD, two units) [363, 362]. In particular, the SXS includes a X-ray Calorimeter Spectrometer with an energy resolution of 5 eV in 0.3-10 keV, and a FOV of $\sim 3'$. During operations, *Hitomi* successfully observed the core region of the Perseus cluster with SXS, and provided very high-resolution spectra of the ICM emission (see Figure 1.21) [150, 151]. The successful observation of *Hitomi* SXS on Perseus realistically demonstrates the potential of X-ray calorimeters, and therefore opens a new window for the future X-ray astronomy, especially on the studies of galaxy clusters [175].

eROSITA

The extended ROentgen Survey with an Imaging Telescope Array (eROSITA) [288] was successfully launched on July 13, 2019. At the time of writing,

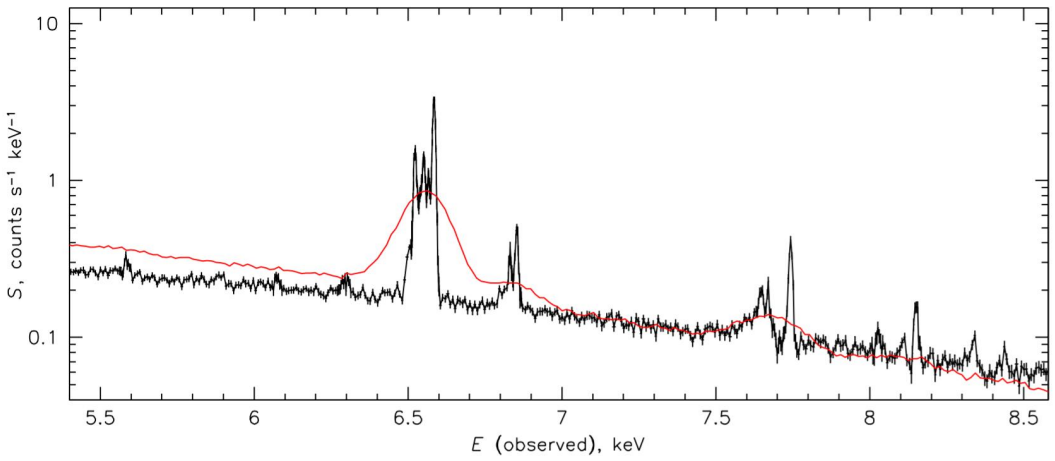

Figure 1.21. *Hitomi* SXS spectrum of the center of the Perseus cluster. Red line overlaid is the CCD spectrum of the same region observed by *Suzaku* XIS. The difference in the continuum slope is due to the difference effective areas of *Hitomi* and *Suzaku* [150].

eROSITA has started working efficiently. eROSITA will survey the X-ray sky in 0.3–10 keV band. In the soft band (0.3–2 keV), it has a 25 times higher sensitivity than ROSAT. At the same time eROSITA will be provide the first all-sky survey in the 2–10 keV band. eROSITA is expected to detect the ICM of 50–100 thousand galaxy clusters and groups and the hot gas in filaments between them, which is crucial to study the large scale structure and cosmic structure evolution.

XRISM

The X-ray Imaging and Spectroscopy Mission (XRISM), formerly named the X-ray Astronomy Recovery Mission (XARM), is a JAXA/NASA collaborative mission, with ESA participation [138]. Started immediately after the loss of *Hitomi*, XRISM is expected to be launched in 2022. As a successor of *Hitomi*. The main characteristics of the instruments on board of XRISM are similar to those of *Hitomi*. The primary detector is a soft X-ray spectrometer, which combines an X-Ray Mirror Assembly with an X-ray calorimeter spectrometer, and provides a spectral energy resolution of 5–7 eV in the 0.3–12 keV bandpass with a FOV of $\sim 3' \times 3'$. Another key instrument aboard is a soft X-ray imager named Xtend, which is a CCD detector that extends the field of view to $38' \times 38'$ over the energy range 0.4–13 keV, although the angular resolution

of $1'$ only allows imaging analysis with moderate resolution.

Athena

The Advanced Telescope for High-ENergy Astrophysics (*Athena*), is a European Space Agency (ESA) large-class mission expected to launch in early 2030s [19, 21, 22]. With a $5''$ on-axis angular resolution, *Athena* will be highly powerful in X-ray imaging observations. There will be two primary instruments on the focal plane. One is the Wide Field Imager (WFI), which will provide sensitive wide field imaging and spectroscopy covering an energy range of 0.2–15 keV, and spanning a large FOV of $40' \times 40'$. The other is the X-ray Integral Field Unit (X-IFU) [20] delivering spatially resolved X-ray spectroscopy with an exquisite energy resolution of 2.5 eV over a relatively small FOV ($5' \times 5'$). All these powerful facilities, including XRISM, *Athena*, and the other missions in the near future will lead to a revolutionary development of science in X-ray astronomy.

1.4 This thesis

This thesis is dedicated to study the nature of the intracluster medium with X-ray data. I will particularly focus on two specific aspects, namely the chemical and dynamical properties of the ICM.

In Section 1.2 we have summarized the confusing situation in the study of the chemical evolution of galaxy clusters: while early works were consistent with a decrease of ICM metallicity with redshift (or, better, an increase of the average ICM metallicity with cosmic epochs), at least below $z \sim 1.3$, recent studies suggest no or negligible evolution. After a careful examination of the literature, including previous works done by our science team, we argue that the key point to solve this problem is a full modelization of the spatial distribution of iron in the ICM. Therefore, on the basis of the state-of-the-art knowledge we can reach to date, we establish a simple but effective modelization, which consists of multiple components including a large-scale iron plateau, an iron peak, and a central iron drop. The main content of this Thesis (Chapters 2, 3, and 4) consists in a thorough investigation of the physical properties of these components as well as their roles in the global picture of ICM chemical

evolution. Chapters 5 and 6 are dedicated to the study of ICM dynamics with spatially-resolved X-ray spectral analysis. Finally, in Chapter 7, I present an overview of the strategies I intend to use with current and future X-ray facilities to further progress along the lines of research presented in this Thesis.

Chapter 2

Distribution of iron in the ICM: Evolution of the iron peak

Ang Liu[1,2,3], Paolo Tozzi[1], Heng Yu[4], Sabrina De Grandi[5], and Stefano Ettori[6,7]

1. *INAF - Osservatorio Astrofisico di Arcetri, Firenze, Italy*
2. *Department of Physics, Sapienza University of Rome, Rome, Italy*
3. *Department of Physics, University of Rome Tor Vergata, Rome, Italy*
4. *Department of Astronomy, Beijing Normal University, Beijing, China*
5. *INAF - Osservatorio Astronomico di Brera, Merate (LC), Italy*
6. *INAF - Osservatorio di Astrofisica e Scienza dello Spazio, Bologna, Italy*
7. *INFN, Sezione di Bologna, Bologna, Italy*

(Monthly Notices of the Royal Astronomical Society, Volume 481, Page 361.)

Abstract

We investigate the spatial distribution of iron in the intra-cluster medium in a selected sample of 41 relaxed clusters in the redshift range $0.05 < z < 1.03$ using *Chandra* archival data. We compute the azimuthally-averaged, deprojected $Z_{\rm Fe}$ profile of each cluster out to $\sim 0.4r_{500}$, and identify a peak in the distribution of iron followed by a flatter distribution at larger radii. Due to the steep gradient both in gas density and abundance, we find that the emission-weighted iron abundance within $0.2r_{500}$, which entirely includes the iron peak in most of

the cases, is on average ∼25% higher than the mass-weighted value, showing that spatially resolved analysis and accurate deprojection are key to study the evolution of iron enrichment in the very central regions of cool core clusters. We quantify the extent of the iron distribution in each cluster with a normalized scale parameter $r_{\rm Fe}$, defined as the radius where the iron abundance excess is half of its peak value. We find that $r_{\rm Fe}$ increases by a factor of ~ 3 from $z \sim 1$ to $z \sim 0.1$, suggesting that the spatial distribution of iron in the ICM extends with time, possibly due to the mixing with the mechanical-mode feedback from the central galaxy. We also find that the iron mass excess within $0.3r_{500}$, when normalized to the total baryonic mass within the same region, does not evolve significantly, showing that this iron mass component is already established at $z \sim 1$.

2.1 Introduction

In Chapter 1 we have summarized that we are currently far from having a coherent description of the cosmic evolution of iron in the ICM. Not only we do not know which is the radial range where most of the iron evolution takes place, but we do not even know whether some amount of evolution does actually take place, nor whether it depends on the cluster selection itself. A general lesson we learned from state-of-the-art studies, is that it is mandatory to follow the spatial distribution of the iron abundance as a function of redshift, halo mass, and thermodynamical properties of the ICM to successfully constrain any physical model for its chemical enrichment.

This goal can be barely achieved on the basis of present-day data and X-ray facilities. Currently, due to the limited statistics of high-z cluster samples, the photon-starved X-ray follow-up observation of high-z clusters, and the frustrating perspective of X-ray astronomy (with *Chandra*, the only high-resolution instrument, rapidly losing efficiency in the soft band), it is a hard task to improve the measurement of the evolution of the iron abundance in the ICM. Despite this, the evolution of heavy element enrichment of the ICM across the cosmic epochs is gaining increasing interest. In particular, the relative ratio of the abundance of various ions provides important clues on the ratio of type Ia supernovae and core-collapse supernovae, which eject different amount

of heavy elements [395, 202, 212, 210]. Thus the evolution of ICM enrichment can be used, in principle, to constrain the SNe rates in cluster galaxies, once absolute yields are robustly constrained. In turn, the prediction of absolute yields constitutes a key aspect which is still highly debated [106, 30, 67, 222], but is far beyond the goal of this work.

For these reasons we adopt an approach that begins by exploiting nearby and bright clusters, where we can successfully constrain the distribution of the heavy elements as a function of the cluster radius, and eventually extend our investigation to higher redshifts. Some of the general properties of the iron distribution at low redshifts are well known. Degrandi et al. [66, 65] investigated the projected iron profiles for a sample of 17 low-z clusters observed by *BeppoSAX*, and clearly showed that cool-core clusters show a strong iron enhancement towards the center. This property is now commonly observed in all the regular/relaxed clusters, suggesting a physical link between the processes that shape the thermodynamics of the ICM and its chemical enrichment. In particular, in high S/N data, it is possible to identify a well defined peak in the iron distribution above the average abundance level, which allows one to measure a relative *excess* of iron with respect to the global iron distribution. This excess may be associated with relatively recent star formation events in the brightest cluster galaxy [65], but its origin and evolution are still unclear. The shape of the iron excess is clearly very sensitive to the many complex physical processes occurring in the center of galaxy clusters, such as gas motions driven by outflows of the central AGN [338, 299, 96], the sloshing of cool cores [217, 127], stochastic gas motions [293], sinking of highly enriched low-entropy gas [59, 60], and galactic winds [372, 300]. De Grandi et al. (2014) [68] have already shown that, at least in the case of WARPJ1415.1+3612 (the brightest cool-core cluster at $z \sim 1$), the peak in the iron distribution is significantly narrower than in local clusters, when compared to the stellar light distribution of the underlying BCG (see Figure 2.1).

We argue that in this respect, the exquisite angular resolution of *Chandra* may play a key role in providing well defined abundance profiles not only at low redshift. Therefore, in this work, we start a systematic investigation of the spatial distribution of iron abundance in the ICM at different epochs (up to $z \sim 1$) with a limited but ideal sample of relaxed clusters observed

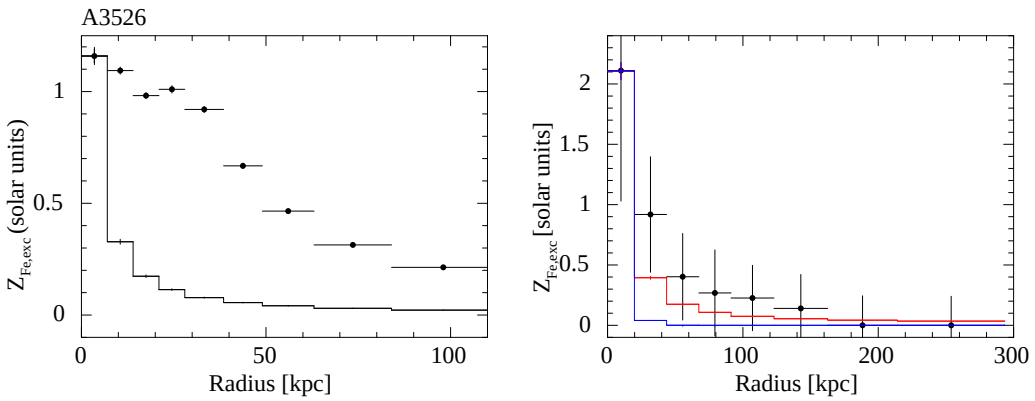

Figure 2.1. Left: The observed (black dots) and expected (solid line) iron abundance excess profiles of the cluster Abell 3526 measured by De Grandi et al. (2014) [68]. The predictions are based on the simple assumption that the metal profile should follow the optical light. The profile is arbitrarily normalized to the innermost bin. Right: Same as the left panel for WARPJ1415.1+3612. The red and blue lines indicate the results taking the upper and lower limit of uncertainties into account. Despite the larger scatter in the X-ray iron abundance measurements in WARPJ1415.1+3612, its observed iron abundance excess profile is much closer to the predicted one, compared to the local clusters.

with *Chandra*. Massive, relaxed clusters constitute the best targets where we can attempt to disentangle different components in the iron distribution. Our goal here is to extend the few works currently available in the literature [14, 92, 207], putting most of the emphasis on the spatial distribution and its physical implications. Our final aim is to build a universal physical model for the iron distribution and use it to extend our study to all the clusters with X-ray detections.

We will present this work as follows. In Section 2.2, we will describe the sample selection, the *Chandra* data, and data reduction. In Section 2.3, we briefly discuss the global properties of the sample. In Section 2.4, we derive the deprojected iron abundance profiles. In section 2.5, we discuss the correlation between entropy, gas cooling time and iron abundance. In Section 2.6, we discuss our results on the iron excess and the width of the iron peak. Our conclusions are summarized in Section 2.7. Throughout this paper, we adopt the seven-year WMAP cosmology ($\Omega_\Lambda = 0.73$, $\Omega_m = 0.27$, and $H_0 = 70.4$ km

s^{-1} Mpc^{-1} [176]. Quoted error bars correspond to a 1 σ confidence level unless noted otherwise.

2.2 Sample selection and data reduction

To achieve our science goal, the selection criteria include both the physical properties of the targets and the data quality. In this work we do not aim at measuring the global evolution of iron as a function of cosmic epoch, and we use an optimally selected cluster sample to fully exploit the power of spatially-resolved spectroscopy.

First, we set our requirements on the physics of the targets. To constrain the shape of the iron distribution in the ICM as a function of the radial distance from the center, we are required to select clusters for which an azimuthally averaged $Z_{\rm Fe}$ value as a function of the cluster radius is well defined, which implies an approximate spherical symmetry and a relaxed dynamical state. Obviously, any major merger event makes the temperature and abundance distribution highly asymmetric and patchy, undermining any attempt to define a meaningful radial distribution of $Z_{\rm Fe}$. Therefore, this requirement forces us to select relaxed, round-shaped clusters classified as such on the basis of morphological information.

We start from the sample presented in Mantz et al. (2015) [206], where the symmetry(s)-peakiness(p)-alignment(a) (SPA) criterion is used to select relaxed clusters. By applying the criterion $s > 0.87$, $p > -0.82$, and $a > 1.00$ to a sample of 361 clusters, they identify 57 clusters in the redshift range $0.01 < z < 1.03$ as relaxed.

We check the 0.5–7 keV *Chandra* images of these clusters, obtained by merging all the useful observations. We exclude from the sample the clusters which show clear signatures of non-equilibrium previously missed by the SPA test, such as obvious substructures in X-ray surface brightness distribution (e.g., A133 and RXJ1347.5-1145). There are 52 clusters surviving these criteria. We also include a relaxed cluster which passes the SPA criterion but is not included in Mantz et al. (2015): PLCKG266.6-27.3 at z=0.940, a remarkable cluster with a high S/N and high redshift [23].

We require a number of net counts ≥ 6000 in the 0.5–7 keV energy band

Table 2.1. The sample of clusters used in this work and the corresponding *Chandra* archival data. The total effective exposure time in ks is listed in the last column.

Cluster	$z_{\rm opt}$	ObsID	Exptime (ks)
Hydra-A	0.055	575	20.9
Abell2029	0.077	891,4977,6101	106.7
Abell2597	0.083	6934,7329	110.2
Abell478	0.088	1669,6102	51.5
PKS0745-191	0.103	12881	117.8
RXJ1524.2-3154	0.103	9401	40.8
Abell1068	0.138	1652	26.8
Abell2204	0.152	499,6104,7940	96.6
Abell1204	0.171	2205	23.6
Abell383	0.188	524,2320,2321	48.7
RXJ0439.0+0520	0.208	527,9369,9761	37.9
ZwCL2701	0.214	12903	95.6
RXJ1504.1-0248	0.215	4935, 5793	52.3
ZwCL2089	0.235	10463	40.5
RXJ2129.6+0005	0.235	552,9370	39.4
RXJ1459.4-1811	0.236	9428	39.3
Abell1835	0.253	6880,6881,7370,495,496	221.5
Abell3444	0.253	9400	36.3
MS1455.0+2232	0.258	7709,543,4192	107.8
MS2137.3-2353	0.313	928,4974,5250	119.5
MACSJ2229.7-2755	0.324	3286,9374	30.3
MACSJ0947.2+7623	0.345	7902	38.3
MACSJ1931.8-2634	0.352	9382	97.6
MACSJ1115.8+0129	0.355	3275,9375	53.1
RXJ1532.9+3021	0.362	14009	88.2
MACSJ0011.7-1523	0.378	3261,6105	58.8
MACSJ1720.2+3536	0.391	3280,6107,7718	60.8
MACSJ0429.6-0253	0.399	3271	22.4
MACSJ0159.8-0849	0.404	3265,6106,9376	72.5
MACSJ2046.0-3430	0.423	5816,9377	49.2
IRAS09104+4109	0.442	10445	75.9
MACSJ0329.6-0211	0.450	3257,3582,6108,7719	76.1
MACSJ1621.3+3810	0.463	[3254,3594,6109,6172, 7720,9379,10785]	161.1
3C295	0.464	2254	87.2
MACSJ1423.8+2404	0.543	4195	38.9
SPT-CLJ2331-5051	0.576	9333,11738	31.8
SPT-CLJ2344-4242	0.596	13401,16135,16545	118.0
SPT-CLJ0000-5748	0.702	9335	28.4
SPT-CLJ2043-5035	0.723	13478	73.3
PLCKG 266.6	0.940	[14017–8,14349–51,14437 15572|4|9,15582|8|9]	240.6
CLJ1415+3612	1.030	12255,12256,13118,13119	276.5

and within the extraction radius of $\sim 0.4r_{500}$ to have at least 6 independent annuli with more than ∼1000 net counts each. This threshold is required to achieve typical errors on the iron abundance of the order of 30% or less in each ring. We also require that $\sim 0.4r_{500}$ (our maximum extraction radius) be included entirely within the ACIS field of view. Depending on the position of the aimpoint, the maximum radius from the cluster center covered by ACIS-I is about 8 arcmin, which corresponds to ∼400 kpc at $z \sim 0.04$ in our seven-year WMAP cosmology. If we assume a typical r_{500} of 1 Mpc, this threshold thus excludes some nearby clusters (e.g. Perseus). There are 41 clusters left after applying the data quality threshold. Our final sample in the redshift range $0.05 < z < 1.03$ is listed in Table 2.1, where we show the redshift of each cluster, and the details of the *Chandra* data we used in this work. The X-ray emission peak is determined as the position of the brightest pixel of the image in 0.5–7 keV band after removing the unresolved sources (mostly foreground and background AGN) and smoothing with a Gaussian function with FWHM $= 1.5''$.

We performed a standard data reduction starting from the level=1 event files, using the `CIAO 4.9` software package, with the most recent version (at the time of writing) of the *Chandra* Calibration Database (`CALDB 4.7.8`). When observations are taken in the VFAINT mode, we run the task 'acis process events' to flag background events that are most likely associated with cosmic rays and remove them. With this procedure, the ACIS particle background can be significantly reduced compared to the standard grade selection. The data are filtered to include only the standard event grades 0, 2, 3, 4 and 6. We checked visually for hot columns left after the standard reduction. For exposures taken in VFAINT mode (the large majority of our dataset), there are practically no hot columns or flickering pixels left after filtering out bad events. We also apply CTI correction to ACIS-I data. We finally filter time intervals with high background by performing a 3σ clipping of the background level using the script `analyze_ltcrv`. The final effective exposure times are generally very close to the original observing time.

When the concentric annuli for spectral analysis are selected, we extract the full spectrum after masking unresolved sources, which are previously identified with `wavdetect` and eventually checked manually to identify faint sources

missed by the detection algorithm due to the dominating ICM emission. For clusters with multiple observations, we extract the spectrum and compute the response matrix file and ancillary response file for each Obsid separately, and fit the spectra with linked parameters. Background spectra are extracted from a selection of regions far from the ICM emission in each Obsid. When the ICM emission fills the entire field of view, we use the background generated from the 'blank sky' files with the `blanksky` script in `CIAO`, which finds the correct blank sky files, reprojects them to match the data, and properly determines the scaling. The 'blank sky' background is used only in one case: ObsID 575 for Hydra-A. The spectral analysis is done with `Xspec 12.9.0`. The `apec` thermal plasma emission model [345] is used to fit the ICM spectrum, with abundance relative to the solar values of Asplund et al. (2009) [12]. C-statistics [44] are used in the spectral analysis. Galactic absorption is described by the model `tbabs` [399], where the Galactic column density $n_{\rm H}$ is frozen to the value corresponding to the cluster position in the HI survey of Kalberla et al. (2005) [165].

2.3 Global properties

In this section we derive the global properties of each cluster, namely the X-ray redshift, the emission weighted global temperature, and the radius r_{500}. The global properties will be used uniquely to characterize the sample, and will not be used in our analysis except for the normalization of the radii to the value of r_{500}.

We measure the global temperature from the cumulative spectrum extracted in the region $0.1r_{500} < r <\sim 0.4r_{500}$. This choice is often adopted in the literature to obtain temperature values that more closely trace the virial value, avoiding the effect of the cool core when present. We use a single-temperature `apec` model, therefore $\langle kT \rangle$ is an emission weighted value resulting from the range of temperatures present in the explored radial range. To estimate r_{500}, we use the average relation presented in Vikhlinin et al. (2006) [388]:

$$r_{500} = \frac{0.792}{hE(z)} \left(\frac{\langle kT \rangle}{5 \text{ KeV}} \right)^{0.53} \text{Mpc}, \tag{2.1}$$

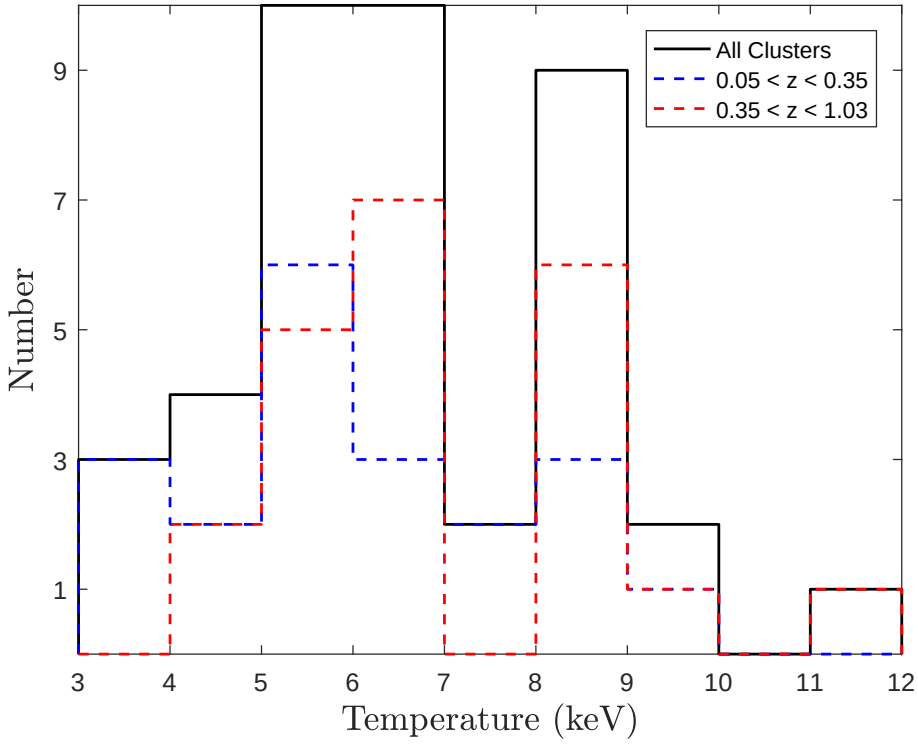

Figure 2.2. Histogram of the global temperature $\langle kT \rangle$ measured in the radial range $0.1r_{500} < r < 0.4r_{500}$ with a single-temperature `apec` model.

where $E(z) = (\Omega_{\rm m}(1+z)^3 + \Omega_\Lambda)^{0.5}$. The global temperatures $\langle kT \rangle$ and r_{500} are evaluated iteratively until we obtain a stable temperature. As shown in column 3 of Table 2.2, our sample spans a large range of temperatures of $3 < \langle kT \rangle < 12$ keV with a peak at 6 keV. As we show in Figure 2.2, we find higher temperatures at higher redshift, however this does not necessarily imply significantly larger masses. We check the mass M_{500} with the self-similar model $M_{500} \propto \langle kT \rangle^{3/2}/E(z)$, with the normalization measured in Vikhlinin et al. (2006) [388], and plot M_{500} as a function of redshift in Figure 2.3. We notice that the mass range spanned by our sample is not significantly changing with redshift. In particular, the mass range (spanning a factor of ~ 5) is more or less equally populated up to redshift $z \sim 0.6$, with only four clusters at $z > 0.6$.

We note that, in principle, we can measure mass and r_{500} directly from our spectrally resolved analysis, by measuring the total mass from the hydrostatic equation, and computing the radius corresponding to the average overdensity $\Delta = 500$ with respect to the critical density at the cluster redshift. However, in

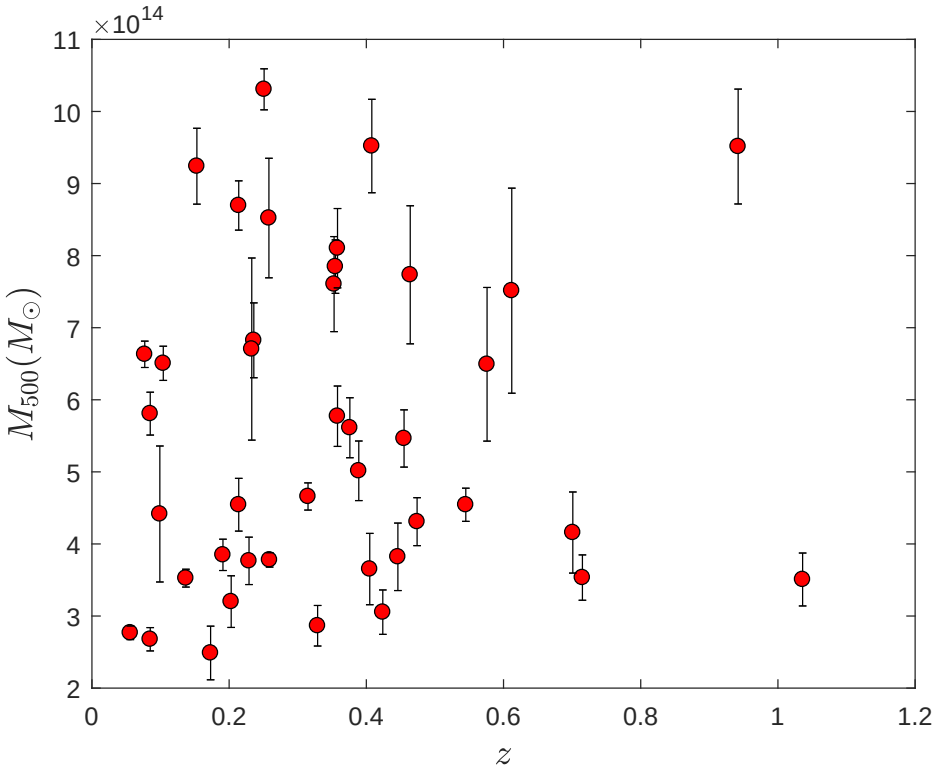

Figure 2.3. The total mass within r_{500} M_{500} obtained from the scale relation $M_{500} \propto \langle kT \rangle^{3/2}/E(z)$ plotted against redshift for our sample.

order to do this we should measure robust density and temperature profiles and therefore sample the ICM emission carefully at radii larger than r_{500}, which is beyond the goal of this work. We perform a check on the four clusters in our sample with the highest S/N (Abell2597, PKS0745-191, MACSJ2229.7-2755 and MACSJ1423.8+2404) and confirm that the extrapolated value of r_{500} obtained from our hydrostatic mass profile is consistent with that obtained from Equation (2.1) within 5%, and that the mass proxy we used in Figure 2.3 is accurate within 8%.

Since the measurement of iron abundance is sensitive to the X-ray redshift, we also investigate possible discrepancies between the optical redshift and the X-ray redshift, as obtained from the fit to the global emission with an `apec` model leaving the redshift parameter free. For simplicity, we measure the X-ray redshift of the clusters by fitting the 2.0–7.0 keV spectra so that the best-fit redshift is determined uniquely by the H-like and He-like iron line complex at 6.7–6.9 keV rest frame. As shown in Figure 2.4, we find that the X-ray and

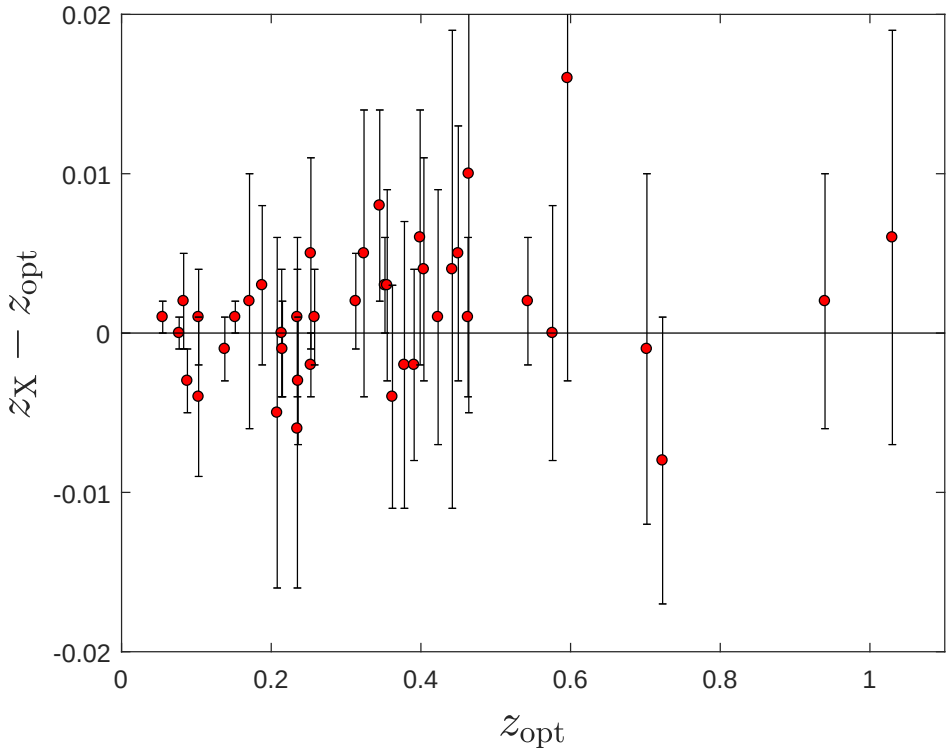

Figure 2.4. The difference between X-ray redshift and optical redshift of all clusters.

spectroscopic redshifts are consistent within $\sim 1\sigma$. We fix the redshift at the best-fit global X-ray value in the following X-ray analysis.

2.4 Iron abundance profiles

In order to measure the iron density profiles (together with the temperature and ICM density profiles), the first step is to derive the azimuthally-averaged, projected iron abundance profiles, as measured in a series of concentric annuli centered on the peak of X-ray emission out to the maximum radius $\sim 0.4r_{500}$. The annuli are chosen with an adaptive criterion based on a smoothly varying S/N threshold on the 0.5–7 keV image, to ensure a roughly equal number of net counts ≥ 1000 (0.5–7 keV band) in each bin for the inner annuli, and a doubled number of net counts in the outermost ring. This choice is key to keep a comparable quality of the spectral fit in the outer regions, which are mostly affected by the background due to the rapidly declining ICM density profile

and the correspondingly larger extraction regions. The number of independent bins per cluster ranges from 6 to 13.

The next step is the measurement of the actual 3D profile from the projected one, under the assumption of spherical symmetry. Both the *projct* model in Xspec [8] and the tool *dsdeproj* presented in Sanders et al. (2007) [314] can perform a direct and non parametric deprojection of ICM spectra. However, *projct* may produce large unphysical oscillations in the 3D profiles in some situations (see Fabian et al. (2006) [100], and examples in Russell et al. (2008) [307]). This instability has been claimed to be due to departure from spherical or ellipsoidal symmetry or the presence of multiphase gas [100]. In this work, we use the tool *dsdeproj* to produce 3D profiles, who deprojects the spectrum of a shell by subtracting the rescaled count rate of the foreground and background emission. The deprojected iron abundance profiles of all the clusters are presented in Figure 2.5.

Our spectral analysis provides profiles for the temperature, iron abundance and the electron density, which can be used to compute the gas density. These three quantities are essentially independent: the electron density mainly depends on the normalization of the emission, with little effects from temperature and abundance. Temperature measurements are determined by spectral shape and by line ratio, and therefore relatively independent from the line intensities. Abundances are measured directly from the equivalent width of the emission lines. Temperature, metallicity and electron density can become strongly coupled in presence of strong gradients across the annulus or along the line of sight, a case in which the spectra from single annulus can no longer be approximated with a single temperature `apec` model. Moreover, the ICM in an annulus may also consist of multiple temperature components due to azimuthal variations, clumpiness or cooling gas [164]. However, the quality of our data does not allow for a thorough investigation of the multiple components in each annulus. Therefore, within the limitation of our data, we assume that the angular resolution (number of annuli) in our analysis is sufficient to provide quasi-isothermal spectra.

The deprojection procedure provides us with the iron abundance, $Z_{\rm Fe}$, temperature and gas density, hence total ICM mass, within each spherical shell. Therefore, we can finally calculate the mass-weighted iron abundance

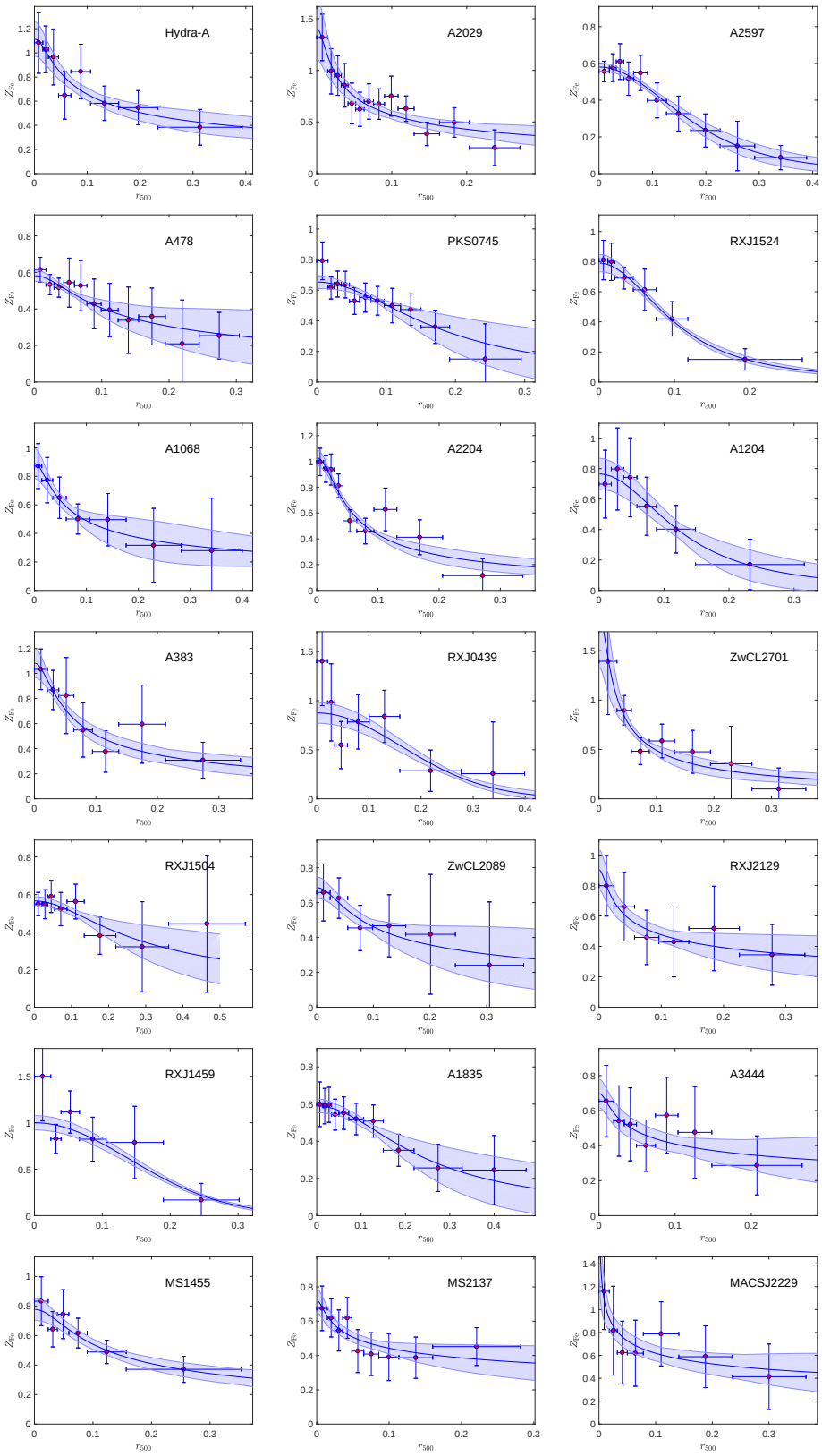
Hydra-A
A2029
A2597
A478
PKS0745
RXJ1524
A1068
A2204
A1204
A383
RXJ0439
ZwCL2701
RXJ1504
ZwCL2089
RXJ2129
RXJ1459
A1835
A3444
MS1455
MS2137
MACSJ2229
Z_{Fe}
r_{500}

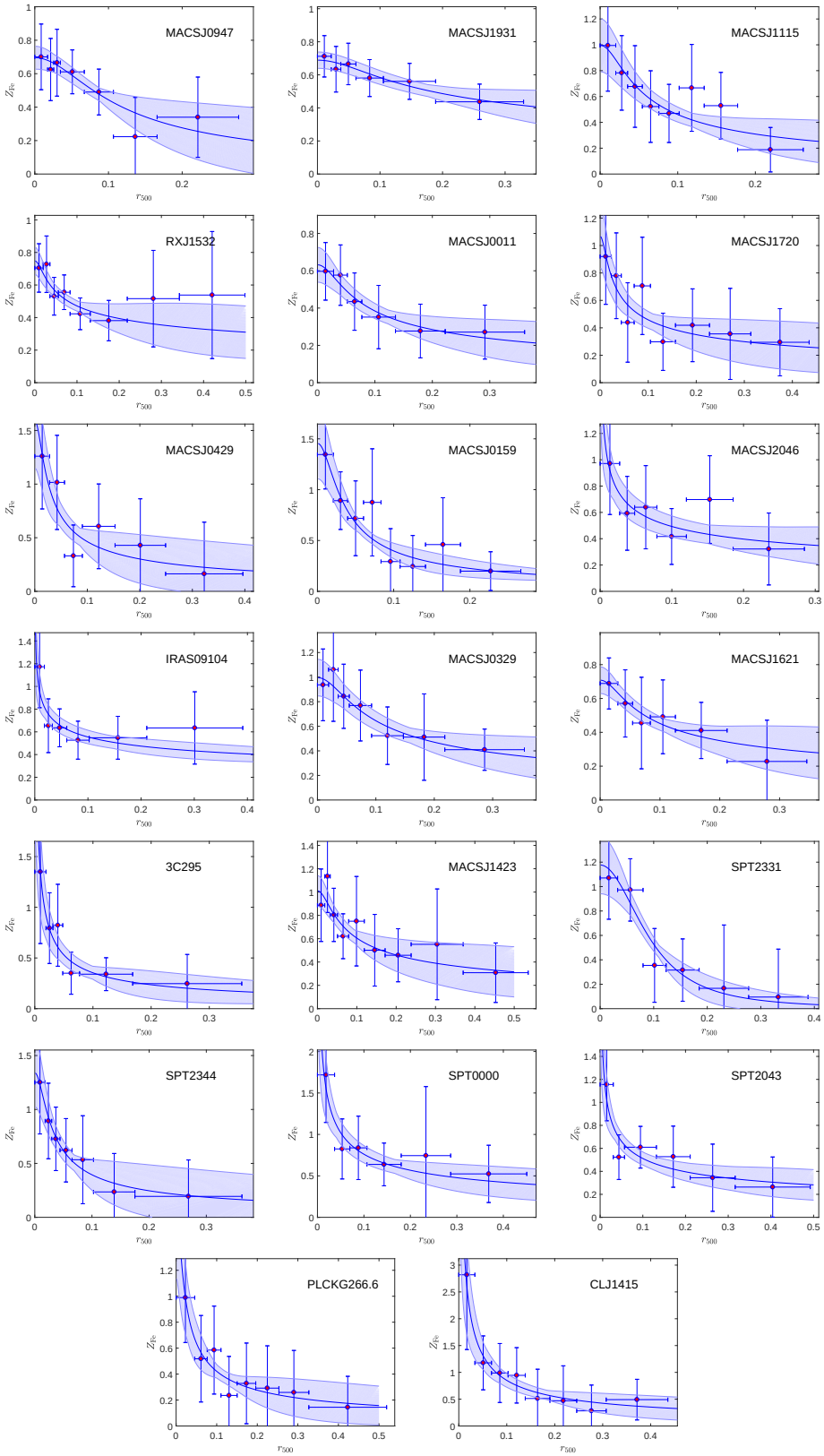

Figure 2.5. Deprojected $Z_{\rm Fe}$ profiles of the clusters. The solid blue line shows the best fit model. The shaded area corresponds to 1σ confidence interval.

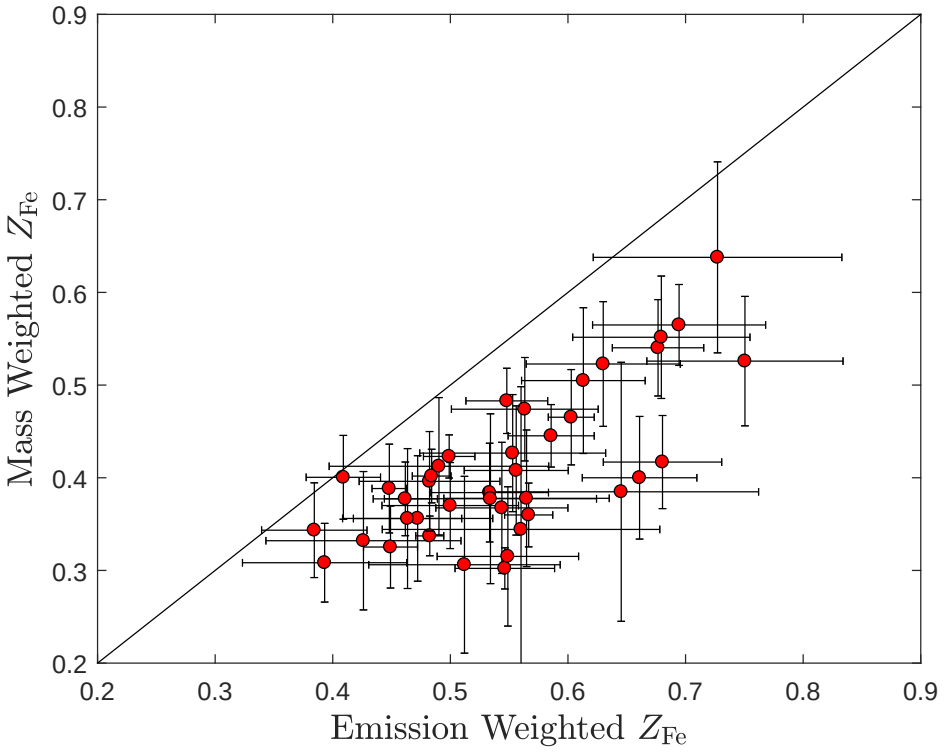

Figure 2.6. The global iron abundance $\langle Z_{\rm Fe}\rangle \times M_{\rm gas}$ versus emission weighted iron abundance obtained with our spatially resolved analysis in the radial range $r < 0.2r_{500}$.

$Z_{\rm mw}$ defined as $Z_{\rm mw} \equiv \sum(Z^i_{Fe} \cdot M^i_{\rm gas})/\sum M^i_{\rm gas}$, where i is the index of the shell. We compare $Z_{\rm mw}$ with the average spectral abundance $\langle Z_{\rm Fe}\rangle$ measured from a single-temperature fit of the global emission within the same radius. This is the quantity that is often reported in the literature, mainly because of the difficulty in resolving the ICM profiles for low S/N data (typically medium and high-z clusters). The average abundance can be well approximated with the emission-weighted value $Z_{\rm ew}$, defined as $\int_0^R \Lambda(T,Z)n_e^2 Z_{\rm Fe}/\int_0^R \Lambda(T,Z)n_e^2$, where R is the extraction radius. In Figure 2.6, we show $Z_{\rm mw}$ versus $\langle Z_{\rm Fe}\rangle$ for all the clusters, computed within $0.2r_{500}$, which entirely includes the iron peak in most of the cases, and therefore the difference between $Z_{\rm mw}$ and $\langle Z_{\rm Fe}\rangle$ is maximized. This radial range usually is described with at least 4-6 shells, since it is the region with the brightest emission. We find that the average abundance is about 25% higher than the mass-weighted value. Qualitatively, the result is expected, since $\langle Z_{\rm Fe}\rangle \sim Z_{\rm ew}$ is weighted by $\Lambda(kT,Z)n_e^2$, and higher

$Z_{\rm Fe}$ is ubiquitously associated with much higher density and slightly lower temperature, therefore corresponds to higher emission weights.

We note that the quantity $Z_{\rm mw} \times M_{\rm gas}$ is by construction different from $\langle Z_{\rm Fe} \rangle \times M_{\rm gas}$. The use of $\langle Z_{\rm Fe} \rangle \times M_{\rm gas}$ as a proxy for the mass of iron in the ICM may provide a significant artificial increase of the iron mass. In addition, any cosmic evolution of temperature and density gradients in the core of clusters would impact also on the observed evolution of the average iron abundance. Although this effect is expected to be smaller when including regions beyond $0.2r_{500}$ (therefore for bright clusters at low and medium redshift), for high-z clusters with strong cool cores we do expect to obtain abundance values $\sim$25% higher from single measurements based on global emission. The overall impact on iron evolution clearly depends on the quality of the sample and the evolution of the cool-core clusters, and it is beyond the goal of this paper. We claim that the study of the evolution of chemical properties of ICM should be based on mass-weighted quantities in all cases, obtained directly from spatially resolved spectral analysis, when possible, or by physically motivated models of the ICM profiles that allow one to associate mass-weighted quantities to global quantities. In this way, the uncertainties will be directly associated with the adopted models, allowing a better control on the predictions of iron abundance distributions for the low S/N groups and cluster population.

2.5 $Z_{\rm Fe}$-K and $Z_{\rm Fe}$-$t_{\rm cool}$ relations

Given the lack of correlation between density and temperature, the quantity $K(kT, n_e) \equiv kT \cdot n_e^{-2/3}$ as a function of the radius, often called pseudo-entropy, has been historically used to characterize the thermal history of the ICM [285]. Pseudo-entropy stays constant during any adiabatic process, like adiabatic compression, while it may change due to gain or loss of internal energy, mostly due to shocks, turbulence dissipation, or cooling. Therefore, its behavior as a function of radius can be used to identify regions dominated by shock heating (see Tozzi et al. 2001 [375], with a slope $\propto r^{1.1}$), adiabatic compression (flat profiles) and cooling. Since the metallicity also has a strong dependence with radius in some clusters, it has been previously claimed that metallicity and pseudo entropy may be associated. In particular, significant increases in

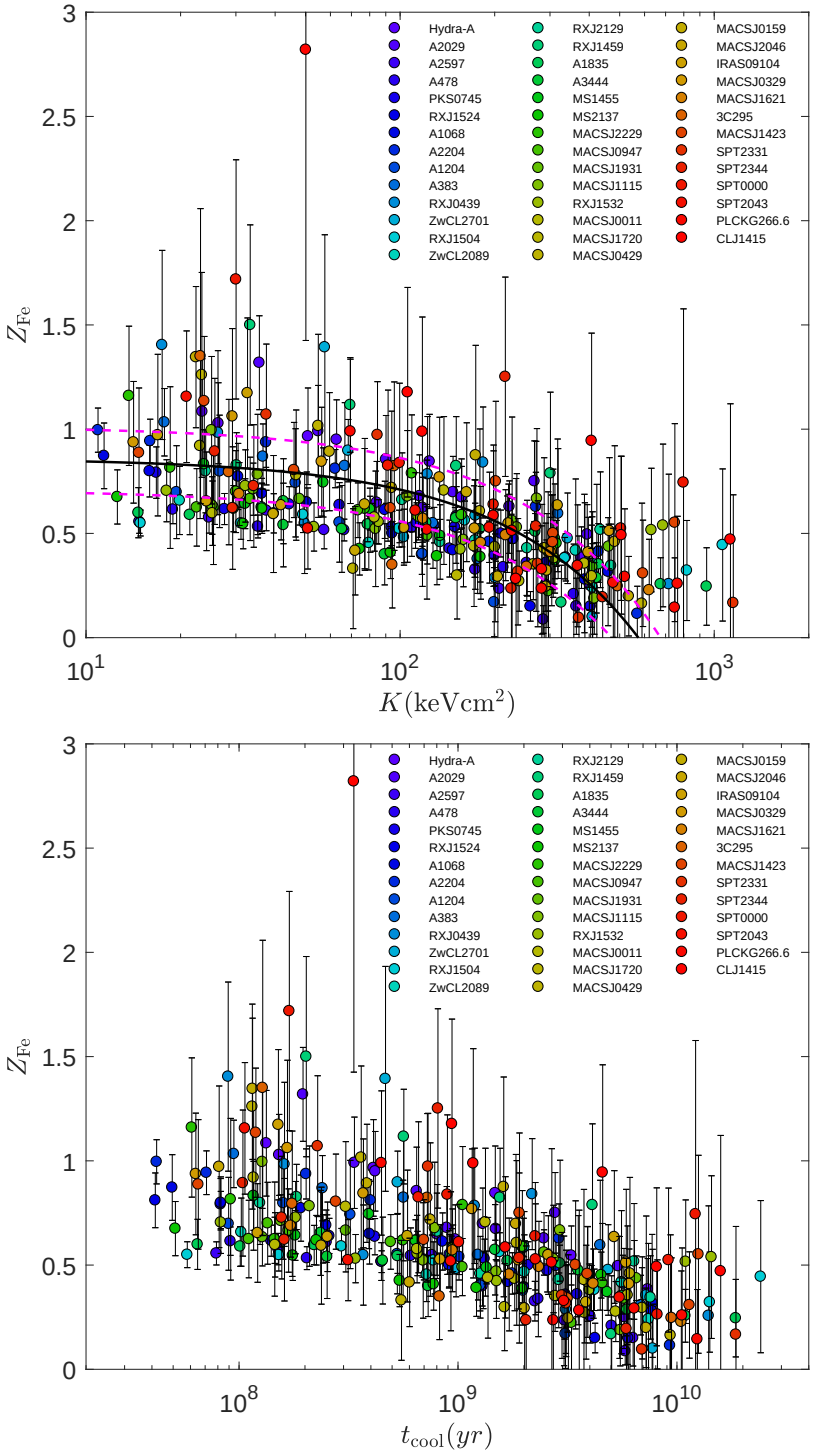

Figure 2.7. *Upper panel*: The distribution of $Z_{\rm Fe}$ versus $K(kT, n_e)$ of all the measured bins in the clusters. The color code denotes the redshift of the clusters, from the lowest (blue) to the highest (red). The solid line is the best fit linear model. The dashed lines show the *rms* dispersion of the distribution. *Lower panel*: The distribution of $Z_{\rm Fe}$ versus the cooling time $t_{\rm cool}$.

metallicity are expected, and often observed, in regions of low entropy where the cooling of the ICM may be associated with events of star formation triggered by the gas dropping out of the cold phase. For example, in local clusters, $Z_{\rm Fe}$ and $K(kT, n_e)$ are found to have a negative correlation [65, 187, 127].

On these premises, we first investigate the correlation between $Z_{\rm Fe}$ and $K(kT, n_e)$ for all the independent bins in the clusters of our sample. We fit the $Z_{\rm Fe} - K(kT, n_e)$ distribution with a linear function $Z = Z_0 - \alpha \cdot K/1000$, and obtain the best fit values $Z_0 = 0.86 \pm 0.18$ and $\alpha = 1.49 \pm 0.51$. The $Z_{\rm Fe}$-$K(kT, n_e)$ distribution and the best fit function are shown in the upper panel of Figure 2.7.

Similarly, we also show the distribution of $Z_{\rm Fe}$-$t_{\rm cool}$ in the lower panel of Figure 2.7. The cooling time of the gas $t_{\rm cool}$ is defined as the gas enthalpy divided by the energy loss per unit volume (see Equation (1.37) in section 1.2.2). We find that the $Z_{\rm Fe}$ shows a similar correlation with $t_{\rm cool}$ as with $K(kT, n_e)$, given the strong similarity of the two quantities.

The interpretation of this average, highly scattered relation, may be understood only on the basis of a comprehensive model for chemical enrichment of the ICM through the lifetime of groups and clusters. The association of higher abundance values with low entropy and shorter cooling time gas may be, in fact, not simply associated with gas cooling and star formation with consequent local chemical enrichment, but the result of two independent process, like radiative cooling and iron production and diffusion. These processes are both more efficient at the cluster center, but proceed independently and with different time scales. Namely, the spatially resolved analysis we present in this paper is a first step towards a comprehensive model.

2.6 The width of the iron excess profiles

In this section we present the characterization of the distribution of iron abundance throughout the ICM, focusing on the innermost regions. To do that, we fit the deprojected profile of the iron abundance with a phenomenological model with no direct physical meaning. There are two models which have been used in the literature to fit the profiles of ICM iron abundance: a double-β model [326], and the empirical function adopted in Mernier et al. (2017) [235],

which is a simple power-law for $r >\sim 0.02r_{500}$ (in the innermost regions they model the possible decrease of the metallicity by subtracting a Gaussian). However, we often see a strong abundance gradient beyond $\sim 0.02r_{500}$, and therefore adopt a simpler model which is preferable with respect to a composite model with many free parameters (6 in the case of a double-β model). Given the low number of bins we have (particularly for the high-z clusters) we want to have no more than 3 free parameters. We adopt a single β model in the form

$$Z_{\rm Fe}(r) = Z_0 \cdot (1 + (r/r_0)^2)^{-\beta}. \tag{2.2}$$

The best fits are obtained minimizing the χ^2 over the 3 free parameters. The best fit models for the iron abundance profiles are shown in Figure 2.5.

After fitting the profiles, we first obtain the iron abundance at $r = 0.3r_{500}$ for all the clusters, and plot $Z(0.3r_{500})$ versus redshift in Figure 2.8. We group the clusters into three redshift bins: [0.05,0.25], [0.25,0.5], [0.5,1.03], and calculate the average value and *rms* dispersion respectively. As a result, we find that $Z(0.3r_{500})$ of the three redshift bins are 0.26, 0.30, and 0.29, with *rms* dispersion of 0.10, 0.08, and 0.13. This result suggests that the average iron abundance at $0.3r_{500}$ is consistent with a constant value at $\sim 0.3Z_\odot$ at least up to redshift 1.

The width of the iron profiles is quantified with a newly defined scale parameter $r_{\rm Fe}$, expressed in units of r_{500}. The definition of $r_{\rm Fe}$ is as follows. We calculate the excess abundance profile $Z_{\rm exc}(r) = Z(r) - Z(0.3r_{500})$, and the peak excess abundance $Z_{\rm exc,0} = Z_{\rm peak} - Z(0.3r_{500})$, where $Z_{\rm peak}$ is the peak abundance. Rather than directly adopting Z_0 of the best-fit beta-model as $Z_{\rm peak}$, we instead compute the average value within $0.02r_{500}$ to have a more robust estimate. Finally, we define $r_{\rm Fe}$ as the radius where $Z_{\rm exc}(r_{\rm Fe})$ is half of $Z_{\rm exc,0}$. The values of $r_{\rm Fe}$, together with the best-fit parameters obtained from the spatially resolved spectral analysis of our sample, are listed in Table 2.2.

Since the distribution of iron differs significantly in cool-core and non-cool-core clusters, the width of iron profiles may also be correlated with the strength of cool-core. To decouple the evolution of the iron distribution from that of the cool core in the clusters, we check whether $r_{\rm Fe}$ can quantify the broadening of the iron peak, or just shows the strength of the cool core. As a representative

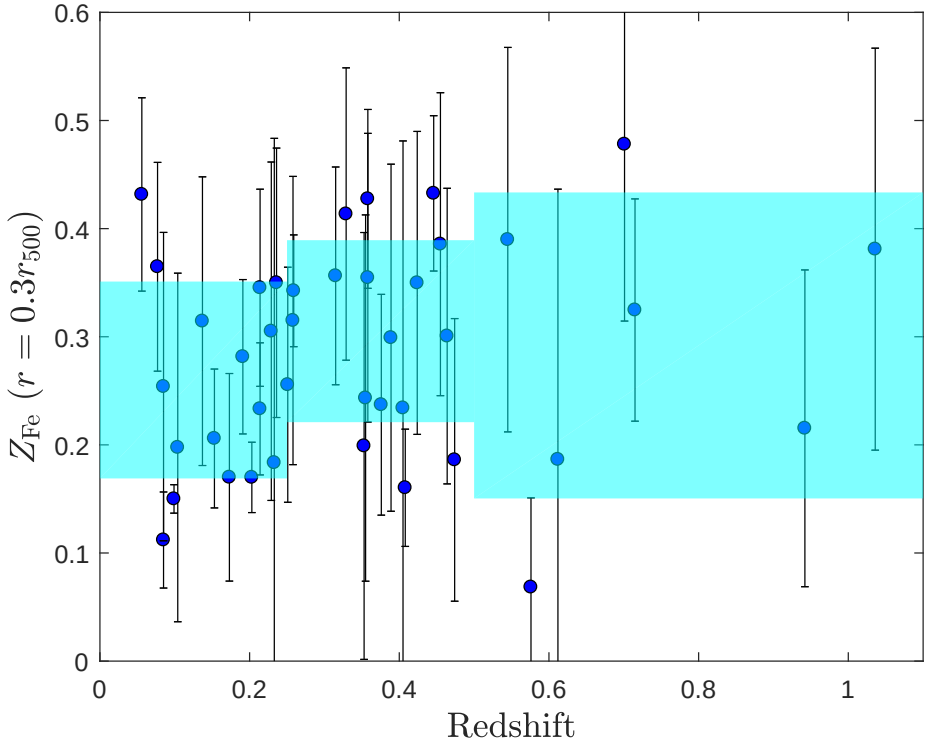

Figure 2.8. The iron abundance at $r = 0.3r_{500}$ for all the clusters. Shaded area shows the *rms* dispersion across three redshift bins: [0.05,0.25], [0.25,0.5], [0.5,1.03].

parameter, we use the surface brightness concentration $c_{\rm SB}$, defined as the ratio of the flux within 40 kpc and 400 kpc [324]. We plot $r_{\rm Fe}$ versus $c_{\rm SB}$ in Figure 2.9. Spearman's test is performed on the distribution taking into account the uncertainties in $c_{\rm SB}$ and $r_{\rm Fe}$, with a resulting $\rho = 0.18 \pm 0.11$, corresponding to a very weak correlation with the probability of null hypothesis $p = 0.31 \pm 0.26$. This result suggests no significant correlation between $r_{\rm Fe}$ and $c_{\rm SB}$, and hence we conclude that the parameter $r_{\rm Fe}$ can quantify the width of the iron distribution independently from the strength of the cool core.

In Figure 2.10, we show the scale of the iron excess peak $r_{\rm Fe}$ as a function of redshift. Since the scatter in $r_{\rm Fe}$ is very large, we again group the data into three redshift bins [0.05,0.25], [0.25,0.5], and [0.5,1.03]. The results show that $r_{\rm Fe}$ decreases significantly with redshift, despite the large scatter in the low redshift bin. We interpret the significant increase of $r_{\rm Fe}$ from high-z to low-z as a clear evolution in the spatial distribution of iron in the ICM. Since

Table 2.2. Summary of the spatially resolved spectral analysis of our cluster sample. Column 1: cluster name; Column 2: redshift of the ICM; Column 3: temperature of the ICM in units of keV within $0.1r_{500}$–$0.4r_{500}$; Column 4: r_{500} in units of Mpc measured using the temperature in column 3; Column 5: the scale of the iron excess peak: $r_{\rm Fe}/r_{500}$; Column 6: the cool core strength $c_{\rm SB}$ (as defined in Santos et al. 2008 [324]).

Cluster	$z_{\rm X}$	kT	r_{500}	$r_{\rm Fe}$	$c_{\rm SB}$
Hydra-A	0.056 ± 0.001	3.94 ± 0.14	1.00	$0.067^{+0.036}_{-0.025}$	0.249 ± 0.002
Abell2029	0.077 ± 0.001	6.89 ± 0.19	1.30	$0.043^{+0.031}_{-0.019}$	0.164 ± 0.001
Abell2597	0.085 ± 0.001	3.89 ± 0.24	0.96	$0.145^{+0.020}_{-0.017}$	0.303 ± 0.001
Abell478	0.085 ± 0.002	6.35 ± 0.33	1.24	$0.094^{+0.144}_{-0.042}$	0.165 ± 0.001
PKS0745	0.104 ± 0.003	6.86 ± 0.25	1.28	$0.137^{+0.088}_{-0.043}$	0.219 ± 0.001
RXJ1524	0.099 ± 0.004	5.36 ± 1.15	1.12	$0.094^{+0.009}_{-0.008}$	0.342 ± 0.002
Abell1068	0.137 ± 0.002	4.70 ± 0.17	1.03	$0.062^{+0.052}_{-0.025}$	0.287 ± 0.003
Abell2204	0.153 ± 0.001	8.69 ± 0.50	1.41	$0.059^{+0.011}_{-0.009}$	0.294 ± 0.001
Abell1204	0.173 ± 0.008	3.81 ± 0.57	0.92	$0.111^{+0.034}_{-0.027}$	0.355 ± 0.005
Abell383	0.191 ± 0.005	5.05 ± 0.29	1.03	$0.060^{+0.021}_{-0.014}$	0.254 ± 0.003
RXJ0439	0.203 ± 0.011	4.51 ± 0.51	0.98	$0.167^{+0.025}_{-0.029}$	0.292 ± 0.005
ZwCL2701	0.214 ± 0.004	5.65 ± 0.46	1.11	$0.038^{+0.023}_{-0.017}$	0.153 ± 0.002
RXJ1504	0.214 ± 0.003	8.52 ± 0.33	1.35	$0.158^{+0.105}_{-0.061}$	0.336 ± 0.002
ZwCL2089	0.229 ± 0.010	5.04 ± 0.44	1.02	$0.083^{+0.132}_{-0.043}$	0.292 ± 0.004
RXJ2129	0.236 ± 0.005	7.36 ± 0.56	1.24	$0.048^{+0.055}_{-0.026}$	0.188 ± 0.003
RXJ1459	0.233 ± 0.004	7.27 ± 1.37	1.24	$0.153^{+0.014}_{-0.015}$	0.222 ± 0.003
Abell1835	0.251 ± 0.002	9.60 ± 0.27	1.42	$0.156^{+0.074}_{-0.047}$	0.231 ± 0.001
Abell3444	0.258 ± 0.005	8.53 ± 0.83	1.33	$0.051^{+0.109}_{-0.032}$	0.189 ± 0.002
MS1455	0.259 ± 0.003	5.10 ± 0.14	1.02	$0.093^{+0.033}_{-0.027}$	0.280 ± 0.002
MS2137	0.315 ± 0.003	5.93 ± 0.24	1.06	$0.051^{+0.076}_{-0.028}$	0.316 ± 0.002
MACSJ2229	0.329 ± 0.008	4.38 ± 0.43	0.90	$0.042^{+0.058}_{-0.023}$	0.338 ± 0.006
MACSJ0947	0.353 ± 0.006	8.19 ± 0.71	1.24	$0.100^{+0.121}_{-0.044}$	0.280 ± 0.003
MACSJ1931	0.355 ± 0.003	8.36 ± 0.40	1.24	$0.123^{+0.076}_{-0.056}$	0.254 ± 0.002
MACSJ1115	0.358 ± 0.006	8.54 ± 0.58	1.26	$0.060^{+0.047}_{-0.030}$	0.194 ± 0.003
RXJ1532	0.358 ± 0.006	6.89 ± 0.50	1.13	$0.060^{+0.085}_{-0.034}$	0.251 ± 0.002
MACSJ0011	0.376 ± 0.009	6.81 ± 0.50	1.11	$0.076^{+0.058}_{-0.035}$	0.148 ± 0.003
MACSJ1720	0.389 ± 0.006	6.37 ± 0.53	1.05	$0.045^{+0.053}_{-0.026}$	0.200 ± 0.004
MACSJ0429	0.405 ± 0.008	5.24 ± 0.71	0.95	$0.040^{+0.038}_{-0.022}$	0.275 ± 0.007
MACSJ0159	0.408 ± 0.007	9.62 ± 0.66	1.30	$0.044^{+0.020}_{-0.017}$	0.177 ± 0.003
MACSJ2046	0.424 ± 0.007	4.71 ± 0.48	0.88	$0.038^{+0.058}_{-0.022}$	0.271 ± 0.006
IRAS09104	0.446 ± 0.014	5.47 ± 0.67	0.95	$0.042^{+0.051}_{-0.022}$	0.319 ± 0.005
MACSJ0329	0.455 ± 0.006	6.88 ± 0.52	1.06	$0.086^{+0.057}_{-0.039}$	0.249 ± 0.004
MACSJ1621	0.464 ± 0.005	8.60 ± 1.07	1.19	$0.076^{+0.076}_{-0.038}$	0.205 ± 0.003
3C295	0.474 ± 0.011	5.96 ± 0.46	1.22	$0.029^{+0.032}_{-0.015}$	0.262 ± 0.005
MACSJ1423	0.545 ± 0.004	6.32 ± 0.32	0.97	$0.071^{+0.072}_{-0.034}$	0.310 ± 0.004
SPT2331	0.576 ± 0.008	8.01 ± 1.31	1.07	$0.087^{+0.023}_{-0.021}$	0.181 ± 0.005
SPT2344	0.612 ± 0.015	8.90 ± 1.69	1.11	$0.042^{+0.038}_{-0.020}$	0.334 ± 0.008
SPT0000	0.701 ± 0.010	6.32 ± 0.86	0.88	$0.034^{+0.042}_{-0.019}$	0.209 ± 0.006
SPT2043	0.715 ± 0.009	5.73 ± 0.51	0.83	$0.036^{+0.040}_{-0.020}$	0.237 ± 0.005
PLCKG266	0.942 ± 0.008	11.64 ± 0.98	1.06	$0.035^{+0.040}_{-0.020}$	0.098 ± 0.002
CLJ1415	1.036 ± 0.013	6.40 ± 0.68	0.73	$0.028^{+0.035}_{-0.015}$	0.137 ± 0.004

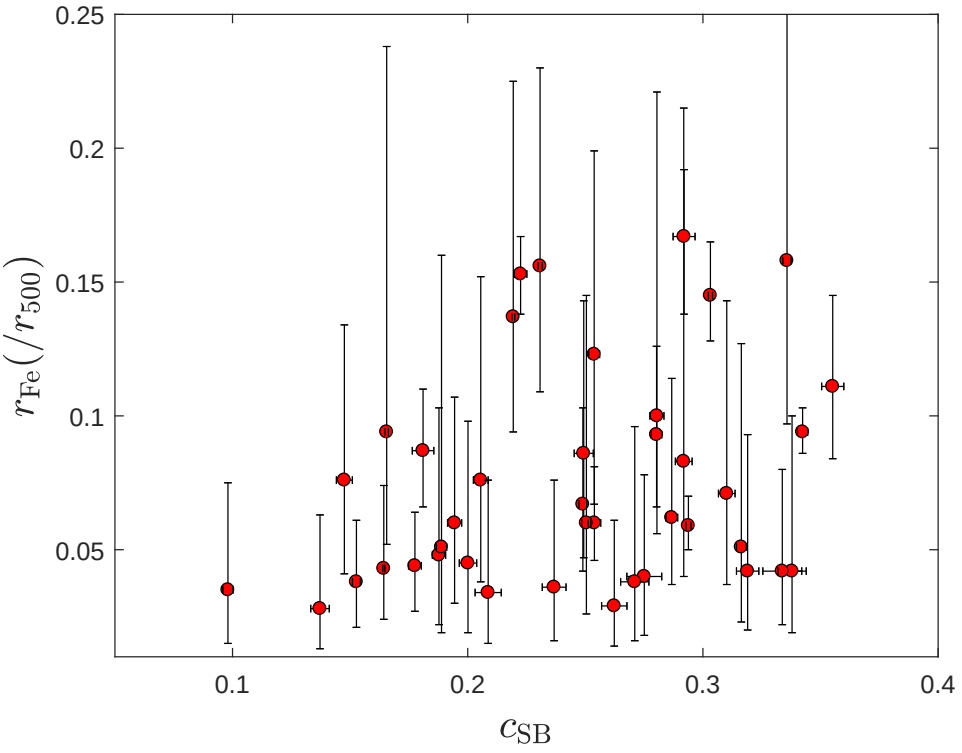

Figure 2.9. The scale of the iron excess peak, $r_{\rm Fe}$, normalized to the scale radius r_{500}, plotted versus the cool core strength $c_{\rm SB}$ (as defined in Santos et al. 2008 [324]).

we only investigate the most relaxed clusters in our sample, the broadening of the iron peak should not be associated with large scale motions of the ICM, such as those due to major mergers, but it may be associated with the turbulent mixing and uplifting due to the feedback activities of the central galaxy. Another mechanism that could contribute to the widening of the peak is the core sloshing due to minor mergers [127].

Another important clue comes from the mass of the iron excess, computed within $0.3r_{500}$. In Figure 2.11, we plot the iron mass excess normalized by the gas mass within $0.3r_{500}$ versus redshift. Spearman's test on the distribution gives $\rho = -0.09 \pm 0.12$, and the probability of no evolution $p = 0.50 \pm 0.29$, suggesting no significant evolution of iron mass excess with redshift. Therefore, we conclude that the bulk of the mass in iron is already present at $z \sim 1$, and that the increase in the quantity $r_{\rm Fe}$ should not be ascribed to an increase of the iron excess in the ICM with cosmic epoch, but mostly to the evolution of

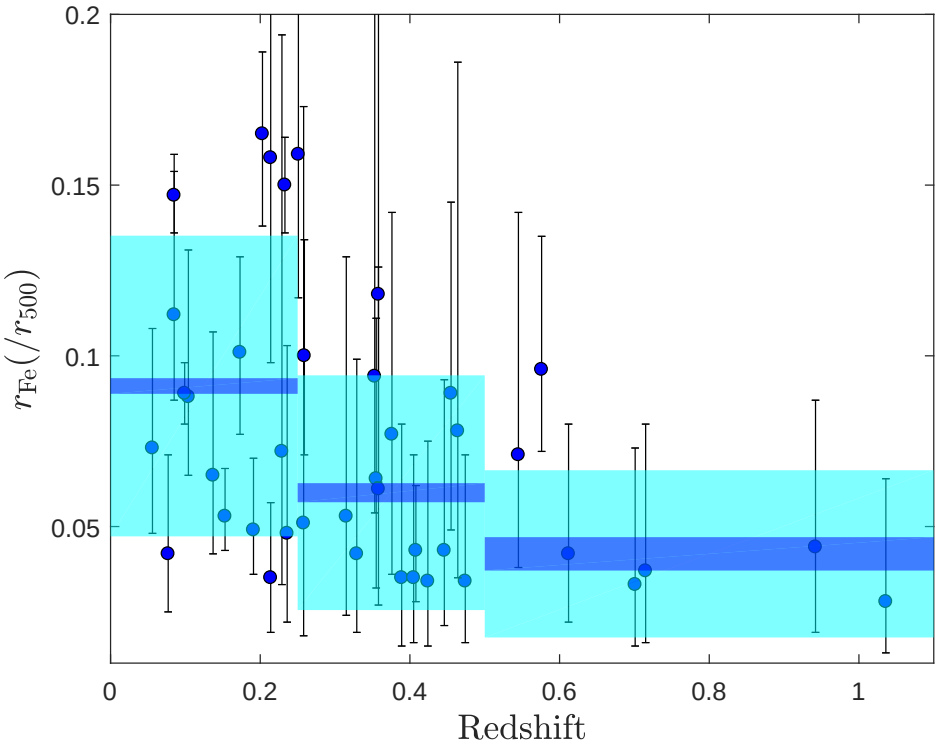

Figure 2.10. The scale of the iron excess peak, $r_{\rm Fe}$, normalized to the scale radius r_{500}, plotted versus redshift. Blue and cyan shaded areas show the weighted average and *rms* in three redshift bins, respectively.

the iron distribution.

2.7 Conclusions

We perform a systematic study on the evolution of iron distribution in the ICM with deprojected $Z_{\rm Fe}$ profiles in a sample of 41 relaxed galaxy clusters in the redshift range $0.05 < z < 1.03$. Our conclusions are summarized as follows:

- We confirm that for all of our clusters from $z \sim 0.05$ to $z \sim 1.03$, the shape of the deprojected $Z_{\rm Fe}$ radial profiles shows a steep negative gradient followed by a roughly constant value out to $\sim 0.4r_{500}$, as commonly observed in relaxed/cool-core clusters. The average $Z_{\rm Fe}$ at $\sim 0.3r_{500}$ is approximately $0.3Z_{\odot}$, and shows no significant evolution with redshift.

- From the deprojected iron profile, we calculate the mass weighted iron

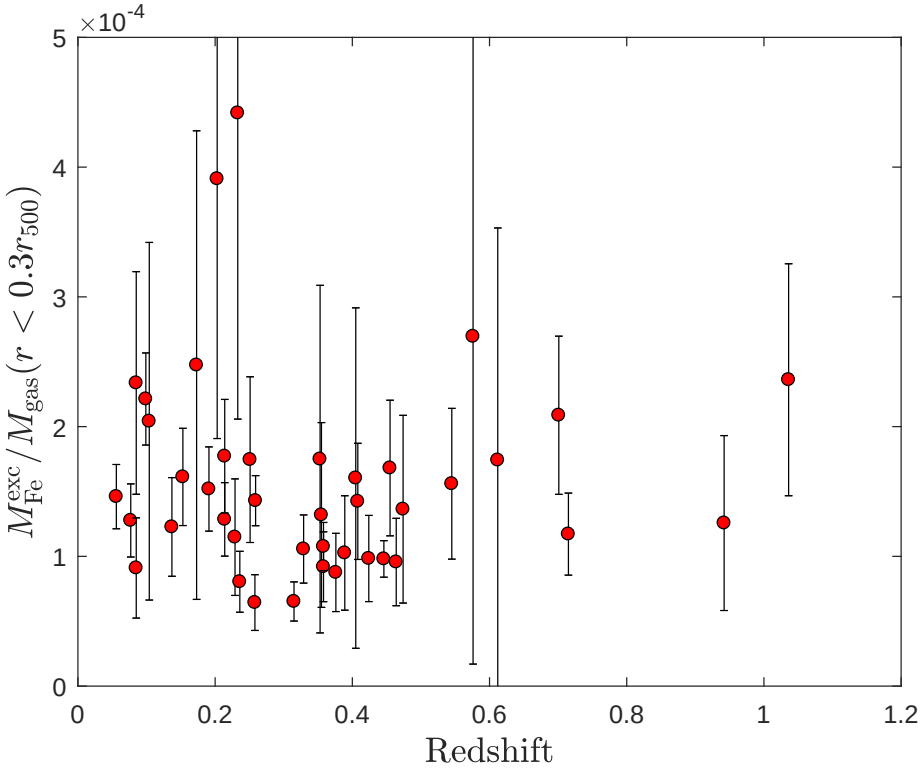

Figure 2.11. The mass of the Fe excess, normalized to the total gas mass, within $0.3r_{500}$ as a function of redshift. No significant correlation is observed.

abundance $Z_{\rm mw}$ within $0.2r_{500}$ for the clusters, and make a comparison with the average iron abundance $\langle Z_{\rm Fe}\rangle$ which is obtained by simply fitting the overall emission within the same radius. As a result, we find that the average value is always larger than the mass weighted value by **$\sim$25%**, showing a potential issue when computing the cosmic evolution of the global enrichment of the ICM without having its spatial distribution under control.

- We investigate the correlation between $Z_{\rm Fe}$ and the pseudo entropy K_{T,n_e}, and the correlation between $Z_{\rm Fe}$ and the cooling time $t_{\rm cool}$ in all the measured bins of all clusters. We confirm that higher $Z_{\rm Fe}$ corresponds to lower $K(kT, n_e)$ and shorter $t_{\rm cool}$, with large scatters. We suggest that this association is relevant to the interplay of the radiative cooling of the gas and the production and diffusion of iron.

- We quantify the width of the iron profiles with the parameter $r_{\rm Fe}$, defined

as the radius where the iron abundance excess is half of its maximum value. We find that $r_{\rm Fe}$ decreases significantly with redshift, but not with the core strength, and that the total mass excess in iron is not evolving with redshift. This shows that we are witnessing the evolution in the distribution of the iron mass excess in the inner region of cool cores, possibly associated with the turbulent mixing and uplifting of highly enriched material due to the mechanical-mode feedback from the central galaxy.

This work is the first on a series of papers aiming at establishing a robust modeling of the iron distribution in the ICM based on a central peak and a large scale flat component. This has been obtained in this paper thanks to a detailed analysis of bright, low and moderate z clusters. Eventually, the evolution of the iron abundance across the largest cluster population observable to date in terms of mass and redshift range, can be investigated by using these spatial distribution models.

Acknowledgments

We thank the anonymous referee for his/her helpful comments. We acknowledge financial contribution from the agreement ASI-INAF n.2017-14-H.0. S.E. acknowledges also financial contribution from the contracts NARO15 ASI-INAF I/037/12/0, and ASI 2015-046-R.0.

Chapter 3

Origin of the central abundance drops in the ICM

Ang Liu[1,2,3], Meng Zhai[4], and Paolo Tozzi[1]

1. INAF - Osservatorio Astrofisico di Arcetri, Firenze, Italy

2. Department of Physics, Sapienza University of Rome, Rome, Italy

3. Department of Physics, University of Rome Tor Vergata, Rome, Italy

4. Key Laboratory of Optical Astronomy, National Astronomical Observatories, Chinese Academy of Sciences, Beijing, China

(Monthly Notices of the Royal Astronomical Society, Volume 485, Page 1651.)

Abstract

A central drop of ICM Fe abundance has been observed in several cool-core clusters. It has been proposed that this abundance drop may be due, at least partially, to the depletion of Fe into dust grains in the central, high-density regions. According to this scenario, noble gas elements such as Ar and Ne are not expected to be depleted into dust, and therefore should not show any drop, but follow the general increase of metal abundance toward the center. In this work, we test this scenario by measuring with *Chandra* data the radial profiles of Ar and Ne in a sample of 12 groups and clusters where a central drop in Fe abundance has been detected. We confirm the presence of the Fe drop in 10 out of 12 clusters at more than 2σ c.l., and 4 Ar drops with similar significance. We also find 4 Ne drops, with the caveat that Ne abundance measurement from

CCD spectra suffers from systematics not completely under control. Our results are consistent with an abundance drop common to the three elements. When comparing the profiles, we find that, on average, the abundance profiles of Ar and Ne are significantly higher than Fe and steeper toward the center, while they all gradually become consistent with solar composition at $r \geq 0.05 r_{500}$. We also check that Si and S profiles are mostly consistent with Fe. This result confirms a scenario in which some fraction of Fe is depleted into dust grains in the inner regions, although the global central abundance drop is mostly due to mechanical processes, like the displacement of metal-rich ICM from the very center to larger radii by AGN-driven feedback. Finally, we report the detection of an Fe drop in the cluster MACSJ1423.8+2404 at $z = 0.543$, showing that this feature appears early on in cool-core clusters.

3.1 Introduction

X-ray observations of galaxy groups and clusters have shown that the intracluster medium in the core can be so dense that the central cooling time is significantly shorter than the cluster lifetime, particularly in the innermost few tens of kpc, as measured in high resolution *Chandra* data [46]. If the cooling proceeded isobarically, the ICM would cool rapidly and form a cooling flow with a mass deposition rate $\dot{M}$ of $100 - 1000 M_{\odot}$ yr^{-1}, as directly derived from the total X-ray luminosity of the core region [95]. Among the unavoidable consequences, one would expect a large amount of cold gas falling onto the BCG and a star formation rate comparable to the predicted $\dot{M}$. However, only modest SFRs of the order of few $M_{\odot}$ yr^{-1} have been observed in BCGs, as expected if the star formation was entirely fueled by the stellar mass loss from the BCG itself [392]. The amount of cold gas is also found out to be much lower than expected by the high cooling-flow rates [230, 89]. In addition, the observations of XMM-Newton RGS on clusters cores showed the absence of metal emission lines associated to gas cooler than $\sim 1/3$ of the virial temperature [274, 273]. These findings imply that the bulk of the gas in the core must be prevented from cooling by some heating mechanisms, leaving only a minority available for complete cooling. Therefore, the cooling-flow model was superseded by the cool-core picture [245].

Many candidates have been proposed as contributors of the heating of cool cores, including cosmic rays [31], star formation and supernovae explosion [76, 188], gas turbulence induced either by the movement of bubbles produced by the central active galactic nucleus or by minor and major mergers [229, 96, 178, 145, 115], or the mixing and heating associated with vortices formed during the inflation of the bubbles [149]. So far, processes related to AGN feedback are considered to be the most likely candidate as the main heating source [99, 100, 150] due to the large amount of mechanical energy stored in the ICM bubbles created by the radio jets of the AGN. However, a coherent picture of the cycle of baryons in cool cores is still missing.

An unambiguous signature of these processes in cool cores is left in the metal abundance distribution and its evolution, a topic which rapidly gained attention from the scientific community since the beginning of the era of *Chandra* and XMM-Newton. Evidence of chemo-dynamical impact of AGN feedback are now directly observed in the X-ray data [339, 173, 261, 199], and, at the same time, supported by continuously improving hydrodynamical simulations [299, 338, 51]. A striking example is provided by the observed enhancement of metals around the bubbles [174], strongly suggesting that the inflation of the cavities uplifts the highly enriched ICM bringing it at larger radii. Further insights came from detailed studies of the metallicity peaks commonly observed at the center of cool-core clusters at moderate and high redshift [65, 228]. In particular, the measurement of the broadening of the distribution of metals across cosmic epochs in cool-core clusters provides further support to the nuclear activity as the main contributor of metal mixing in the ICM [68]. As discussed in the Chapter 2, in Liu et al. (2018) [192] we showed that the width of the iron (Fe) peak increases by a factor of $\sim$3 from redshift $z \sim 1$ to $z \sim 0.05$.

In this paper we focus on an apparently minor property of the metal distribution in the ICM, which, instead, may provide a relevant missing link between the hot and cold phases of the baryons cycling in and around the BCGs. It consists in a small-scale (of the order of 10 kpc) decrement at the center of the abundance peak in cool cores, a feature that we call *central abundance drop*, and that has long been known thanks to *Chandra* and XMM-Newton studies of single, low-redshift clusters [312, 162, 314, 239, 264] and

confirmed recently by more extensive studies [265, 235]. This feature is better observed exploiting the high spatial resolution of the *Chandra* satellite in cool-core clusters, but has also been confirmed with XMM-Newton in low redshift clusters [235]. In addition, the abundance drop has been observed both in Fe, which is the most prominent line-emitting element in X-ray spectra, and in other elements like sulphur (S) and silicon (Si) [235, 265]. The Fe abundance drop has been observed usually in association with cavities, and therefore it may be ascribed to the local effects of AGN feedback, effectively pushing the highly-enriched gas from the innermost regions toward larger radii [339, 174]. As a result, the measured abundance will decrease somehow at small radii and correspondingly increase at larger radii, at the point of inverting locally the abundance gradient on a spatial scale corresponding to the efficiency of the uplifting of the metal-enriched gas, and creating the abundance drop. Clearly, the uplifting of the innermost, mostly enriched gas implies a similar decrease for all the elements, also if the mechanism is not due to the inflation of bubbles from the ICM, but to other mechanical processes like core sloshing [127].

Other possible interpretations have been proposed, like contamination from a central X-ray emitting AGN in the ICM spectrum, or an underestimate of the helium content at small radii as a result of mass sedimentation [94, 235]. However, the former interpretation cannot explain abundance drops which are observed far from the AGN position, nor the second interpretation can justify why many cool-core clusters do not exhibit central abundance drop. Another possible effect is the non-negligible optical depth of some resonance line, that may result, in principle, in a decrease of the global ion abundance measured assuming an optically-thin medium in the densest ICM regions. Resonance scattering has been now measured for the Helium-like iron emission line by *Hitomi* [151], however, it appears to be relevant only in the analysis of high-resolution spectra, while it has a limited impact on the global metallicity measured from CCD spectra and it is not effective in removing the central dip [313, 124]. See [343], however, for a more comprehensive discussion on the comparison of high-resolution spectra with those obtained from CCD data on the measurement of the abundance pattern in the ICM.

Finally, a relevant physical mechanism that may play a role here, is the depletion of Fe and several other metals (including Si and S) into dust grains

present in the diffuse gas close to the BCG. This is supported by the detection of cold dust filaments in optical and infrared in clusters with central abundance drop [264, 265]. Depletion of Fe and other reactive metals is expected if the enriched gas from star formation and stellar mass-loss in the BCG remains cool and distinct from the hot surrounding ICM, due to the higher ambient pressure [392]. Being trapped into dust filaments, a significant part of Fe is released into the ICM on a longer time scale and displaced with respect to non-reactive elements, namely when the dust-rich gas is uplifted by nuclear activity into lower-density and hotter regions [264]. This dust-depletion mechanism can be tested by comparing the radial abundance profiles of Fe to that of noble gas elements that are not expected to be embedded into dust grains. The two noble elements that are potentially detectable in high S/N spectra of clusters are neon (Ne) and argon (Ar). While the former is hard to measure because blended with the dominant emission from the Fe L-shell complex in CCD spectra, the latter can be firmly detected thanks to the Ar XVII and Ar XVIII emission lines which appear isolated in the range 3.0–3.3 keV for low-z clusters. Therefore, in this paper we aim at exploiting the angular resolution of *Chandra* data to measure the spatially-resolved abundance profiles of Ar, and possibly of Ne, in a sample of groups and clusters in which a central Fe abundance drop has been previously detected, and compare them to the profiles of Fe and other elements.

We will present this work as follows. In Section 3.2, we will introduce the selection of clusters and groups we studied in this work, and describe the reduction and analysis of *Chandra* data. In Section 3.3, we present the radial abundance profiles of iron, argon, neon, silicon, and sulfur, and show how our results can be used to constrain the dust grain scenario. In Section 3.4, we discuss the robustness of our spectral analysis strategy. Our conclusions are summarized in Section 3.5. Throughout this paper, we adopt the seven-year WMAP cosmology with $\Omega_\Lambda = 0.73$, $\Omega_m = 0.27$, and $H_0 = 70.4$ km s^{-1} Mpc^{-1} [176]. Quoted error bars correspond to a 1 σ confidence level, unless noted otherwise.

3.2 Cluster Sample, Data reduction and analysis

Table 3.1. The sample of groups and clusters with a significant detection of central Fe abundance drop considered for this work. The exposure times are computed after data reduction. The values of r_{500} are taken from the cluster compilation in Pinto et al. (2015) [278] and Liu et al. (2018) [192]. The central Fe abundance drop detection is obtained from the following references: P15: [265]; M17: [235]; SF02: [312]; M10: [239]; J02: [162]; L18: [192].

Cluster	z	r_{500} (Mpc)	*Chandra* ObsID	Exptime (ks)	Reference
NGC4636	0.0031	0.35	323,324,3926,4415	203.5	P15,M17
NGC5846	0.0057	0.36	7923	90.0	P15,M17
NGC5813	0.0065	0.44	[5907,9517,12951, 13247,13253,13255, 12952,12953,13246]	635.3	P15,M17
NGC5044	0.0093	0.56	[798,9399,17195–6, 17653,17654,17666]	417.7	P15,M17
Centaurus	0.0114	0.83	[4944,4945,5310, 16223,16224,16225, 16534,16607–10]	666.3	SF02,P15,M17
A262	0.0161	0.74	2215,7921	28.7	P15
A3581	0.0220	0.72	12884	83.9	M17
Ophiuchus	0.0280	1.22	[16142,16143,16464, 16626–7,16633–5, 16645,3200]	259.9	M10
A2199	0.0303	1.00	[497,498,10748 10803,10804,10805]	157.3	J02
2A0335	0.0349	1.05	919,7939,9792	102.5	P15,M17
A1991	0.0590	0.82	3193	38.1	P15
MACSJ1423	0.5431	0.97	4195	38.9	L18

3.2.1 Selection of the sample

Our main scientific goal is to find a signature of dust depletion in the ICM of galaxy groups and clusters, in terms of a selective decrement in the abundance of

Fe, Si and S with respect to noble elements in the central regions. Dust depletion into dust grains is expected to be efficient in high density environments, where some of the enriched gas, particularly that associated to the stellar mass-loss, remains cool and distinct from the hot ICM due to the high pressure. Therefore, to constrain the impact of dust depletion on the Fe distribution, we select a sample of cool-core clusters with a firm detection of a central Fe drop. Due to the high angular resolution needed for this study, we also require the use of *Chandra* data.

So far, the largest systematic investigation of abundance drop across the *Chandra* archive is provided by the work of Panagoulia et al. (2015) [265], where eight groups and clusters are reported to have central abundance drop with high statistical significance (NGC 4696/Centaurus, NGC 5846, 2A0335+096, NGC 4636 Abell 1991, Abell 262, NGC 5813, NGC 5044). Detection of Fe drop in single objects are reported for Abell 2199 [162], Ophiuchus [239], NGG 4696/Centaurus [312, 264], and Perseus [314]. In addition, 14 objects have been shown to have a decrease of the Fe abundance in their core on the basis of XMM-Newton data in Mernier et al. (2017) [235]. All of them have been observed also by *Chandra*, and six were already included among the clusters with significant drop in Panagoulia et al. (2015). Among the remaining eight, one is the Perseus clusters, while the remaining seven are M49, M86, Abell 189 (NGC 533), Fornax, HCG62, NGC4325 and Abell 3581, with the last three also included in Panagoulia et al. (2015) among those with low-significance Fe drop.

To draw a final list of targets relevant for our study, we combine all these sources and perform a preliminary test on the detectability of the Ar line complex, by fitting the spectrum of each cluster in the innermost 20 kpc, then setting the Ar abundance $Z_{\rm Ar}$ to zero and checking whether the $\Delta C_{\rm stat} \geq 2.7$. With this criterion, we select all the 8 clusters with high-significance drop in Panagoulia et al. (2015), plus Abell 2199, Ophiuchus, and Abell 3581. We exclude the Perseus cluster [314] since the exceptional data quality for this cluster (1.4 Ms total exposure with *Chandra*) allows one to attempt such an investigation in single 2D regions, rather than an azimuthally-averaged profile. For this reason we decided to postpone the analysis of Perseus to another paper with a dedicated 2D, spatially-resolved spectral analysis.

Therefore, we identify 11 groups and clusters viable for our study. Since all these well-documented cases are found at low redshift ($z < 0.1$), we also include, for the sake of discussion, a high-redshift cluster where we serendipitously detected for the first time a shallow central Fe drop (MACSJ1423.8+2404 at $z = 0.543$ in Liu et al. 2018 [192]). The list of the 12 clusters and groups discussed in this work is shown in Table 3.1, where we also report the X-ray data, redshift, total exposure time and r_{500} as measured in the literature. Clearly, we made best use of the *Chandra* archive, and include all the available observations for each cluster. However, we exclude a few obsid when they have different data acquisition mode or period, and, at the same time, provide a minor contribution to the total exposure time. Therefore, we discard Obsid 788 for NGC5846, Obsid 1650 for A3581, Obsid 1657 for MACSJ1423, and Obsid 504, 505, 4190 and 4191 for Centaurus. We remind that we are not interested in a complete sample of clusters and groups with a central abundance drop, but we just require a reliable sample to investigate whether we can identify the signature of dust depletion with our analysis strategy. Essentially, our sample is mostly based on the results of Panagoulia et al. (2015) and Mernier et al. (2017) for the Fe profile, with the inclusion of a few other well studied cases.

3.2.2 Data reduction

Data reduction is performed with `CIAO 4.10`, adopting the latest release of the *Chandra* Calibration Database at the time of writing (`CALDB 4.7.8`). Unresolved sources within the ICM, typically due to AGN not associated to the cluster, are identified with `wavdetect`, checked visually and eventually removed. In particular, we pay attention to possible nuclear emission from the BCG, that may affect the spectrum of the innermost bin. Nuclear emission from the BCG is found in about 20% of all the clusters, and preferentially in cool cores, despite the AGN luminosity is typically low, of the order of 10^{43} erg s^{-1} [402]. Thanks to the angular resolution of *Chandra*, this consists in removing a circle of ~ 1.2 arcsec at the center of the innermost bin.

The spectra are extracted in circular concentric rings, centered at the peak of X-ray emission in 0.5–7 keV band image, smoothed with a Gaussian function with full width at half-maximum $\sim$ 1.5 arcsec after removing unresolved

sources. The annuli are chosen adaptively on the image to ensure a roughly equal number of net counts, and in any case larger than 2000 in the 0.5–7 keV band, in each annulus. For clusters with multiple observations, we extract the spectrum and compute the response matrix file (RMF) and ancillary response file (ARF) for each observation separately. Background spectra are extracted from regions far from the ICM emission in each Obsid. When the ICM emission fills the entire CCD, we use the background generated from the 'blank sky' files with the `blanksky` script. This choice may not be accurate in the outermost regions beyond $0.1r_{500}$ which, however, are not relevant in this work. In the core regions we discuss here, the accuracy of few percent provided by the 'blank sky' background spectra is not affecting our results.

3.2.3 Spectral analysis strategy

The spectral fits are performed with `Xspec 12.10.1` [9] using C-statistics [44]. All the abundance values in this paper are relative to the solar values of Asplund et al. (2009) [12]. We note that these photospheric results are significantly smaller, for the most abundant elements like C, N, O, Ne and Fe, than those recommended in the widely used compilations of Anders et al. (1989) [2] and Grevesse et al. (1998) [135]. In particular, the Fe abundance in solar units turns out to be larger by a factor ~ 1.6. Galactic absorption is described by the model `tbabs` [399], where the best-choice for the value of Galactic HI column density is initially set to the value corresponding to the cluster position in the HI survey of Kalberla et al. (2005) [165]. However, we notice in several cases that a different value of NH_{Gal} is needed to obtain an acceptable fit, therefore we leave the NH_{Gal} parameter free to vary (see the Discussion section for further details). For clusters with multiple observations, the spectra corresponding to the same ring are fitted with linked parameters.

Particular care must be taken in modeling the thermal structure of the ICM, since we necessarily have more than one temperature component in each spectrum. This may be simply due to projection effects of background and foreground ICM belonging to outer shells in presence of strong temperature and abundance gradients across the line of sight, particularly in the innermost regions. We also know that the complex ICM structure in strong cool-cores

with cavities can create strong departure from spherical symmetry. This complexity is clearly emerging thanks to the high signal spectra in our sample, and, therefore, it is not possible to assume a dominant single-temperature component in each bin, particularly because this choice may bias the metallicity low, as noticed in several studies [38, 39, 119]. Therefore, in this work we adopt the simplest approach which provides statistically acceptable fits, which consists in using two temperatures in each spectrum. Previous works investigating the abundance drop in cool core clusters already showed that a two-temperature model is relatively unaffected by projection effects and return reliable values of metal abundance [264]. We also verify *a posteriori* the goodness of the fit to make sure that our strategy provides an acceptable modelization of the observed spectrum. Finally, we assume that the abundance of each element we consider is the same in both temperature components, a choice that is necessary to obtain robust results and will be further detailed in the Discussion section.

The emission lines of Ar and Ne have very different diagnostics. The signal from Ar is contributed by the K_α lines of Ar XVII and Ar XVIII (He-like and H-like Ar) which appear clearly above the continuum in the energy range ∼3.0–3.3 keV, far from other emission lines. In this case, the capability of detecting Ar depends merely on the strength of the signal, on the Ar abundance itself, and on the ICM temperature, so that the associated error is essentially dominated by Poisson noise. The diagnostics for Ne is completely different, since the K_α lines from Ne X and Ne IX are blended with the overwhelming Fe XXII–XIX line complex (plus the less prominent O VII and O VIII line complex) at ~ 1 keV, and cannot be resolved into single lines at the spectral resolution of ACIS-I or ACIS-S. Clearly, the value and the associated error of the Ne abundance is dramatically dependent on the capability of properly modeling the complex line blend around 1 keV, which may well not reproduced with only two temperatures. For this reason the Ne profile has been measured only in a few cases so far [70]. Despite that, we present and discuss our measurements of Ne abundance obtained with the two-temperature assumption, with the caveat that the associated errors is a lower limit to the real uncertainty.

According to this scheme, we measure the abundance of metals by fitting the projected spectrum in each annulus with a double `vapec` thermal plasma

emission model [345] with AtomDB version 3.0.9, leaving free the two temperatures and the corresponding emission measure (normalization), the Galactic absorption NH_{Gal}, and the abundances of Fe, Ar, Ne, S, Si, O, Mg, and Ca which are assumed to be the same in the two temperature components. All the other abundance values are linked to Fe. The abundance of Helium is always fixed to solar value.

Finally, in this work we focus on the projected quantities, with no attempt to deproject the abundance profiles we obtain, similarly to the approach of Mernier et al. (2017). Deprojection procedures, which are commonly adopted in the literature mostly to obtain 3D temperature profiles and measure hydrostatic masses [50, 307] are known to have little effects on the abundance profiles [291]. In addition, the complexity of the thermal structure in cool cores, particularly with evident cavities, would result in an incorrect result if deprojected under the assumption of spherical symmetry, as noticed by Panagoulia et al. (2015).

3.3 Radial Abundance Profiles

In this work we are mostly interested in the comparison of the Fe profiles to those of Ar and, with the mentioned caveats, Ne. We also discuss S and Si that are expected to be also depleted similarly to Fe, while we are not able to obtain an accurate characterization of the profiles of O, Ca and Mg, which, therefore, are not included in this investigation.

The azimuthally-averaged, projected abundance profiles of $Z_{\rm Fe}$, $Z_{\rm Ar}$ and $Z_{\rm Ne}$ for the 12 clusters in our sample are shown in Figure 3.1, while the profiles of Si and S are shown in Figure 3.2. From a visual inspection, we see that we are able to confirm a statistically significant Fe drop in most of the clusters, and to identify drop in the Ar abundance in some of them. We also notice that the shape of the Ne profiles often appears to be consistent or at least comparable with that of Fe and Ar, suggesting that Ne profiles are plausible, and that, despite our measured Ne profile may be affected by unknown statistical uncertainties, we definitely have a statistically-significant global detection of Ne across the sample in the core region.

Since the Fe profiles of these clusters have been already published, despite with different analysis techniques and, in some cases, different data sets, we

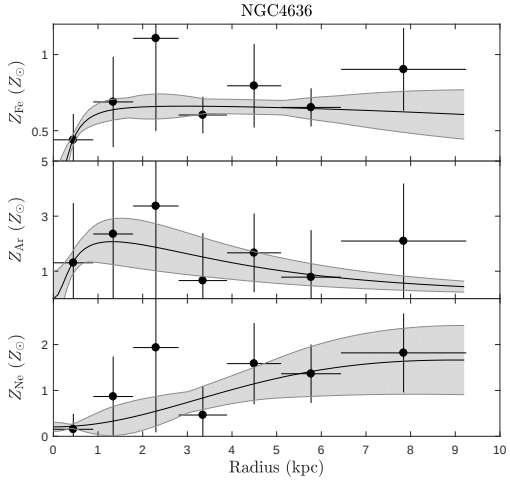
NGC4636
Z_{Fe} ($Z_\odot$)
Z_{Ar} ($Z_\odot$)
Z_{Ne} ($Z_\odot$)
Radius (kpc)

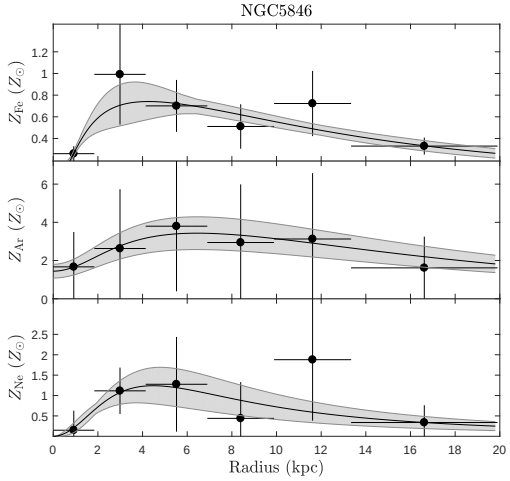
NGC5846
Z_{Fe} ($Z_\odot$)
Z_{Ar} ($Z_\odot$)
Z_{Ne} ($Z_\odot$)
Radius (kpc)

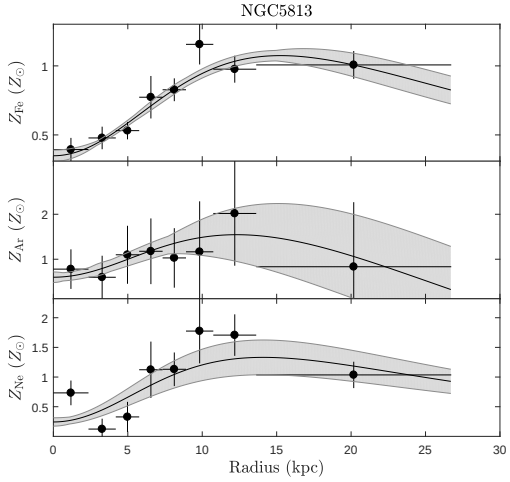
NGC5813
Z_{Fe} ($Z_\odot$)
Z_{Ar} ($Z_\odot$)
Z_{Ne} ($Z_\odot$)
Radius (kpc)

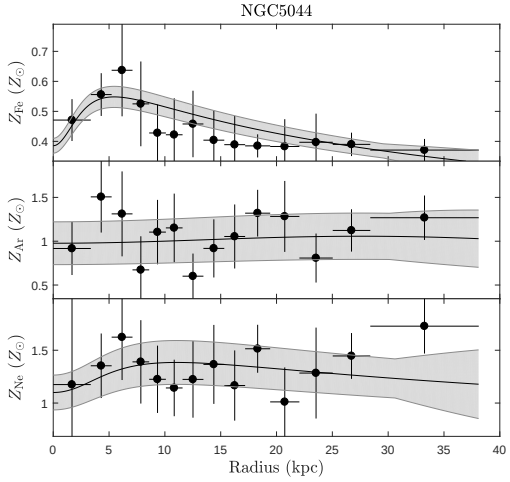
NGC5044
Z_{Fe} ($Z_\odot$)
Z_{Ar} ($Z_\odot$)
Z_{Ne} ($Z_\odot$)
Radius (kpc)

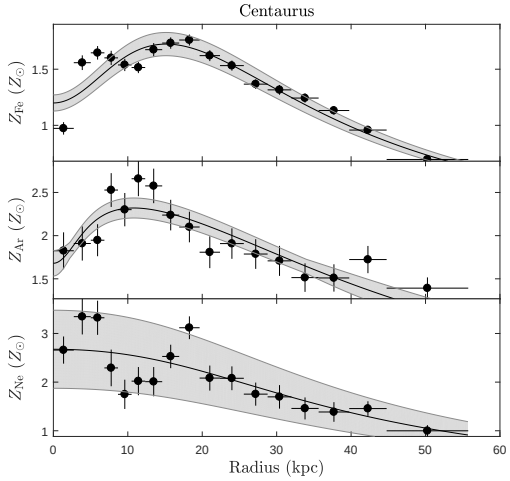
Centaurus
Z_{Fe} ($Z_\odot$)
Z_{Ar} ($Z_\odot$)
Z_{Ne} ($Z_\odot$)
Radius (kpc)

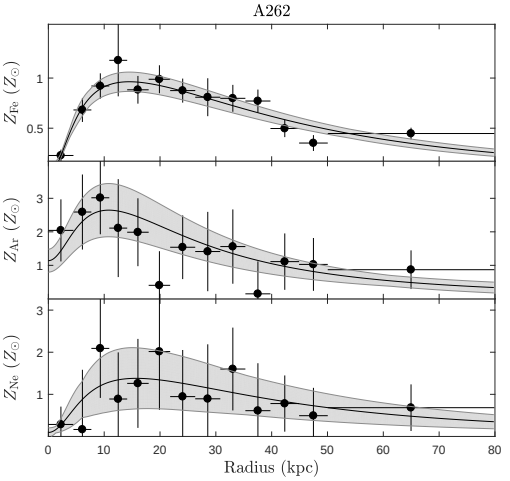
A262
Z_{Fe} ($Z_\odot$)
Z_{Ar} ($Z_\odot$)
Z_{Ne} ($Z_\odot$)
Radius (kpc)

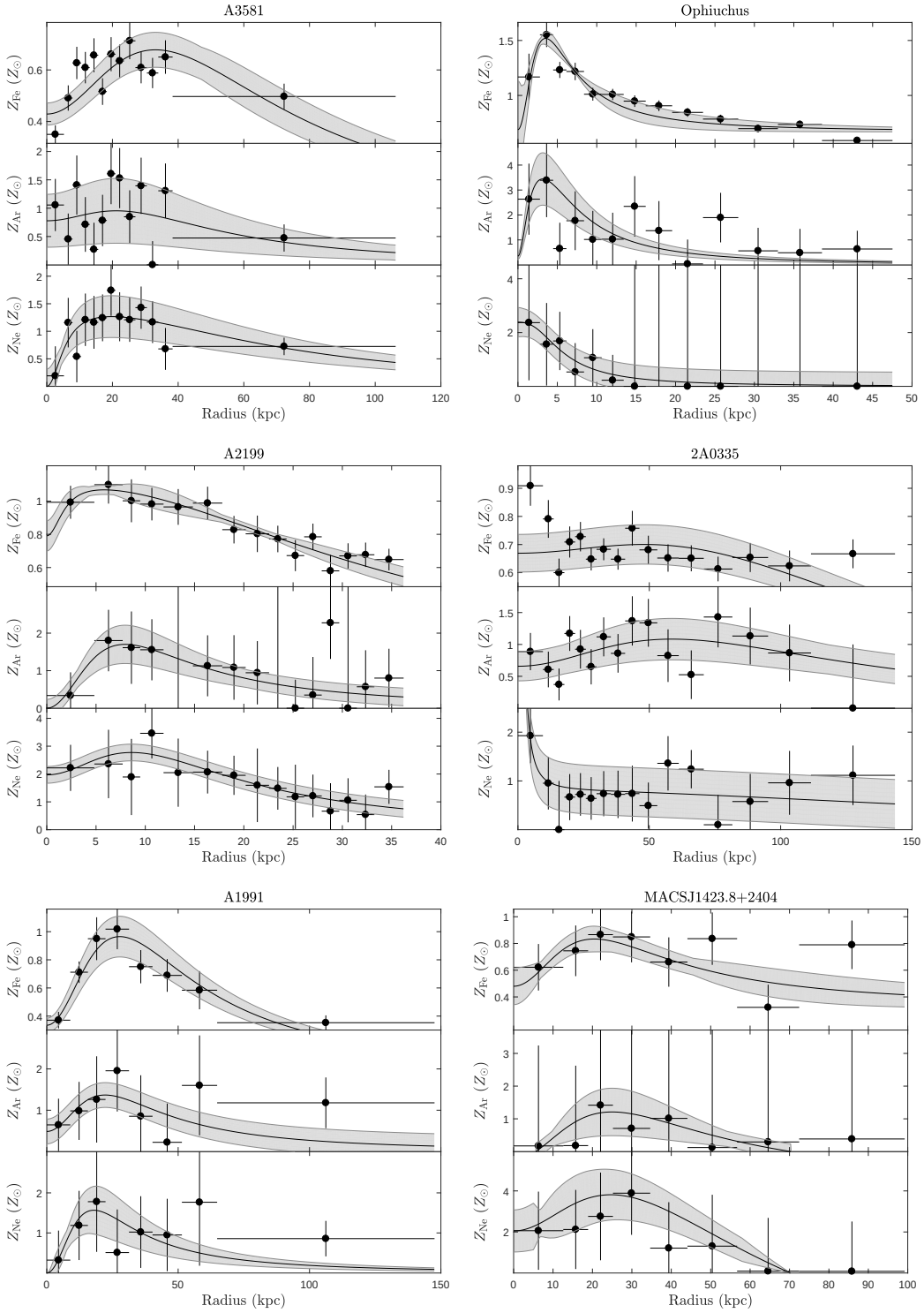

Figure 3.1. The abundance profiles of Fe (top), Ar (middle), and Ne (bottom) for all the groups and clusters in our sample, as a function of the physical radius in kpc. Abundances are expressed in units of solar values as in Asplund et al. (2009) [12]. Solid lines and shaded areas show the best fit functions given in Equation (3.1), and the 1σ confidence range, respectively.

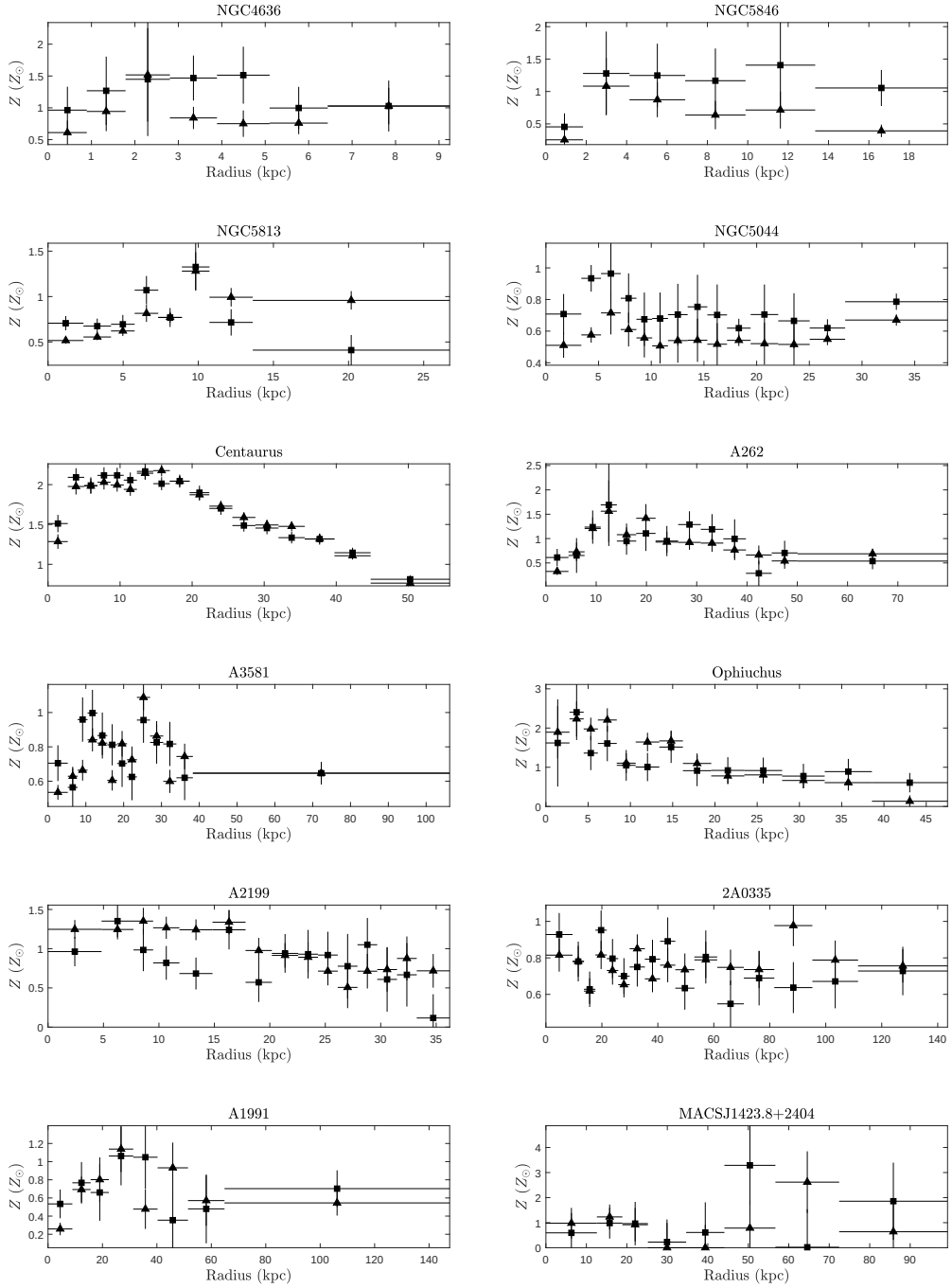

Figure 3.2. Abundance profiles of Si (solid triangles) and S (solid squares) for all the groups and clusters in our sample as a function of the physical radius in kpc. Abundances are expressed in units of solar values as in Asplund et al. (2009) [12].

carefully check for differences between our results and the literature. If we compare our projected profiles with the deprojected Fe profiles in Panagoulia et al. (2015), we find a good agreement, except in a few remarkable cases. In NGC5813 we find a smooth drop in the innermost 5 kpc, opposed to the sharp drop within 5 kpc in Panagoulia et al. (2015). We also find a smoother and more pronounced iron drop in A3581, which is considered only a possible drop in Panagoulia et al. 2015, despite their large error bars create no tension with our profile. While these differences may be due to the deprojection procedure, the results for 2A0335 are dramatically discrepant. In this cluster we find an iron peak opposed to the well defined iron drop shown in Panagoulia et al. (2015). We actually find that switching from 1T `apec` model to our reference 2T `apec` model is critical to find the peak. We also find a strong dependence of the temperature profile on the NH_{Gal} value, which we measure to be 3.1×10^{21} cm^{-2} as in Pinto et al. (2015), as opposed to lower value used for this clusters in Panagoulia et al. (2015). The value of NH_{Gal} is found to strongly affect the Fe abundance particularly for a 2T `apec` model. Our result is in agreement with Werner et al. (2006) [394]. However, the peculiar nature of the core of 2A0335, characterized by bright blobs and a complex metallicity map in the 2D analysis [318] suggests that assuming azymuthally average value for the ICM may provide contradictory results depending on details of the analysis, including the choice of the center (we assumed the BCG position in this case). We conclude that 2A0335 should not be included among the list of clusters showing a central Fe drop. We also find consistency with Lakhchaura et al. (2019) [182] for the Fe and Ar profiles of the Centaurus cluster, despite the different choice of the size of the radial bins hampers a detailed comparison. We also find that our projected Fe profile of the Ophiuchus cluster and the deprojected one in Million et al. (2010) [239] are compatible. Despite the different angular resolution makes it very difficult the comparison of *Chandra* and XMM-Newton profiles in the innermost regions, we find a broad consistency with the Fe profiles of NGC4636, NGC5044, NGC5813 measured with XMM-Newton in Mernier et al. (2017) [235], while we notice some differences in the cases of A3581, NGC5846 and Perseus. Significant difference, instead, are found for A262 and A1991, which were, in fact, not classified as Fe-drop by Mernier et al. (2017) [235]. Overall, we find that the Fe profiles obtained with

our approach are broadly consistent with literature, while significant differences occur in particular cases with extremely complex core structure, or in data with lower angular resolution.

We note, however, that the precise identification of the central drop is not straightforward and may be rather uncertain if based on, e.g., the distance between the highest and the lowest values in each profile, since it would be sensitive to the width of the annuli, and blurred by the statistical noise. Therefore, to better quantify the abundance drops in a uniform way, we fit each profile with an empirical function with five free parameters, able to reproduce a smooth, non-monotonic profile:

$$Z(r) = A \cdot \frac{\frac{r}{B} + C}{\frac{r}{B} + 1} \cdot \frac{1}{(1 + (\frac{r}{D})^2)^E} \,, \tag{3.1}$$

where the parameters B and D are the spatial scales corresponding to the drop in the inner few tens of kpc, and the outer profile, respectively, while the parameter C corresponds to the minimum value in the center. This functional shape is a simplified version of the profile used to described the temperature in Vikhlinin et al. (2006) [388], and it is overdetermined given our data quality. However, this function can reasonably reproduce the behaviour of all the different profiles. We stress that the parameters in the function have no direct physical meanings, but allow us to obtain a fit to all the profiles and the associated uncertainty as a function of the physical radius. The fit of the profile and the uncertainty on ΔZ are obtained with a Monte Carlo approach. Eventually, we visually inspect the profiles to search for any poor fitting and check the χ^2 values, finding that in all the cases we obtain acceptable fits. We remark that in the fits we allowed the minimum abundance values in each bin to be negative, an aspect that hardly affect single-cluster profiles (only a few points in Ophiuchus and A2199 turn out to be negative) but is relevant particularly in the stacking procedure, that may be slightly biased high if all the values are forced to be positive.

From the the best-fit analytic function, we can directly quantify the central abundance drop as $\Delta Z = Z_{\rm peak} - Z_{\rm in}$, where $Z_{\rm in}$ is the fitted abundance at the radius of the innermost bin, and $Z_{\rm peak}$ is the maximum value of the fitted abundance. The uncertainty on ΔZ is obtained by assuming the 1σ uncertainties of $Z_{\rm peak}$ and $Z_{\rm in}$ and summing them in quadrature. A central

Table 3.2. The magnitudes of the abundance drop, defined as $\Delta Z = Z_{\rm peak} - Z_{\rm in}$, for Fe, Ar and Ne are shown in columns 2, 3, and 4, respectively. In columns 5, 6, and 7, we list the distance between the maximum of the X-ray emission and the peak of the abundance profiles in kpc. The offset between the BCG and the X-ray emission peak is also given in column 8.

Cluster	ΔZ (Fe)	ΔZ (Ar)	ΔZ (Ne)	-
NGC4636	0.25 ± 0.08	0.86 ± 0.92	-	-
NGC5846	0.49 ± 0.17	1.78 ± 0.95	1.04 ± 0.45	-
NGC5813	0.71 ± 0.05	0.92 ± 0.45	1.06 ± 0.30	-
NGC5044	0.09 ± 0.04	-	0.26 ± 0.26	-
Centaurus	0.51 ± 0.12	0.58 ± 0.16	-	-
A262	0.74 ± 0.10	1.22 ± 0.90	1.11 ± 0.74	-
A3581	0.24 ± 0.08	0.17 ± 0.74	1.01 ± 0.45	-
Ophiuchus	0.42 ± 0.16	1.03 ± 1.29	-	-
A2199	0.07 ± 0.07	1.18 ± 0.56	0.63 ± 0.42	-
2A0335	0.03 ± 0.09	0.41 ± 0.40	-	-
A1991	0.57 ± 0.16	0.99 ± 0.45	1.25 ± 0.61	-
MACSJ1423.8+2404	0.25 ± 0.12	1.15 ± 0.76	1.63 ± 1.45	-

Cluster	$D_{\rm Fe}$ (kpc)	$D_{\rm Ar}$ (kpc)	$D_{\rm Ne}$ (kpc)	$D_{\rm BCG}$ (kpc)
NGC4636	2.9 ± 2.0	1.3 ± 0.7	-	0.16
NGC5846	4.3 ± 2.2	6.4 ± 3.4	4.4 ± 1.7	0.12
NGC5813	14.8 ± 2.5	12.2 ± 4.3	14.0 ± 5.4	0.16
NGC5044	5.5 ± 2.5	-	10.4 ± 7.1	0.22
Centaurus	14.9 ± 4.8	10.4 ± 5.6	-	1.56
A262	14.3 ± 5.4	10.7 ± 6.0	15.4 ± 9.0	0.99
A3581	33.1 ± 12.6	21.1 ± 21.1	19.0 ± 11.0	0.19
Ophiuchus	3.5 ± 0.7	3.1 ± 1.5	-	2.25
A2199	5.6 ± 3.1	7.8 ± 3.1	8.5 ± 3.9	1.98
2A0335	46.7 ± 42.7	56.7 ± 33.5	-	7.06
A1991	27.5 ± 10.0	21.9 ± 10.4	17.8 ± 7.3	4.76
MACSJ1423.8+2404	20.4 ± 7.7	24.7 ± 11.0	24.3 ± 8.3	-

drop is identified only when ΔZ has a significance level higher than 2σ. The measured values of ΔZ are shown for Fe, Ar and Ne in the second, third and fourth column, respectively, of Table 3.2. Our results confirm that all the

clusters in our sample exhibit a central Fe abundance drop at more than 2σ c.l., except for A2199 and 2A0335. However, we find a significant Ar drop in only 4 sources (NGC5813, Centaurus, A2199, and A1991) at more than 2σ, despite we have hints of a drop in most of the other sources. Formally, we also find a central drop in Ne abundance in 4 clusters (NGC5846, NGC5813, A3581, and A1991) at more than 2σ. We notice that, given the larger uncertainties in the profiles of Ar and Ne, our results are consistent with an abundance drop common to the three elements, which suggests a mechanical process removing the highly enriched ICM from the innermost region as an explanation for the observed profiles. We also remark that the detection of abundance drop in MACSJ1423.8+2404 at $z = 0.543$ implies that this feature is also present in high redshift clusters, and that the mechanism generating it has already taken place at a look-back time of $\sim$6 Gyr.

We can push further our analysis by stacking the abundance profiles of each element after rescaling the radius of each cluster by r_{500}. We divide the [0–0.15] r_{500} interval into 6 bins choosing the width in order to have a comparable number of data points in each bin. The values of r_{500} are taken from the compilation of clusters presented in Pinto et al. (2015) [278] and Liu et al. (2018) [192]. We then average all the data points in each bin weighted by the inverse squared errors and by the overlap of the geometric area of each physical annulus with the final bin, following the method of Leccardi et al. (2008) [186]. In addition, we also allow the free abundance parameters to be negative for the stacking, since this is the only way to properly deal with noise. As discussed in Leccardi et al. (2008) [186], forcing the abundance to be always positive may result in a positive statistical bias when averaging out the profiles. In the investigation of the stacked profiles we consider also S and Si, whose single-cluster profiles are shown in Figure 3.2.

The stacked abundance profiles of Fe, Ar, Ne, Si, and S are shown in the top panel of Figure 3.3. We find that in the central regions, the average abundances of Ar and Ne in our sample are significantly higher than that of Fe, while they tend to be consistent in the outermost bin, corresponding to [0.05–0.15] r_{500}. On the other hand, the profiles of Si and S are consistent with Fe within 1σ, despite they tend to show a slight increase. However, the most interesting and convincing feature is the much larger gradient of the Ar and Ne profiles with

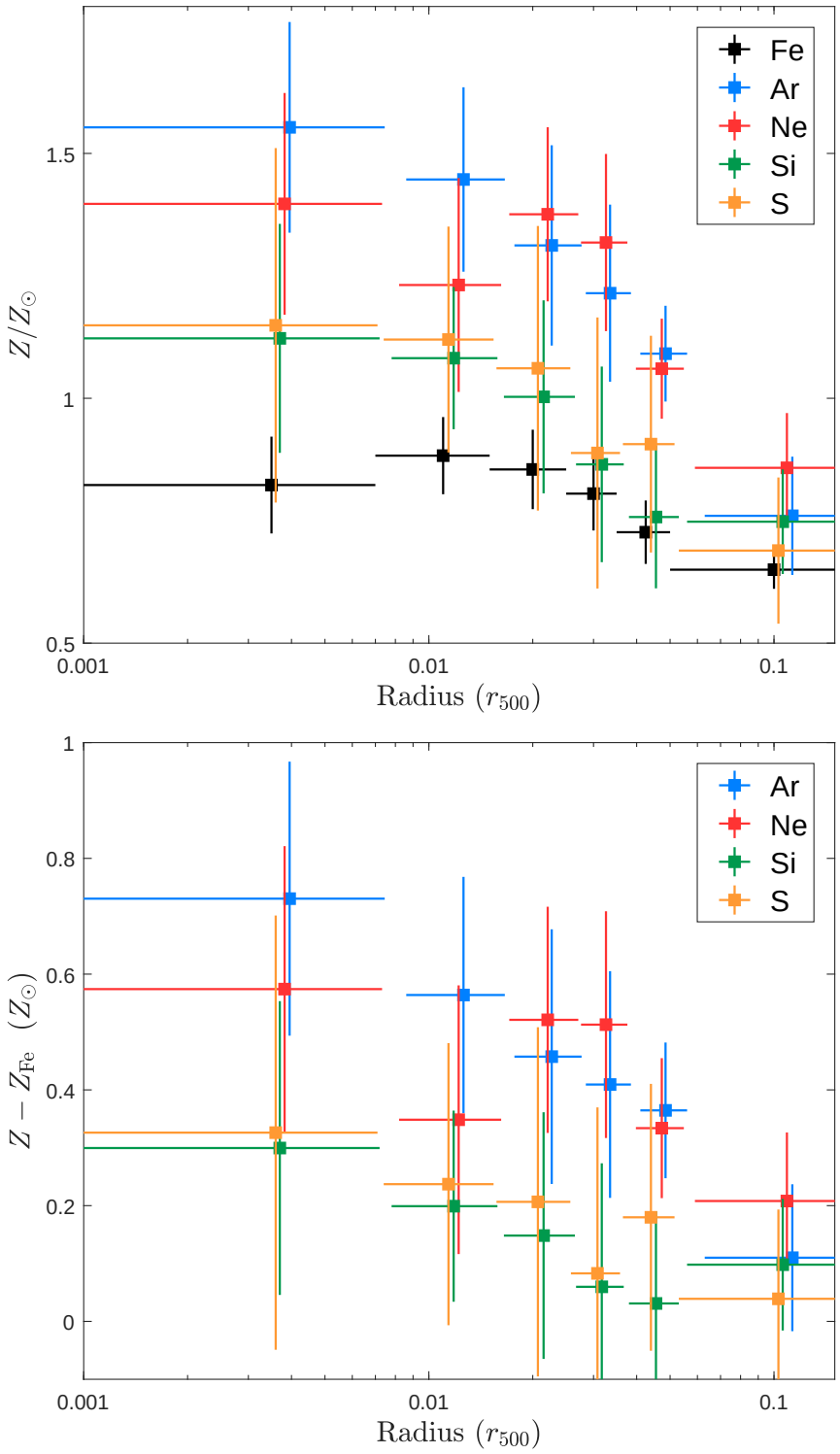

Figure 3.3. Upper panel: the stacked abundance profiles of Fe, Ar, Ne, Si, and S in our sample, as a function of the rescaled radius r/r_{500}. Bottom panel: abundance excess profiles of Ar, Ne, Si, and S relative to Fe. The data points have been slightly shifted on the x-axis for clarity.

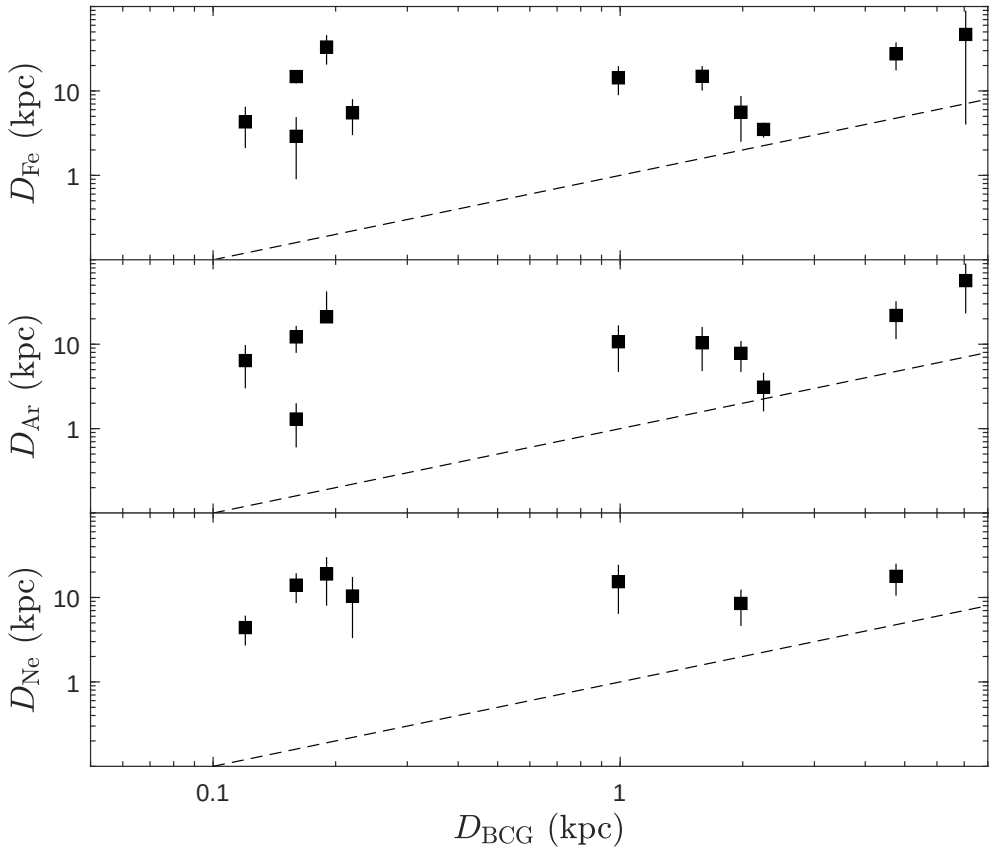

Figure 3.4. The displacement of the abundance peak with respect to the X-ray centroid are shown for Fe, Ar and Ne as a function of the offset between the BCG position and the X-ray centroid $D_{\rm BCG}$. The dashed line shows the $D_Z = D_{\rm BCG}$ relation as a reference.

respect to Fe, Si and S, which are all elements that may be depleted into cold dust grains. It is useful to remind that at larger radii, Ar abundance has been shown to be comparable or lower with respect to Fe [235]. The same behaviour can be seen in the absolute difference of the abundance of different elements as a function of radius, which is shown in the lower panel of Figure 3.3. We find that the difference $Z_{\rm Ar} - Z_{\rm Fe}$ decreases systematically with radius, while $Z_{\rm Si} - Z_{\rm Fe}$ and $Z_{\rm S} - Z_{\rm Fe}$ show a much milder decrease with radius. We cannot draw any conclusion on the quantity $Z_{\rm Ne} - Z_{\rm Fe}$ given the large uncertainties, not to mention the unknown systematics. Finally, we verified *a-posteriori* that

the stacked profiles are not dominated by the Centaurus cluster, despite it has by far the highest quality spectra. The stacked profiles obtained after excluding the Centaurus cluster have only negligible differences with respect to the results shown in Figure 3.3.

In Table 3.2 we also list the distance of the abundance peak of each element from the peak in the X-ray surface brightness, and, in the last column, the displacement of the BCG from the X-ray peak. We unambiguously identify the BCG of all the clusters but MACSJ1423.8+2404. The coordinates of the BCG come from the 2MASS catalog or NED/SIMBAD. The position of the abundance peak is measured from the best-fit of the abundance profile of the corresponding element. For most of the clusters, we find that $D_{\rm BCG}$ is much smaller than the distance from the abundance peak to the cluster center, implying that the BCG is inside the 'hole' carved into the abundance distribution. There is only one exception: the Ophiuchus cluster, with $D_{\rm BCG}$=2.25 kpc, and $D_{\rm Fe}$=3.5 $\pm$ 1.1 kpc. This is consistent with the clear signatures of an ongoing merger found by Million et al. (2010) [239]. For this cluster, we recompute the abundance profiles after setting the center on the position of the BCG, and we obtain a consistent result. In Figure 3.4 we show the relation between $D_{\rm Fe}$, $D_{\rm Ar}$, $D_{\rm Ne}$ and $D_{\rm BCG}$. We find no statistically significant trend among the BCG displacement and the position of the peak of the abundance profiles. Therefore, we conclude that there is no association between the displacement of the abundance peak (as a proxy for the size of the abundance drop region) and the offset of the BCG with respect to the X-ray centroid in our sample.

To summarize, we find 4 clusters with a drop in the Ar abundance profile at more than 2σ c.l., compared to 10 clusters with an Fe drop at the same significance level. This indication of a different spatial distribution among this two elements is further strengthened by our analysis of the stacked profiles, where the normalization and the slope of the Ar profile are clearly different from that of Fe, implying a larger Ar abundance in the core regions at radii $\leq$ 0.05 r_{500}. Possibly, the same trend is present in the Ne profile. At the same time, we find overall consistency between the profile of Fe, Si, and S, confirming a significant difference in the spatial distribution of elements that may be depleted into dust grains, and of noble elements. Therefore, despite our analysis confirms that the abundance drop is a characteristic shared by all

the elements, suggesting that the uplifting of high metallicity gas driven by bubbles is an effective process, we also found a significant difference between Ne and Ar and the other elements. This result implies that the depletion of Fe into dust grains during the baryon cycle in cool-core groups and clusters is also an effective process in shaping the abundance profiles. Since here we focus on projected values, further assumptions and a detailed modelization are both needed before quantifying the effects of dust depletion in terms of Fe mass-loss, a task which goes beyond the scope of this paper.

3.4 Discussion: robustness of the spectral analysis

In this section we discuss some aspects of our spectral analysis which may potentially introduce fitting bias. The first aspect is the choice of leaving the Galactic absorption parameter NH_{Gal} free to vary in each bin. It is a common choice in X-ray spectral fitting to freeze NH_{Gal} to the value of Kalberla et al. (2005) [165]. However, given the high signal of our spectra, and the complex thermal structure in each bin, a fluctuation in NH_{Gal} (which, we remind, is obtained from an HI map smoothed on a scale of ~ 1 degree) may bias one or both the temperature components of our model. To investigate the robustness of our strategy, we compare the best-fit values of NH_{Gal}, averaged across the annuli in each cluster, with the value from Kalberla et al. (2005) [165]. As shown in Figure 3.5, the values are often consistent within 1σ, but a slight positive bias is observed with the best fit values being on average $\sim 20\%$ higher. We repeated our fit forcing NH_{Gal} to be equal to the HI value, and found that our results do not change qualitatively, except in the remarkable case of 2A0335, as discussed in Section 3.3. However, in many cases the quality of the fit is significantly worse, and this is reflected in a systematic underestimation of the statistical error bars on the abundance values. The results presented in this work therefore are conservatively based on the fits obtained with free NH_{Gal}.

A more fundamental and critical aspect of our analysis is the model of thermal structure of the ICM, which we approximate with two temperature

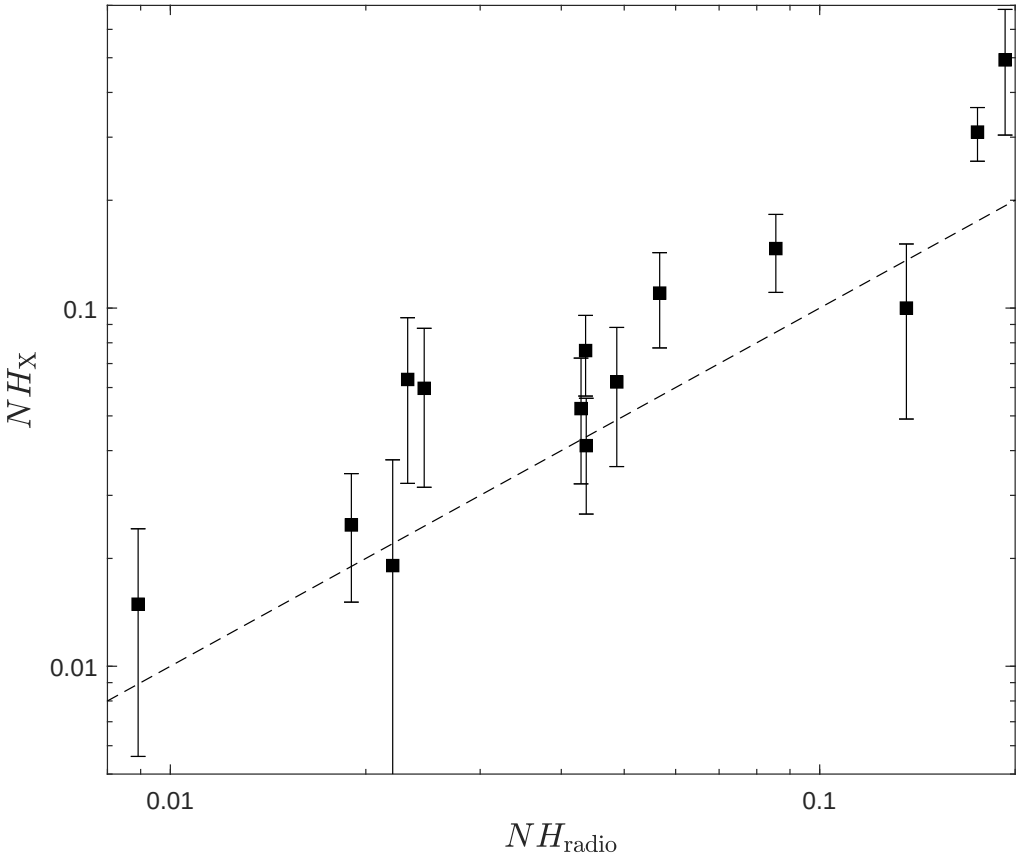

Figure 3.5. The Galactic HI column density from [165] compared to the average NH_{Gal} best-fit values obtained in each source of our sample. The dashed line shows the $NH_{\rm X} = NH_{\rm radio}$ relation. The unit for both axes is $10^{22}{\rm cm}^{-2}$.

components. We explore the effects of assuming a more complex underlying temperature structure, despite it cannot be constrained efficiently with CCD data. To do that, we repeat our fit with a `cevmkl` model, which is used to model the emission from a multi-temperature plasma. Emission measures from different temperature components follow a power-law in temperature, while the abundance ratios are defined in the usual way and are shared by all the temperature components. While we fix the minimum temperature to a reference value of 0.5 keV, the maximum temperature is set to a value somewhat larger than the largest temperature we found in our reference analysis, and leave the slope of the emission measure-temperature relation free to vary. In

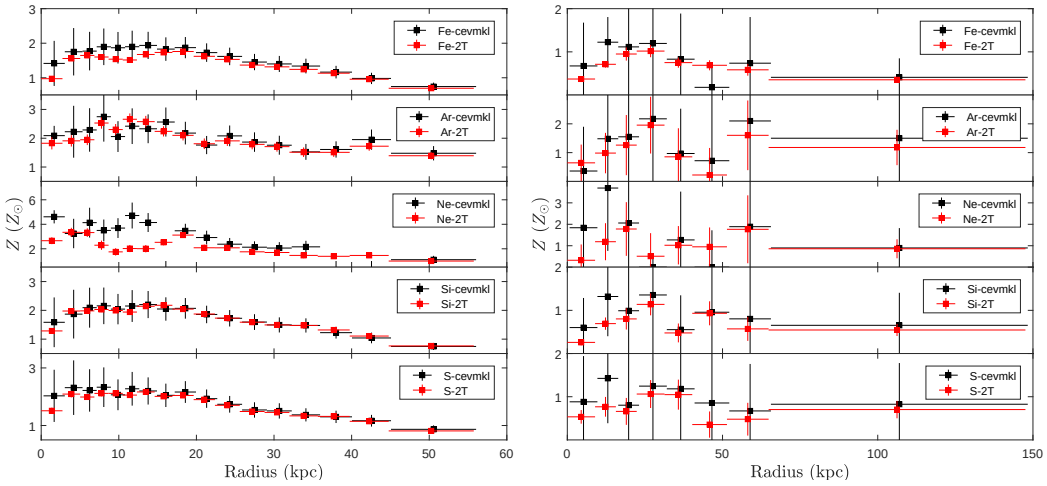

Figure 3.6. The abundance profiles of Fe, Ar, Ne, Si and S for the Centaurus (left panels) and Abell 1991 (right panels) obtained with the `cevmkl` model (filled black squares) and our reference two-temperature `vapec` modelization (filled red squares). The points of the `cevmkl` model have been slightly shifted along the x-axis for clarity.

this way we can explore the effects of having a continuous distribution of temperatures with respect to assuming only two values. We find that our results do not change significantly, as shown in Figure 3.6, where we plot the Fe, Ar, Ne, Si and S profiles obtained in the two modelizations (2T `vapec` compared to `cevmkl`) for Centaurus and Abell 1991, which represent the highest and lowest quality spectra in our sample. Not unexpectedly, the Ne profile is the only one that is noticeably affected, confirming our caveats that our results for Ne strongly depend on the modelization of the $\sim$ 1 keV line emission blend, and therefore are particularly sensitive to the thermal model we assume. Since we have no reasons to prefer a `cevmkl` rather than a double `vapec` model, we decide to keep Ne profiles according to our reference analysis, confirming the warning on unknown systematic uncertainties in addition to the statistical errors. Finally, we warn that differences between the results from `vapec` and `cevmkl` may also be due to different modelization of the Fe-L line complex built-in the two models. In particular, our reference model `vapec` is continuously updated, while `cevmkl` and `mekal` are no longer updated since several years. Some differences in the model may show up despite the low

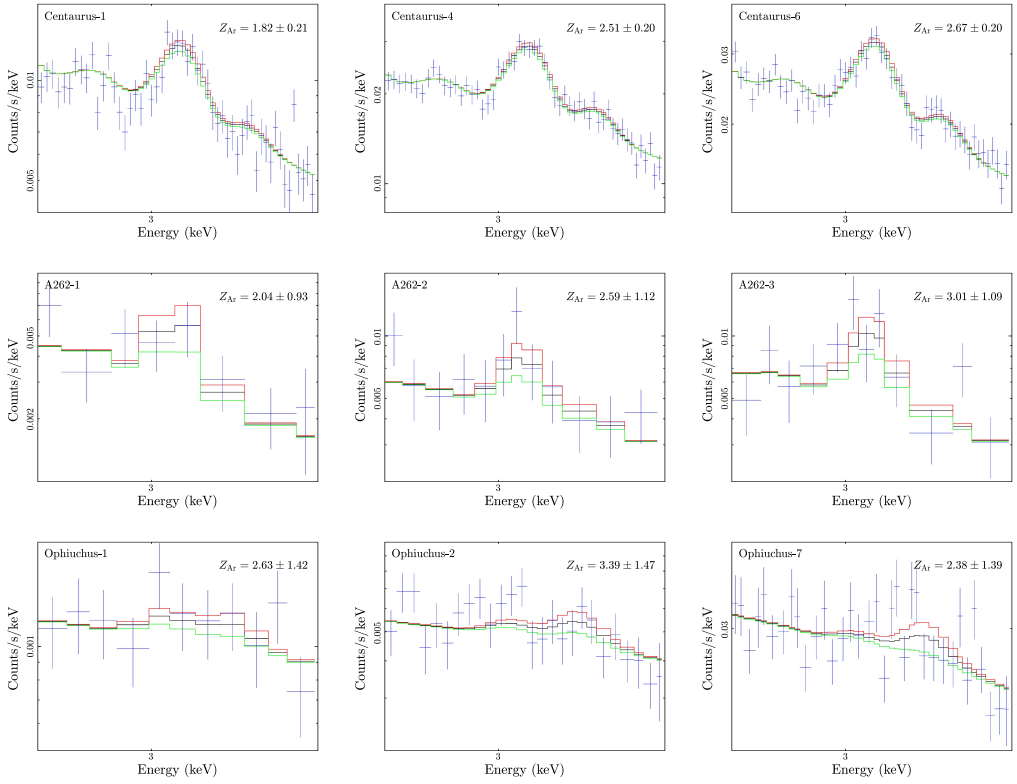

Figure 3.7. Narrow band (2.7–3.5 keV) stacked spectra of the first, fourth, and sixth bins of Centaurus, the first, second, and third bins of A262, and the first, second, and seventh bins of Ophiuchus. The best-fit models with 1σ upper and lower envelopes, as obtained from the broad-band fit, are shown as black, red and green solid lines, respectively.

resolution of CCD spectra, but are typically smaller than the typical statistical uncertainties we have in our data. A systematic comparison of the different atomic models goes beyond the goals of this paper (A detailed comparison can be found in `http://www.atomdb.org/Issues/mekalspex.php`, and also see the recent work of Mernier et al. [233], where the impact of atomic code uncertainties on the ICM abundance measurements has been discussed.)

Another source of potential systematics in our approach can be due to the use of a single abundance value common to the two temperature components. In general, the two temperatures should be considered a proxy for the real temperature structure of the ICM along the line of sight. This, in turn, can be due to the projection of ICM at different temperature, or to the presence of

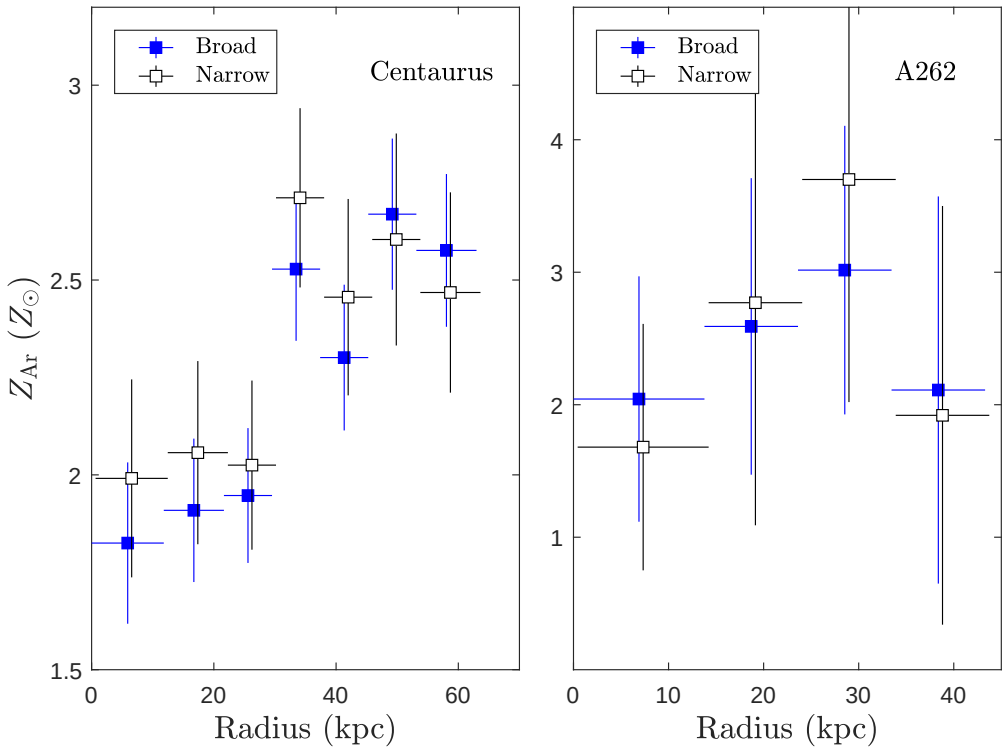

Figure 3.8. $Z_{\rm Ar}$ profiles of the inner most regions of Centaurus and A262. Solid-blue and empty-black squares represent the results from the 0.5–7 keV broad band, and the 2.9–3.5 keV narrow band, respectively. The black data points have been slightly shifted along the x-axis for clarity.

different phases at the same radius, or both. In any case, the abundance values associated to different temperature components may well be different, and there are no compelling reasons to force them to be equal. This is expected on the basis of the much scattered but clear correlation between metallicity and temperature in the core of clusters, or between metallicity and entropy (see Liu et al. 2018 [192] for a recent measurement of the abundance-entropy correlation in a sample of *Chandra* clusters). However, because of the modest CCD spectral resolution, if we relax the hypothesis of a single abundance value dominating the emission in each ring, the degeneracy between the temperature and abundance would be so large to hamper the measurement of abundance radial profiles other then Fe. The next major step forward to take in this

direction will be offered by X-ray bolometers, which will allow one to resolve single lines across the soft X-ray spectrum and provide a mean to associate an abundance value to each temperature component, enabling at the same time a much more structured thermal modelization. Admittedly, in this work we are compelled to assume a single abundance value for all the temperature components in each annulus, but we are aware that this assumption may be tested at least in the only available data obtained with an X-ray bolometer thanks to the *Hitomi* mission [150]. Therefore, we postpone this test to a more detailed work on the Perseus cluster.

Finally, it has been found that effective area calibrations are different among major, currently-available X-ray CCDs [343], and this effect can bias the measurement of metal abundance, particularly when the fit is driven by energy range far from that where the relevant lines are. In other words, the level of continuum can be poorly fitted, and this can severely affect the equivalent width of faint lines. For example, we notice that in a few cases (Centaurus, A262 and Ophiuchus) the maximum measured value of the Ar abundance is remarkably higher than $2\,Z_{\odot}$. To investigate whether these high values were actually spurious, first we perform a visual check, finding that the continuum level appears to be properly fitted in our spectra. A few relevant examples are presented in Figure 3.7, where we show the 2.7–3.5 keV range of the stacked spectra corresponding to three bins of Centaurus (bin 1 , 4, and 6 with $Z_{\rm Ar} = 1.82 \pm 0.21$, 2.51 ± 0.20 and 2.67 ± 0.20, respectively), A262 (bin 1, 2, and 3 with $Z_{\rm Ar} = 2.04 \pm 0.93$, 2.59 ± 1.12 and 3.01 ± 1.09, respectively), and Ophiuchus (bin 1, 2, and 7 with $Z_{\rm Ar} = 2.63 \pm 1.42$, 3.39 ± 1.47 and 2.38 ± 1.39, respectively). We recall that the best-fit models, shown as solid lines, are obtained separately fitting the spectra from single Obsid, and not the stacked spectrum. In all the cases the uncertainties in the continuum appear to be well within the statistical uncertainties, despite for the Ophiuchus cluster the spectrum is very noisy and the uncertainty on Ar abundance may be larger than the estimated error bars. We verified that our results do not change after removing the profile of the Ophiuchus cluster from the stacked abundance profiles. We conclude that the unexpectedly high values of Ar abundance found in some bins are properly characterized and have well-measured uncertainties, except one case (the Ophiuchus cluster) that may be affected by systematics,

but its removal is not affecting our main conclusions.

To better test the robustness of our results with respect to calibration uncertainties, we adopt the strategy followed in Lakhchaura et al. (2019) [182], where the abundances are remeasured in the 2.9–3.5 keV narrow band by leaving the normalization free, and the temperature, Galactic absorption frozen to the best-fit values of the broad band fit. In particular, we show in Figure 3.8 the Ar abundance profiles in Centaurus and A262 computed in the narrow band and broad band fits. Although some difference is present, the significance of the drop in the Ar abundance is not affected. Therefore, we confirm that our results are not significantly affected by clear uncertainties in the broad-band Chandra calibration.

3.5 Conclusions

In this work we analyze the abundance profiles in clusters where a central drop in the Fe abundance has been reported in the literature. Our aim is to test the origin of this feature, which may be associated to a mechanical process, like the uplifting of highly-enriched ICM in the center by AGN feedback, or to Fe depletion into dust grains, or to both processes. We exploit the exquisite angular resolution of *Chandra* to measure the abundance in the innermost regions of a sample of 12 cool-core clusters, thanks to the spectral resolution of the ACIS detectors. In particular, we compute the abundance profile of Ar and, within the limits of our assumptions, Ne, that cannot be incorporated into dust, and therefore should not exhibit a central abundance drop if due to dust depletion, when compared to the abundance profiles of other elements like Fe, Si or S. Our conclusions are summarized as follows.

- We confirm the detection of the Fe drop in 10 out of 12 clusters at a significance level larger than 2σ, in broad agreement with the literature.
- We are able to compute Ar abundance profiles out to $\sim 0.15 r_{500}$ after assuming a two-temperature structure for the ICM. We also present the profiles of Ne, which, however, are likely affected by systematics due to partial modeling of the line emission blend including Ne lines. We are, however, able to show that our abundance profiles for all the other

metals (Fe, Ar, Si and S) are not significantly affected by our specific choice for the thermal modelization of the ICM.

- We find central abundance drops of Ar in 4 clusters at a confidence level of more than 2σ, and, formally, 4 clusters with abundance drops of Ne. Si and S abundance profiles are found to be broadly consistent with Fe. Overall, our results are consistent with all the metals showing a central drop in abundance, therefore suggesting that a mechanical process directly removing the highly enriched ICM from the center, as the observed uplift of dense ICM driven by cavities carved by the central AGN, should be the main origin of the central abundance drops.

- We further extend our results by stacking the profiles in six bins in the range $[0–0.15]r_{500}$, finding that Ar (and possibly Ne) has significantly larger abundance in the center with respect to Fe, Si and S, and that its profile shows a much steeper gradient. This result, in turn, suggests that the dust grain scenario is indeed taking place in the center of these clusters, and has a significant effect in producing the Fe drop, which sums up to the mechanical removal of the most enriched gas. We successfully test the robustness of our conclusions with respect to the thermal modelization of the ICM, the spectral analysis strategy and possible calibration uncertainties.

- We confirm the detection of central Fe abundance drop in the galaxy cluster MACSJ1423.8+2404 at redshift 0.543, indicating that this feature is not confined to low redshift clusters, but has occurred in this cool-core cluster at least ~ 6 Gyr ago.

To summarize, we conclude that the signature of dust depletion can be observed in the abundance profiles of nearby, bright groups and clusters as a difference between the abundance profiles of noble gas like Ar and Ne and that of dust-depletable elements like Fe, Si and S. While some additional work can be done in this field on the basis of CCD data from the *Chandra* and XMM-Newton archives, a major improvement will be enabled only by the use of future X-ray bolometers. The capability of measuring with high accuracy the amount of Fe lost from the ICM because of dust depletion will be an important

information to constrain the cycle of baryons in the center of cool-core clusters and the interplay of the ICM with the insterstellar medium of the BCG.

Acknowledgments

We thank Simone Bianchi for useful discussions. We also thank the anonymous referee for a detailed and constructive report which significantly improved the paper. We acknowledge financial contribution from the INAF PRIN-SKA 2017 program 1.05.01.88.04 (*ESKAPE*) and from the agreement ASI-INAF n.2017-14-H.0.

Chapter 4

Chemical Evolution of Galaxy Clusters: Dissecting the Iron Mass Budget of the ICM

Ang Liu[1,2,3], Paolo Tozzi[1], Stefano Ettori[4,5], Sabrina De Grandi[6], Fabio Gastaldello[7], Piero Rosati[8], Colin Norman[9]

1. INAF - Osservatorio Astrofisico di Arcetri, Firenze, Italy

2. Department of Physics, Sapienza University of Rome, Rome, Italy

3. Department of Physics, University of Rome Tor Vergata, Rome, Italy

4. INAF - Osservatorio di Astrofisica e Scienza dello Spazio, Bologna, Italy

5. INFN, Sezione di Bologna, Bologna, Italy

6. INAF - Osservatorio Astronomico di Brera, Merate (LC), Italy

7. INAF - Istituto di Astrofisica Spaziale e Fisica cosmica di Milano, Milano, Italy

8. Dipartimento di Fisica e Scienze della Terra, Universitá degli Studi di Ferrara, Ferrara, Italy

9. Department of Physics and Astronomy, Johns Hopkins University, 3400 N. Charles Street, Baltimore, MD 21218, USA

(*Submitted to Astronomy & Astrophysics.*)

Abstract

We study the chemical evolution of galaxy clusters by measuring the iron mass in the ICM after dissecting the abundance profiles into different components.

We use *Chandra* archival observations of 186 morphologically regular clusters in the redshift range [0.04, 1.07]. For each cluster we compute the azimuthally-averaged iron abundance and gas density profiles. In particular, we aim at identifying a central peak in the iron distribution, associated with the central galaxy, and an approximately constant plateau reaching the largest observed radii, possibly associated with early enrichment occurred before and/or shortly after the formation of the cluster. We are able to firmly identify the two components in the iron distribution in a significant fraction of the sample, simply relying on the fit of the iron abundance profile. We compute the iron mass included in the iron peak and iron plateau, and the mass-weighted iron abundance of the ICM, out to an extraction radius of r_{500}. We find that the iron plateau shows no evolution with redshift either when considering the abundance $Z_{\rm plateau}$, or the iron mass $M_{\rm Fe}^{\rm plateau}$ rescaled by the gas mass. On the other hand, we find marginal ($< 2\sigma$ c.l.) decrease with redshift in the rescaled iron mass included in the iron peak. We measure that the fraction of iron peak mass is typically a few percent ($\sim 1\%$) of the total iron mass within r_{500}. Therefore, since the total iron mass budget is dominated by the plateau, we find that the global mass-weighted iron abundance does not evolve significantly across our sample. We are also able to reproduce past claims of evolution in the global iron abundance which turn out to be due to the use of cluster samples with different selection methods combined to the use of emission-weighted instead of mass-weighted abundance values. Finally, while the intrinsic scatter in the iron plateau mass is consistent with zero, the iron-peak mass exhibits a large scatter, in line with the fact that the peak is produced after the virialization of the halo and depends on the formation history of the hosting cool core and the strength of the associated feedback processes. We conclude that only a spatially-resolved approach can resolve the issue of the iron abundance evolution in the ICM, reconciling the contradictory results obtained in the last ten years. Evolutionary effects below $z \sim 1$ are marginally measurable with present-day data, while at $z > 1$ the constraints are severely limited by the poor knowledge of the high-z cluster population. The path towards a full and comprehensive chemical history of the ICM necessarily requires the use of high-angular resolution X-ray bolometers and a dramatic increase in the statistics of faint, extended X-ray sources.

4.1 Introduction

Massive galaxy clusters ($M_{\rm tot} > 10^{14} M_{\odot}$) are considered as closed boxes that retain the past history of their cosmic evolution. The majority of their total mass is in the form of dark matter, which contributes 80–90% of the mass budget. While the stellar mass in member galaxies or in a diffuse component only constitutes a minor faction (about 1–2% of the total and 6–12% of the baryonic mass, see [190] for example), the baryonic mass is dominated by the intracluster medium (ICM), which is a hot, optically thin diffuse plasma at low densities, in a local collisional equilibrium with temperatures of the order of 10^7 to 10^8 K. The thermodynamical and dynamical status of the ICM is non-trivially linked to the mass accretion history of the dark matter halo, the nuclear feedback from the central galaxy, and the star formation process in the member galaxies. The last process, in particular, leaves its imprint in the ICM as a widespread chemical enrichment by heavy elements, mostly produced by supernovae explosions in the member galaxies, that can be efficiently measured with X-ray spectroscopy [32], as also supported by simulations (see [26] and references therein). Tracing the evolution of metal abundance in the ICM can therefore provide useful information to reveal the star formation history in cluster galaxies across cosmic time and the process of mixing of the intergalactic medium (IGM) with the ICM [30, 69].

The abundance of heavy elements (also generically referred as "metals") in the ICM can be measured through the equivalent width of their emission lines in the X-ray spectrum. In particular, iron is the element with the most prominent emission line complex, and it is therefore the only heavy element that has been detected in galaxy clusters up to redshift 1.6 [303, 377, 378, 209] thanks to the K_α emission line complex at 6.7–6.9 keV. The detection of other metals, instead, typically requires high S/N spectra and, therefore, is basically limited to lower temperatures ($kT < 3$ keV), low redshifts, and central regions [67, 366, 235]. In this framework, iron is the only element that can be robustly used to investigate the spatial distribution in the ICM and the cosmic evolution of metals on a timescale of ~ 10 Gyr.

Several attempts have been made in the past decades to derive an average cosmic evolution of iron abundance in the ICM. After the first attempts

[248, 376], about ten years ago the first reliable assessment of the cosmic evolution of iron abundance in the ICM has been obtained thanks to the exploitation of *Chandra* and XMM-Newton archives. These works suggested a significant evolution of a factor of 2 in the redshift range $0 < z < 1.3$ [17, 223, 3]. The picture became less clear in the recent years, when new analysis showed little or no evolution [92, 227]. In addition, spatially resolved analysis adds further complications: the results are not only influenced by the radial range used to measure the abundance [14, 207], but also change significantly when using SZ-selected samples of clusters, instead of the former X-ray selected clusters [227]. Moreover, several works have shown that the spatial distribution of iron in the central regions evolves significantly with time [68], despite this does not necessarily imply a change in the amount of metals in the ICM, but rather a simple redistribution of metals [192]. In addition, we also found that the measurement of iron abundance without resolving its spatial distribution can potentially introduce systematic uncertainties as high as $\sim$25% [192]. A further critical aspect, is that very little is known on the distribution of metals at large radii, so that statistical studies are meaningful only for radii well below r_{500} [244].

We argue that, in order to reach a more clear picture of the evolution of iron in the ICM on the basis of current X-ray data archives, we should most efficiently exploit what we know about the iron distribution. Both simulations and observations have indicated that the spatial distribution of iron in the ICM often appears to be well described as a combination of two main components: a peak in the inner regions which is usually centered on the brightest cluster galaxy (BCG), and a large-scale component with approximately uniform [358, 339, 396, 370, 383, 341, 199] or slightly decreasing [235, 27] abundance across the cluster (see Figure 1.15). The BCG is thought to be largely responsible of the iron peak, while multiple processes, including AGN outflow, gas turbulence, galactic winds, ram pressure stripping etc., extract the metal rich IGM from the member galaxies across the entire lifetime of the clusters, and leave their imprints on the distribution of iron in ICM [30, 173, 339, 192]. Another minor, but interesting component, is a characteristic drop of the iron abundance in the very center, which is associated both to the mechanical feedback from the AGN and to the iron depletion associated

to recent star formation in the BCG [265, 182, 197]. The almost uniform large-scale iron plateau, with a typical abundance of $\sim 1/3\, Z_{\odot}$, is expected to come from early star formation in the member galaxies around cosmic noon, therefore, before the formation/virialization of the cluster itself [207].

In this work, we reconsider the cosmic evolution of iron in the ICM, by performing spatially resolved spectroscopic analysis on a large sample of high-quality *Chandra* data to measure the mass-weighted iron abundance and fit the iron profile with a double-component model (an iron peak and a plateau), and investigate the evolution of these components separately. The paper is organized as follows. In Section 2, we describe the selection of cluster sample, and the reduction of *Chandra* data. In Section 3, we investigate the global properties of the clusters and the azimuthally-averaged profiles of density, iron abundance, and, therefore, iron mass. In Section 4, we discuss the results of our analysis. Our conclusions are summarized in Section 5. Throughout this paper, we adopt the seven-year WMAP cosmology with $\Omega_{\Lambda} = 0.73$, $\Omega_m = 0.27$, and $H_0 = 70.4$ km s^{-1} Mpc^{-1} [176]. Quoted error bars correspond to a 1 σ confidence level, unless noted otherwise.

4.2 Sample selection and data reduction

4.2.1 Sample selection

We start from a complete list of galaxy clusters with public *Chandra* archival observations as of February 2019. Our aim is to identify and disentangle spatial components under the assumption of spherical symmetry, within the largest radius that still allows a robust spectral analysis. Clearly, the requirement on spherical symmetry puts a strong constraints on the morphology of clusters suitable for our analysis. We select our final sample of clusters on the basis of the following criteria.

First, we require our extraction radius $R_{\rm ext}$ to be entirely covered by the field of view of the *Chandra* data. The adopted minimum value for $R_{\rm ext}$ is needed to sample ICM regions far enough from the central peak, in order to measure independently the large scale plateau. Several studies have shown that $\sim 0.4\, r_{500}$, or $\sim 0.25 r_{200}$, is typically well beyond the extension of the

iron peak, and reaches the iron plateau [383, 199]. We also find that setting $R_{\rm ext} = 0.4\,r_{500}$ allows a robust spectral analysis for the large majority of the clusters in our sample. While for some of them it would be possible to extend the measurement of the abundance profile out to [0.5–0.6] r_{500}, this would have a minor impact on the final profile given the large error in the outermost bin. Finally, $0.4\,r_{500}$ is considered a safe limit, due to the fact that also the thermodynamical structure of the gas at larger radii, which heavily impacts the abundance measurement, is increasingly uncertain [244]. On the other hand, we remark that the surface brightness can be measured out to r_{500}, allowing a proper constraint on the gas mass within r_{500}. Since we are ultimately interested in the average mass-weighted abundance obtained as the ratio of iron mass and total gas mass within a given radius, and considering that we assumed a constant plateau for the abundance at large radii, we can express our results as obtained within r_{500}. The values of r_{500} used for sample selection are obtained from literature [33, 275], or estimated from scaling relations [388]. When we apply this criterion, most of the nearby clusters at $z < 0.05$ are excluded.

Second, to produce iron abundance profiles with acceptable quality, we require a number of net counts ≥ 5000 in the 0.5–7 keV energy band and within the extraction radius. This requirement is needed in order to have at least six independent annuli with more than ~ 800 net counts each. The criterion adopted here is slightly weaker than in the previous Chapters (where it was 1000 net counts per bin) because here we want to privilege the spatial resolution with respect to the error on the single-bin abundance measurement. Clearly, this will apply only to the faintest targets, while in most of the cases the profiles will be sample with a better photon statistics.

Third, since we necessarily assume spherical symmetry when deprojecting the azimuthally averaged profiles, clusters with clear signatures of non-equilibrium, such as an irregular morphology and obvious substructures or mergers (some well known cases are 1E0657-56, Abell520, Abell3667), should not be included in the sample. Major mergers are observed to affect mostly the inner regions, while at large radii often shows a rather flat abundance distribution, similar to relaxed clusters [384]. There are many morphological parameters that can be used to determine whether a cluster is regular or

not, such as the X-ray surface brightness concentration [324, 45], the power ratio [40, 41], and the centroid shift [256, 45, 200]. In Chapter 2 we adopted a sophisticated criterion making use of the best morphological parameters available for the clusters in the Mantz et al. sample. Since here the sample is larger by a factor of 3, and the morphological information do not have the same quality for all the clusters, we choose to rely on a simplet parameter, based on the centroid shift, which measures the variance of the separations between the X-ray peak and the centroids of emission obtained within a number of apertures of different radii:

$$w = \frac{1}{R_{\rm max}} \times \sqrt{\frac{\sum(\Delta_i - \bar{\Delta})^2}{N-1}}, \tag{4.1}$$

where $R_{\rm max}$ is set as $[0.3-1]\,r_{500}$, N is the total number of apertures within $R_{\rm max}$, Δ_i is the separation of the X-ray peak and the centroid computed within the $i_{\rm th}$ aperture. The definition of the parameter varies slightly across the literature. In this work, we set $R_{\rm max}$ to $0.4r_{500}$, and the number of apertures to 10. The boundary between regular and disturbed clusters adopted in the literature ranges from 0.01 to 0.02 [256, 45]. Here we use a relatively loose criterion: $w < 0.025$, so that only the most disturbed targets are excluded at this step. Then, we check visually the X-ray image of all the clusters that satisfy the centroid-shift criterion to further identify clusters with a clearly disturbed morphology.

Starting from a total of ~ 500 targets in the *Chandra* data archive, the sample reduces by $\sim 50\%$ with the first and second criteria. After the morphology criterion and final check, we obtain a final sample consisting of 186 clusters, spreading over a redshift range [0.04, 1.07]. We remind that, since the sample is selected from the *Chandra* archive, rather than any existing flux-limited or volume-limited catalogs, it has no completeness in mass, or luminosity, etc., and might be subject to selection bias. This aspect clearly constitutes a limitations for the investigation of the cosmic evolution in the enrichment of the ICM. However, our main goal here is to identify potential difference in the evolution of the two components. The dependence of the evolution on the sample selection will be discussed in Section 4.4, while a complete treatment of this aspect is beyond the goal of this paper and it is

deferred to a further work based on the entire *Chandra* and XMM-Newton archives.

4.2.2 Data reduction

Data reduction is performed with `CIAO 4.10`, with the latest release of the *Chandra* Calibration Database at the time of writing (`CALDB 4.7.8`). Unresolved sources within the ICM are identified with `wavdetect`, checked visually, and eventually removed. Time intervals with high background is filtered by performing a 3σ clipping of the background level. The light curves are extracted in the 2.3–7.3 keV band, and binned with a time interval of 200 s. For clusters with multiple observations, we extract the spectrum and compute the ancillary response file (ARF) and redistribution matrix file (RMF) for each observation separately with the command `mkarf` and `mkacisrmf` (for several observations with the temperature of the focal plane equal to -110 K we use `mkrmf` instead). The background spectrum is extracted from the 'blank sky' files, and processed using the `blanksky` script, due to the large extent of the sources and our goal of measuring the low-surface brightness of the ICM out to $\sim r_{500}$. Whenever possible, we also repeat our analysis using the local background, generated by directly extracting the data from a source-free region on the same CCD chip. We confirm that the fitting results using this two backgrounds are in generally good agreement.

The spectral fits in this work are performed with `Xspec 12.10.1` [9] using C-statistics [44]. The AtomDB version is 3.0.9. All the abundance values in this paper are relative to the solar values of Asplund et al. (2009) [12]. The emission of the ICM within a projected annulus is fitted with a double-`vapec` thermal plasma emission model [345] for a better fit to the multiple-temperature structure [164]. It has also been shown that the use of two temperatures is sufficient to remove the systematics associated to the thermal structure of the ICM, while the inclusion of more thermal components do not provide significant improvements [244]. The metal abundances of the two `vapec` components are linked. The abundances of O, Ne, Mg, Al, Si, and S, which are mostly ejected by core-collapse supernovae, are independent from the Fe abundance and linked together. Other metals are linked to Fe, while the abundance of He is always

fixed to solar value. Due to the high temperature of the clusters in our sample and the relatively low S/N of the data, in most of the cases we are not able to obtain robust constraints on the abundance of the other elements, which, however, are not the main goal of this paper. Galactic hydrogen absorption is described by the model `phabs` [18], where the Galactic column density $n_{\rm H}$ at the cluster position is initially set as $n_{\rm H,tot}$ from Willingale et al. (2013) [398], which takes into account not only the neutral hydrogen, but also the molecular and ionized hydrogen that may bias the spectral fitting if not considered properly [199]. When fitting the global emission, we set the $n_{\rm H}$ free to vary below a very loose upper limit at $10\times n_{\rm H,tot}$, and measure the best-fit $n_{\rm H,free}$. This value is then adopted as the input $n_{\rm H}$ in further spatially-resolved analysis, but it is allowed to fluctuate within its 1σ statistical confidence interval, or $\pm 50\%$ if its uncertainty is lower than 50%. We will discuss the impact of the $n_{\rm H}$ value on our results in Section 4.4.

To determine the X-ray center of each cluster, we smooth the 0.5–7 keV image of the extended emission (after removing point sources) with a Gaussian kernel with FWHM $= 3''$, and find the position of the brightest pixel. This is a very quick and efficient method to identify the X-ray centroid for relaxed, cool-core clusters. In the case of a very low surface brightness also in the central regions, a more robust method is to perform a 0.5–7 keV band photometry within a circle with a fixed radius (typically ~ 40 kpc), and choose the position that maximize the net counts. Clearly, having removed the clusters with irregular morphology, any change in the X-ray centroid within the uncertainties, has a negligible impact on the final results.

4.3 Imaging and spectral analysis

4.3.1 Global properties: redshift, temperature, r_{500}, and concentration

We first derive the global properties of the clusters, including the X-ray redshift, the global temperature, the value of r_{500} and M_{500}. The X-ray redshift is measured by fitting the spectrum of the global emission within the radius maximizing the signal to noise ratio in the 0.5–7 keV band image. Among the

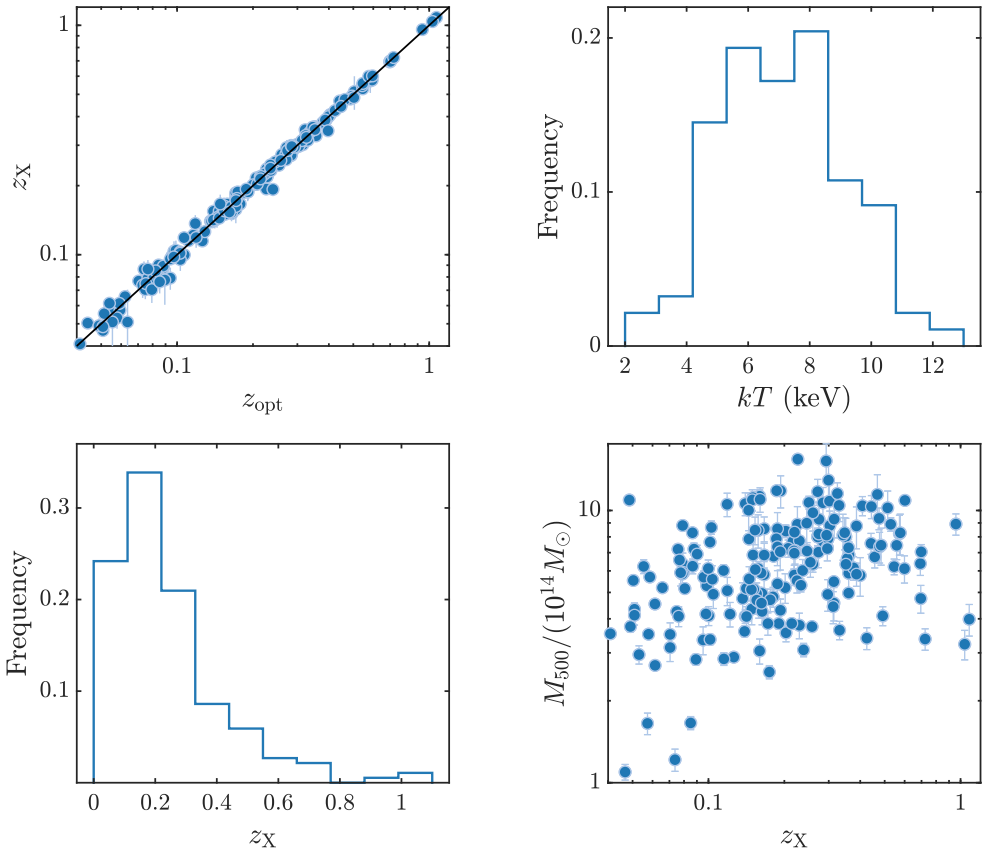

Figure 4.1. General properties of the cluster sample used in this work (186 clusters). *Upper left*: X-ray redshift measured in this work compared to the optical redshift from the literature. *Lower left*: Distribution of the redshift of the clusters in our sample. *Upper right*: Distribution of the emission weighted temperature within $[0.1, 0.4]r_{500}$ across the sample. *Lower right*: Distribution of M_{500} plotted vs redshift.

186 clusters in our sample, 184 have optical spectroscopic redshifts published in the literature. In Figure 4.1 (top-left panel) we compare the X-ray and optical redshifts, and find that the *rms* of $(z_X - z_{opt})$ is slightly lower than the average statistical uncertainty in the redshift measurements, implying a good agreement between z_X and z_{opt}. Therefore, we fix the redshift at the best-fit X-ray value in the following analysis. In some clusters, the difference in X-ray and optical redshifts may slightly influence the measurement of abundance, but this influence is rather small and negligible for our purpose [192]. In general, our sample contains a large fraction of low redshift clusters, with ∼70% clusters

at $z < 0.3$ and only less than ten clusters at $z > 0.6$ (see bottom-left panel of Figure 4.1). This is mostly due to the requirement on the minimum number of net counts.

The global temperature $\langle kT \rangle$ is measured by fitting the spectrum extracted in the region $0.1r_{500} < r < 0.4r_{500}$, a choice that is often adopted to obtain temperature values that more closely trace an ideal virial value, avoiding the effect of the cool core, when present. We use a single-temperature `apec` model, therefore $\langle kT \rangle$ is an emission weighted value resulting from the range of temperatures present in the explored radial range. We find that the values of $\langle kT \rangle$ range from 4 to 12 keV, with a minority of clusters with $\langle kT \rangle < 4$ keV (see top-right panel of Figure 4.1).

To estimate r_{500}, we use the average relation described in Vikhlinin et al. (2006) [388], which has been widely adopted in literature [14, 192, 232]:

$$r_{500} = \frac{0.792}{hE(z)} \left(\frac{\langle kT \rangle}{5 \text{ KeV}} \right)^{0.527} \text{Mpc}, \tag{4.2}$$

where $E(z) = (\Omega_{\rm m}(1+z)^3 + \Omega_\Lambda)^{0.5}$. The global temperature $\langle kT \rangle$ and r_{500} are evaluated iteratively. The total mass within r_{500} is also estimated from Vikhlinin et al. (2006) [388], or, equivalently, can be written as:

$$M_{500} = \frac{4\pi}{3} r_{500}^3 \cdot 500 \rho_{\rm c}(z), \tag{4.3}$$

where $\rho_{\rm c}(z) = 3H^2(z)/8\pi G$ is the critical density at cluster's redshift. Our sample spans a mass range of [1, 16] $\times 10^{14} M_\odot$, with only four clusters with $M_{500} < 2 \times 10^{14} M_\odot$ (see bottom-right panel of Figure 4.1).

Since cool-core and non-cool-core clusters are significantly different in both the abundance and spatial distribution of iron in the ICM, we estimate the fraction of cool-core clusters in our sample with the surface brightness concentration $c_{\rm SB}$ [324, 325], defined as the ratio of the fluxes observed within 40 kpc and 400 kpc:

$$c_{\rm SB} \equiv \frac{\rm S(40kpc)}{\rm S(400kpc)}. \tag{4.4}$$

The fluxes in equation (4.4) are computed in the 0.5–2 keV band, and are estimated directly from the net count rate after considering the "beheading effect", due to the K-correction that depends on redshift and the minimum temperature observed in the core (see [325] for more details). We remark that

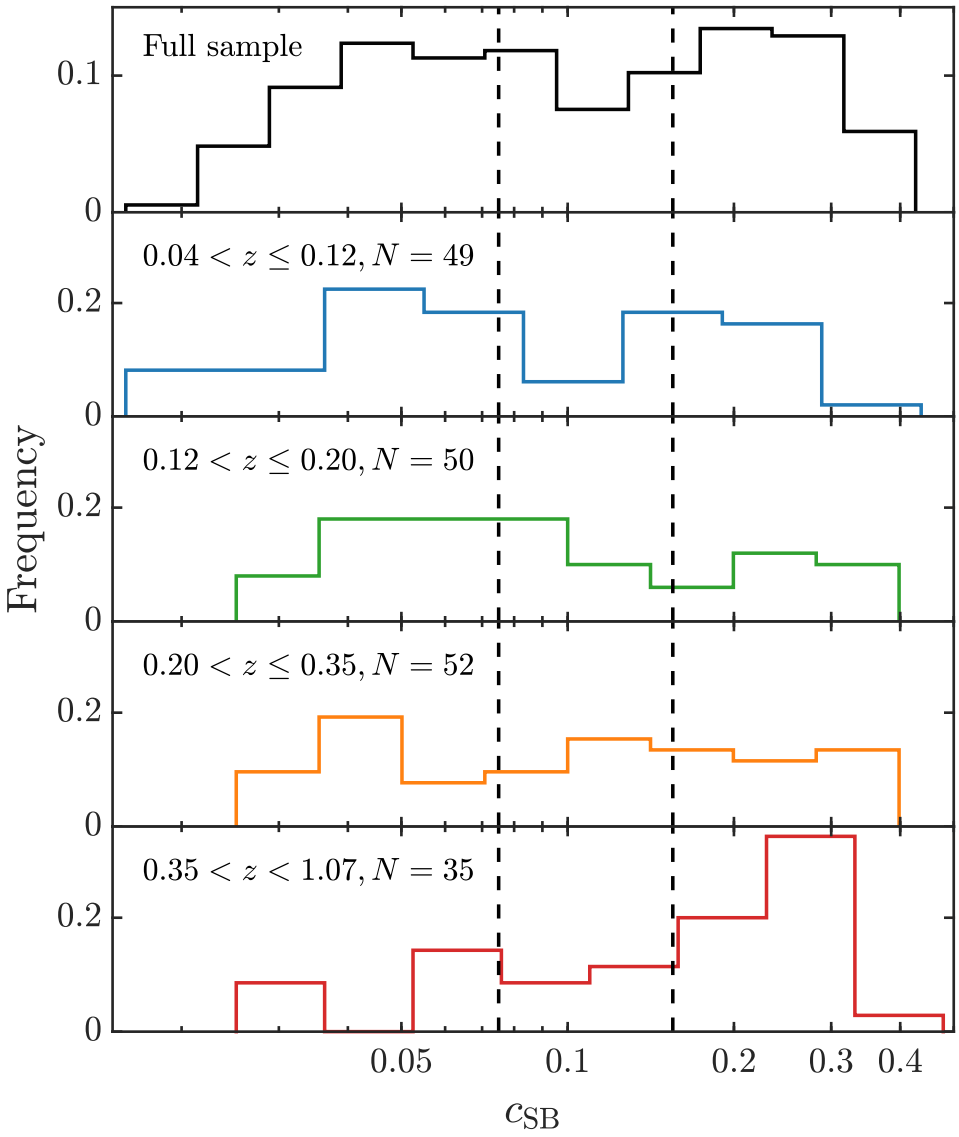

Figure 4.2. Distribution of the surface brightness concentration c_{SB} of the clusters in the full sample and in 4 redshift bins with roughly the same number of clusters. The vertical dashed lines indicate the threshold for non-cool-core and weak cool-core clusters: $c_{\mathrm{SB}} = 0.075$ and $c_{\mathrm{SB}} = 0.155$.

the concentration parameter is a simple and reliable parameter to classify the cool-core strength, which is, in reality, a definition that involve complex physics [155]. A bimodal distribution can be seen in the upper panel of Figure 4.2, which reflects the bimodality of cool-core and non-cool-core clusters as already

investigated in other properties like pseudo-entropy [322, 155]. Clearly, a more robust classification of cool-core and non-cool-core clusters should rely on more diagnostics, e.g. central cooling time, temperature drop, etc. However, since this is not the main focus of this paper, we will not make further analysis on the cool-core properties of the clusters, but merely investigate the global fraction of cool cores in our sample. Using $c_{\rm SB} < 0.075$ and $c_{\rm SB} > 0.155$ as the thresholds between non-cool-core/weak cool-core, and weak/strong cool-core clusters, respectively [324], we find that 72 (38.7%) clusters in our sample are non-cool-core clusters, while 46 (24.7%) and 68 (36.6%) are weak- and strong-cool-core clusters.

Interestingly, the balance between cool-core and non-cool-core clusters in our sample is redshift dependent. In the lower panels of Figure 4.2 we show how the bimodality disappears at $z > 0.2$, while the cool-core clusters become dominant in the range $z > 0.35$. Given the coarse redshift binning, this is not in contradiction with previous claims on the dearth of cool-core clusters at $z > 0.7$ [324], considering that we have only 7 clusters at $z > 0.7$. In addition, we note that the requirement on the S/N slightly favors CC clusters as the redshift increases. Therefore, no claim can be made on the evolution of cool cores with cosmic time with the current sample.

Overall, the fraction of $\sim 61\%$ of clusters hosting a cool core in our sample, is in line with what is usually found in X-ray selected samples, such as MACS, where Rossetti et al. (2017) [305] found a cool-core fraction of $(59 \pm 5)\%$, but is significantly higher than the fraction found in SZ selected samples ($\sim$30% for *Planck* clusters as found in Rossetti et al. (2017) [305]). This discrepancy, which is robust against differences in the detailed definition of cool-core, is the well known "cool core bias" [84, 4], and may affect the overall thermal and chemical properties of a sample. In general, our sample shares the same core properties as other X-ray selected samples, despite it includes a sizeable fraction of SZ-selected clusters.

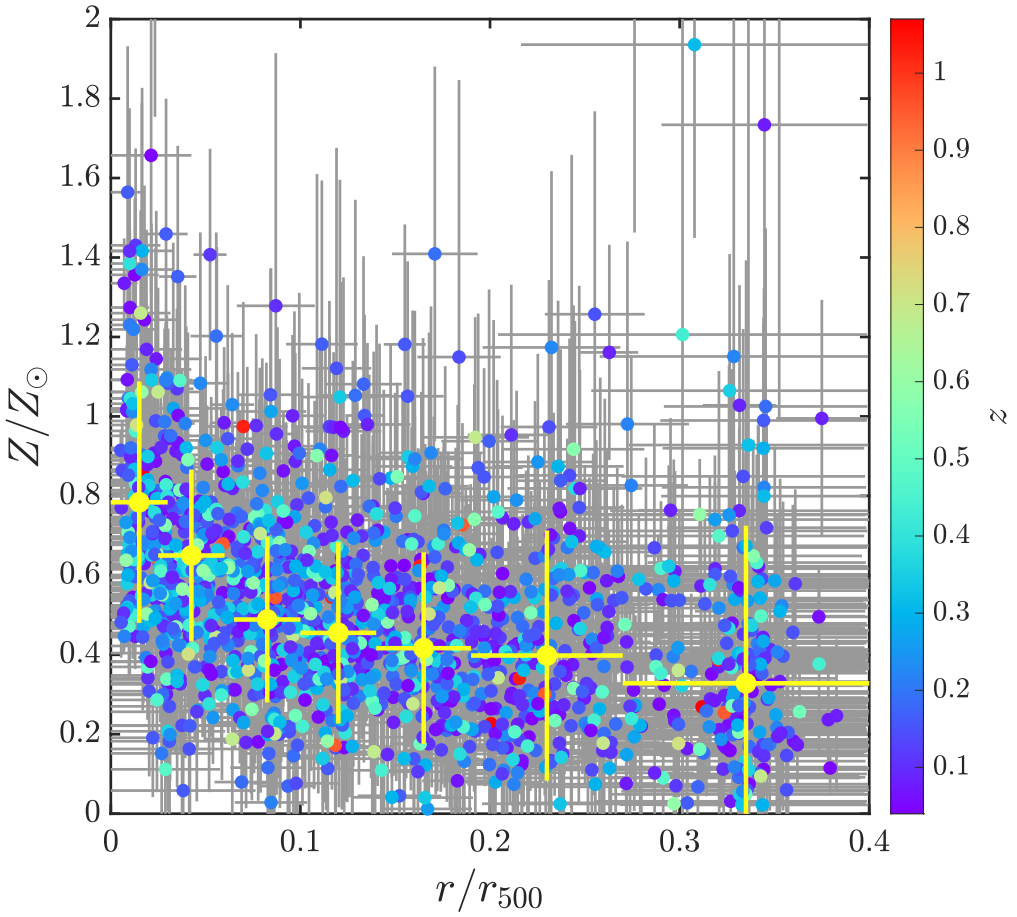

Figure 4.3. Projected iron abundance profiles for all the clusters in our sample. Each point, color coded by redshift, is the best-fit value in the corresponding radial bin. For clarity error bars are shown in light grey. The yellow points show the sample-average abundance and *rms* within seven radial bins.

4.3.2 Azimuthally-averaged profiles of electron density, iron abundance, and iron mass

We now measure the azimuthally-averaged profiles of gas density and iron abundance, and consequently the iron mass cumulative profile. While accurate deprojection is always mandatory for density profiles, we choose to use only the projected profiles for iron abundance. The reason for this choice is twofold. First, since the typical metallicity variation across a cluster is usually smaller than a factor of ~ 3 ($\sim Z_\odot$ at the iron peak to $\sim Z_\odot/3$ in the outskirts),

projection effect has an actually mild impact on the measured abundance in most of the cases. Second, deprojection on metallicity usually requires much more photons but results in a much larger error in single measurement. If the cluster deviates from perfect spherical symmetry, which is in fact very common, deprojection induces extra uncertainty, which can not be properly assessed. For these reasons we adopt deprojected profiles of density, and projected profiles of iron abundance, a procedure that is commonly adopted in recent papers dealing with ICM abundance [235, 199]. The potential impact of this assumption is discussed in Section 4.4.

Each iron abundance profile contains 6–13 radial bins out to the extraction radius $R_{\rm ext} \sim 0.4\, r_{500}$, roughly corresponding to $\sim 0.25\, r_{200}$. As previously discussed, this extraction radius is chosen on the basis of the expected iron plateau in most of the clusters, which is typically reached at these radii (see Urban et al. 2017 [383] for example). The inner and outer radii are adjusted to ensure that each bin encloses similar number of net photons. The minimum net photons in 0.5–7 keV energy band within each bin is 800, and can reach $>$ 20000 in some bright clusters with very deep observations. The spectrum of each bin is fitted with a metallicity-linked double-temperature `vapec` model, as described in Section 4.2.

With this modelization, we efficiently remove the bias on the best-fit abundance value when the temperature gradient is significant within the spatial bin [244]. On the other hand, no attempt is made of considering different abundance values associated to different gas phase within a projected bin, since it is not possible to investigate such an effect with present-day data. In fact, a relevant effect would be given by correlated fluctuations in the ICM density and abundance on small ($\sim$ kpc) scale, an occurrence which has been never observed and is not expected. The only exception is given by the presence of low-surface brightness infalling clumps at large radii, which has been treated in dedicated works and is not expected to affect radii smaller than r_{500} [85]. Therefore, we conclude that the assumption of a constant abundance in each projected bin is accurate for our science goals, and it provides a robust description of the actual azymuthally-averaged abundance profile.

The projected iron abundance profiles of all the clusters in our sample are plotted in Figure 4.3, where the yellow points show the sample-average in

seven radial bins. We confirm that, on average, the iron peak appears at radii $< 0.1r_{500}$, while a plateau, or a very weakly decreasing profile, is evident at radii $> 0.2r_{500}$.

The projected iron abundance profiles are fitted with a double-component model. The first component is a β model to fit the iron peak, while the second component is a constant representing the iron plateau:

$$Z = Z_{\rm peak} \cdot \left[1 + \left(\frac{r}{r_0}\right)^2\right]^{-\alpha} + Z_{\rm plateau}. \tag{4.5}$$

The central drop component is not considered if not in the few cases where the innermost 2-3 bins are significantly lower than the outer bins. In this way we do not force this component to be used when the statistical significance is low. In fact, a systematic study of the iron drop is feasible only for nearby clusters [197], while a search throughout our sample would be dominated by noise. Despite this, the few cases where a central drop improves significantly the fit are discussed in Section 4.3.4.

For the electron density profiles, we extend the maximum extraction radius to $\sim r_{500}$, and adopt a lower criterion of net photons in each bin in order to increase the spatial resolution. The spectrum in each bin is deprojected using the `dsdeproj`[1] routine [314, 307], which deprojects a spectrum directly by subtracting the geometrically rescaled count rates of the foreground and background emission. The deprojected spectrum is then fitted with a single `apec` model. Electron density is derived directly from the geometrically scaled normalization of the deprojected spectrum:

$$\texttt{norm} = \frac{10^{-14}}{4\pi[D_{\rm A}(1+z)]^2}\int n_{\rm e} n_{\rm p} {\rm d}V, \tag{4.6}$$

where z is the redshift of the cluster, $D_{\rm A}$ is the corresponding angular diameter distance, V is the volume of the emission region. $n_{\rm e}$ and $n_{\rm p}$ ($n_{\rm H}$) are the number densities of electron and proton. The ICM gas density is then computed by $\rho_{\rm gas} = n_{\rm e} m_{\rm p} A/Z$, where $m_{\rm p}$ is proton mass, A and Z are the average nuclear charge and mass of the ICM. For ICM with 1/3 solar abundance, $A \approx 1.4$ and $Z \approx 1.2$, and therefore $n_{\rm e} \approx 1.2 n_{\rm p}$.

[1] http://www-xray.ast.cam.ac.uk/papers/dsdeproj/

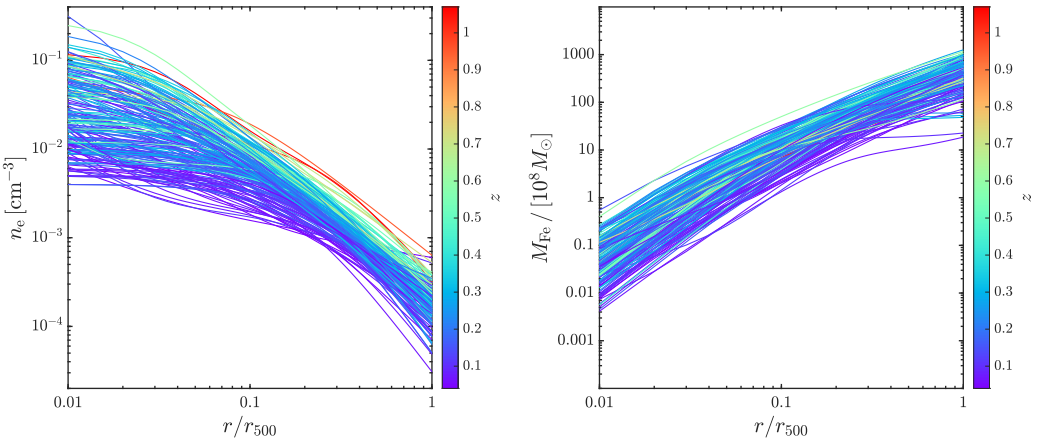

Figure 4.4. *Left panel:* best-fit double-β model of the deprojected density profiles, color-coded by redshift, for all the clusters in our sample. *Right panel:* total iron mass profiles obtained by convolving the gas density profile with the best fit abundance profile for each cluster in our sample. Note that at $r > 0.4\,r_{500}$ the iron mass is computed extrapolating the constant plateau up to r_{500}.

The deprojected electron density profiles are fitted with a double-β model, which can produce reasonable fit to the central density peak when a cool core is present. In the literature, the usual form of a double-β model used to describe density profiles, where density is computed from the surface brightness, is the square root of the quadratic sum of two β model components [91, 155, 93]. Instead, the density in this work is measured directly from the deprojected spectrum, thus we simply adopt a double-β model as a linear summation of two β model components, that reads:

$$n_{\mathrm{e}} = n_{01} \cdot \left[1 + \left(\frac{r}{r_{01}}\right)^2\right]^{-3\beta_1/2} + n_{02} \cdot \left[1 + \left(\frac{r}{r_{02}}\right)^2\right]^{-3\beta_2/2} . \tag{4.7}$$

For completeness, we also repeat the fit of the density profiles using the more conventional form of the quadratic sum of two β models, and find that the results are in very good agreement with those obtained using Equation 4.7.

The best fits for $n_{\mathrm{e}}(r)$ obtained with the double-β model are shown in the left panel of Figure 4.4. From the iron abundance $Z \equiv [n_{\mathrm{Fe}}/n_{\mathrm{H}}]/[n^{\odot}_{\mathrm{Fe}}/n^{\odot}_{\mathrm{H}}]$, assuming the same solar abundance used in the `Xspec` spectral fits $[n^{\odot}_{\mathrm{Fe}}/n^{\odot}_{\mathrm{H}}] = 3.16 \times 10^{-5}$ [12], we then derive the cumulative profile of the Fe mass $M_{\mathrm{Fe}}(< r)$, as shown in the right panel of Figure 4.4. We remind that, since our iron abundance

profiles extend only up to $0.4\,r_{500}$, at larger radii the iron mass is computed extrapolating the constant plateau up to r_{500}, differently from the gas mass that is obtained from the data extending up to $\sim r_{500}$. Therefore, the cumulative mass value above $0.4\,r_{500}$ depends on the assumption of a constant plateau at any radius.

4.3.3 The identification of two components in $Z_{\rm Fe}$ profiles

A necessary step before proceeding in our analysis is to check whether the use of a double-component model is statistically preferred to a simpler model. In other words, we want to assess the relevance of the two components not only on the basis of theoretical premises, but also from a blind fit of the measured abundance profile. The relevance of this check is twofold. First, the distribution of iron in the ICM is sensitive to many dynamical processes, such as the outflow of central AGN, and large-scale sloshing. Some of these processes have relatively weak impact on the global morphology, but may significantly affect the distribution of iron. In these cases, the iron profile may not follow our idealized pattern of a central peak plus a constant plateau, even in the case of a rather regular morphology. Second, due to the relatively small extraction radii of the profiles ($0.4r_{500}$), the iron plateau may not be well identified in cases where the iron peak has a large extension. Therefore, we repeat the fit of the iron abundance profiles, using a single β model, without the iron plateau, and compare the goodness of the fit, estimated by the P-value, of the two models. We note that a β model can provide an accurate description also in the case of a power-law behavior, which is typically obtained with small values for the core radius and the radial slope. Moreover, we are aware that the fit with a single β model clearly predicts a rapidly declining metallicity value in the regions at radii $> 0.4r_{500}$ not sampled by our data. This is clearly in contradiction with the current knowledge about the ICM metallicity in the few clusters where outskirts have been studied [339, 236] and with the hypothesis of a ubiquitous and homogeneous trace of pristine enrichment. However, here we just want to test the efficiency of our description without using any prior.

We plot in Figure 4.5 the (1-P) value, which indicates the confidence level

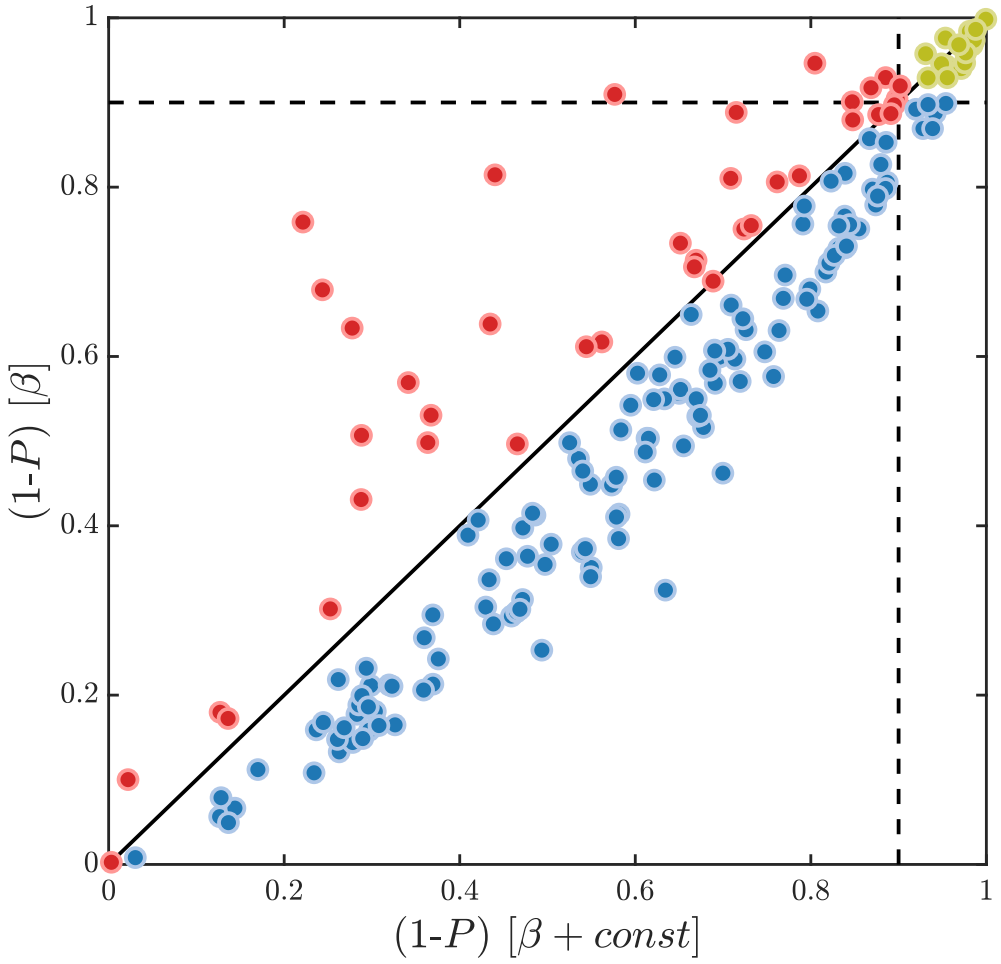

Figure 4.5. Probability of rejection of the abundance profiles with and without the iron plateau. The dashed lines mark $(1 - P) = 0.90$, hence the yellow points shows clusters for which both the single- and double-component models are rejected at $> 90\%$ c.l. Clusters colored in red favor the double-component model, while both models provide similar quality fits to the clusters colored in blue. In these cases, the double-component model returns a slightly lower goodness, because of the inclusion of an additional parameter in the fit.

at which the fit is rejected. If we consider the 90% c.l. as our tolerance threshold, we find 16 clusters, shown as yellow circles in Figure 4.5, for which both models are formally rejected. We check the images of the 16 clusters with these peculiar iron abundance profiles, and find no obvious signs of a disturbed morphology. Despite that, the iron profile appears to be dominated by significant intrinsic scatter between different annuli, making it impossible

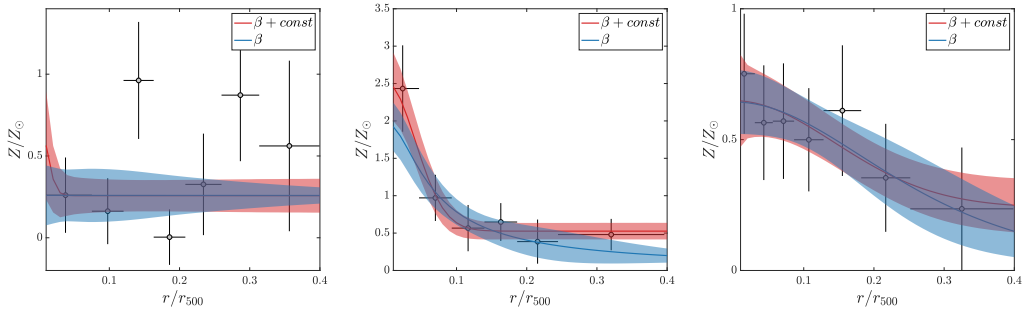

Figure 4.6. Examples of abundance profiles with the corresponding double-component (red) and single-component (blue) best-fit models. From left to right: Abell 2050, CLJ1415+3612, and PSZ2 G241.77-24.00. The three examples are extracted from the yellow, red, and blue dots in Figure 4.5, which are clusters that cannot be fitted with either model (yellow); favor the double-component model (red); and can be fitted with both models in the observed radial range (blue). The best-fit values and uncertainties (of all the curve fittings in this paper, unless noted otherwise) are obtained using the MCMC tool of [108].

to fit the profile with a smoothly varying function. As we mentioned, there are various processes that can result in these peculiar profiles, e.g. unnoticed mergers, major AGN outflows, core-sloshing in different scales, and projected gas clumps in cluster outskirts, among others. A concrete diagnosis on the physical reasons of the peculiar distribution of iron in these cases requires a more in-depth and case-by-case study of the dynamics of each cluster, which goes well beyond the goal of this paper. Therefore, we decide to exclude these 16 clusters in our following analysis where the fitting of the abundance profile is required, and focus on a sample of the remaining 170 clusters.

In 39 clusters (colored in red), the double-component model provides a smaller $(1 - P)$ value. Despite in several cases the difference is not significant, we find that at least in 1/5 of the sample the use of a double component in the iron distribution provides a significantly better fit, after considering the additional parameter. In the remaining 131 clusters, the profiles can be well fitted with both models within a confidence level of $> 90\%$. In these cases, the double-component model returns a larger $(1 - P)$ value, simply due to the fact that it has an additional free parameter and therefore a larger number of degrees of freedom.

One example for each one of these three classes is shown in Figure 4.6. The left panel shows a noisy iron abundance profile, that can be hardly reconciled with any smoothly-varying azimuthal function of the kind we consider here. In the central panel, the data clearly show a flat plateau that cannot be fitted with a single β model. In several cases, the central iron profile is better described by a broad bump rather than a well-defined peak, so that the plateau does not stand out clearly in the data. This situation is shown in the right panel, where it is not possible to differentiate statistically between the two models, and the abundance profile itself is indistinguishable from a simple power-law, at least in the explored range. For completeness, we repeat the same test, but using a power-law instead of a β model with no plateau. The results are very close to what we obtained in Figure 4.5.

In general, we conclude that the β model with a constant plateau is statistically preferred with respect to the use of a single β model or power-law for a significant fraction of our sample. Clearly, a more complete modelling of the profiles would be a β model plus an transitional power-law, constrained to have a mild slope, plus a constant for external regions. A slow decrease is actually expected in some modelization of the iron distribution [235, 27] and can be used to describe an intermediate regime where the iron distribution, far from the core, is still slowly decreasing before reaching the flat plateau associated to the pristine, uniform enrichment. However, the quality of data we use in this work is clearly not sufficient to assess the presence of this transitional component between the iron peak and plateau. We will dedicate a future work on a more extended modelization of the iron distribution, mostly in the perspective of the future X-ray missions (Tozzi et al., in preparation).

To summarize, we find that a β model plus a constant plateau is a good compromise between a comprehensive physical modelization and the data quality, in order to effectively describe a large sample of clusters observed with *Chandra* with a wide range in data quality. While a two-component model is physically motivated and favoured by the data, more sophisticated approach are not able to extract more information. Ideally, we should try to have more handle on the abundance profile at large radii. However, due to the limited field of view of ACIS, but mostly because of the rapidly decreasing signal, this is unfeasible. In fact, as we already mentioned, despite that the surface

brightness is detected up to r_{500} in most of our clusters, at radii larger than $0.4\,r_{500}$ the spectral analysis would be strongly affected by uncertainties in the background subtraction. There are two ways to tackle this issue. The first is to use XMM-Newton for the clusters that have been observed with both instruments, exploiting the $\sim 5\times$ larger collecting efficiency, and the larger field of view. However, the discrepancy in the temperature measurements between *Chandra* and XMM-Newton [213] increases the complexity of such a combined analysis. The second method is to wait for the X-ray bolometer, e.g., on XRISM, able to identify the iron line thanks to the $\sim 10\times$ larger spectral resolution, in external regions of nearby clusters where angular resolution is not an issue. The first method goes beyond the goal of this paper and it is deferred to a further work on the entire *Chandra* and XMM-Newton archives. The second approach is definitely one of the most efficient ways to use XRISM in the next future to attack this problem, as we will mention also in the discussion Section.

4.3.4 The effect of the central iron drop

The central iron drop observed in a few clusters is a significant feature with a typical scale of ~ 10 kpc [265, 197, 182]. It requires a high spatial resolution and a high S/N to be firmly observed, and has a negligible impact on the iron mass in most cases. We do not perform here a systematic investigation of the iron drop in our sample, due to the lack of signal. However, after a visual inspection of all the abundance profiles, we do find hint of a central iron drop in 8 clusters. In these clusters we allow for this component in our fit in the form of a "negative Gaussian" as follows:

$$Z = Z_{\rm peak} \cdot \left[1 + \left(\frac{r}{r_0}\right)^2\right]^{-\alpha} - a \cdot \exp\left[\frac{-(r-\mu)^2}{2\sigma^2}\right] + Z_{\rm plateau}. \qquad (4.8)$$

Note that this modelization of the central drop is simpler than the one used in [197] due to the lower quality of the profiles, and it has been used also in Mernier et al. (2017) [235]. Then, we collect all the cases where the improvement of the χ^2 formally corresponds to a confidence level of 90%. In the end, we do find a central iron drop in 8 out of 186 clusters. An example is

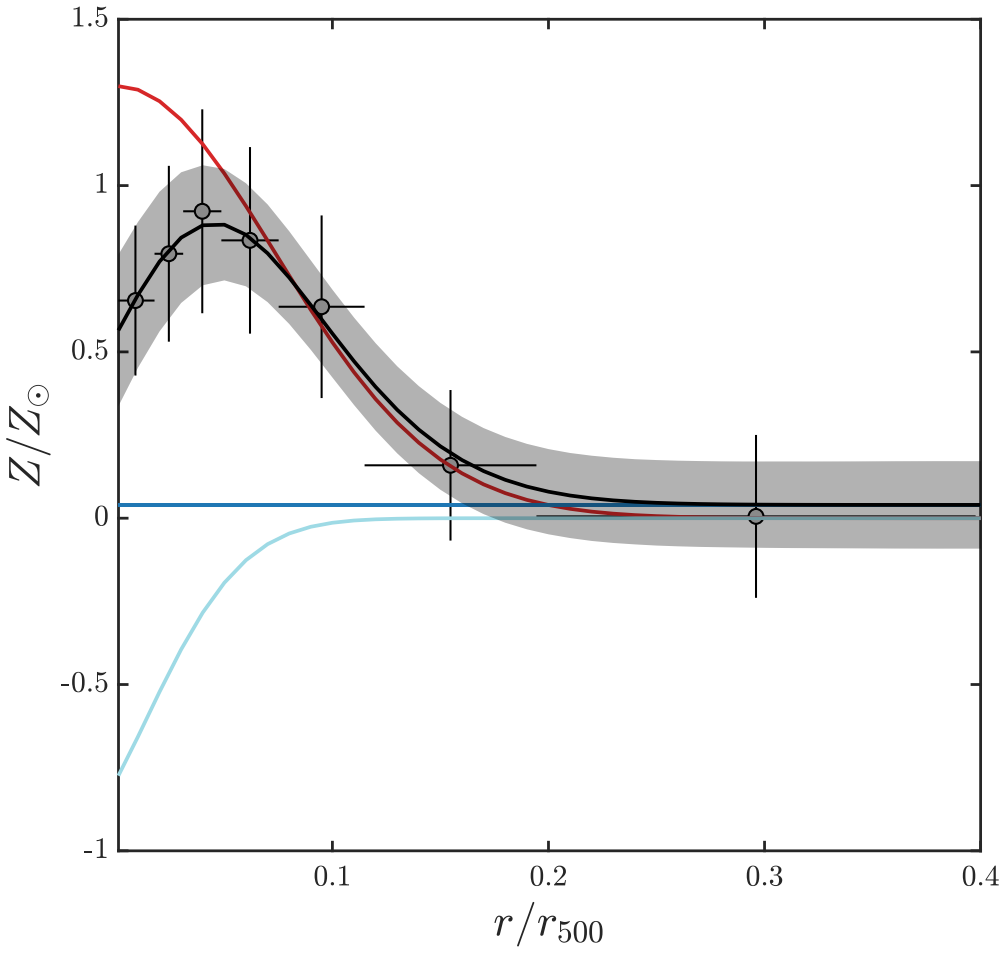

Figure 4.7. The iron abundance profile of MACSJ0242.5-2132 with the best-fit showing a pronounced central iron drop. The red, cyan, and blue curves are the iron peak, iron drop, and iron plateau, respectively, as described by equation (4.8).

shown in Figure 4.7. The typical size of the iron drop in these clusters is $\sim$ [0.05–0.1]r_{500}, larger than what has been found in nearby clusters and groups [265, 197]. However, this is probably due to the relatively low resolution of the profiles we have in this work, which masks the small-scale iron drops, leaving only the large-scale ones. For these clusters, the final iron peak component is therefore computed by considering the "hole" in the iron distribution. Clearly, the amount of mass removed by the drop is limited, and it is often compensated by the re-adjustment of the iron peak profile, so that the impact on our final results is negligible. Nevertheless, we claim that the presence of a central

drop in the iron distribution is an important component to be included when more detailed profiles will be available, not only for its effect on the total iron budget, but also for its physical relevance. The effects of feedback and of dust depletion, which are responsible of the iron drop, are indeed expected to be present at least since $z \sim 1$.

4.3.5 Mass-weighted iron abundance

As already mentioned, we first compute the average mass-weighted iron abundance, defined as $Z_{\rm mw} \equiv \sum(Z^i_{\rm Fe} \cdot M^i_{\rm gas})/\sum M^i_{\rm gas}$, without making any distinction between the two components. Liu et al. (2018) [192] have shown that mass-weighted value is more appropriate than the emission-weighted value in quantifying the average abundance of iron in the ICM, because the latter, despite much easier to measure, can be affected by a significant bias in cool-core clusters. We show the mass-weighted iron abundance within r_{500} as a function of redshift in the upper panel of Figure 4.8. From a visual inspection, a good guess is to assume a value constant with redshift. If we compute the root mean square value around the mean over the redshift, or the *raw* scatter as defined in [287], we find that both quantities are comparable to the average statistical error. This implies that the intrinsic scatter, which is beyond any doubt present in a complex quantity such as $Z_{\rm mw}(r < r_{500})$, is negligible with respect to the measurement uncertainty. Considering that the uncertainty on the redshift is not relevant here, we can safely search for a best-fit function by a simple χ^2 minimization. If we fit the $Z_{\rm mw} - z$ relation with a simple power-law defined as $Z_{\rm mw} = Z_{\rm mw,0} \cdot (1+z)^{-\gamma_{\rm mw}}$, we obtain the best-fit parameters $Z_{\rm mw,0}$=(0.35±0.02) $Z_\odot$ and $\gamma_{\rm mw}$=0.08±0.17, consistent with no evolution of $Z_{\rm mw}$ across our sample.

Limited by the extraction radius of our iron abundance profiles, the comparison between the mass- and emission-weighted abundances is only possible within $0.4\,r_{500}$. The last quantity is simply obtained fitting with a double-temperature `vapec` model to the total emission within the same radius. In the lower panel of Figure 4.8 we compare the two quantities. We find that, on average, the emission-weighted abundance within $0.4r_{500}$ is higher than the mass-weighted value by $\sim 18\%$. We note that this is slightly lower than that

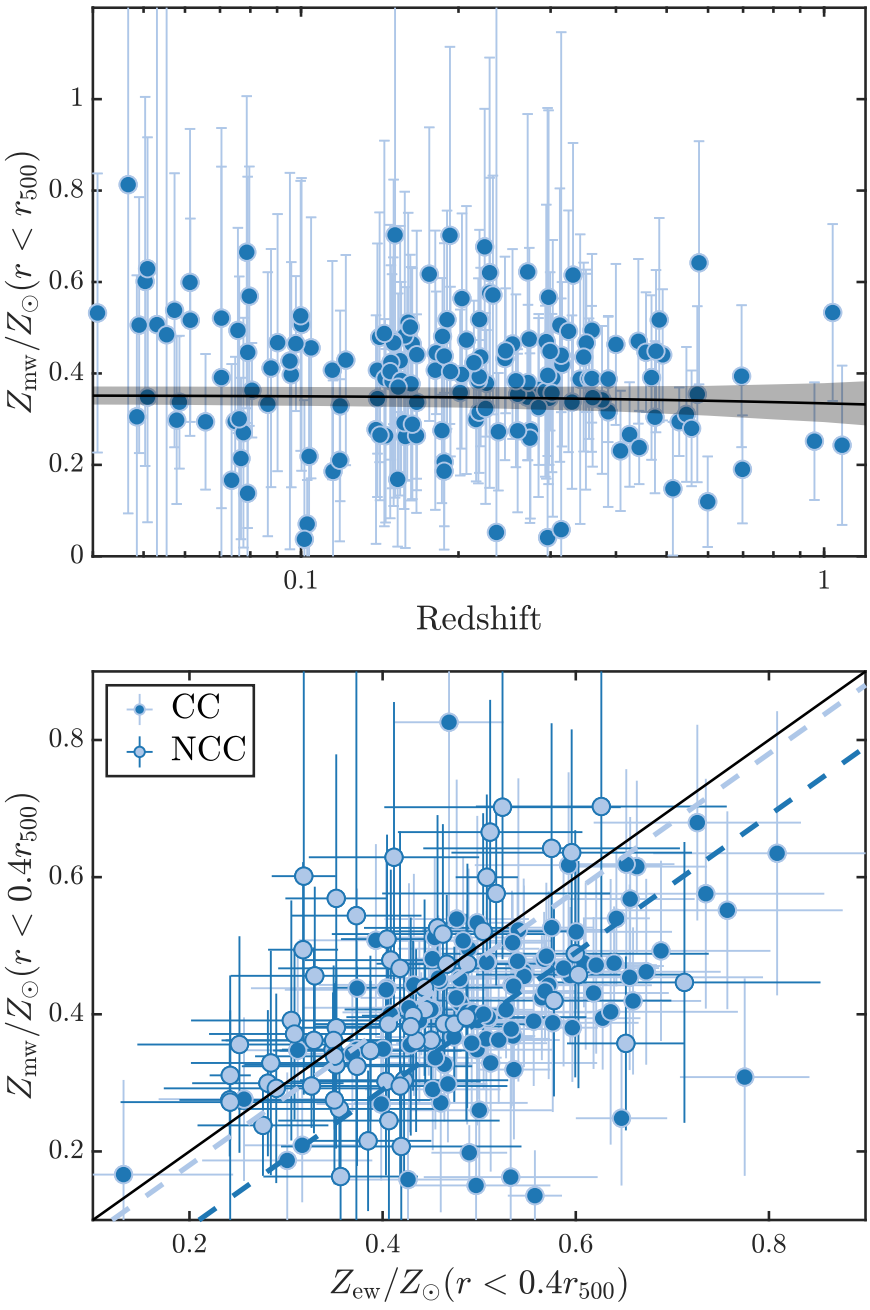

Figure 4.8. *Upper panel*: the correlation between the average, mass-weighted iron abundance (within r_{500}) and the redshift of all the clusters. The black curve and shaded area show the best-fit function $Z_{\rm mw} = Z_{\rm mw,0} \cdot (1+z)^{-\gamma_{\rm mw}}$ with $Z_{\rm mw,0} = (0.35 \pm 0.02)\ Z_\odot$ and $\gamma_{\rm mw} = 0.08 \pm 0.17$. *Lower panel*: the mass-weighted abundance within $0.4\,r_{500}$ plotted against the emission-weighted value in the same radial range. The solid line corresponds to $Z_{\rm mw} = Z_{\rm ew}$. Dashed lines show the average discrepancies of cool-core and non-cool-core clusters, $Z_{\rm mw}^{\rm CC} = Z_{\rm ew} - 0.11$ and $Z_{\rm mw}^{\rm NCC} = Z_{\rm ew} - 0.02$.

found in Liu et al. (2018) [192], where $(Z_{\rm ew} - Z_{\rm mw})/Z_{\rm mw} \approx 0.25$. However, this is expected, because most of the clusters in Liu et al. (2018) [192] host a strong cool core, and the investigated radius is $0.2r_{500}$, thus more affected by the iron peak. We expect that the difference between mass- and emission-weighted abundance will further decrease with larger extraction radius and higher fraction of non-cool-core clusters in the sample. This effect is more evident if we split our samples in two halves, populated by cool-core and non-cool-core clusters adopting as a threshold $c_{\rm SB} = 0.075$. We find that this discrepancy becomes 22% for cool-core clusters, and drops to only 4% for non-cool-core clusters. A simple fit to the distribution with a linear function $Z_{\rm mw} = Z_{\rm ew} - \delta Z$ gives $\delta Z = 0.11\, Z_\odot$ for cool-core clusters, and $\delta Z = 0.02 Z_\odot$ for non-cool-core clusters. The different behaviors of cool-core and non-cool-core clusters reflect the effect of the iron peak on the measurement of emission-weighted abundance.

The average emission-weighted abundance within $0.4r_{500}$ of cool-core clusters in our sample is $(0.51\pm0.01)\, Z_\odot$, significantly higher than that of non-cool-core clusters: $(0.41\pm0.01)\, Z_\odot$. This difference has been already noticed in several other works [66, 65]. We find that this difference is significantly reduced but it is still marginally significant when considering the average mass weighted abundance, which turns out to be $(0.41 \pm 0.01)\, Z_\odot$ and $(0.38 \pm 0.02)\, Z_\odot$ for cool-core and non-cool-core clusters, respectively. These results confirm that the difference in iron abundance between cool-core and non-cool-core clusters is largely due to the use of emission weighted abundance, while it almost disappears when using mass weighted values, which are representative of the true iron mass content. At the same time, a residual difference in the average, mass-weighted abundances shows that the effect is not entirely due to the different ICM distribution, but there is also a larger amount of iron in cool-core clusters, further strengthening the hypothesis of two different physical origins for the iron peak and the iron plateau.

4.3.6 The properties of the iron plateau and iron peak

In this section we analyze the profiles of iron abundance and iron mass by resolving the two components, namely the iron plateau and the iron peak. From Figure 4.9, one can immediately assess the contributions of the two

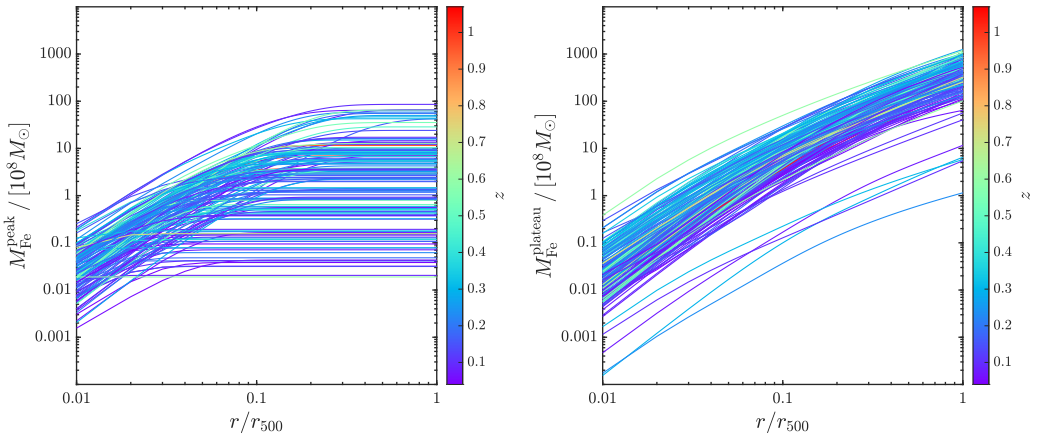

Figure 4.9. *Left panel:* Cumulative iron mass profiles corresponding to the peak component, color-coded by redshift for all the 170 clusters with regular abundance profiles considered in this work. *Right panel:* as in the left panel, but for the plateau component.

components to the iron mass budget. In Figure 4.10 we show the distribution of the ratio of iron peak mass to iron plateau mass within r_{500}, and also the correlation of the ratio with redshift. No redshift-dependence of the ratio is found from Figure 4.10. Despite that the ratio for most clusters are distributed within the range $[5{\times}10^{-5}, 0.5]$, and centered at 0.008, we find clusters with extremely low iron peak mass. We check the spectral fits and profile fits for these cases, and find consistently that the clusters with low iron peak mass are mostly non-cool-core clusters which host no or very weak iron peak in the center. A small number of clusters show $M_{\rm Fe}^{\rm peak}/M_{\rm Fe}^{\rm plateau} > 0.1$; in these cases the central iron distribution is broad and slowly declining, so that it is ascribed mostly to the central peak. These cases would probably be better described by a third component in the form of a shallow power-law, however, the quality of the data makes it impossible to identify such additional component. In these cases the iron mass in the peak should not be associated to the BCG, but rather to the mix of the two components that appears as a broad bump. This is admittedly a limitation of the method, since it is impossible to spatially separate the two components when the central peak has been smeared out.

We also notice, from Figure 4.10 and also the right panel of Figure 4.9, that a few clusters have a very low iron plateau. We check the profiles of these

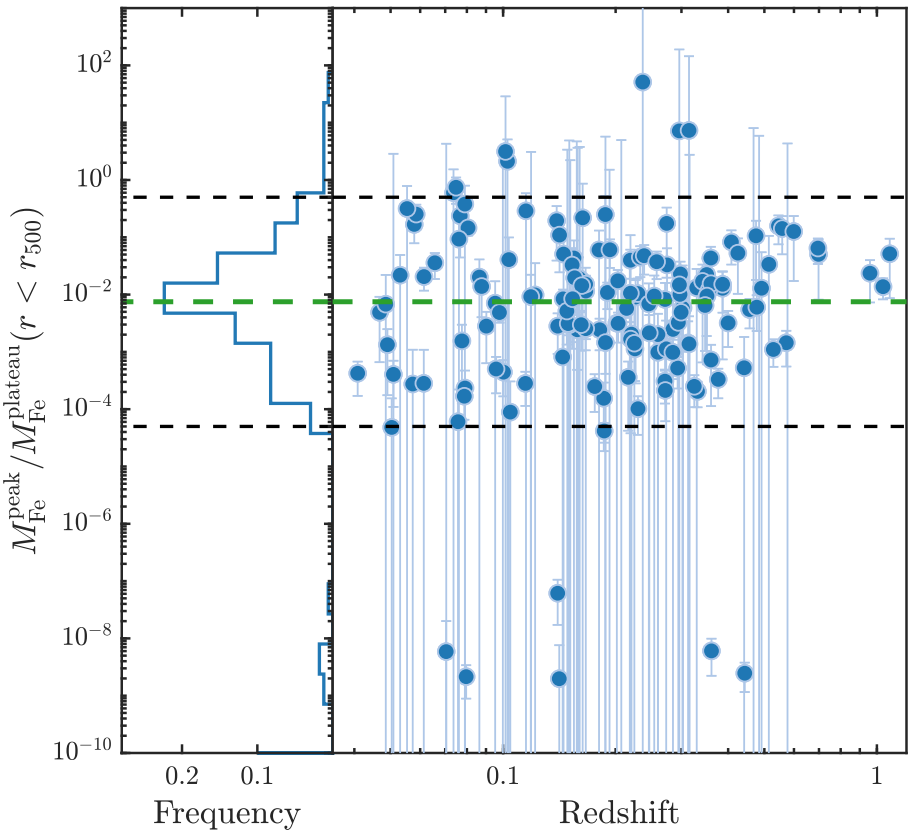

Figure 4.10. Distribution of the ratio of iron peak mass to iron plateau mass within r_{500}, and the correlation with redshift. The green dashed line indicates the weighted average at ∼0.008. The black dashed lines mark the $[5 \times 10^{-5}, 0.5]$ range roughly corresponding to $> 90\%$ of the clusters symmetrically distributed around the central value (as shown in the left-side panel).

clusters, and find that this is mostly driven from one or more measurements of very low abundance in the outskirts, probably due to the low S/N of the data. A bias toward low abundance values in the outer regions has been noticed, and it has been shown that it can be removed by excluding the 0.9–1.3 keV rest-frame band (corresponding to the iron L band emission complex, S. Molendi private communication). However, due to the limited signal of the spectra in the outer bins, we are not able to verify this effect nor the robustness of these low measurements. If, in these cases, we fix the iron plateau to some value, e.g. $0.2\,Z_{\odot}$, we find that the ratio between the iron peak and iron

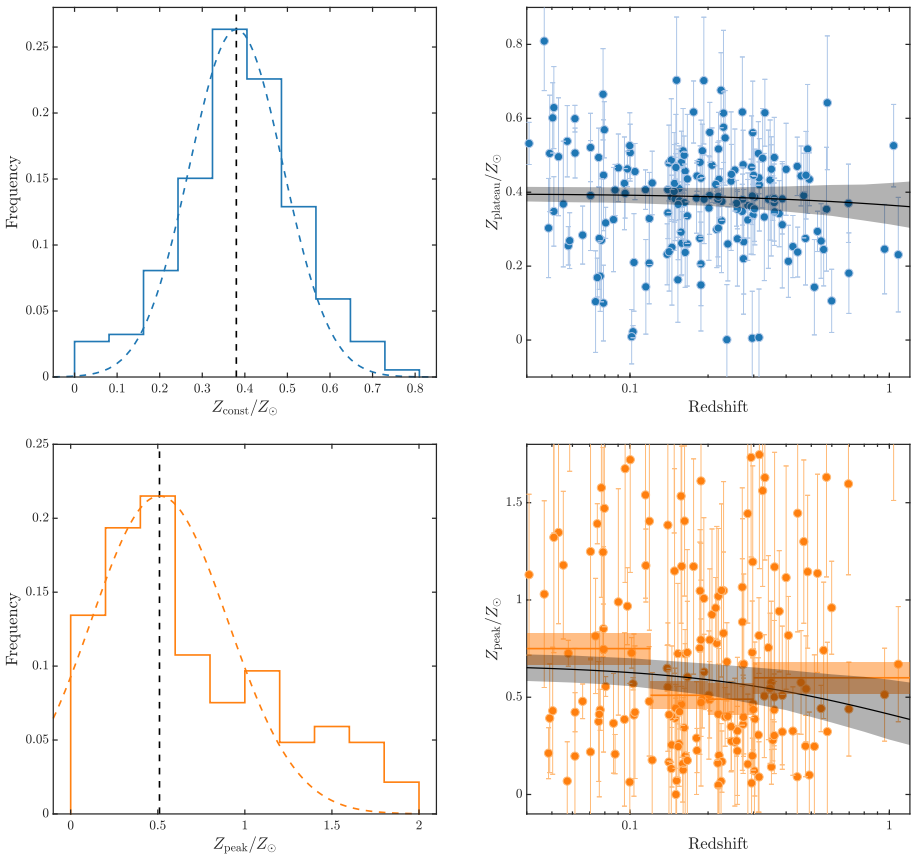

Figure 4.11. *Upper left*: Distribution of the abundance of the iron plateau component Z_{plateau}. The dashed line indicates the weighted average value $\langle Z_{\mathrm{plateau}} \rangle = 0.38\,Z_\odot$. The dashed curve shows a normalized Gaussian with $\sigma = 0.11\,Z_\odot$, corresponding to the average statistical error, and $\mu = 0.38\,Z_\odot$, corresponding to the weighted average value. *Upper right*: The abundance of the iron plateau plotted against cluster redshift. The black curve and shaded area show the best-fit function $Z_{\mathrm{plateau}} = Z_{\mathrm{plateau},0} \cdot (1+z)^{-\gamma_{\mathrm{plateau}}}$ with $Z_{\mathrm{plateau},0} = (0.39 \pm 0.03)\,Z_\odot$ and $\gamma_{\mathrm{plateau}} = 0.12 \pm 0.21$. *Lower left*: Distribution of the normalization of the iron peak component Z_{peak}. The dashed line indicates the weighted average value $\langle Z_{\mathrm{peak}} \rangle = 0.51\,Z_\odot$. The dashed curve shows a normalized Gaussian with $\sigma = 0.39\,Z_\odot$, corresponding to the average statistical error, and $\mu = 0.51\,Z_\odot$, corresponding to the weighted average value. *Lower right*: The normalization of the iron peak component Z_{peak} plotted against cluster redshift. The black curve and shaded area show the best-fit function $Z_{\mathrm{peak}} = Z_{\mathrm{peak},0} \cdot (1+z)^{-\gamma_{\mathrm{peak}}}$ with $Z_{\mathrm{peak},0} = (0.67 \pm 0.07)\,Z_\odot$ and $\gamma_{\mathrm{peak}} = 0.70 \pm 0.50$, which are obtained by fitting the weighted average values and uncertainties of the four bins shown as orange solid line and shaded area.

plateau becomes, by construction, consistent with the average value of the sample, while the fit to the profiles are still good due to the poor statistical weight of the low-abundance data points in outskirts. This, in fact, implies that we have a very loose constraint on the iron plateau in several clusters, which is, nevertheless, already accounted for in the uncertainty of the fitting result. Given the low number of clusters with $Z_{\rm plateau} \sim 0$ (5 out of 170), these cases do not require a change of our fitting strategy nor have an impact on our final results.

We then check the normalization of the iron plateau ($Z_{\rm plateau}$) across the sample. In the upper panels of Figure 4.11 we present the distribution of $Z_{\rm plateau}$ and its relation with redshift. We compute the weighted average of $Z_{\rm plateau}$ (where the weights are defined $w_i = 1/\sigma_i^2$) and find $\langle Z_{\rm plateau} \rangle = 0.38$, with a dispersion of $0.13\,Z_\odot$, thus consistent with a 1/3 solar abundance of the ICM in cluster outskirts. The average statistical error is $0.11\,Z_\odot$, which implies that the intrinsic scatter is negligible with respect to the statistical uncertainty. This is clearly shown in the upper-left panel of Figure 4.11, where the histogram of the best-fit values of $Z_{\rm plateau}$ is shown with a Gaussian centered on $\langle Z_{\rm plateau} \rangle$ and with width equal to the average statistical error. This implies that the intrinsic fluctuations in the plateau, which are naturally expected, are still below our reach. At the same time, we learn that such intrinsic fluctuations are limited, suggesting a uniformity in the pristine enrichment at least in the massive cluster range.

Focusing on the evolution, from the top-right panel of Figure 4.11 one can immediately notice the absence of a significant correlation with redshift. We adopt a simple χ^2 minimization to fit this distribution with an empirical function $Z_{\rm plateau} = Z_{\rm plateau,0} \cdot (1+z)^{-\gamma_{\rm plateau}}$, and obtain $Z_{\rm plateau,0} = (0.39 \pm 0.03)\,Z_\odot$ and $\gamma_{\rm plateau} = 0.12 \pm 0.21$, suggesting no evolution with redshift. This corroborates the hypothesis that the plateau is dominated by the contribution from a pristine and uniform enrichment, possibly occurred before the virialization of the main halo.

Then, we focus on the normalization of the iron peak $Z_{\rm peak}$. In the lower panels of Figure 4.11, we show the statistic of $Z_{\rm peak}$ and the $Z_{\rm peak}-z$ distribution. The weighted average value of $Z_{\rm peak}$ is $\langle Z_{\rm peak} \rangle = 0.51\,Z_\odot$, with a *rms* dispersion of $0.50\,Z_\odot$. Since the average statistical error is $0.39\,Z_\odot$, the estimate intrinsic

(and symmetric) scatter is $\sim 0.31\,Z_{\odot}$. This is clearly seen in the bottom-left panel of Figure 4.11, where the Gaussian centered on the weighted mean and representing the width of the statistical uncertainties, fails in describing the right side of the distribution. The reason is that the high-$Z_{\rm peak}$ values represent a population of clusters which experienced a relatively low number of minor and major mergers, so that the central regions evolved undisturbed for several Gyr with the late, BCG-related iron piling-up in the core. Ideally, all massive clusters should show a high iron peak if the mass growth is smooth, but in reality the stochastic merger events reset the thermodynamic and chemical properties of the cores, creating the distribution of properties we actually observe.

Given the presence of a significant scatter in $Z_{\rm peak}$, we should not fit the $Z_{\rm peak} - z$ relation with a simple χ^2 minimization. To describe the properties of the iron peak as a function of redshift, we decide to focus on four bins of redshift with a similar number of clusters, namely $z < 0.12$, $0.12 < z < 0.2$, $0.2 < z < 0.3$, and $z > 0.3$, with about 42 points each. We inspect the histogram distribution of the $Z_{\rm peak}$ values in each redshift bin, and verify that the weighted mean $\langle Z_{\rm peak,z} \rangle$ closely traces the peak of the distribution. Then, we are allowed to use a χ^2 minimization on the four bins to fit behaviour of the $Z_{\rm peak}$ distribution with redshift. Using the same empirical function for $Z_{\rm plateau}$, we obtain $Z_{\rm peak,0} = (0.67 \pm 0.07)\,Z_{\odot}$ and $\gamma_{\rm peak} = 0.70 \pm 0.50$. This result, despite the large scatter of $Z_{\rm peak}$ across the sample, is consistent with an increase of $\sim 60\%$ from $z \sim 1$ to low-redshift, but it is also consistent with no evolution within less then 2σ. Also, we need to bear in mind that, despite our sample spans a redshift range $0.04 < z < 1.1$, the weight of high-z ($z > 0.6$) clusters is limited, and the fit shown in the lower-right panel of Figure 4.11 is actually driven by the data points at redshifts below 0.6. In any case, a mild, positive evolution with cosmic time, if confirmed, supports a different origin of the iron peak, more recent in time and associated with the central BCG and epochs after the cluster formation. In other words, the iron peak is formed within the cluster *in situ* around the BCG, increasing in strength from redshift ~ 1 to local as the feedback cycle associated to the BCG creates short but intense period of star formations, with the associated creation and diffusion of iron. Considering the redshift distribution of our sample, this evolution, if

any, is probably occurring on a time scale of about 5 Gyr, corresponding to the interval $0.05 < z < 0.6$.

Finally, we explore the evolution of iron in terms of the iron mass of the two components. In Figure 4.12, we plot this two components within r_{500} divided by the gas mass within the same radius against cluster redshift. We find that $M_{\rm plateau}/M_{\rm gas}$ appears to be distributed around an average value with a dispersion consistent with the statistical uncertainty, and, therefore, we can investigate its redshift dependence with a χ^2 minimization. On the contrary, the quantity $M_{\rm peak}/M_{\rm gas}$ show a significant intrinsic scatter, so we adopt the same strategy as before, consisting in fitting the weighted mean $\langle M_{\rm peak}\rangle$ in four redshift bins. Using the same function $X = n \cdot (1+z)^{-\gamma}$, we obtain $M_{\rm Fe}^{\rm plateau}/M_{\rm gas} = (5.2 \pm 0.3) \times 10^{-4} \times (1+z)^{-0.24\pm0.19}$ for the iron plateau, and $M_{\rm Fe}^{\rm peak}/M_{\rm gas} = (1.4 \pm 0.3) \times 10^{-5} \times (1+z)^{-0.98\pm0.63}$ for the iron peak. Therefore we confirm that the plateau does not seem to evolve significantly in this redshift range, implying an early enrichment. On the other hand, the iron peak mass shows some hint of an increase with cosmic time. This growth is not statistically significant, similarly to that observed in the peak normalization. If confirmed, we can interpret this trend, regardless of its large uncertainty, large scatter, and the incompleteness of our sample particularly at high-z, as an average increase of $\sim 100\%$ of the amount of iron produced and/or released within the clusters in the central region at $z < 1$, most likely at $z < 0.6$. This interpretation is corroborated by the scatter of the two distributions. For the iron plateau mass (divided by gas mass), the *rms* turns out to be $\sim 90\%$ of the average measurement ($1\ \sigma$) uncertainty, therefore implying no intrinsic scatter. Once again, this suggests an early and uniform enrichment. On the other hand, the distribution of the iron peak mass has a scatter several times higher than the statistical uncertainty: $\sigma_{\rm tot} \sim 6 \times \sigma_{\rm stat}$. This fact implies a large diversity in the star formation histories in the BCG responsible for the iron mass excess, as already discussed for the $Z_{\rm peak}$ distribution.

We know that the fraction of mass included in the iron peak is only ~ 1 percent of the total iron mass in the ICM within r_{500}. Therefore, the evolution of iron in the ICM is dominated by the amplitude of the iron plateau. The lack of evolution in the iron plateau, therefore, drives the total (peak plus plateau) iron abundance to be almost constant with redshift, as we already show in

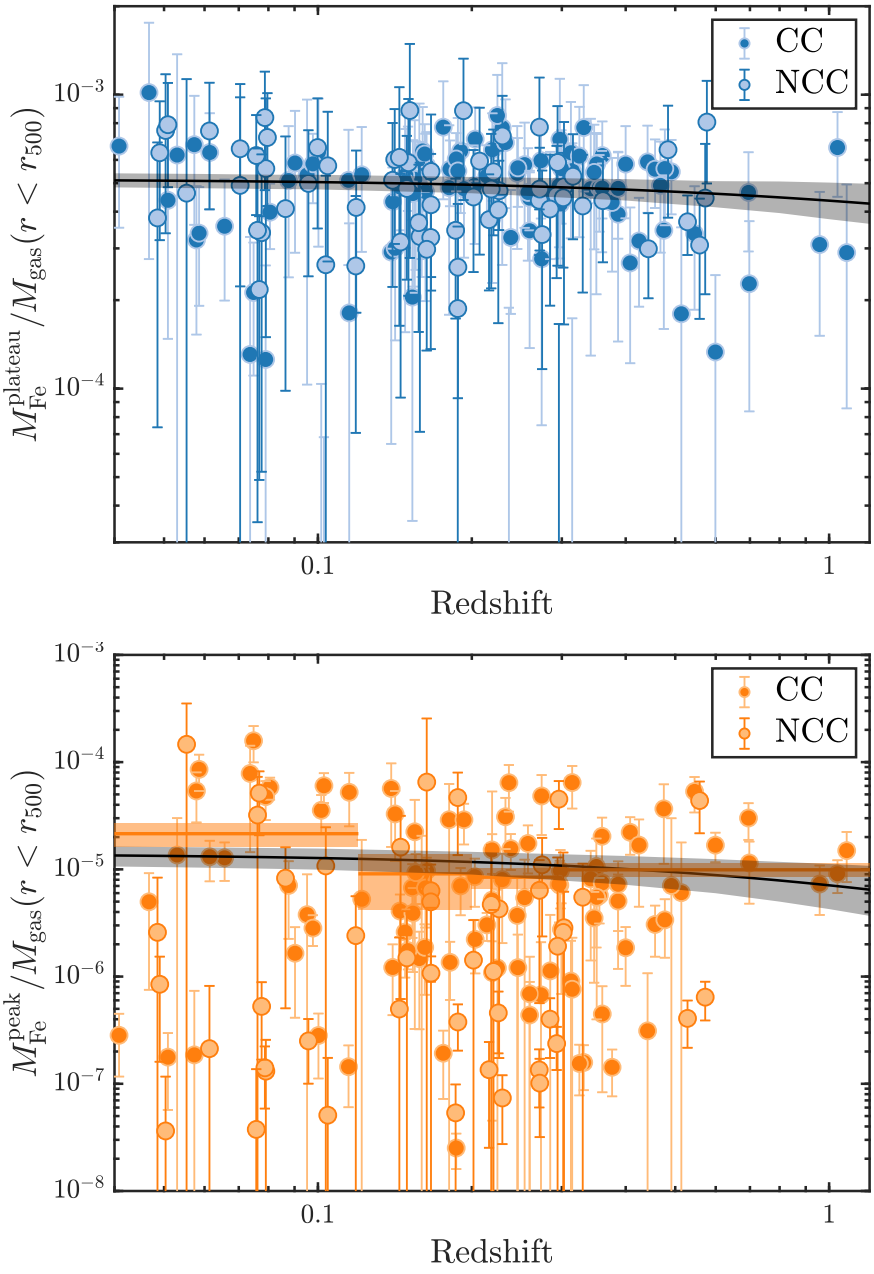

Figure 4.12. The ratio of iron mass of the plateau (upper panel) and the peak (lower panel) to the gas mass within r_{500} versus cluster redshift. The black curves show the best-fit functions $M_{\rm Fe}^{\rm plateau}/M_{\rm gas} = 5.2 \times 10^{-4} \cdot (1+z)^{-0.24}$ and $M_{\rm Fe}^{\rm peak}/M_{\rm gas} = 1.4 \times 10^{-5} \cdot (1+z)^{-0.98}$. Shaded area indicates the 1 σ confidence interval of the best-fit model. For the iron peak, the best-fits are obtained by fitting the weighted average values and uncertainties of the four bins shown as orange solid line and shaded area.

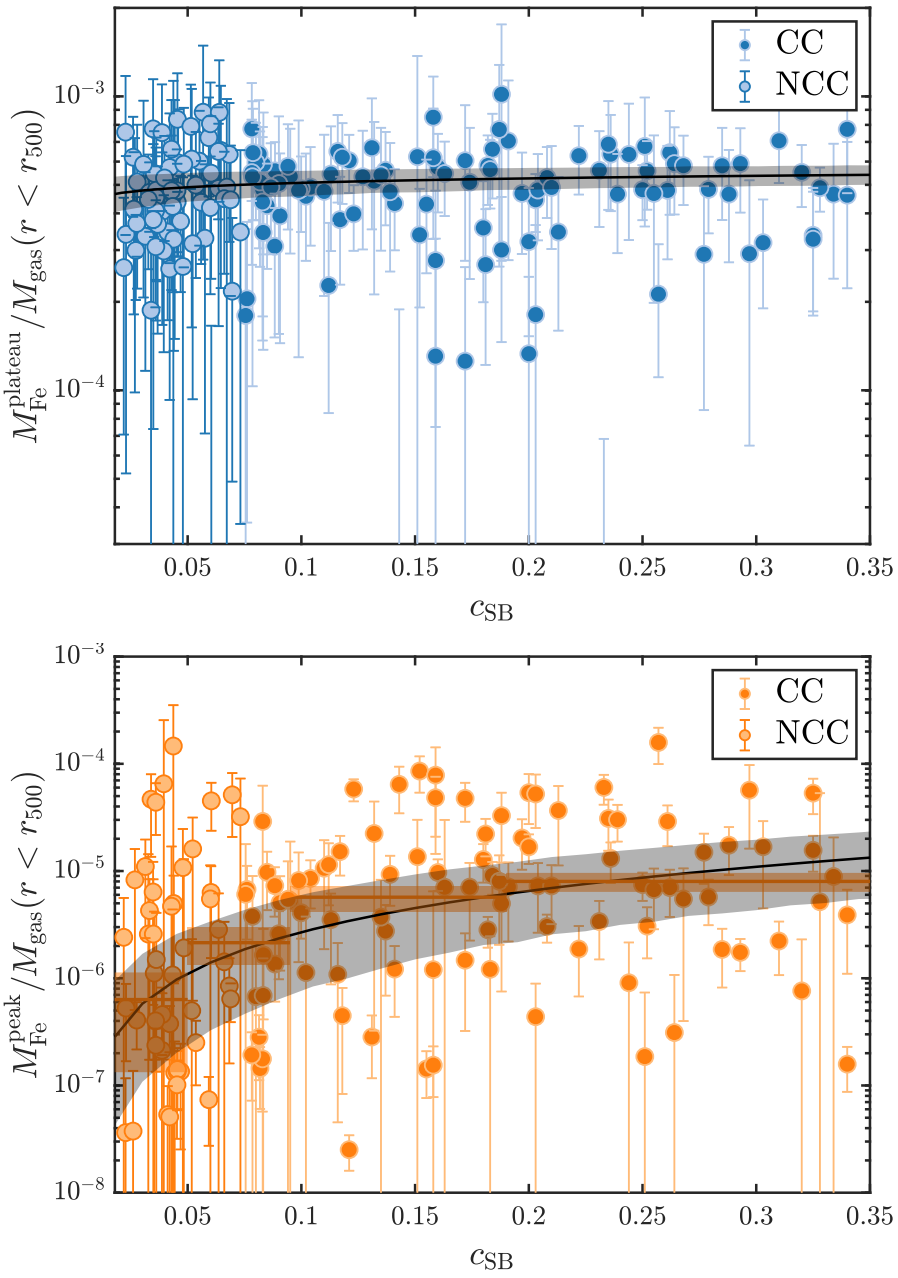

Figure 4.13. The correlation between the iron mass of the two components and the surface brightness concentration $c_{\rm SB}$. The black curves show the best-fit functions $M_{\rm Fe}^{\rm plateau}/M_{\rm gas} = 5.7 \times 10^{-4} \cdot (c_{\rm SB})^{0.05}$ and $M_{\rm Fe}^{\rm peak}/M_{\rm gas} = 5.4 \times 10^{-5} \cdot (c_{\rm SB})^{1.32}$. Shaded area indicates the 1 σ confidence interval of the best-fit model. For the iron peak, the best-fits are obtained by fitting the weighted average values and uncertainties of the four bins shown as orange solid line and shaded area.

Figure 4.8. Our approach also demonstrates that considering only the global abundance is not adequate to properly constrain the evolution and the physical origin of the (at least) two different components of the iron distribution.

We also investigate the possible difference in the behaviors of cool-core ($c_{\rm SB} \geq 0.075$) and non-cool-core ($c_{\rm SB} < 0.075$) clusters. As can be seen in the upper panel of Figure 4.12, cool-core and non-cool-core clusters do not show a different behaviour when considering the iron plateau. However, we find from the lower panel of Figure 4.12 the expected result that non-cool-core clusters tend to be lower than cool-core clusters in the iron peak mass. To further explore the link between the iron peak and the presence of a cool core, we also investigate the correlation between the iron to gas mass ratios in the two components with the surface brightness concentration $c_{\rm SB}$, as shown in Figure 4.13. We fit the distribution with a simple power-law, $M_{\rm Fe}/M_{\rm gas} = A \cdot (c_{\rm SB})^B$. For the iron plateau, we obtain $A = (5.7 \pm 0.4) \times 10^{-4}$ and $B = 0.05 \pm 0.03$. As expected, the strength of the cool core does not affect much the properties of the iron distribution on large scales. For the iron peak, we again divide the sample into four bins as before: $c_{\rm SB} < 0.05$, $0.05 < c_{\rm SB} < 0.095$, $0.095 < c_{\rm SB} < 0.19$, and $c_{\rm SB} > 0.19$, and fit the weighted average of the four bins. We obtain $A = (5.4 \pm 3.0) \times 10^{-5}$ and $B = 1.32 \pm 0.33$, which implies a significant correlation between the amount of iron in the peak, and the strength of the cool core, possibly because of the strong correlation of metallicity and density (or anticorrelation of metallicity and entropy) in the cluster center. This result is in line with the general picture that the iron peak is strongly associated with the formation of cool core, and it is mainly created *in situ* thanks to the periodic starburst occurring in the BCG.

4.3.7 The correlation between M_{500} and iron abundance

In Figure 4.14 we explore the relation between the mass-weighted abundance within r_{500} and M_{500}, the total mass of the cluster within r_{500}. As usual, we use a simple power-law $Z_{\rm mw} = Z_0 \cdot (M_{500}/10^{14} M_\odot)^{-\alpha}$. We perform a linear regression for the $\log(Z) - \log(M)$ relation requiring a minimization of the orthogonal distance of the points from the best-fit relation, thus considering uncertainties in both quantities. The best-fit gives $Z_0 = (0.52 \pm 0.08) Z_\odot$ and

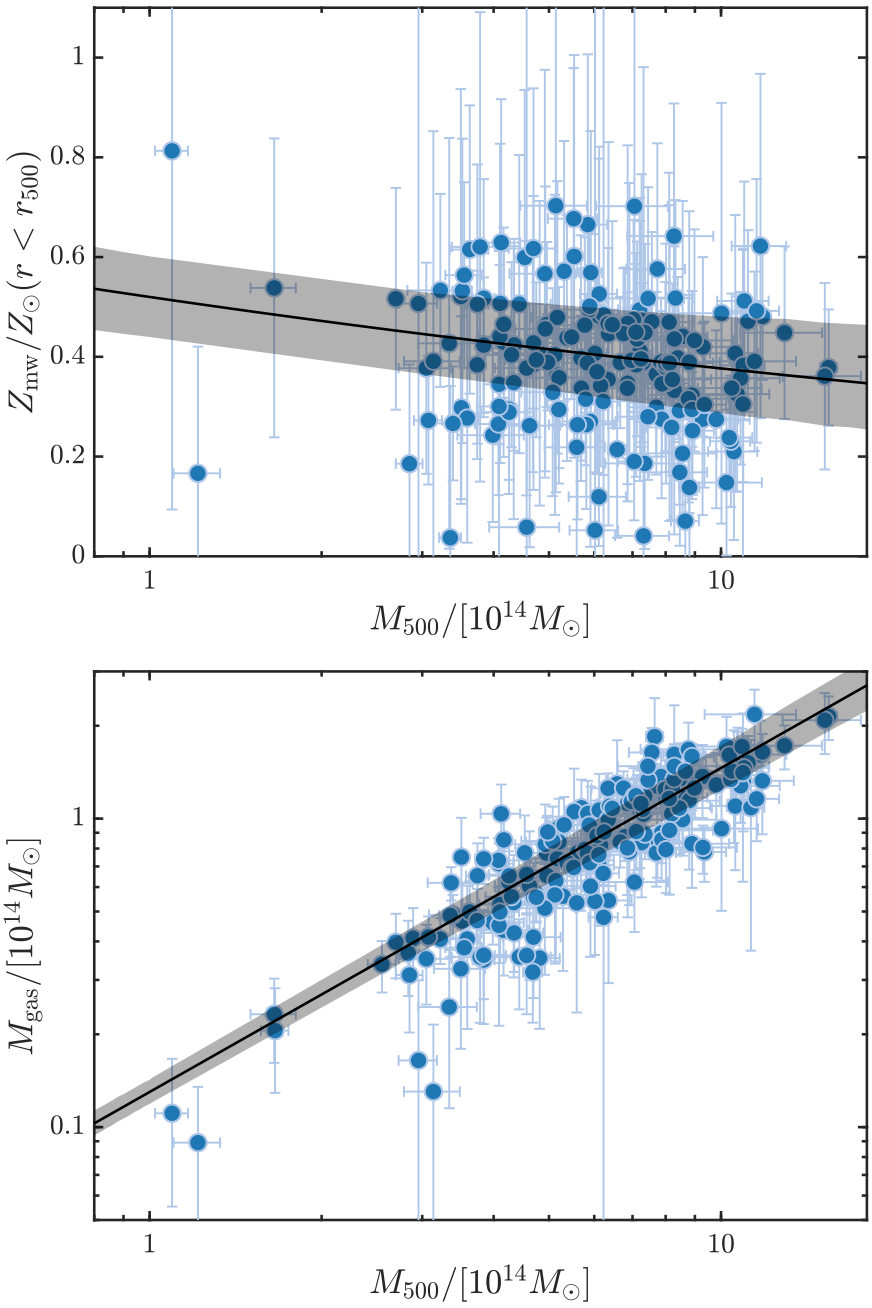

Figure 4.14. *Upper*: The correlation between mass weighted abundance within r_{500} and the total mass M_{500} for all the clusters in the sample. The black curve and shaded area denote the best fit function and the 1 σ confidence interval: $Z_{\rm mw} = (0.52 \pm 0.08) \cdot (M_{500}/10^{14}M_\odot)^{-0.14\pm0.09}$. *Lower*: The correlation between the gas mass and M_{500}. The black curve and shaded area denote the best fit function and the 1 σ confidence interval: $M_{\rm gas}/10^{14}M_\odot = (0.131 \pm 0.012) \cdot (M_{500}/10^{14}M_\odot)^{1.05\pm0.06}$.

$\alpha = 0.14 \pm 0.09$. This implies that in the mass range [3–10]$\times 10^{14} M_{\odot}$, the global mass weighted abundance change only by less than 20%, being slightly higher at lower halo masses. Given the small mass range probed here, this is comparable to the correlation of stellar mass with halo mass found by Lin et al. (2012) [190]. Taken at face value, this relation would imply a rapidly increasing average abundance at lower masses (below $2 \times 10^{14} M_{\odot}$ into the group regime), a range which is not explored here, in the assumption that the entire stellar-mass budget is contributing to the chemical enrichment of the ICM. We must bear in mind though, that Lin et al. (2012) [190] do not include the contribution of the intracluster light [289], that can be larger at high masses, making flatter the stellar mass-halo mass relation.

In the lower panel of Figure 4.14 we also show the correlation between the gas mass (within r_{500}) and the total mass M_{500}. Also in this case the statistical errors in both quantities is relevant. The best-fit function of $M_{\rm gas}/10^{14} M_{\odot} = A \cdot (M_{500}/10^{14} M_{\odot})^{B}$ gives $A = 0.131 \pm 0.012$ and $B = 1.05 \pm 0.06$. The slope we find here is indeed consistent with the value of 1.13 ± 0.03 found by Lin et al. (2012) [190]. This confirms that smaller mass halos have slightly less ICM within r_{500} compared to the most massive clusters. If we include also a dependence on redshift of the form $(1+z)^{\gamma_3}$ we find $A = 0.130 \pm 0.010$, $B = 1.04 \pm 0.06$ and $\gamma_3 = 0.08 \pm 0.21$, again in good agreement with Lin et al. (2012) [190] and with previous claims by Vikhlinin et al. (2009) [391]. However, we remark that the observed evolution of $f_{\rm ICM}$ depends on cosmology [1], and therefore we do not discuss possible physical implications for the trend found here.

A comprehensive discussion on the correlations between the integrated quantities (global metallicity, temperature, mass) is postponed to a forthcoming work.

4.4 Discussion

In this Section we discuss several aspects, ranging from the control of the systematics in our spectral analysis[2], to the physical interpretation of our

[2]We do not discuss two potential sources of systematics such as the calibration of the X-ray instruments and the plasma code used to fit the data, both of which are expected to

results, and a direct comparison with previous works. We start from this last aspect, which is relevant here since the original motivation of this work was the contradictory results obtained in the last 10 years on the iron evolution in the ICM.

4.4.1 Comparison with previous works

Since the beginning of *Chandra* and XMM era, a number of attempts have been made to explore the cosmic evolution of ICM metal abundance. Although early works such as Tozzi et al. (2003) [376] and Balestra et al. (2007) [17] are likely to suffer from the limited volume of cluster sample and the low S/N of the data, more recent works based on large samples and deeper observations present contradictory results, and no obvious solution could be found to explain the observed discrepancies. Both the selection of sample and the extraction radius used to measure the ICM abundance vary in these works, which increases the difficulty in comparing the previous results. Another issue is that all these previous results are obtained from emission-weighted measurements, thus might be influenced by the fraction of cool-core clusters in the sample. This effect, as we know, would disappear once the mass-weighted abundances are used. Given these caveats, we only adopt the evolving models on the basis of core-excised analysis from the previous works, namely, those using a radial range of 0.1 (or 0.15)–1 r_{500}. The evolving model in the form of $Z \propto (1+z)^{-\gamma}$ is commonly used, and we can directly compare the slope γ. We list the measurements of γ in different works in Table 4.1, and compare them to the result we obtained by fitting the distribution of the mass-weighted abundance within r_{500} in this work.

We note that our result on γ is inconsistent only with Maughan et al. (2008) [223], where $\gamma = 1.63 \pm 0.35$ is obtained based on a sample of 111 clusters[3], suggesting a strong evolution at $> 4\sigma$. However, we notice that a number of high-redshift clusters in the sample of Maughan et al. (2008) [223] have just upper limits for the measured abundance, often with small uncertainties. This

affect the iron abundance at the level of few percent [244].

[3]The sample of Maughan et al. [223] consists of 115 clusters, in which 111 clusters have measurements of metallicity within the extraction radius [0.15–1]r_{500}. The $\gamma = 1.63 \pm 0.35$ is obtained in this work by fitting the data points presented in Maughan et al.

Table 4.1. γ measured in this work and compiled from literature.

Reference	$r(r_{500})$	Sample	γ
Maughan et al. (2008) [223]	0.15–1	111	1.63 ± 0.35
Ettori et al. (2015) [92]	0.15–1	83	0.48 ± 0.35
McDonald et al. (2016) [227]	0.15–1	153	0.03 ± 0.06
Mantz et al. (2017) [207]	0.10–1	245	0.51 ± 0.46
This work (mass-weighted)	0.00–1	186	0.08 ± 0.17

is probably due to the low S/N of the data. For example, Maughan et al. (2008) [223] report an abundance $0.00^{+0.21}_{-0.00}$ (adopting the solar abundance of Asplund et al. 2009) for CLJ1415.1+3612 at redshift 1. However, recent studies using deeper observations have presented much higher abundance of this cluster. For example, Santos et al. (2012) [326] present a result of $Z = 0.88 \pm 0.11$ within $\sim 0.35 r_{500}$, and in this work we consistently measure $Z = 0.76 \pm 0.12$ within $0.4 r_{500}$. If we remove this single data point, the best-fit slope decreases immediately from 1.63 ± 0.35 to 0.76 ± 0.35. Therefore, we suppose that the evolutionary signal detected by Maughan et al. (2008) [223] is likely to be caused, at least partially, by several low S/N clusters at high redshifts which return unreliable low values of metallicity.

Moreover, we also explore the impact of the use of emission weighted abundance on the evolutionary signal found in Maughan et al. Among the 115 clusters in the sample of Maughan et al., 48 are also in our sample. We therefore make a comparison between the mass-weighted abundance measured in this work, and the emission-weighted value provided in Maughan et al., as shown in Figure 4.15. As expected, no significance evolution is found in the mass-weighted abundance, with $\gamma = 0.25 \pm 0.28$, in perfect agreement with the full sample. On the other hand, for the emission-weighted abundance measured in Maughan et al., we obtain a best-fit γ of 0.95 ± 0.39. This result indicates that the use of emission-weighted abundance also contributes to the claim of evolution previously reported. In conclusion, we can explain past claims of evolution (or no evolution) as the combined effect of the use of different sample selections (mostly X-ray versus SZ selected samples with different cool-core fractions) and emission weighted values, with the latter amplifying the effect

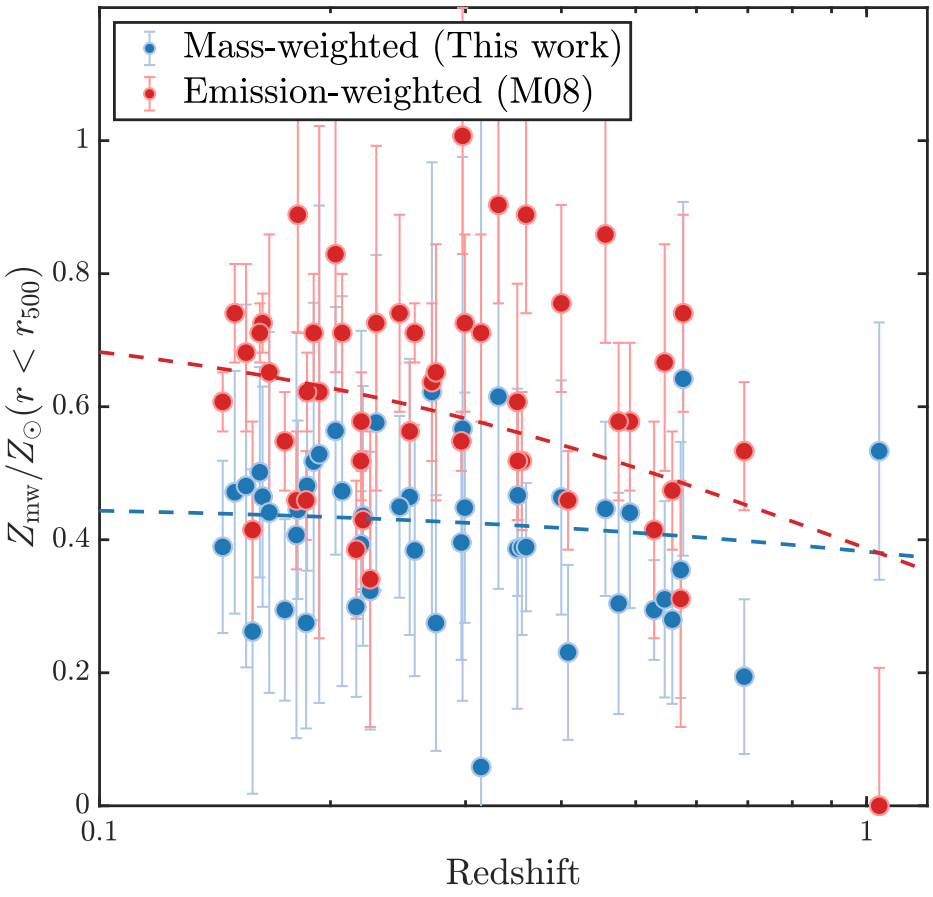

Figure 4.15. Comparison between the mass-weighted abundance measured in this work (red circles), and the emission-weighted abundance provided by Maughan et al. (2008) (blue circles), for the overlapping 48 clusters. Red and blue dashed lines represent the best fit of the corresponding data points. The reference solar abundance for the data points of Maughan et al. has been adjusted from Anders et al. (1989) to Asplund et al. (2009), for a direct comparison with our results.

of sample selection, especially in small samples. The use of larger samples, with a mixed selection function, and of mass-weighted measurements, shows a small amount of evolution within r_{500}, if any, which is, anyhow, limited to the iron peak.

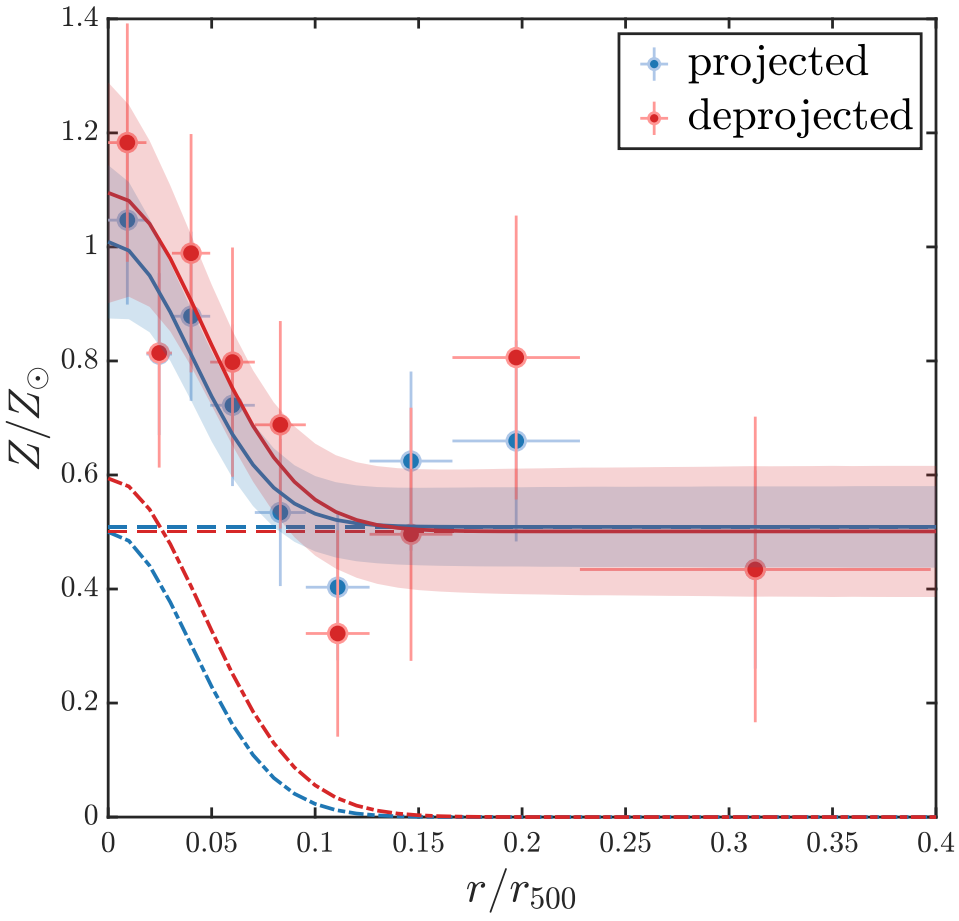

Figure 4.16. The projected and deprojected iron abundance profiles of Abell 383: an example to show the impact of projection effect. The iron peak and iron plateau components in the best-fit model are plotted with dash-dotted lines and dashed lines, respectively.

4.4.2 Projection effects

In this section we will estimate the impact of projection effect on the iron abundance profiles, and consequently the final results. We repeat our analysis in a fraction (about 10%) of our sample including clusters with the steepest abundance gradient, to maximize the effects of projection. We find that, as expected, the plateau is almost unaffected, while the peak is somewhat biased toward higher values. The normalization of the abundance in the iron peak is about 10–20% larger, and a larger effect of the order of ∼40% is found for the

iron peak mass. This is because a small change in the extension of the peak component is amplified by the volume effect.

We show the case of Abell 383, that hosts a strong cool core, a steep iron peak and an intermediate S/N, therefore it suffers a strongest projection effects among the clusters in our sample. The projected and deprojected abundance profiles of Abell 383 and the best-fit models are shown in Figure 4.16. We find that the deprojection of the profile only induces a negligible change on the iron plateau. The main reason for this is that the plateau is dominated by the outer regions, where the projection effects are weak if not absent due to the flat temperature profile. Therefore, since the mass of the iron plateau contributes $> 95\%$ of the total iron mass budget, the impact of the projection effect on the total iron mass and the mass weighted iron abundance within r_{500}, is also negligible.

Instead, the iron peak is somewhat amplified by deprojection. In the case of Abell 383, the differences in the total iron mass, the iron plateau mass, and the mass-weighted abundance within r_{500} between projected and deprojected values are all lower than 3%. On the other hand, the normalization of the iron peak measured from the deprojected profile is 0.59 ± 0.21, $\sim$18% higher than that measured from the projected profile 0.50 ± 0.14. The deprojected iron peak mass within r_{500} is $\sim$43% higher than the projected value, since the slightly larger extension of the peak are amplified by the volume weighting. This increase, however, is smaller than the 1σ statistical uncertainty. The average uncertainty of the normalization of the iron peak and of the iron peak mass within r_{500} across all the clusters are 48% and 67%. Since Abell 383 hosts one of the strongest iron peaks in our sample, these results can be conservatively taken as an upper limit of the magnitude of projection effect.

To summarize, we acknowledge the fact that the strongest iron peaks in our analysis may be biased towards lower values by $\sim few \times 10\%$, mostly because of the uncertainty in the extension of the iron peak, which is a key quantity in determining $M_{\rm peak}$. We are also aware that any unnoticed irregular morphology in the central region may alter the deprojection results, which are based on a perfect spherical asymmetry, and, even in the absence of such features, it is prone to amplification of noise. In other words, by applying deprojection, we risk to introduce large random uncertainties possibly larger than the bias

we aim to correct. Clearly, accurate and stable quantification of projection effect is possible only by taking into account many aspects, including the 3D morphology of the cluster emission, and the 3D distributions of temperature and iron abundance, which is far beyond the goal of this paper, as well as the current state of the art. Therefore, we decide to ignore the deprojection correction in this work, and to present results based on the projected values of iron abundance.

4.4.3 The impact of $n_{\rm H}$ on the measurement of iron abundance

The HI column density which quantifies the absorption of X-rays is an important factor that affects the fitting of X-ray spectra, and therefore the measurement of ICM metallicity. Usually there are three resources/strategies to fix the value of $n_{\rm H}$: i) $n_{\rm H,LAB}$, the measurement from the Leiden/Argentine/Bonn (LAB) survey [165], which only takes into account the neutral hydrogen; ii) $n_{\rm H,tot}$ from Willingale et al. (2013) [398], which also calculates the contribution of molecular and ionized hydrogen; iii) $n_{\rm H,free}$, which is obtained by fitting the X-ray spectrum with $n_{\rm H}$ set as a free parameter. The impact of these different values of $n_{\rm H}$ on the measurement of metal abundance has been discussed in detail in Lovisari et al. (2019) [199]. In general, $n_{\rm H,tot}$ provides a better fit to the spectrum than $n_{\rm H,LAB}$. However, Lovisari et al. (2019) also find that in a few cases using $n_{\rm H,tot}$ does not guarantee a proper fit. Therefore, a relatively safe strategy is setting $n_{\rm H}$ free, and putting some constraint on the range of possible values, to avoid strong degeneracies with other parameters. This allows the fit to identify the preferred $n_{\rm H}$ value without being too far from the reference value $n_{\rm H,tot}$. However, a caveat here is that the calibration uncertainties of *Chandra*, e.g. if the time-dependent contamination corrections of ACIS are not perfect, may also bias the measurement of $n_{\rm H}$. Therefore, we stress that leaving $n_{\rm H}$ free and setting a constraint according to $n_{\rm H,tot}$, despite being an already very conservative strategy, does not always guarantee to return the 'true' astrophysical $n_{\rm H}$. Having all these knowledge in mind, in this work we choose to adopt a two-step strategy: first, we fit the spectrum of the global emission by setting $n_{\rm H}$ free to vary below a very loose upper limit at

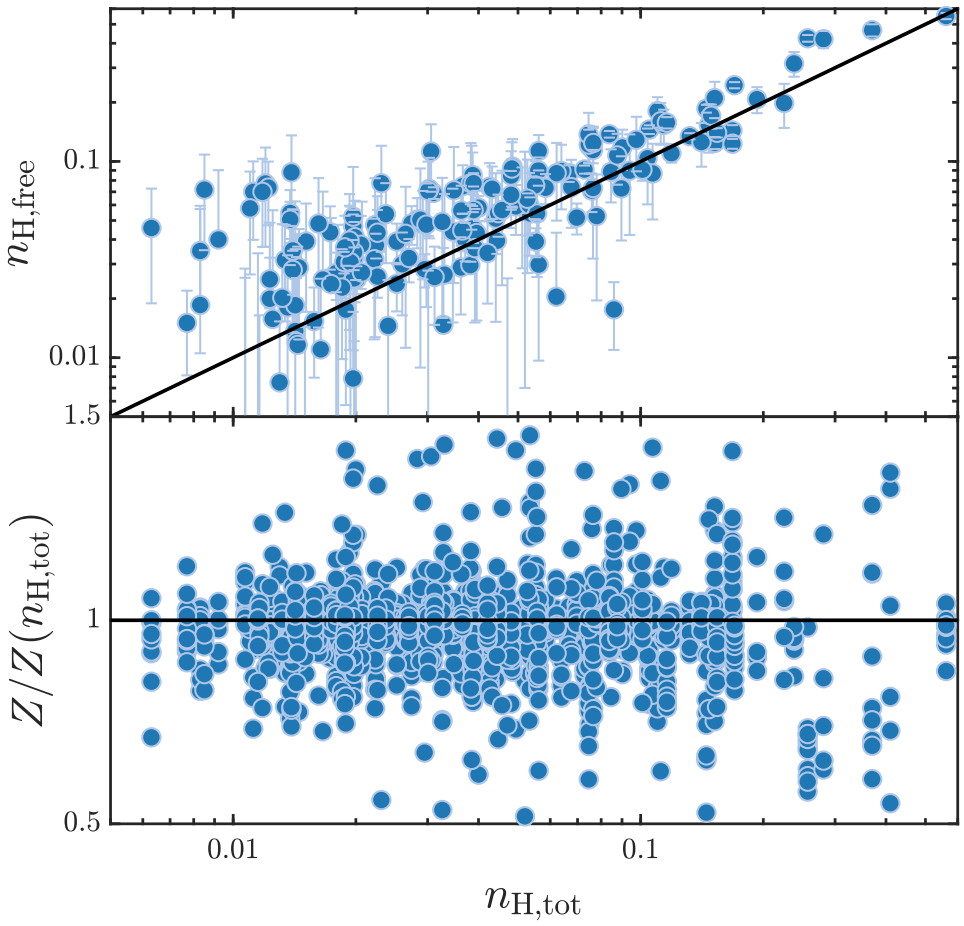

Figure 4.17. *Upper panel:* Comparison of the measured $n_{\rm H,free}$ and $n_{\rm H,tot}$. The $n_{\rm H}$ values are in units of 10^{22} cm^{-2}. The vertical dashed line denotes 0.05×10^{22} cm^{-2}. The solid line corresponds to $n_{\rm H,free} = n_{\rm H,tot}$. *Lower panel:* the ratio of all the abundance measured by adopting our strategy in $n_{\rm H}$ (free to vary in a limited interval around $n_{\rm H,free}$) and by fixing $n_{\rm H}$ to $n_{\rm H,tot}$, as a function of $n_{\rm H,tot}$. The typical error of the data points is ∼0.5.

$10\times n_{\rm H,tot}$, and obtain the $n_{\rm H,free}$; then for the spatially-resolved analysis, we adopt the measured $n_{\rm H,free}$, and allow it to vary within its statistical confidence interval, or within ±50% when its uncertainty is too small. With this strategy, we take into account not only the possible discrepancy between $n_{\rm H,tot}$ and $n_{\rm H,free}$, but also the fluctuation of $n_{\rm H}$ within the solid angle covered by the cluster emission. In Figure 4.17 we show the comparison between $n_{\rm H,tot}$ and $n_{\rm H,free}$ found with our strategy. Similar to the result of Lovisari et al. (2019),

we find a general agreement between $n_{\rm H,tot}$ and $n_{\rm H,free}$ above $0.05\times10^{22}{\rm cm}^{-2}$, while the discrepancy is relatively large for low column densities, for which the best fit values are systematically larger than $n_{\rm H,tot}$, despite still consistent within 1σ. In the lower panel of Figure 4.17, we plot the ratio of all the abundance measured by adopting our strategy in $n_{\rm H}$ (free to vary in a limited interval around $n_{\rm H,free}$) and by fixing $n_{\rm H}$ to $n_{\rm H,tot}$, as a function of $n_{\rm H,tot}$. We find only a slight bias of few percent, $Z/Z(n_{\rm H,tot}) \sim 0.98$, with no dependence on $n_{\rm H,tot}$. Despite it is hard to decide whether $n_{\rm H,free}$ or $n_{\rm H,tot}$ is better to describe the absorption effects of the HI Galactic column density, we conclude that any effect related to $n_{\rm H}$ is under control and it does not bias our results.

4.4.4 Physical interpretation of the results and future perspectives

Our results are in general agreement with the picture that the bulk of iron in the ICM is produced at early epochs. On the other hand, the signal of evolution of the iron peak, despite statistically weak, shows the complex effects of recent processes, including the star formation and supernova explosion in member galaxies, the galaxy-scale dynamical activities which eject metals from the galaxies to the ICM, and the ICM motions induced by AGN feedback activities that continuously transport the metals from the cluster center to the outer regions. In particular, in Liu et al. (2018) [192] we have shown the spatial broadening of the iron peak in a sample of 41 most relaxed *Chandra* clusters. However, in order to measure the size of the iron peak accurately, the sample of Liu et al. (2018) [192] was selected with a strict requirement on cluster relaxation, and we were not able to to obtain any significant constraint on the evolution of the iron peak in mass. Whereas in this work, using a > 4 times larger sample, we are able to find evidence for the mass evolution of the iron peak. We stress, however, that both the samples of Liu et al. (2018) [192] and this work, suffer by a not-well-defined selection in cluster mass. Therefore, a coherent evolutionary picture of iron in the ICM will be reached only with a complete and large sample of galaxy clusters.

At present, the best sample is provided by the combination of the *Chandra* and XMM-Newton archives. Depending on the mass selection one could adopt,

the total number of clusters may reach ~ 1000. Clearly, a proper spatially resolved analysis is feasible only for about 1/3 of the sample, while most of the clusters could be characterized by the X-ray morphology, a single temperature, and a single, average abundance. The abundance measurement would clearly be emission weighted, unless some priors on the abundance profile are assumed, to be combined with the observed surface brightness profile. In practice, the application of what we have learned with this sample to the largest sample that can be assembled today, would provide us with the most comprehensive study on ICM chemical evolution. Clearly, the ultimate test on the robustness of this approach would be available only when a mission like *Athena* will provide the access to a large number of well-characterized, spatially resolved cluster in a wide range of halo mass and redshift.

The present-day perspective allows a significant improvement only for relatively nearby clusters. XMM-Newton and, more slowly, *Chandra*, can provide a slow but steady growth in the number of spatially resolved clusters through pointed observations. At the same time, the survey mission eROSITA will dramatically increase the number of known clusters. However, the moderate resolution, but mostly the limited energy range of its spectral response, imply that abundance profiles can be attempted only for massive, medium and high-z clusters, for which the hydrogen and helium-like iron line complex enters in the effective energy range. This however, occurs for clusters that would require a better angular resolution for the approach outlined here, so that the amount of eROSITA data that can be used here is necessarily limited. Finally, in the next future, XRISM will be able to add a substantial piece of information by observing the outer regions of local clusters with poor angular resolution but 10 times better spectral resolution. In summary the only perspective before the advent of *Athena*, is to invest on the characterization of local and moderate redshift cluster to improve the educated guess to be applied to the high-redshift cluster sample that is available to date. This step would constitute, in our view, the state-of-the-art picture that we could ever achieve before the year 2030.

4.5 Conclusions

We measure the amount of mass in iron in a sample of galaxy clusters observed with *Chandra*. We select 186 morphologically regular clusters in the redshift range [0.04, 1.07], from deep and medium-deep *Chandra* archival observations. Most of the clusters in the sample are found at $z < 0.6$, so that any evolutionary behaviour would reflect this range of redshift, corresponding to about 5 Gyr. The mass range of M_{500} is [1–16]$\times 10^{14} M_{\odot}$, with the large majority of the clusters spanning the [3–10]$\times 10^{14} M_{\odot}$ interval. For each cluster we compute the azimuthally-averaged iron abundance and gas density profiles. We fit the iron abundance profile with a two-component model, namely a peak in the center, and an approximately constant plateau across the entire cluster. In a few cases, we need to model a central drop in the iron abundance, as we already explored in a limited sample of nearby clusters [197]. This approach is physically motivated by a picture in which the central peak is associated with relatively recent star formation in the BCG, occurring after the formation of the cluster. Moreover, the almost constant plateau extending to large radii is possibly associated with uniform, early enrichment before cluster formation. With this approach we are able to derive the total iron mass (and therefore the mass-weighted average iron abundance of the ICM) in each component separately out to a typical extraction radius $\sim r_{500}$. Therefore, we can investigate the chemical evolution of the ICM across cosmic epochs separately in the central regions and at large radii. Our conclusions are summarized as follows:

- We find that at least two components (a central peak and a constant plateau) are statistically preferred to model the iron distribution within $0.4 r_{500}$ in at least 39 clusters (more than 1/5 of the sample). Most of the remaining clusters are also well described with a single component (β model).

- The iron mass included in the central peak component is typically a fraction of $\sim 1\%$ with respect to the total iron mass included within r_{500}. The large majority of iron in the ICM is therefore in the iron plateau.

- The normalization of the iron peak component has a large spread, ranging from ~ 0 (when the peak is totally absent, as often happens in non-cool-

core clusters) to $\sim 2Z_{\odot}$, reflecting the wide difference in the shape and strength of the central peak, as already shown in Liu et al. (2018) [192].

- We find a more regular distribution of the normalization of the iron plateau, centered around $\langle Z \rangle = 0.38\,Z_{\odot}$ with a *rms* of about $0.13\,Z_{\odot}$ (adopting the solar abundance table of Asplund et al. 2009), consistent with an average 1/3 solar abundance of the ICM in cluster outskirts. This supports a pristine, uniform enrichment of the diffuse baryons before the cluster virialization.

- Among the two components in the abundance profiles, the iron plateau, which contributes the majority of the total iron mass, shows no evolution with redshift. On the other hand, we find marginal ($< 2\sigma$ c.l.) decrease with redshift in both the iron mass and the normalization associated with the iron peak. This is summarized in the upper and lower panels of Figure 4.18, where we show the best-fit relations and their 1σ uncertainties for the quantities $Z_{\rm Fe}^{\rm peak}$-$Z_{\rm Fe}^{\rm plateau}$ and $M_{\rm Fe}^{\rm peak}$-$M_{\rm Fe}^{\rm plateau}$ as a function of redshift.

- While the intrinsic scatter in the iron plateau mass is consistent with zero, the iron peak mass exhibits an extremely large intrinsic scatter, in line with the fact that the peak is produced after the virialization of the halo and depends on the formation of a cool core and the strength of the feedback processes, which leave their imprint in a larger variance.

- By fitting the distribution of the global, average mass-weighted iron abundance within r_{500} with a power law of $(1+z)$, $Z_{\rm mw} = Z_{\rm mw,0} \cdot (1+z)^{-\gamma}$, we obtain $Z_{\rm mw,0} = 0.35 \pm 0.02$, and $\gamma = 0.08 \pm 0.17$, consistent with no significant evolution of $Z_{\rm mw}$ across our sample.

- We find that the average emission-weighted abundance within $0.4r_{500}$ is higher than the average mass-weighted abundance within the same radius by $\sim$22% in cool-core clusters, and by $\sim$ 4% in non-cool-core clusters. Quantifying this well known effect is not only a mere exercise, but is also helpful to estimate the impact of the iron peak on the measurement of the global ICM abundance, particularly for cool-core clusters, where the

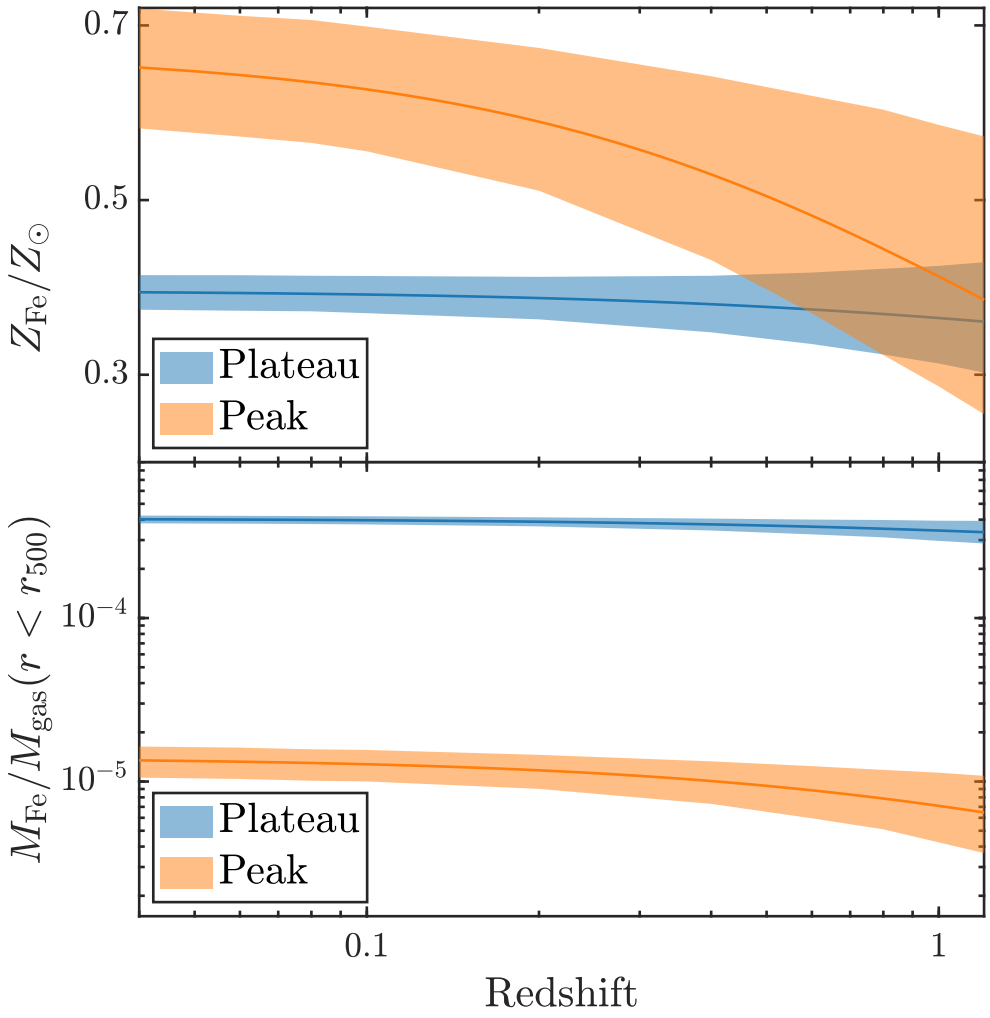

Figure 4.18. *Upper panel*: the dependence of $Z_{\rm Fe}^{\rm peak}$ and $Z_{\rm Fe}^{\rm plateau}$ on redshift as described by the best-fit power-law $X = n \cdot (1+z)^{-\gamma}$, with its 1σ uncertainty. *Lower panel*: the dependence of $M_{\rm Fe}^{\rm peak}/M_{\rm gas}$ and $M_{\rm Fe}^{\rm plateau}/M_{\rm gas}$ on redshift. These two plots represent a synthetic description of the cosmic evolution of the iron abundance obtained in this work. The curves and shaded areas have been already shown in Figures 4.11 and 4.12.

emission-weighted abundance is significantly amplified by the presence of the iron peak.

- Our results confirm that the majority of iron mass in the ICM of massive galaxy clusters is produced at epochs earlier than $z \sim 1$. On the other

Table 4.2. The best-fit parameters describing the evolution of the quantities investigated in this paper, assuming the power law behaviour $X = n \cdot (1+z)^{-\gamma}$.

X	n	γ
$Z_{\rm mw}(r < r_{500})$	$(0.35 \pm 0.12)\, Z_\odot$	0.08 ± 0.17
$Z_{\rm plateau}$	$(0.39 \pm 0.03)\, Z_\odot$	0.12 ± 0.21
$Z_{\rm peak}$	$(0.67 \pm 0.07)\, Z_\odot$	0.70 ± 0.50
$M_{\rm Fe}^{\rm plateau}/M_{\rm gas}\,(r < r_{500})$	$(5.2 \pm 0.3) \times 10^{-4}$	0.24 ± 0.19
$M_{\rm Fe}^{\rm peak}/M_{\rm gas}\,(r < r_{500})$	$(1.4 \pm 0.3) \times 10^{-5}$	0.98 ± 0.63

hand, the iron peak component, despite contributing a minority fraction in the total iron mass, shows a low-significance decrease with redshift and a large intrinsic scatter. In general, our results confirms the early-enrichment scenario suggested by recent works, and limits the possible evolution in ICM iron abundance to the central peak component.

- We are able to explain the previous claims of evolution in the average iron abundance in the ICM between $z \sim 1.3$ and $z \sim 0$ as the combined effect of sample selection and the use of emission-weighted abundance, possibly combined with the evolution of cool-core fraction with redshift across the sample.

In Table 4.2 we summarize the best-fit parameters describing the evolution of the quantities investigated in this paper, assuming the power law behavior $X = n \cdot (1+z)^{-\gamma}$, which are also shown in Figure 4.18. The overall picture of the iron distribution and its evolution as we obtained in this work, will be important to extend our analysis to the total *Chandra* archive including lower S/N data, therefore reaching a larger mass and redshift range. Another important extension of this work will be provided by the XMM-Newton data, already available for a fraction of our sample. This addition will be important to have a better handle on the iron plateau at large radii. Next future facilities, like XRISM, may provide further relevant information on the outer regions. Only future ($\sim$ 2030) X-ray facilities, e.g. *Athena* with the X-IFU on board, will provide high quality observations for a large number of high redshift clusters, and will promisingly provide a coherent picture of chemical evolution of the ICM.

Acknowledgments

A.L., P.T. and S.E. acknowledge financial contribution from the agreement ASI-INAF n.2017-14-H.0. PT acknowledges financial contribution from the Istituto Nazionale di Astrofisica (INAF) PRIN-SKA 2017 program 1.05.01.88.04 (ESKAPE). S.E. acknowledges financial contribution from the contracts ASI 2015-046-R.0, and from INAF "Call per interventi aggiuntivi a sostegno della ricerca di main stream di INAF".

4.6 Appendix: Properties of the sample.

In Table 4.3 we list the result of our spectral analysis for the global quantities of the entire cluster sample. The 186 clusters (including the 16 clusters discarded from the final analysis because of the irregular abundance profile) are listed in alphabetical order according to the target name. The positions correspond to the X-ray centroid identified as described in Section 4.2. We report the X-ray redshift, which is the value used in our analysis, and the core-excised temperature, which is the emission-weighted value obtained fitting the projected emission in the range (0.1–0.4) r_{500} with a single `apec` model. M_{500} is the total halo mass obtained from equations (2) and (3), while the ICM mass within r_{500} is measured directly from the deprojected ICM density profile integrated over the spherical volume within r_{500}. Finally, we list the three abundance measurements used in this work: the emission weighted iron abundance within $0.4r_{500}$, and the mass weighted iron abundance within $0.4r_{500}$ and r_{500}.

Table 4.3. The properties we measured for the 186 clusters. Column 1: cluster name. Column 2–3: center of the cluster emission measured in Section 4.2. Column 4: X-ray redshift of the cluster. Column 5: temperature of the cluster measured within (0.1–0.4) r_{500}. Column 6: M_{500} in units of $10^{14} M_{\odot}$. Column 7: gas mass within r_{500} in units of $10^{14} M_{\odot}$. Column 8: Emission weighted iron abundance within $0.4 r_{500}$. Column 9–10: Mass weighted iron abundance within $0.4 r_{500}$ and r_{500}.

Name	RA [deg]	Dec [deg]	$z_{\rm X}$	kT [keV]	M_{500} $[10^{14} M_{\odot}]$	$M_{\rm gas,500}$ $[10^{14} M_{\odot}]$	$Z_{\rm ew}$ $[Z_{\odot}]\,(0.4 r_{500})$	$Z_{\rm mw}$ $[Z_{\odot}]\,(0.4 r_{500})$	$Z_{\rm mw}$ $[Z_{\odot}]\,(r_{500})$
3C186	116.0728	37.8882	1.082 ± 0.020	7.32 ± 0.62	3.99 ± 0.53	0.46 ± 0.07	0.46 ± 0.09	0.27 ± 0.16	0.24 ± 0.17
4C+37.11	61.4550	38.0589	0.058 ± 0.001	4.62 ± 0.09	3.51 ± 0.10	0.75 ± 0.26	0.54 ± 0.02	0.37 ± 0.10	0.30 ± 0.18
Abell0021	5.1329	28.6630	0.079 ± 0.006	6.77 ± 0.42	6.35 ± 0.62	0.54 ± 0.25	0.71 ± 0.14	0.45 ± 0.20	0.45 ± 0.38
Abell0085	10.4603	-9.3033	0.059 ± 0.001	6.28 ± 0.06	5.70 ± 0.09	1.08 ± 0.25	0.51 ± 0.01	0.39 ± 0.07	0.34 ± 0.15
Abell0119	14.0596	-1.2562	0.050 ± 0.002	6.15 ± 0.13	5.53 ± 0.18	1.05 ± 0.40	0.32 ± 0.03	0.60 ± 0.32	0.60 ± 0.40
Abell0209	22.9711	-13.6110	0.216 ± 0.010	8.01 ± 0.53	7.71 ± 0.81	1.28 ± 0.23	0.28 ± 0.08	0.30 ± 0.11	0.30 ± 0.14
Abell0267	28.1764	1.0125	0.230 ± 0.010	8.07 ± 0.60	7.74 ± 0.91	0.84 ± 0.20	0.52 ± 0.12	0.58 ± 0.13	0.58 ± 0.25
Abell0383	42.0142	-3.5293	0.190 ± 0.003	5.11 ± 0.14	3.84 ± 0.17	0.35 ± 0.09	0.57 ± 0.04	0.53 ± 0.10	0.52 ± 0.24
Abell0399	44.4572	13.0478	0.076 ± 0.003	7.32 ± 0.19	7.20 ± 0.30	0.85 ± 0.21	0.32 ± 0.04	0.49 ± 0.13	0.49 ± 0.22
Abell0401	44.7380	13.5827	0.086 ± 0.005	8.02 ± 0.22	8.28 ± 0.36	1.62 ± 0.71	0.65 ± 0.06	0.36 ± 0.13	0.33 ± 0.29
Abell0478	63.3537	10.4650	0.088 ± 0.002	7.36 ± 0.24	7.21 ± 0.37	1.06 ± 0.37	0.56 ± 0.04	0.42 ± 0.09	0.41 ± 0.26
Abell0586	113.0840	31.6325	0.181 ± 0.002	7.30 ± 0.17	6.79 ± 0.25	0.87 ± 0.14	0.46 ± 0.03	0.45 ± 0.05	0.45 ± 0.13
Abell0611	120.2371	36.0560	0.285 ± 0.004	8.20 ± 0.43	7.70 ± 0.64	0.77 ± 0.17	0.47 ± 0.08	0.37 ± 0.09	0.36 ± 0.16
Abell0644	124.3564	-7.5082	0.077 ± 0.002	6.91 ± 0.16	6.58 ± 0.23	1.30 ± 0.50	0.45 ± 0.03	0.36 ± 0.09	0.21 ± 0.18
Abell0697	130.7395	36.3662	0.271 ± 0.008	10.65 ± 0.74	11.72 ± 1.29	1.61 ± 0.47	0.60 ± 0.12	0.64 ± 0.18	0.62 ± 0.35
Abell0744	136.8359	16.6519	0.074 ± 0.006	2.37 ± 0.14	1.21 ± 0.11	0.09 ± 0.05	0.31 ± 0.06	0.35 ± 0.14	0.17 ± 0.25
Abell0750	137.3031	10.9747	0.181 ± 0.005	5.87 ± 0.31	4.81 ± 0.40	0.35 ± 0.14	0.40 ± 0.07	0.44 ± 0.11	0.41 ± 0.31
Abell0773	139.4695	51.7273	0.207 ± 0.004	7.69 ± 0.36	7.26 ± 0.53	0.84 ± 0.28	0.47 ± 0.07	0.47 ± 0.10	0.47 ± 0.29
Abell0795	141.0239	14.1737	0.140 ± 0.003	5.23 ± 0.20	4.09 ± 0.24	0.71 ± 0.12	0.40 ± 0.06	0.35 ± 0.09	0.34 ± 0.12
Abell0907	149.5915	-11.0638	0.163 ± 0.002	5.95 ± 0.12	4.96 ± 0.16	0.65 ± 0.13	0.57 ± 0.03	0.48 ± 0.07	0.46 ± 0.17
Abell0963	154.2651	39.0476	0.203 ± 0.002	8.42 ± 0.29	8.40 ± 0.45	1.12 ± 0.20	0.66 ± 0.07	0.42 ± 0.11	0.40 ± 0.16
Abell1033	157.9392	35.0377	0.115 ± 0.004	6.62 ± 0.21	6.02 ± 0.29	0.54 ± 0.18	0.45 ± 0.05	0.41 ± 0.10	0.41 ± 0.24
Abell1068	160.1859	39.9531	0.139 ± 0.002	4.82 ± 0.14	3.60 ± 0.16	0.41 ± 0.20	0.54 ± 0.04	0.32 ± 0.10	0.28 ± 0.25
Abell1132	164.6091	56.7950	0.140 ± 0.006	9.54 ± 0.58	10.59 ± 1.02	1.10 ± 0.42	0.44 ± 0.08	0.41 ± 0.12	0.41 ± 0.28
Abell1204	168.3354	17.5945	0.174 ± 0.003	3.92 ± 0.14	2.55 ± 0.14	0.34 ± 0.06	0.47 ± 0.05	0.31 ± 0.10	0.29 ± 0.14
Abell1246	170.9906	21.4810	0.188 ± 0.012	8.48 ± 0.79	8.56 ± 1.26	0.99 ± 0.23	0.42 ± 0.12	0.21 ± 0.12	0.21 ± 0.23

Table 4.3. continued.

Name	RA [deg]	Dec [deg]	$z_{\rm X}$	kT [keV]	M_{500} $[10^{14}\,M_{\odot}]$	$M_{\rm gas,500}$ $[10^{14}\,M_{\odot}]$	$Z_{\rm ew}$ $[Z_{\odot}]\,(0.4r_{500})$	$Z_{\rm mw}$ $[Z_{\odot}]\,(0.4r_{500})$	$Z_{\rm mw}$ $[Z_{\odot}]\,(r_{500})$
Abell1302	173.3196	66.3786	0.122 ± 0.005	5.25 ± 0.34	4.16 ± 0.43	0.43 ± 0.12	0.57 ± 0.11	0.44 ± 0.14	0.43 ± 0.13
Abell1413	178.8247	23.4050	0.145 ± 0.002	7.91 ± 0.16	7.85 ± 0.25	1.37 ± 0.23	0.44 ± 0.03	0.40 ± 0.06	0.39 ± 0.13
Abell1423	179.3217	33.6112	0.219 ± 0.006	6.69 ± 0.36	5.80 ± 0.49	0.80 ± 0.12	0.50 ± 0.08	0.35 ± 0.11	0.32 ± 0.94
Abell1576	189.2387	63.1895	0.296 ± 0.010	7.98 ± 0.55	7.32 ± 0.79	1.03 ± 0.22	0.36 ± 0.08	0.16 ± 0.09	0.04 ± 0.10
Abell1650	194.6728	-1.7623	0.081 ± 0.001	5.94 ± 0.05	5.17 ± 0.08	0.85 ± 0.13	0.48 ± 0.01	0.42 ± 0.05	0.36 ± 0.28
Abell1651	194.8427	-4.1966	0.090 ± 0.002	7.17 ± 0.35	6.91 ± 0.54	0.78 ± 0.26	0.61 ± 0.08	0.47 ± 0.12	0.47 ± 0.13
Abell1664	195.9270	-24.2455	0.126 ± 0.001	4.18 ± 0.04	2.89 ± 0.05	0.41 ± 0.10	0.46 ± 0.01	0.30 ± 0.05	0.27 ± 0.14
Abell1682	196.7088	46.5579	0.193 ± 0.006	10.41 ± 0.89	11.81 ± 1.60	1.33 ± 0.44	1.04 ± 0.20	0.56 ± 0.22	0.53 ± 0.20
Abell1689	197.8731	-1.3416	0.186 ± 0.002	10.39 ± 0.15	11.82 ± 0.27	1.64 ± 0.24	0.45 ± 0.02	0.48 ± 0.05	0.48 ± 0.15
Abell1703	198.7780	51.8240	0.271 ± 0.008	8.38 ± 0.39	8.02 ± 0.59	1.16 ± 0.23	0.35 ± 0.05	0.35 ± 0.08	0.35 ± 0.42
Abell1763	203.8230	41.0011	0.221 ± 0.008	7.64 ± 0.53	7.13 ± 0.78	1.13 ± 0.25	0.44 ± 0.09	0.44 ± 0.13	0.44 ± 0.29
Abell1795	207.2192	26.5913	0.066 ± 0.002	5.94 ± 0.12	5.20 ± 0.17	0.93 ± 0.23	0.46 ± 0.03	0.33 ± 0.08	0.29 ± 0.21
Abell1800	207.3650	28.1060	0.070 ± 0.005	4.63 ± 0.30	3.50 ± 0.36	0.33 ± 0.15	0.50 ± 0.10	0.52 ± 0.17	0.52 ± 0.32
Abell1835	210.2583	2.8783	0.250 ± 0.002	9.98 ± 0.34	10.70 ± 0.58	1.63 ± 0.35	0.52 ± 0.04	0.46 ± 0.07	0.46 ± 0.15
Abell1918	216.3421	63.1830	0.155 ± 0.005	5.73 ± 0.42	4.70 ± 0.54	0.41 ± 0.15	0.55 ± 0.09	0.46 ± 0.14	0.43 ± 0.31
Abell1978	222.7750	14.6110	0.149 ± 0.006	5.44 ± 0.43	4.34 ± 0.54	0.43 ± 0.11	0.48 ± 0.10	0.42 ± 0.13	0.42 ± 0.21
Abell2009	225.0817	21.3695	0.158 ± 0.004	6.78 ± 0.27	6.11 ± 0.38	0.71 ± 0.26	0.57 ± 0.07	0.48 ± 0.11	0.48 ± 0.18
Abell2029	227.7333	5.7445	0.079 ± 0.002	8.32 ± 0.21	8.81 ± 0.36	1.35 ± 0.35	0.65 ± 0.05	0.25 ± 0.10	0.14 ± 0.16
Abell2050	229.0679	0.0890	0.137 ± 0.009	5.74 ± 0.52	4.75 ± 0.68	0.57 ± 0.11	0.31 ± 0.10	0.26 ± 0.12	0.26 ± 0.12
Abell2104	235.0333	-3.3049	0.160 ± 0.002	10.00 ± 0.35	11.28 ± 0.63	1.09 ± 0.71	0.59 ± 0.07	0.42 ± 0.10	0.42 ± 0.28
Abell2107	234.9100	21.7890	0.041 ± 0.002	4.61 ± 0.11	3.53 ± 0.14	0.47 ± 0.15	0.50 ± 0.04	0.53 ± 0.16	0.53 ± 0.24
Abell2111	234.9242	34.4167	0.225 ± 0.012	8.80 ± 0.90	8.90 ± 1.44	0.83 ± 0.23	0.37 ± 0.12	0.32 ± 0.15	0.32 ± 0.20
Abell2204	248.1951	5.5757	0.150 ± 0.001	9.89 ± 0.18	11.15 ± 0.32	1.52 ± 0.33	0.61 ± 0.02	0.47 ± 0.06	0.47 ± 0.27
Abell2218	248.9625	66.2105	0.186 ± 0.007	8.03 ± 0.33	7.87 ± 0.52	0.90 ± 0.27	0.24 ± 0.05	0.28 ± 0.08	0.28 ± 0.30
Abell2219	250.0827	46.7109	0.226 ± 0.002	12.47 ± 0.26	15.43 ± 0.51	2.14 ± 0.35	0.46 ± 0.03	0.39 ± 0.06	0.38 ± 0.34
Abell2244	255.6773	34.0609	0.098 ± 0.001	6.07 ± 0.09	5.29 ± 0.12	0.56 ± 0.24	0.47 ± 0.02	0.40 ± 0.09	0.38 ± 0.32
Abell2255	258.2055	64.0654	0.080 ± 0.004	6.47 ± 0.19	5.92 ± 0.27	0.99 ± 0.28	0.35 ± 0.05	0.57 ± 0.21	0.57 ± 0.20
Abell2259	260.0345	27.6698	0.158 ± 0.008	5.68 ± 0.47	4.62 ± 0.60	0.60 ± 0.30	0.36 ± 0.10	0.26 ± 0.10	0.26 ± 0.15
Abell2261	260.6136	32.1331	0.219 ± 0.005	8.42 ± 0.38	8.32 ± 0.60	1.20 ± 0.23	0.60 ± 0.10	0.52 ± 0.11	0.52 ± 0.30
Abell2294	261.0594	85.8868	0.166 ± 0.006	8.42 ± 0.56	8.57 ± 0.90	1.17 ± 0.33	0.60 ± 0.11	0.46 ± 0.17	0.44 ± 0.19

Table 4.3. continued.

Name	RA [deg]	Dec [deg]	$z_{\rm X}$	kT [keV]	M_{500} $[10^{14}\,M_\odot]$	$M_{\rm gas,500}$ $[10^{14}M_\odot]$	$Z_{\rm ew}$ $[Z_\odot]\,(0.4r_{500})$	$Z_{\rm mw}$ $[Z_\odot]\,(0.4r_{500})$	$Z_{\rm mw}$ $[Z_\odot]\,(r_{500})$
Abell2409	330.2200	20.9695	0.155 ± 0.005	5.93 ± 0.36	4.95 ± 0.47	0.77 ± 0.23	0.55 ± 0.09	0.48 ± 0.13	0.48 ± 0.74
Abell2415	331.4109	-5.5922	0.057 ± 0.005	2.87 ± 0.16	1.65 ± 0.15	0.23 ± 0.07	0.48 ± 0.07	0.54 ± 0.20	0.54 ± 6.98
Abell2420	332.5791	-12.1732	0.079 ± 0.005	6.42 ± 0.33	5.85 ± 0.48	1.04 ± 0.29	0.51 ± 0.10	0.67 ± 0.19	0.67 ± 0.72
Abell2426	333.6400	-10.3691	0.100 ± 0.007	5.17 ± 0.26	4.11 ± 0.33	0.53 ± 0.19	0.39 ± 0.08	0.51 ± 0.14	0.51 ± 0.27
Abell2533	346.8087	-15.2242	0.115 ± 0.002	4.12 ± 0.14	2.85 ± 0.15	0.31 ± 0.11	0.77 ± 0.07	0.31 ± 0.14	0.19 ± 0.14
Abell2537	347.0922	-2.1910	0.298 ± 0.005	8.37 ± 0.37	7.88 ± 0.55	0.85 ± 0.14	0.51 ± 0.07	0.36 ± 0.10	0.35 ± 0.34
Abell2552	347.8884	3.6351	0.303 ± 0.010	8.99 ± 0.74	8.80 ± 1.15	1.14 ± 0.46	0.49 ± 0.09	0.39 ± 0.13	0.39 ± 0.83
Abell2556	348.2558	-21.6346	0.089 ± 0.002	4.08 ± 0.12	2.84 ± 0.13	0.37 ± 0.10	0.61 ± 0.05	0.58 ± 0.15	0.58 ± 0.09
Abell2566	349.0213	-20.4639	0.085 ± 0.002	2.90 ± 0.10	1.66 ± 0.09	0.21 ± 0.08	0.67 ± 0.07	0.65 ± 0.13	0.65 ± 0.29
Abell2631	354.4064	0.2680	0.275 ± 0.013	9.20 ± 0.90	9.28 ± 1.44	1.37 ± 0.36	0.42 ± 0.11	0.30 ± 0.15	0.27 ± 0.28
Abell2665	357.7110	6.1485	0.053 ± 0.004	4.14 ± 0.20	2.96 ± 0.23	0.16 ± 0.13	0.54 ± 0.10	0.52 ± 0.22	0.51 ± 0.25
Abell2667	357.9142	-26.0842	0.236 ± 0.003	6.90 ± 0.43	6.02 ± 0.59	0.91 ± 0.23	0.50 ± 0.08	0.15 ± 0.11	0.05 ± 0.21
Abell2717	0.8029	-35.9356	0.047 ± 0.002	2.20 ± 0.09	1.09 ± 0.07	0.11 ± 0.06	0.47 ± 0.06	0.83 ± 0.30	0.81 ± 0.25
Abell2734	2.8404	-28.8548	0.051 ± 0.014	5.27 ± 0.18	4.34 ± 0.24	0.53 ± 0.23	0.37 ± 0.06	0.35 ± 0.14	0.35 ± 0.18
Abell3112	49.4899	-44.2384	0.075 ± 0.001	5.24 ± 0.08	4.26 ± 0.11	0.62 ± 0.16	0.60 ± 0.03	0.38 ± 0.08	0.29 ± 0.19
Abell3158	55.7225	-53.6296	0.061 ± 0.001	5.44 ± 0.09	4.53 ± 0.11	0.77 ± 0.25	0.51 ± 0.03	0.60 ± 0.12	0.60 ± 0.57
Abell3391	96.5964	-53.6962	0.055 ± 0.004	6.63 ± 0.25	6.23 ± 0.37	0.48 ± 0.46	0.37 ± 0.07	0.54 ± 0.47	0.48 ± 0.27
Abell3444	155.9592	-27.2563	0.260 ± 0.002	7.19 ± 0.29	6.34 ± 0.41	1.25 ± 0.15	0.43 ± 0.04	0.36 ± 0.06	0.35 ± 0.23
Abell3532	194.3404	-30.3696	0.051 ± 0.009	5.10 ± 0.26	4.12 ± 0.33	1.04 ± 0.25	0.41 ± 0.09	0.63 ± 0.23	0.63 ± 0.32
Abell3562	203.3985	-31.6721	0.049 ± 0.003	4.80 ± 0.14	3.75 ± 0.17	0.65 ± 0.18	0.40 ± 0.05	0.51 ± 0.15	0.51 ± 0.25
Abell3695	308.7049	-35.8230	0.078 ± 0.012	6.46 ± 0.44	5.91 ± 0.63	0.60 ± 0.25	0.24 ± 0.11	0.27 ± 0.18	0.27 ± 0.20
Abell3827	330.4726	-59.9461	0.101 ± 0.001	7.67 ± 0.16	7.65 ± 0.26	1.84 ± 0.61	0.43 ± 0.04	0.36 ± 0.10	0.36 ± 0.17
Abell3866	335.1400	-35.1650	0.160 ± 0.005	4.37 ± 0.29	3.05 ± 0.32	0.35 ± 0.10	0.50 ± 0.08	0.39 ± 0.11	0.38 ± 0.17
Abell3921	342.4893	-64.4294	0.096 ± 0.002	6.34 ± 0.22	5.69 ± 0.31	0.77 ± 0.27	0.43 ± 0.05	0.40 ± 0.11	0.40 ± 0.19
CIZAJ0107.7+5408	16.9138	54.1375	0.119 ± 0.005	9.44 ± 0.59	10.53 ± 1.04	1.38 ± 0.55	0.38 ± 0.07	0.22 ± 0.10	0.21 ± 0.17
CLJ1415+3612	213.7963	36.2010	1.038 ± 0.011	6.30 ± 0.49	3.23 ± 0.40	0.41 ± 0.07	0.76 ± 0.12	0.55 ± 0.14	0.53 ± 0.19
G000.44-41.83	316.0750	-41.3300	0.151 ± 0.007	6.06 ± 0.51	5.14 ± 0.68	0.63 ± 0.28	0.63 ± 0.13	0.70 ± 0.23	0.70 ± 0.17
G002.74-56.18	334.6721	-38.9047	0.141 ± 0.008	6.06 ± 0.38	5.17 ± 0.52	0.74 ± 0.23	0.41 ± 0.09	0.48 ± 0.13	0.48 ± 0.19
G003.90-59.41	338.6120	-37.7400	0.149 ± 0.007	9.77 ± 0.55	10.94 ± 0.98	1.32 ± 0.41	0.41 ± 0.08	0.39 ± 0.12	0.38 ± 0.46
G008.44-56.35	334.4421	-35.7228	0.148 ± 0.008	6.04 ± 0.51	5.12 ± 0.69	0.57 ± 0.23	0.43 ± 0.11	0.41 ± 0.18	0.40 ± 0.29

Table 4.3. continued.

Name	RA [deg]	Dec [deg]	$z_{\rm X}$	kT [keV]	M_{500} $[10^{14}\,M_{\odot}]$	$M_{\rm gas,500}$ $[10^{14}\,M_{\odot}]$	$Z_{\rm ew}$ $[Z_{\odot}]\,(0.4r_{500})$	$Z_{\rm mw}$ $[Z_{\odot}]\,(0.4r_{500})$	$Z_{\rm mw}$ $[Z_{\odot}]\,(r_{500})$
G049.33+44.38	245.1258	29.8897	0.104 ± 0.008	6.29 ± 0.48	5.59 ± 0.68	0.53 ± 0.30	0.41 ± 0.11	0.24 ± 0.14	0.22 ± 0.19
G086.45+15.29	294.5821	54.1573	0.273 ± 0.008	7.71 ± 0.60	7.03 ± 0.86	1.20 ± 0.25	0.51 ± 0.09	0.48 ± 0.12	0.47 ± 0.18
G114.33+64.87	198.7775	51.8242	0.272 ± 0.006	8.36 ± 0.39	7.99 ± 0.59	1.25 ± 0.30	0.35 ± 0.05	0.38 ± 0.09	0.38 ± 0.14
G115.71+17.52	336.6142	78.3200	0.360 ± 0.006	7.11 ± 0.56	5.88 ± 0.73	0.95 ± 0.14	0.49 ± 0.07	0.50 ± 0.12	0.49 ± 0.16
G139.59+24.18	95.4502	74.7013	0.274 ± 0.005	8.50 ± 0.52	8.20 ± 0.80	1.04 ± 0.19	0.45 ± 0.07	0.34 ± 0.10	0.26 ± 0.18
G163.72+53.53	155.6138	50.1045	0.166 ± 0.008	6.58 ± 0.49	5.81 ± 0.68	0.73 ± 0.20	0.35 ± 0.10	0.27 ± 0.12	0.26 ± 0.25
G165.08+54.11	155.9338	49.1381	0.145 ± 0.010	6.39 ± 0.44	5.61 ± 0.61	0.77 ± 0.18	0.40 ± 0.10	0.30 ± 0.14	0.26 ± 0.15
G167.65+17.64	99.5200	47.7917	0.188 ± 0.008	7.70 ± 0.72	7.35 ± 1.08	1.18 ± 0.28	0.42 ± 0.11	0.30 ± 0.14	0.19 ± 0.41
G171.94-40.65	48.2420	8.3708	0.293 ± 0.016	12.65 ± 1.25	15.19 ± 2.38	2.09 ± 0.47	0.43 ± 0.10	0.36 ± 0.13	0.36 ± 0.13
G172.88+65.32	167.9046	40.8339	0.070 ± 0.006	4.32 ± 0.31	3.14 ± 0.35	0.13 ± 0.08	0.31 ± 0.10	0.39 ± 0.18	0.39 ± 0.31
G226.17-21.91	88.2113	-21.0660	0.105 ± 0.008	5.81 ± 0.42	4.93 ± 0.56	0.83 ± 0.29	0.33 ± 0.09	0.46 ± 0.13	0.46 ± 0.30
G229.21-17.24	94.1020	-21.9430	0.157 ± 0.014	8.32 ± 0.74	8.45 ± 1.18	1.08 ± 0.31	0.29 ± 0.12	0.29 ± 0.14	0.29 ± 0.36
G241.74-30.88	83.2475	-37.0277	0.260 ± 0.011	9.48 ± 0.86	9.81 ± 1.41	1.29 ± 0.34	0.26 ± 0.09	0.28 ± 0.12	0.27 ± 0.21
G241.77-24.00	91.4663	-35.3073	0.142 ± 0.004	5.22 ± 0.29	4.08 ± 0.35	0.73 ± 0.13	0.49 ± 0.08	0.36 ± 0.11	0.27 ± 0.20
G244.69+32.49	146.3592	-8.6683	0.163 ± 0.010	5.40 ± 0.36	4.26 ± 0.45	0.65 ± 0.17	0.31 ± 0.09	0.37 ± 0.12	0.29 ± 0.21
G250.90-36.25	77.5542	-45.3247	0.202 ± 0.009	6.22 ± 0.49	5.21 ± 0.65	0.84 ± 0.17	0.33 ± 0.10	0.36 ± 0.14	0.36 ± 0.24
G253.47-33.72	81.4540	-47.2500	0.188 ± 0.011	6.31 ± 0.47	5.37 ± 0.64	0.72 ± 0.19	0.37 ± 0.11	0.44 ± 0.15	0.44 ± 0.17
G263.66-22.53	101.3713	-54.2291	0.153 ± 0.009	8.32 ± 0.61	8.47 ± 0.98	1.34 ± 0.41	0.30 ± 0.09	0.19 ± 0.13	0.17 ± 0.42
G264.41+19.48	150.0087	-30.2655	0.193 ± 0.009	7.51 ± 0.68	7.05 ± 1.01	0.62 ± 0.19	0.52 ± 0.12	0.70 ± 0.22	0.70 ± 0.22
G266.56-27.31	93.9667	-57.7810	0.958 ± 0.020	11.63 ± 0.66	8.91 ± 0.80	1.58 ± 0.15	0.40 ± 0.07	0.27 ± 0.11	0.25 ± 0.22
G269.31-49.87	52.1579	-55.7104	0.076 ± 0.006	5.12 ± 0.27	4.09 ± 0.34	0.45 ± 0.24	0.43 ± 0.10	0.38 ± 0.16	0.30 ± 0.18
G275.21+43.92	172.5875	-14.6028	0.100 ± 0.005	6.66 ± 0.31	6.12 ± 0.46	1.07 ± 0.33	0.46 ± 0.08	0.53 ± 0.16	0.53 ± 0.16
G280.19+47.81	177.4400	-12.3140	0.150 ± 0.007	7.28 ± 0.78	6.86 ± 1.16	0.80 ± 0.32	0.42 ± 0.13	0.47 ± 0.20	0.47 ± 0.15
G284.99-23.70	110.8230	-73.4550	0.386 ± 0.011	9.25 ± 1.03	8.77 ± 1.54	1.68 ± 0.37	0.51 ± 0.11	0.33 ± 0.16	0.32 ± 0.13
G294.66-37.02	45.9712	-77.8707	0.284 ± 0.011	10.08 ± 0.88	10.67 ± 1.48	1.48 ± 0.43	0.35 ± 0.09	0.33 ± 0.12	0.33 ± 1.09
G295.33+23.33	183.8700	-39.0297	0.119 ± 0.008	5.95 ± 0.45	5.07 ± 0.60	0.85 ± 0.25	0.28 ± 0.08	0.33 ± 0.16	0.33 ± 0.15
G313.87-17.10	240.4588	-75.7494	0.160 ± 0.007	9.83 ± 0.64	10.98 ± 1.13	1.46 ± 0.36	0.45 ± 0.08	0.51 ± 0.12	0.51 ± 0.24
G325.70+17.31	221.9054	-40.3306	0.302 ± 0.014	10.24 ± 1.10	10.82 ± 1.84	1.28 ± 0.31	0.35 ± 0.11	0.36 ± 0.11	0.36 ± 0.19
G332.88-19.28	273.3396	-61.4633	0.144 ± 0.007	9.23 ± 0.93	10.02 ± 1.59	0.93 ± 0.43	0.60 ± 0.14	0.49 ± 0.18	0.49 ± 0.13
Hercules	252.7838	4.9925	0.155 ± 0.002	5.72 ± 0.14	4.68 ± 0.18	0.32 ± 0.10	0.63 ± 0.04	0.39 ± 0.07	0.38 ± 0.18

Table 4.3. continued.

Name	RA [deg]	Dec [deg]	$z_{\rm X}$	kT [keV]	M_{500} $[10^{14}\,M_\odot]$	$M_{\rm gas,500}$ $[10^{14}M_\odot]$	$Z_{\rm ew}$ $[Z_\odot]\,(0.4r_{500})$	$Z_{\rm mw}$ $[Z_\odot]\,(0.4r_{500})$	$Z_{\rm mw}$ $[Z_\odot]\,(r_{500})$
Hydra	139.5245	-12.0949	0.061 ± 0.002	3.91 ± 0.06	2.70 ± 0.06	0.40 ± 0.09	0.64 ± 0.03	0.54 ± 0.10	0.52 ± 0.32
IRAS09104+4109	138.4397	40.9415	0.441 ± 0.004	8.60 ± 0.48	7.57 ± 0.67	1.64 ± 0.33	0.62 ± 0.06	0.47 ± 0.13	0.47 ± 0.19
MACSJ0011.7-1523	2.9285	-15.3890	0.376 ± 0.007	7.36 ± 0.46	6.16 ± 0.61	0.82 ± 0.19	0.37 ± 0.06	0.34 ± 0.08	0.34 ± 0.13
MACSJ0035.4-2015	8.8604	-20.2632	0.361 ± 0.017	7.84 ± 0.58	6.86 ± 0.80	1.12 ± 0.22	0.39 ± 0.09	0.35 ± 0.10	0.35 ± 0.16
MACSJ0159.8-0849	29.9554	-8.8333	0.408 ± 0.007	10.39 ± 0.53	10.41 ± 0.84	1.34 ± 0.28	0.50 ± 0.08	0.26 ± 0.10	0.23 ± 0.07
MACSJ0242.5-2132	40.6495	-21.5407	0.314 ± 0.007	5.96 ± 0.53	4.57 ± 0.64	0.66 ± 0.17	0.53 ± 0.09	0.16 ± 0.17	0.06 ± 0.18
MACSJ0257.1-2325	44.2873	-23.4348	0.514 ± 0.061	10.70 ± 1.03	10.22 ± 1.56	1.71 ± 0.43	0.13 ± 0.11	0.17 ± 0.14	0.15 ± 0.14
MACSJ0257.6-2209	44.4223	-22.1549	0.350 ± 0.013	8.62 ± 0.92	8.01 ± 1.35	0.79 ± 0.22	0.49 ± 0.13	0.40 ± 0.16	0.39 ± 0.15
MACSJ0308.9+2645	47.2329	26.7611	0.330 ± 0.013	10.11 ± 0.82	10.44 ± 1.34	1.43 ± 0.28	0.39 ± 0.10	0.35 ± 0.14	0.34 ± 0.18
MACSJ0329.6-0211	52.4234	-2.1965	0.457 ± 0.005	8.05 ± 0.45	6.75 ± 0.60	1.26 ± 0.17	0.59 ± 0.06	0.46 ± 0.10	0.45 ± 0.30
MACSJ0429.6-0253	67.4000	-2.8853	0.400 ± 0.007	7.14 ± 0.73	5.78 ± 0.94	0.80 ± 0.12	0.59 ± 0.10	0.47 ± 0.14	0.46 ± 0.10
MACSJ0520.7-1328	80.1750	-13.4799	0.342 ± 0.010	8.67 ± 1.05	8.13 ± 1.56	0.92 ± 0.35	0.64 ± 0.13	0.40 ± 0.19	0.39 ± 0.17
MACSJ0647.7+7015	101.9603	70.2483	0.572 ± 0.046	9.53 ± 1.01	8.22 ± 1.38	1.25 ± 0.21	0.25 ± 0.11	0.36 ± 0.16	0.35 ± 0.14
MACSJ0744.8+3927	116.2201	39.4576	0.693 ± 0.012	8.50 ± 0.51	6.38 ± 0.61	1.10 ± 0.13	0.42 ± 0.08	0.22 ± 0.10	0.19 ± 0.15
MACSJ0947.2+7623	146.8029	76.3874	0.355 ± 0.002	7.68 ± 0.29	6.66 ± 0.39	0.84 ± 0.15	0.51 ± 0.04	0.40 ± 0.08	0.39 ± 0.11
MACSJ1115.8+0129	168.9661	1.4990	0.360 ± 0.006	8.15 ± 0.37	7.30 ± 0.53	1.07 ± 0.19	0.45 ± 0.05	0.41 ± 0.10	0.39 ± 0.27
MACSJ1149.5+2223	177.3970	22.4027	0.528 ± 0.007	9.85 ± 0.36	8.90 ± 0.51	1.59 ± 0.15	0.33 ± 0.04	0.30 ± 0.06	0.29 ± 0.18
MACSJ1206.2-0847	181.5511	-8.8006	0.468 ± 0.016	11.29 ± 1.30	11.45 ± 2.09	2.18 ± 0.44	0.44 ± 0.11	0.39 ± 0.12	0.39 ± 0.21
MACSJ1311.0-0310	197.7565	-3.1771	0.491 ± 0.006	5.95 ± 0.30	4.10 ± 0.33	0.50 ± 0.08	0.48 ± 0.06	0.45 ± 0.08	0.44 ± 0.22
MACSJ1423.8+2404	215.9496	24.0784	0.545 ± 0.003	7.90 ± 0.33	6.22 ± 0.41	0.66 ± 0.11	0.56 ± 0.04	0.39 ± 0.09	0.31 ± 0.29
MACSJ1427.2+4407	216.8174	44.1251	0.477 ± 0.008	8.57 ± 0.70	7.36 ± 0.95	0.89 ± 0.15	0.55 ± 0.08	0.46 ± 0.13	0.45 ± 0.08
MACSJ1427.6-2521	216.9143	-25.3508	0.313 ± 0.007	5.84 ± 0.50	4.44 ± 0.60	0.36 ± 0.12	0.48 ± 0.09	0.51 ± 0.12	0.51 ± 0.41
MACSJ1532.8+3021	233.2244	30.3498	0.360 ± 0.001	6.40 ± 0.13	4.97 ± 0.17	0.91 ± 0.12	0.49 ± 0.03	0.40 ± 0.05	0.39 ± 0.13
MACSJ1621.3+3810	245.3536	38.1690	0.475 ± 0.007	9.96 ± 0.58	9.35 ± 0.86	0.78 ± 0.16	0.52 ± 0.06	0.36 ± 0.09	0.30 ± 0.12
MACSJ1720.2+3536	260.0700	35.6071	0.387 ± 0.005	7.15 ± 0.44	5.83 ± 0.57	0.77 ± 0.12	0.50 ± 0.06	0.40 ± 0.11	0.39 ± 0.10
MACSJ1931.8-2634	292.9569	-26.5760	0.351 ± 0.002	7.44 ± 0.22	6.35 ± 0.30	0.99 ± 0.16	0.51 ± 0.03	0.48 ± 0.08	0.47 ± 0.12
MACSJ2046.0-3430	311.5022	-34.5049	0.425 ± 0.006	5.15 ± 0.30	3.40 ± 0.31	0.49 ± 0.08	0.45 ± 0.07	0.29 ± 0.09	0.27 ± 0.30
MACSJ2129.4-0741	322.3591	-7.6908	0.577 ± 0.017	9.59 ± 1.04	8.27 ± 1.42	1.34 ± 0.24	0.57 ± 0.13	0.64 ± 0.18	0.64 ± 0.22
MACSJ2135.2-0102	323.7976	-1.0479	0.315 ± 0.012	9.35 ± 0.87	9.30 ± 1.36	0.81 ± 0.14	0.58 ± 0.12	0.42 ± 0.14	0.42 ± 0.47
MACSJ2211.7-0349	332.9413	-3.8301	0.347 ± 0.011	8.79 ± 0.75	8.28 ± 1.12	1.48 ± 0.27	0.53 ± 0.10	0.44 ± 0.14	0.44 ± 0.17

Table 4.3. continued.

Name	RA [deg]	Dec [deg]	$z_{\rm X}$	kT [keV]	M_{500} $[10^{14}\,M_{\odot}]$	$M_{\rm gas,500}$ $[10^{14}\,M_{\odot}]$	$Z_{\rm ew}$ $[Z_{\odot}]\,(0.4r_{500})$	$Z_{\rm mw}$ $[Z_{\odot}]\,(0.4r_{500})$	$Z_{\rm mw}$ $[Z_{\odot}]\,(r_{500})$
MACSJ2214.9-1359	333.7385	-14.0030	0.484 ± 0.016	8.66 ± 0.85	7.45 ± 1.16	1.33 ± 0.22	0.46 ± 0.11	0.52 ± 0.16	0.52 ± 0.30
MACSJ2229.7-2755	337.4382	-27.9264	0.331 ± 0.005	5.19 ± 0.25	3.63 ± 0.28	0.50 ± 0.13	0.66 ± 0.07	0.62 ± 0.13	0.62 ± 0.22
MACSJ2243.3-0935	340.8393	-9.5958	0.443 ± 0.016	10.48 ± 0.64	10.34 ± 1.00	1.61 ± 0.17	0.28 ± 0.07	0.24 ± 0.07	0.24 ± 0.19
MACSJ2245.0+2637	341.2695	26.6345	0.297 ± 0.007	6.20 ± 0.52	4.92 ± 0.65	0.51 ± 0.20	0.73 ± 0.12	0.58 ± 0.17	0.57 ± 0.32
MS0015.9+1609	4.6396	16.4358	0.558 ± 0.008	8.90 ± 0.64	7.45 ± 0.85	1.48 ± 0.18	0.47 ± 0.08	0.39 ± 0.11	0.28 ± 0.19
MS2137.3-2353	325.0633	-23.6612	0.314 ± 0.001	6.68 ± 0.14	5.48 ± 0.19	0.69 ± 0.11	0.54 ± 0.03	0.44 ± 0.06	0.44 ± 0.21
PKS0745-191	116.8798	-19.2946	0.103 ± 0.003	8.30 ± 0.30	8.66 ± 0.49	1.42 ± 0.31	0.49 ± 0.04	0.20 ± 0.04	0.07 ± 0.19
RCS2327.4-0204	351.8653	-2.0772	0.698 ± 0.018	9.07 ± 0.36	7.05 ± 0.45	1.18 ± 0.16	0.32 ± 0.06	0.21 ± 0.08	0.19 ± 0.41
RXJ0043.4-2037	10.8523	-20.6247	0.294 ± 0.008	8.51 ± 0.55	8.11 ± 0.82	1.16 ± 0.39	0.49 ± 0.09	0.47 ± 0.15	0.47 ± 0.26
RXJ0118.1-2658	19.5472	-26.9662	0.218 ± 0.013	7.61 ± 0.69	7.11 ± 1.01	0.91 ± 0.23	0.49 ± 0.12	0.40 ± 0.15	0.38 ± 0.08
RXJ0220.9-3829	35.2357	-38.4802	0.229 ± 0.006	5.13 ± 0.35	3.79 ± 0.41	0.36 ± 0.14	0.81 ± 0.13	0.63 ± 0.21	0.62 ± 0.30
RXJ0232.2-4420	38.0774	-44.3467	0.299 ± 0.009	11.44 ± 1.19	12.92 ± 2.11	1.72 ± 0.28	0.66 ± 0.14	0.45 ± 0.14	0.45 ± 0.15
RXJ0237.4-2630	39.3651	-26.5079	0.224 ± 0.005	6.51 ± 0.41	5.52 ± 0.55	0.69 ± 0.17	0.73 ± 0.11	0.68 ± 0.14	0.68 ± 0.16
RXJ0307.0-2840	46.7582	-28.6657	0.245 ± 0.008	8.92 ± 0.95	8.98 ± 1.52	1.26 ± 0.25	0.43 ± 0.10	0.44 ± 0.16	0.43 ± 0.26
RXJ0331.1-2100	52.7747	-21.0087	0.193 ± 0.004	5.49 ± 0.35	4.30 ± 0.43	0.56 ± 0.11	0.67 ± 0.08	0.46 ± 0.14	0.40 ± 0.20
RXJ0336.3-4037	54.0644	-40.6291	0.176 ± 0.005	5.77 ± 0.35	4.70 ± 0.45	0.56 ± 0.16	0.59 ± 0.10	0.62 ± 0.14	0.62 ± 0.14
RXJ0439.0+0520	69.7592	5.3455	0.203 ± 0.004	4.88 ± 0.23	3.55 ± 0.26	0.38 ± 0.07	0.66 ± 0.07	0.57 ± 0.12	0.56 ± 0.16
RXJ0439.0+0715	69.7529	7.2684	0.254 ± 0.007	7.25 ± 0.55	6.45 ± 0.77	1.08 ± 0.23	0.54 ± 0.10	0.48 ± 0.12	0.46 ± 0.10
RXJ0547.6-3152	86.9058	-31.8688	0.166 ± 0.012	7.31 ± 0.48	6.86 ± 0.71	0.80 ± 0.24	0.35 ± 0.08	0.34 ± 0.11	0.34 ± 0.31
RXJ1144.0+0547	176.0283	5.7982	0.095 ± 0.007	4.53 ± 0.34	3.34 ± 0.39	0.25 ± 0.13	0.40 ± 0.10	0.44 ± 0.19	0.43 ± 0.26
RXJ1459.4-1811	224.8706	-18.1793	0.233 ± 0.002	6.37 ± 0.22	5.31 ± 0.29	0.95 ± 0.22	0.65 ± 0.05	0.62 ± 0.14	0.57 ± 0.13
RXJ1504.1-0248	226.0308	-2.8041	0.219 ± 0.001	7.52 ± 0.10	6.97 ± 0.15	1.14 ± 0.12	0.41 ± 0.01	0.40 ± 0.04	0.39 ± 0.14
RXJ1524.2-3154	231.0534	-31.9061	0.102 ± 0.001	4.55 ± 0.13	3.36 ± 0.15	0.49 ± 0.13	0.56 ± 0.03	0.14 ± 0.07	0.04 ± 0.18
RXJ1558.3-1410	239.5908	-14.1666	0.098 ± 0.001	5.21 ± 0.09	4.17 ± 0.12	0.85 ± 0.15	0.64 ± 0.03	0.47 ± 0.08	0.47 ± 0.19
RXJ1720.1+2638	260.0414	26.6257	0.162 ± 0.002	6.63 ± 0.16	5.89 ± 0.22	0.72 ± 0.12	0.53 ± 0.03	0.50 ± 0.07	0.50 ± 0.16
RXJ1750.2+3505	267.5705	35.0829	0.162 ± 0.004	5.65 ± 0.43	4.57 ± 0.55	0.36 ± 0.13	0.58 ± 0.09	0.39 ± 0.13	0.38 ± 0.26
RXJ2014.8-2430	303.7156	-24.5062	0.153 ± 0.002	6.74 ± 0.22	6.07 ± 0.31	0.88 ± 0.20	0.53 ± 0.04	0.38 ± 0.12	0.37 ± 0.20
RXJ2129.6+0005	322.4158	0.0895	0.246 ± 0.005	7.68 ± 0.36	7.10 ± 0.52	1.19 ± 0.17	0.46 ± 0.05	0.45 ± 0.09	0.45 ± 0.14
SPT-CLJ0000-5748	0.2499	-57.8095	0.695 ± 0.008	7.06 ± 0.52	4.75 ± 0.56	0.56 ± 0.09	0.62 ± 0.08	0.43 ± 0.11	0.39 ± 0.16
SPT-CLJ2043-5035	310.8234	-50.5921	0.724 ± 0.008	5.75 ± 0.33	3.37 ± 0.30	0.62 ± 0.08	0.48 ± 0.06	0.42 ± 0.09	0.42 ± 0.12

Table 4.3. continued.

Name	RA [deg]	Dec [deg]	$z_{\rm X}$	kT [keV]	M_{500} $[10^{14}\,M_\odot]$	$M_{\rm gas,500}$ $[10^{14}\,M_\odot]$	$Z_{\rm ew}$ $[Z_\odot]\,(0.4r_{500})$	$Z_{\rm mw}$ $[Z_\odot]\,(0.4r_{500})$	$Z_{\rm mw}$ $[Z_\odot]\,(r_{500})$
SPT-CLJ2331-5051	352.9580	-50.8640	0.599 ± 0.009	7.98 ± 0.58	6.11 ± 0.70	0.76 ± 0.10	0.43 ± 0.07	0.16 ± 0.10	0.12 ± 0.10
SPT-CLJ2344-4242	356.1834	-42.7202	0.602 ± 0.002	11.52 ± 0.26	10.89 ± 0.39	1.71 ± 0.24	0.56 ± 0.02	0.54 ± 0.05	0.54 ± 0.14
Triangulum	249.5710	-64.3579	0.049 ± 0.001	9.45 ± 0.15	10.92 ± 0.28	1.41 ± 0.78	0.24 ± 0.02	0.31 ± 0.09	0.31 ± 0.31
Zwicky0808	45.4091	1.9205	0.172 ± 0.004	5.08 ± 0.30	3.84 ± 0.36	0.36 ± 0.14	0.52 ± 0.08	0.36 ± 0.13	0.35 ± 0.27
Zwicky1358	209.9605	62.5179	0.325 ± 0.004	10.76 ± 0.65	11.54 ± 1.09	1.16 ± 0.31	0.69 ± 0.11	0.49 ± 0.13	0.49 ± 0.26
Zwicky2089	135.1537	20.8943	0.238 ± 0.002	4.51 ± 0.16	3.08 ± 0.17	0.41 ± 0.07	0.47 ± 0.04	0.30 ± 0.09	0.27 ± 0.13
Zwicky2701	148.2050	51.8848	0.214 ± 0.001	5.15 ± 0.11	3.84 ± 0.13	0.74 ± 0.13	0.57 ± 0.03	0.43 ± 0.07	0.42 ± 0.14
Zwicky3146	155.9151	4.1865	0.296 ± 0.003	7.93 ± 0.20	7.25 ± 0.28	1.12 ± 0.26	0.45 ± 0.03	0.41 ± 0.07	0.40 ± 0.18
Zwicky5029	184.4280	3.6610	0.087 ± 0.006	6.71 ± 0.26	6.24 ± 0.39	0.91 ± 0.30	0.37 ± 0.07	0.33 ± 0.11	0.33 ± 0.20
Zwicky7160	224.3128	22.3429	0.258 ± 0.002	5.15 ± 0.11	3.74 ± 0.12	0.47 ± 0.12	0.53 ± 0.03	0.41 ± 0.07	0.38 ± 0.19

Chapter 5

The multiple merging processes in the galaxy cluster Abell 2142

Ang Liu[1,2,3,4], Heng Yu[1], Antonaldo Diaferio[5,6], Paolo Tozzi[2,1], Ho Seong Hwang[7], Keiichi Umetsu[8], Nobuhiro Okabe[9,10,11], and Lilan Yang[1,12]

1. *Department of Astronomy, Beijing Normal University, Beijing, China*
2. *INAF Osservatorio Astrofisico di Arcetri, Firenze, Italy*
3. *Department of Physics, Sapienza University of Rome, Rome, Italy*
4. *Department of Physics, University of Rome Tor Vergata, Rome, Italy*
5. *Dipartimento di Fisica, Università di Torino, Torino, Italy*
6. *Istituto Nazionale di Fisica Nucleare (INFN), Sezione di Torino, Torino, Italy*
7. *Quantum Universe Center, Korea Institute for Advanced Study, Seoul, Korea*
8. *Institute of Astronomy and Astrophysics, Academia Sinica, Taipei, Taiwan*
9. *Department of Physical Science, Hiroshima University, Hiroshima, Japan*
10. *Hiroshima Astrophysical Science Center, Hiroshima University, Hiroshima, Japan*
11. *Core Research for Energetic Universe, Hiroshima University, Hiroshima, Japan*
12. *School of Physics and Technology, Wuhan University, Wuhan, China*

(The Astrophysical Journal, Volume 863, Page 102.)

Abstract

To investigate the dynamics of the galaxy cluster A2142, we compile an extended catalog of 2239 spectroscopic redshifts of sources, including newly measured 237 redshifts, within 30 arcmin from the cluster center. With the

σ-plateau algorithm from the caustic method, we identify 868 members and a number of substructures in the galaxy distribution both in the outskirts, out to $\sim$3.5 Mpc from the cluster center, and in the central region. In the outskirts, one substructure overlaps a falling clump of gas previously identified in the X-ray band. These substructures suggests the presence of multiple minor mergers, which are responsible for the complex dynamics of A2142, and the absence of recent or ongoing major mergers. We show that the distribution of the galaxies in the cluster core and in several substructures are consistent with the mass distribution inferred from the weak lensing signal. Moreover, we use spatially-resolved X-ray spectroscopy to measure the redshift of different regions of the intracluster medium within $\sim$3 arcmin from the cluster center. We find a ring of gas near the two X-ray cold fronts identified in previous analyses and measure a velocity of this ring of $810 \pm 330 \mathrm{kms}^{-1}$ larger than the cluster mean velocity. Our analysis suggests the presence of another ring surrounding the core, whose velocity is $660 \pm 300 \mathrm{kms}^{-1}$ larger than the cluster velocity. These X-ray features are not associated to any optical substructures, and support the core-sloshing scenario suggested in previous work.

5.1 Introduction

Galaxy clusters link the evolution of the large-scale structure to the astrophysical processes on smaller scales, and the study of their assembling is thus crucial to understand the hierarchical evolution of the Universe. The commonly accepted scenario is that clusters form and evolve via accretion and merging of smaller halos. This scenario is suggested by many dynamical features observed in clusters: substructures in the galaxy distribution [120, 393, 139, 131, 405]; apparent global rotation of clusters [157, 205]; clumpy distributions [144, 267, 266] and bow shocks [214, 215] in the intracluster medium (ICM) observed in X-rays; the elongated or peculiar distributions of radio emission [104, 134, 298, 290]; the substructure distribution of the dark matter, inferred from gravitational lensing observations [259, 257, 136, 43]. In addition, 'cold fronts' are frequently observed in X-ray images of clusters [219, 317, 316, 159], including some regular and relaxed clusters [225, 52]. Cold fronts are X-ray surface brightness edges with approximately continuous pressure profile across the density discontinuity,

at odds with the large pressure jump of shock fronts.

The massive cluster A2142 is one of the most representative clusters with cold fronts. Its *Chandra* image exhibits an elongated X-ray morphology, and two prominent cold fronts in the opposite directions along the longest axis [219]. The scenario of A2142, suggested by these observational features, was at first envisioned as a pericentric merging of two subclusters, with the two cold fronts delineating the subcluster cores that have survived the merging. This hypothesis was denoted the 'remnant core' scenario [219], and is appropriate for merging clusters with prominent signatures of recent or ongoing mergers. However, A2142 shows an almost regular morphology and appears relaxed at large radii, unlike 1E 0657-56 [214], A520 [133, 215, 72], and other clusters with cold fronts, which clearly appear unrelaxed. Therefore, [371, 217, 263] proposed an alternative model, where the observed cold fronts derive from a sloshing cool core [218, 50].

More recently, another cold front in A2142, at about 1 Mpc from the center to the southeast, was discovered with XMM-Newton observations [304], showing that the sloshing in A2142 is not confined to the core, but extends to much larger scales. In addition, both XMM-Newton [86] and *Chandra* [87] detected a falling clump of hot gas in the outskirts, suggesting that the merging process is still ongoing. Two giant radio halos possibly involved with the sloshing of the cluster core were also revealed by LOFAR and VLA observations [386].

Additional information on the complex dynamics of A2142 derives from the optical band. The presence of substructures in the galaxy distribution was first pointed out by Oegerle et al. (1995) [255] with 103 spectroscopically confirmed galaxies. Based on the spectroscopic redshifts of 956 member galaxies, Owers et al. (2011) [263] concluded that some earlier minor mergers can have induced the sloshing of the core in A2142. More recently, Einasto et al. (2017) [90] suggested that A2142 formed through past and present mergers of smaller groups, determining the complex radio and X-ray structure observed in this cluster.

All these increasingly rich observational data in different bands provide relevant details of the dynamics of A2142 that, when combined, can further clarify the scenario of the formation of A2142. Here, we provide a step

forward in this direction, by combining the information provided by the optical and X-ray spectroscopy and by the dark matter distribution reconstructed from weak-lensing data. The three methods are complementary, and their combination helps to better understand the assembly history of the cluster and to understand the possible systematic errors of each method [156].

The hierarchical tree method based on optical spectroscopy for the investigation of substructures in galaxy clusters was introduced by Serna et al. (1996) [335]. Diaferio et al. (1999) [73] and Serra et al. (2011) [337] improved this approach by developing the σ-plateau algorithm for the automatic identification of a threshold to trim the hierarchical tree and identify the cluster substructures. The σ-plateau algorithm is part of the caustic method [74, 73] that estimates the mass profile of galaxy clusters out to regions well beyond the virial radius [337] and identifies the galaxies members of the cluster [336]. Yu et al. (2015) [403] investigate in detail the performance of the σ-plateau algorithm to identify the substructures in the distribution of the cluster galaxies. Substructure properties, including their redshift, velocity dispersion, and morphology, can provide relevant information on the dynamics of the cluster.

In addition to the optical information, fitting the position of the iron K_α line in the X-ray spectrum coming from a defined region of the ICM provides an accurate measure of its redshift [78, 79, 81, 195]. By measuring the redshift of different ICM regions, one can infer a map of the radial velocities of the ICM, which, again, provides constraints on the modelling of the ICM dynamics: with this technique, Liu et al. (2016) [196] identified the presence of significant bulk motions in the ICM of A2142 at a 3σ confidence level.

The optical and spatially-resolved X-ray spectroscopy were successfully combined by Song et al. (2017) [348] to unveil the dynamical status of A2199. Here, we apply this new strategy to investigate the dynamics of A2142.

The paper is organized as follows. In Section 5.2, we describe our new and extended optical spectroscopic catalog. In Section 5.3, we identify the substructures in the galaxy distribution. In Section 5.4, we describe the spatially-resolved ICM redshift measurements. In Section 5.5, we present the method and results of the weak-lensing analysis, and in Section 5.6, we infer the dynamical state of A2142 by combining the information coming from our analyses of all the data. We present our conclusions in Section 5.7. Throughout

this paper, we adopt the 7 years *WMAP* cosmology, with $\Omega_{\rm m}$= 0.272, Ω_Λ = 0.728, and H_0 = 70.4 km s^{-1} Mpc^{-1} [176]. All the errors we mention are at 1σ confidence level.

5.2 Optical spectroscopic sample

We compile the currently largest catalog of 2239 spectroscopic redshifts in the field of view of A2142. Our catalog covers an area of $1^\circ \times 1^\circ$ around the cluster center, corresponding to an area 7×7 Mpc^2 at the cluster redshift $z = 0.09$; the redshifts in our catalog are in the range $[0.01, 0.6]$. Our catalog includes 1270 redshifts from the catalog of Owers et al. (2011) [263] which are not in the SDSS DR13 [332]; Owers et al.'s full catalog lists 1635 redshifts in the range $z = [0.0088, 3.8]$. In our sample, we include 731 additional redshifts from SDSS catalog and one redshift from Oegerle et al. (1995) [255]. In June 2014, to secure more redshifts, we made additional spectroscopic observations with the 300 fiber Hectospec multi-object spectrograph on the MMT 6.5m telescope [102]. To obtain a high, uniform spectroscopic completeness in the cluster region, we weighted the targets according to their r-band apparent magnitudes independently of colors. We used the 270 line mm^{-1} grating for Hectospec observations, which gives a dispersion of 1.2 Å pixel^{-1} and a resolution of $\sim$ 6 Å. The resulting spectra cover the wavelength range 3650–9150 Å. We observed one field with $\sim$250 target fibers for 3×20-minute exposures. The spectra were reduced with the pipeline of Mink et al. (2007) [241], and were cross-correlated with template spectra to determine the redshifts using RVSAO [179]. We visually inspected all the spectra, and assigned a quality flag to the spectral fits with 'Q' for high-quality redshifts, '?' for marginal cases, and 'X' for poor fits. We then use only the spectra with reliable redshift measurements (i.e., 'Q'). In total, we obtained 237 additional redshifts in the field.

Owers et al. [263] and Geller et al. [122, 123] show that there is basically no systematic bias, between MMT and SDSS sources; therefore, it is appropriate to merge the two data sets in the same catalog. As mentioned above, the catalog of Owers et al. [263] include redshifts that also appear in the SDSS catalog: we always choose the SDSS measures in this case, because their errors are smaller. In Figure 5.1, we show the spectroscopic completeness for

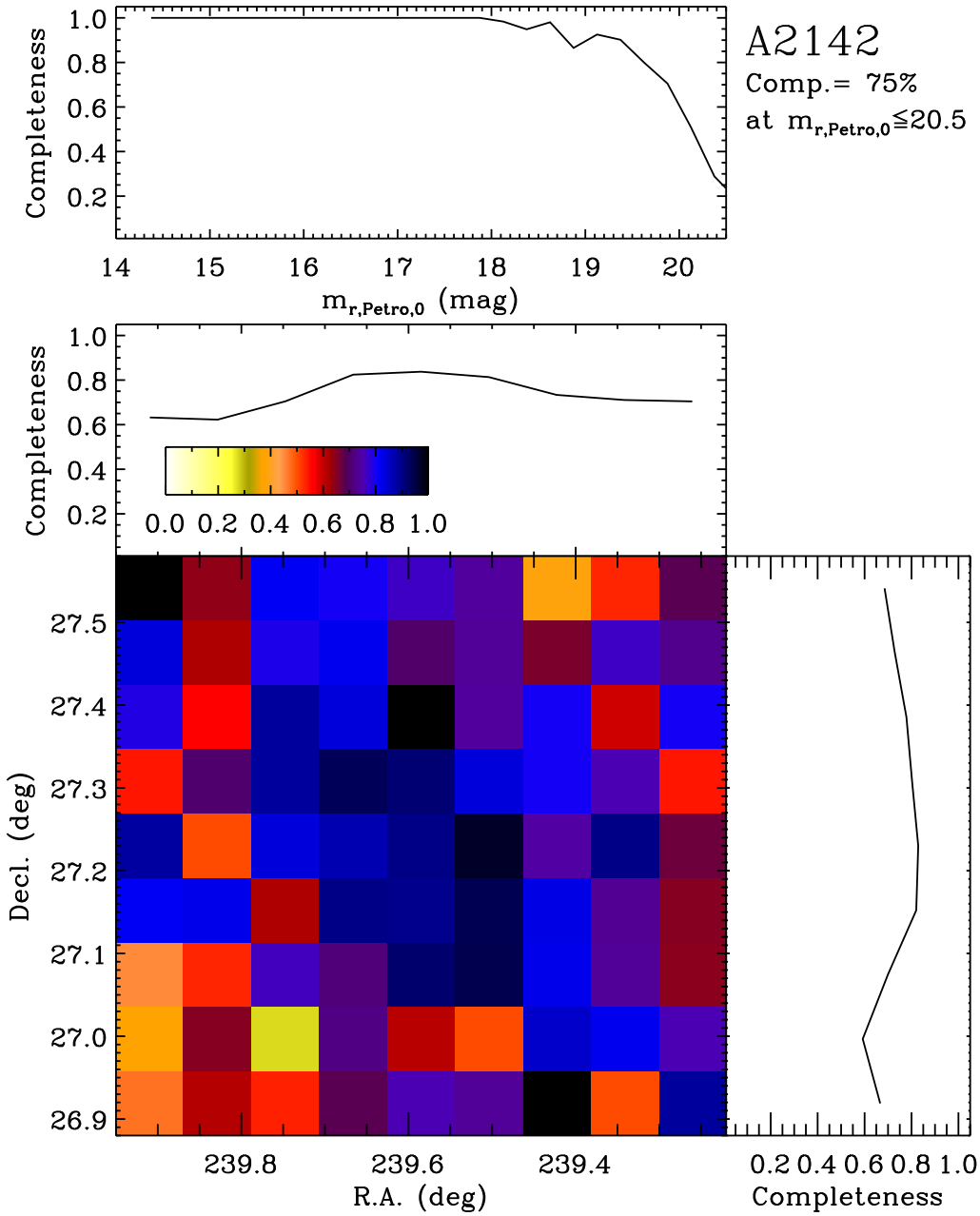

Figure 5.1. Spectroscopic completeness for $m_{\mathrm{r,Petro,0}} \leq 20.5$ in the field of A2142. The two-dimensional completeness map is in 9×9 pixels for the $42' \times 42'$ field of view. The overall completeness throughout this field is 75%, with a small spatial variation.

$m_{\mathrm{r,Petro,0}} \leq 20.5$. The two-dimensional completeness map is in 9×9 pixels for the $42' \times 42'$ field of view. The overall completeness throughout this field is 75%, with a small spatial variation.

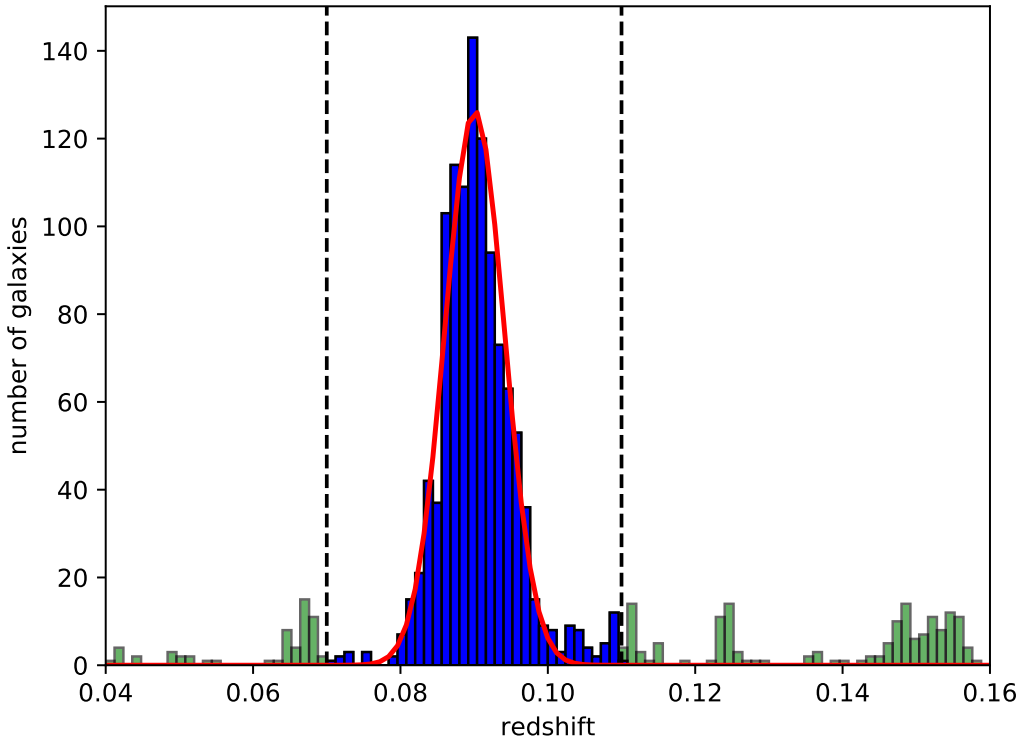

Figure 5.2. The redshift histogram of A2142. The green bars show the distribution of the field galaxies. The blue bars show the galaxies whose redshifts range from 0.07 to 0.11 (vertical dashed lines). The red solid line is the Gaussian fit result after the 3σ clipping [401].

A sample of the redshift catalog is given in Table 5.1. For each galaxy, the table contains the SDSS ObjID, right ascension R.A., declination Dec., r-band Petrosian magnitude with Galactic extinction correction from SDSS, the redshift z, the uncertainty in z, and the spectrum and redshift source. The full version of the table is available in the online journal.

Our catalog contains 604 redshifts in addition to the Owers et al. (2011) [263] catalog. Figure 5.2 shows the distribution of the redshifts in our catalog. There are 1117 redshifts in the range $z = [0.07, 0.11]$, out of which 63 were not in the Owers et al. [263] catalog. The 3σ clipping procedure [401] removes 50 galaxies and thus leaves 1067 galaxies as possible cluster members. The mean redshift and the redshift dispersion of these 1067 galaxies are 0.0901 ± 0.0001 and 0.0040, respectively.

Table 5.1. Redshift catalog in the fields of A2142. This table is available in its entirety in a machine-readable form in the online journal. A portion is shown here for guidance regarding its form and content. (1) MMT: This study; (2) Owers: [263]; (3) SDSS: SDSS DR13; (4) Oegerle:[255]; The SDSS ObjIDs starting with '12' and '58' come from SDSS DR13 and DR7, respectively.

SDSS ObjID	RA (deg)	Dec (deg)	$m_{\mathrm{r,Petro,0}}$ (mag)	z	σ_z	src.
1237662305125859528	239.0412	27.0026	16.950	0.0676	0.0001	SDSS
1237662339475571013	239.0415	27.2335	17.867	0.1898	0.0001	MMT
1237662339475571047	239.0428	27.1777	16.879	0.0965	0.0001	SDSS
1237662339475571048	239.0453	27.1748	20.041	0.0961	0.0002	Owers
1237662305662664876	239.0467	27.4428	18.429	0.1752	0.0001	MMT

5.3 Substructures in the galaxy distribution

For a quantitative investigation of the distribution of galaxies, we adopt the σ-plateau algorithm. To set up a familiar framework to our results, we also provide an analysis based on the Dressler-Shectman (DS) test, which is more commonly used in the literature.

5.3.1 Results from the σ-plateau algorithm

The σ plateau algorithm, implemented within the caustic method [74, 73, 337], is based on optical spectroscopic data and provides an extremely efficient procedure to identify both the cluster members [336] and the cluster substructures [403]. Unlike the DS method, which only suggests the presence of substructures but does not unambiguously identify them, the σ-plateau algorithm returns a list of the individual substructures and their members.

The method consists in a classical approach to cluster analysis for grouping sets of objects with similar properties. The caustic method groups the galaxies in the field of view in a binary tree according to an estimate of their pairwise binding energy, derived from the projected separation and the line-of-sight velocity difference of each galaxy pair.

The main branch of the binary tree is the path determined by the nodes of the tree which contain the largest number of galaxies, or leaves, at each

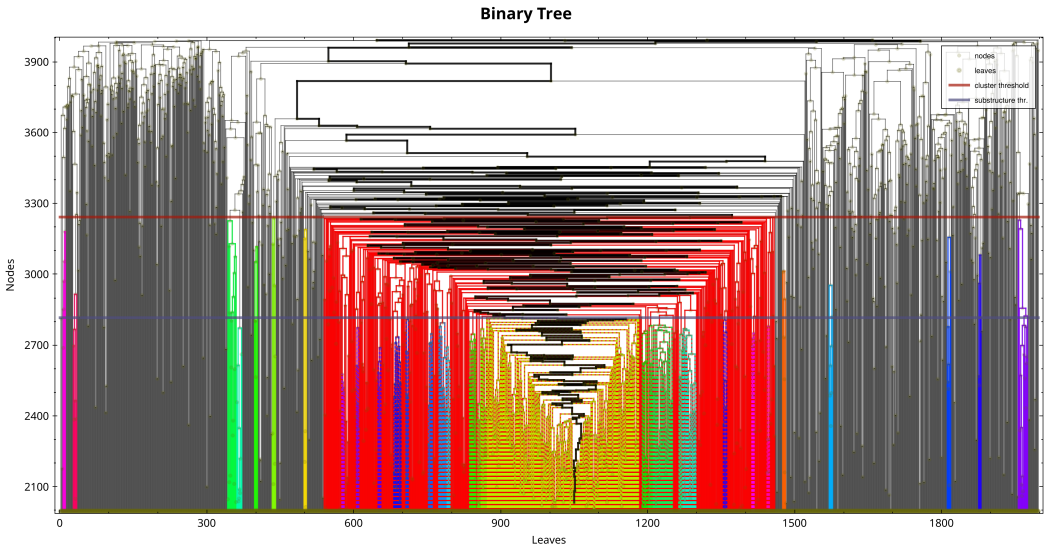

Figure 5.3. The binary tree (or *dendrogram*) of 1997 redshifts in the range [0.01, 1.0]. The two solid horizontal lines are the first and second thresholds. The colors indicate different structures. The red part corresponds to sub0 in Table 5.2. The heavy black line shows the main branch of the binary tree.

bifurcation. The velocity dispersion σ_i of the leaves of each node i decreases, on average, when walking along the main branch from the root to the leaves.

When the binary tree is built with the galaxies in a field of view containing a galaxy cluster (see Figure 5.3 for our redshift catalog of A2142), the velocity dispersion σ_i along the main branch settles onto a σ plateau in between two nodes, as shown in Figure 5.4, where we plot the velocity dispersion σ_i as a function of the main branch node of A2142. This plateau originates from the quasi-dynamical equilibrium of the cluster: the velocity dispersions σ_i of the nodes closer to the root (on the left of Figure 5.4) are larger than the plateau, because these nodes contain a large fraction of galaxies that are not cluster members; the velocity dispersions of the nodes closer to the leaves (on the right of Figure 5.4) are smaller than the plateau because, at this level, the binary tree splits the cluster into its dynamically distinct substructures.

The two boundary nodes of the plateau thus identify two thresholds that are used to cut the tree at two levels: the threshold closer to the root identifies the cluster members; the threshold closer to the leaves identifies the cluster substructures [336, 403]. All the systems with at least 6 galaxies below this second threshold enter our list of substructures. Here, as the minimum number

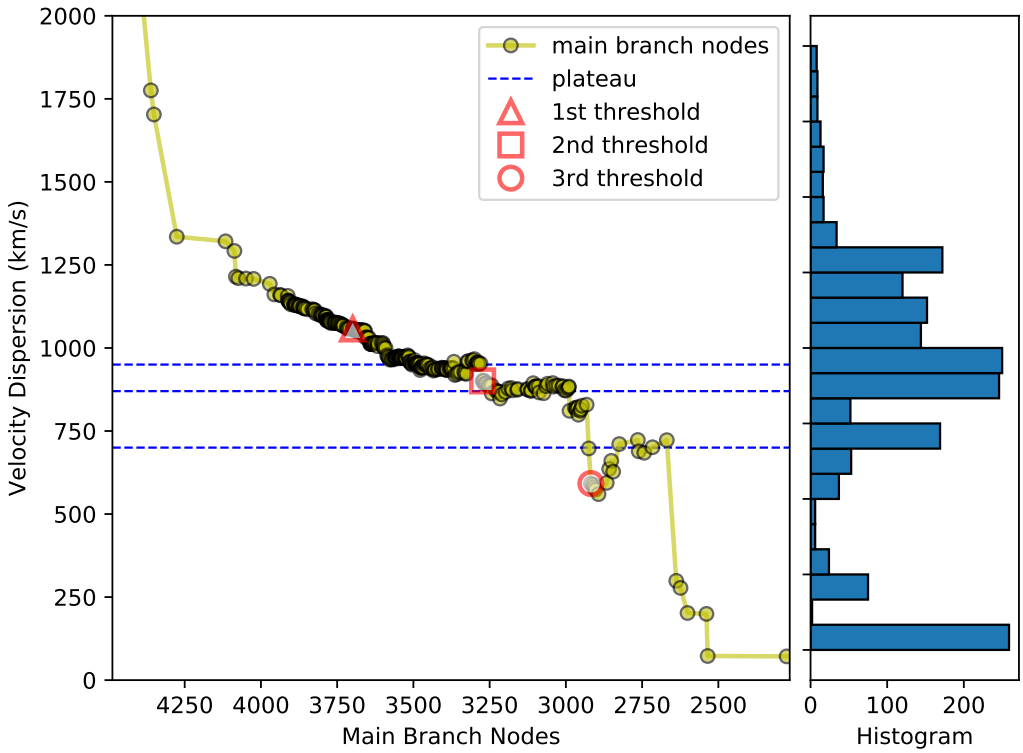

Figure 5.4. The velocity dispersion of the leaves of each node along the main branch of the binary tree of A2142. The histogram in the right panel shows the node numbers in different velocity dispersion bins. The blue dashed lines indicate the σ plateaus. The red symbols are the selected thresholds.

of substructure members, we adopt 6 galaxies, rather than 10 galaxies as chosen by [403], which appears to be too severe and can exclude real, albeit poor, substructures.

In the plot of the velocity dispersion along the main branch of the binary tree of A2142 shown in Figure 5.4 we can see three, rather than one, plateaus: this feature is typical of clusters with complex dynamics [403]. The left node, shown by the open red triangle, of the first plateau at $\sim$950 km s^{-1}, is the threshold that identifies the cluster. The left node, shown by the open red square, of the second plateau at $\sim$870 km s^{-1}, is the threshold that identifies the cluster substructures. The left node of the third plateau at $\sim$700 km s^{-1}, shown by the open red circle, further splits the cluster core into additional substructures, as we illustrate below.

The caustic method uses the galaxies identified by the first threshold only

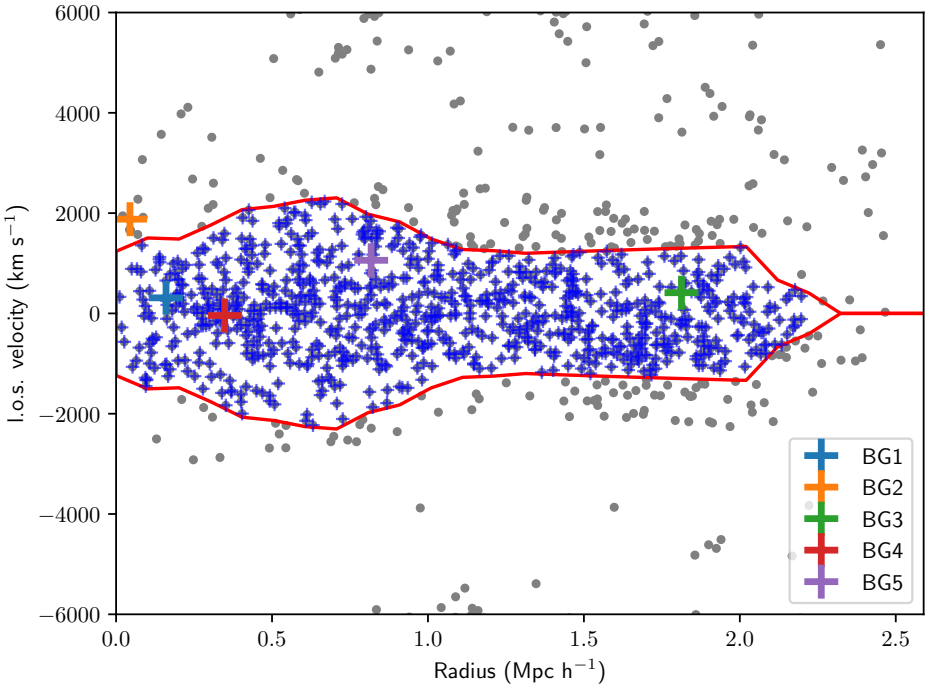

Figure 5.5. The redshift diagram of A2142. The solid lines show the caustic location. The blue crosses show the cluster members identified by the caustic method. We also show the location of the five brightest galaxies BG1−5.

to locate the celestial coordinates and the redshift of the cluster center. As discussed by Serra et al. [337, 336], once the cluster is the dominant system in the field of view, the selection of the cluster center is not strongly affected by the selection of the first threshold of the binary tree. To identify the cluster members, the method first locates the caustics in the cluster redshift diagram, the plane of the line-of-sight velocity of the galaxies and their projected separation from the cluster center (Figure 5.5). The caustics measure the galaxy escape velocity from the cluster, corrected by a function of the velocity anisotropy parameter (see [337] for details): the galaxies within the caustics are thus the members of the clusters. With this approach, we identify 868 galaxy members of A2142. This number is consistent with, albeit smaller than, the 1067 members identified with the 3σ clipping method (see Sect. 5.2), and the 956 members identified by Owers et al. [263] with the van Hartog and Katgert method [71]. The difference derives from the small fraction of interlopers

misidentified as members by the caustic method: on average, only 2% of the caustic members within the cluster virial radius actually are interlopers and only 8% within three times the virial radius are interlopers [336].

Table 5.2 summarizes the basic properties of the substructures, from sub0 to sub19, identified by the second threshold at ∼870 km s^{-1} shown in Figure 5.4. We also list the mean redshifts z_o of the substructures with their uncertainty $\mathrm{err}_z = v_{\mathrm{disp}}/\sqrt{N_{\mathrm{gal}}}$, where v_{disp} is the velocity dispersion and N_{gal} is the number of members of the substructure [160]. Within the substructure sub0, the third threshold at ∼700 km s^{-1} identifies, at a lower level of the hierarchical clustering, six additional substructures that we list as sub00 to sub05 in Table 5.2. To assess whether these substructures correspond to physical systems rather than being chance alignments of unrelated galaxies, below we will combine these results with results from additional probes, including X-ray emission and gravitational lensing measurements.

Here, we also consider the relation between these substructures and the top five brightest (r-band Petrosian magnitudes) galaxies in the cluster (labelled as BG1−5). They are all cluster members, except BG2. BG1 and BG2 are also well known Brightest Cluster Galaxies. As shown in Figures 5.6 and 5.7, the brightest one – BG1 – is in sub00, which is the core of the cluster. BG2 is a member of sub02 with a substantial velocity offset: its line-of-sight velocity is 312 km s^{-1} larger than the mean velocity of the members of sub02. The spiral galaxy BG3 is a member of sub17, a system in the outskirts of the cluster; unfortunately, this region is spectroscopically severely undersampled and we are unable to draw any solid conclusion. Finally, the elliptical galaxy BG4 and the interacting galaxy BG5 are members of sub04 and sub9, respectively. We will discuss the properties of sub9 and BG5 in Sect. 5.6.

5.3.2 Results from the Dressler-Schectman test

The Dressler-Shectman (DS) test is largely used for the investigation of cluster substructures when optical spectroscopic data are available [77, 277]. The test requires the identification of the N cluster members, which is usually obtained by removing the possible interlopers with the 3σ clipping procedure [401]. Around each cluster member i, we identify the $N_{\mathrm{local}} = \sqrt{N}$ closest neighbors

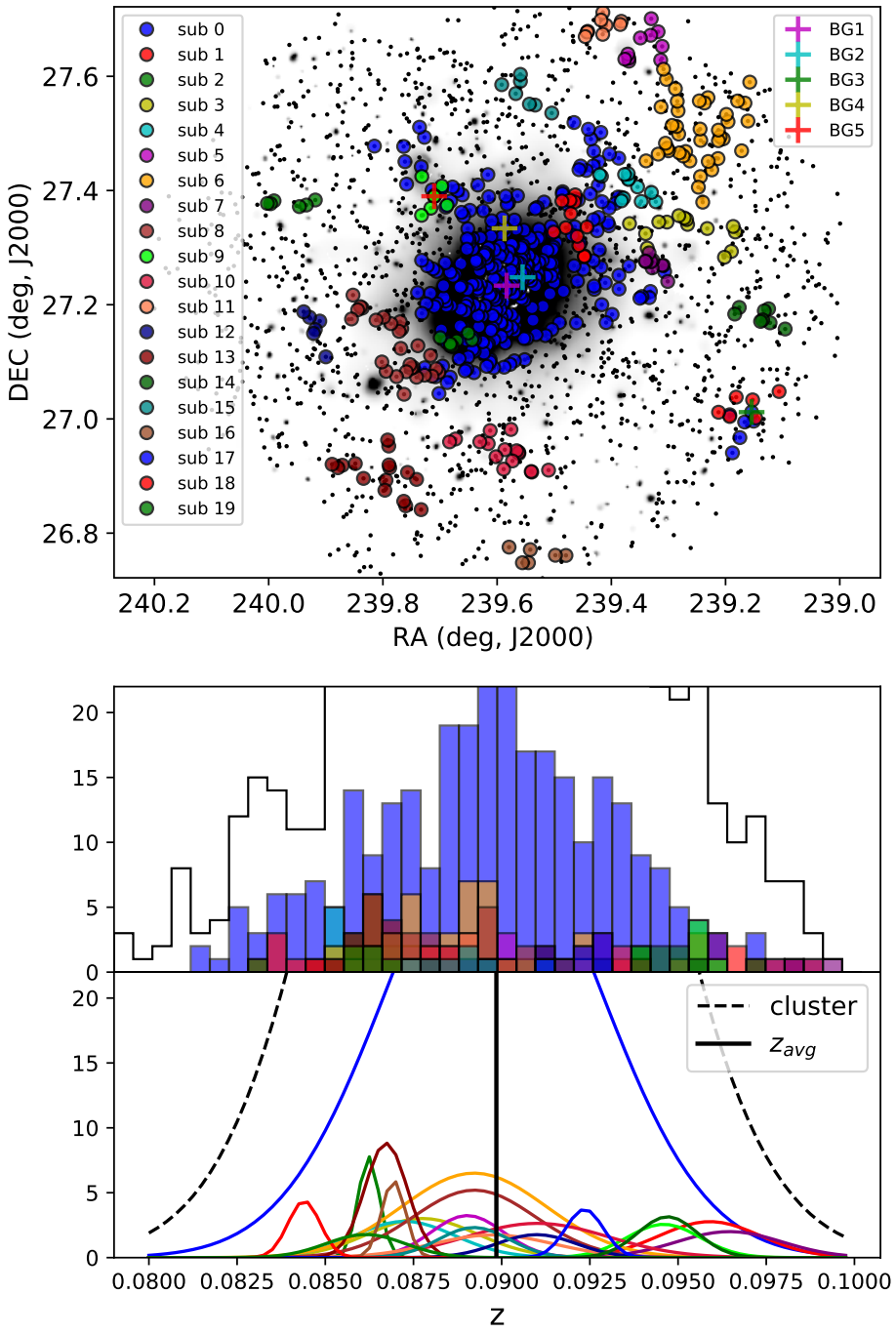

Figure 5.6. The upper panel shows the distribution on the sky of the A2142 substructures identified with the second threshold. The white contours and grey scale of the background image show the X-ray surface brightness from the combined X-ray observations of XMM [369]. The middle and bottom panels show the velocity histograms of the substructures and their best Gaussian fits. The black vertical line shows the position of the mean redshift $z_{\mathrm{avg}} = 0.08982 \pm 0.00010$ as a reference.

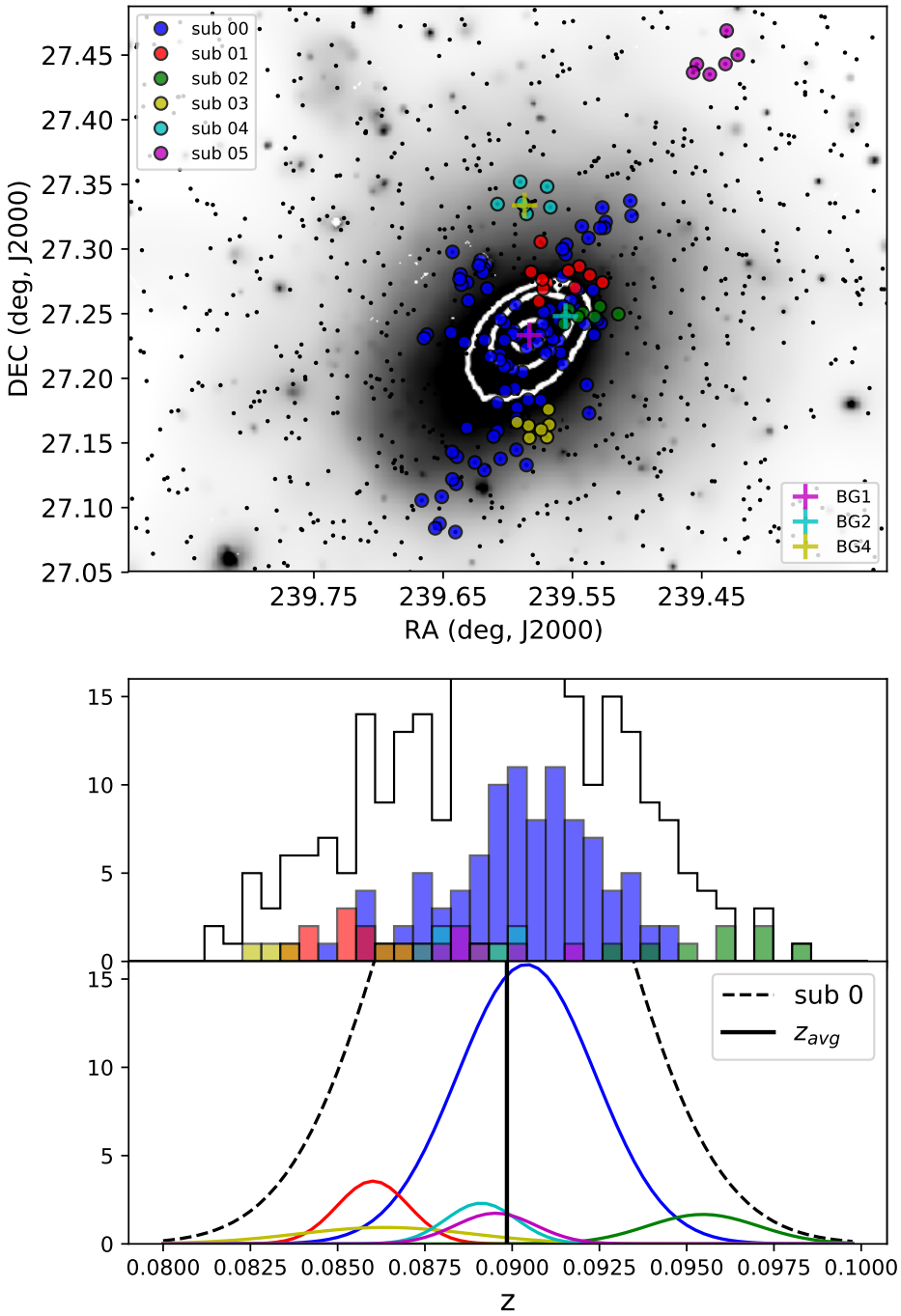

Figure 5.7. Same as Figure 5.6 for the A2142 substructures identified with the third threshold.

Table 5.2. Physical properties of the substructures.

GroupID	$N_{\rm gal}$	z_o	$v_{\rm disp}$ (km s^{-1})
cluster	868	0.08982 ± 0.00010	902 ± 22
sub0	311	0.08977 ± 0.00017	901 ± 36
sub1	12	0.09590 ± 0.00042	431 ± 91
sub2	7	0.08623 ± 0.00011	89 ± 25
sub3	14	0.08776 ± 0.00041	462 ± 90
sub4	12	0.08725 ± 0.00041	428 ± 91
sub5	10	0.08903 ± 0.00032	307 ± 72
sub6	40	0.08922 ± 0.00032	612 ± 69
sub7	9	0.09645 ± 0.00050	447 ± 111
sub8	27	0.08923 ± 0.00033	517 ± 71
sub9	8	0.09459 ± 0.00037	310 ± 83
sub10	16	0.09101 ± 0.00050	604 ± 110
sub11	9	0.08976 ± 0.00057	513 ± 128
sub12	6	0.09099 ± 0.00046	337 ± 106
sub13	16	0.08672 ± 0.00015	180 ± 32
sub14	8	0.09470 ± 0.00030	253 ± 67
sub15	7	0.08921 ± 0.00038	300 ± 86
sub16	6	0.08693 ± 0.00014	100 ± 31
sub17	6	0.09235 ± 0.00022	160 ± 50
sub18	6	0.08440 ± 0.00019	136 ± 43
sub19	6	0.08614 ± 0.00046	335 ± 106
sub00	94	0.09041 ± 0.00020	591 ± 43
sub01	11	0.08601 ± 0.00031	308 ± 68
sub02	8	0.09547 ± 0.00056	478 ± 127
sub03	7	0.08636 ± 0.00094	748 ± 216
sub04	7	0.08911 ± 0.00038	302 ± 87
sub05	6	0.08952 ± 0.00047	344 ± 108

whose mean velocity $v^i_{\rm local}$ and velocity dispersion $\sigma^i_{\rm local}$ is compared with the mean velocity v and velocity dispersion σ of the N members of the entire cluster. We thus define a local kinematic deviation for each cluster member

$$\delta_i^2 = \frac{N_{\rm local}+1}{\sigma^2}[(v^i_{\rm local}-v)^2+(\sigma^i_{\rm local}-\sigma)^2]\ . \tag{5.1}$$

The cumulative deviation $\Delta = \Sigma_i \delta_i$ is used as the test statistic to quantify the statistical significance of the presence of substructures. For a cluster with a Gaussian distribution of the member velocities, Δ is close to N. If the velocity distribution deviates from a Gaussian, Δ could vary significantly from N, either with or without substructures. Therefore, the statistical significance of the presence of substructures can be quantified by the ratio $p \equiv N(\Delta_{\rm simu} > \Delta_{\rm obs})/N_{\rm simu}$, where $\Delta_{\rm simu}$ is the value of Δ estimated in $N_{\rm simu}$ Monte Carlo simulations where the velocities of the galaxies are randomly shuffled while the galaxy celestial coordinates are kept fixed, and $N(\Delta_{\rm simu} > \Delta_{\rm obs})$ is the number of simulations where $\Delta_{\rm simu} > \Delta_{\rm obs}$, where $\Delta_{\rm obs}$ is the value obtained from the original data set. A small p thus suggests a significant presence of substructures.

We apply the DS test to our A2142 catalog. With $N = 1067$ and $N_{\rm local} = 33$, we obtain $\Delta_{\rm obs}/N = 1.46$. We run $N_{\rm simu} = 10000$ simulations and obtain $p = 0.001$, which strongly indicates the existence of substructures. Figure 5.8 shows the δ_i of each cluster member on the plane of the sky. The radius of each circle is proportional to e^{δ_i}. Blue and red circles represent galaxies with smaller and larger peculiar velocities with respect to the cluster mean velocity, respectively. The clustering of circles with similar radii therefore suggests the presence of substructures. We stress that the large circles close to the edge of the field are unreliable, because the cluster outskirts are spectroscopically severely undersampled.

We now compare the results of the σ-plateau algorithm with the DS analysis. The areas including all the members of each substructure sub1–19, and sub01–05 are delimited by ellipses on Figure 5.8. We label sub1, 2, 6, 7, 9, 11, 17, 18, and sub02: they overlap clumps of circles derived from the DS analysis. Sub5, the purple structure in the NE, also overlaps a DS structure, but it is less secure because it is on the border of the field of view where the spectroscopic catalog is largely incomplete.

We note that the DS method looks for galaxy neighbors on the plane of the sky; therefore, clumps of galaxies that might be associated to real substructures might also contain cluster members that have velocities close to the cluster mean velocity. This event can commonly result in clumps of galaxies that are not plotted with the same color. A typical example is the DS clump at

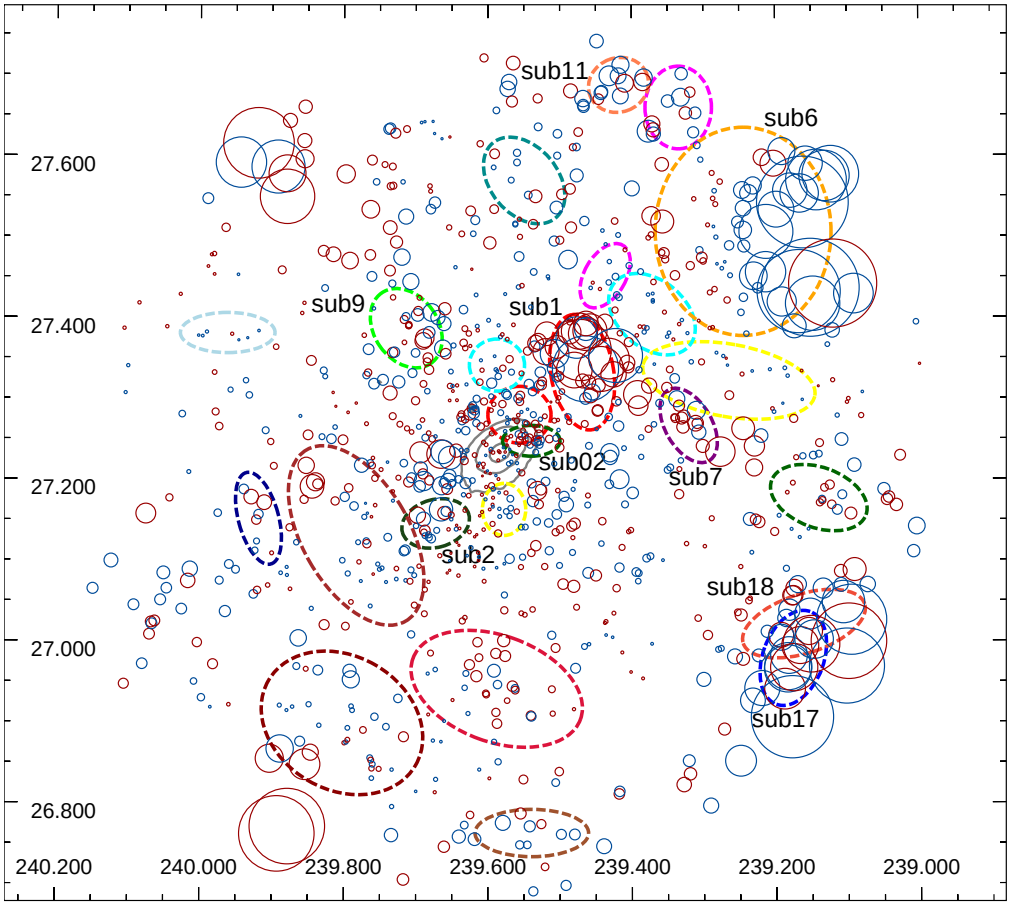

Figure 5.8. Results of the DS analysis based on the 1067 member galaxies identified by the 3σ clipping procedure on galaxy velocities. Blue and red circles represent galaxies with velocities smaller and larger than the cluster mean velocity respectively. The radius of each circle is proportional to e^{δ_i}. The ellipses mark the substructures identified with the σ-plateau algorithm. The color of these substructures are the same as in Figure 5.6 and 5.7. We only label with their names the substructure ellipses that overlap a clump of DS circles. Grey contour levels in the center show the distribution of the X-ray emission.

(RA=239.460, δ=27.33) that overlaps sub1.

Table 5.3. List of XMM and *Chandra* observations of A2142. The three most recent observations we used for the X-ray redshift measurements are highlighted.

CCD	ObsID	Exptime (ks)	Date
EPIC	0111870101	35.5	2002-07-20
EPIC	0111870401	13.7	2002-09-08
EPIC	0674560201	59.4	2011-07-13
ACIS-S	1196	11.4	1999-09-04
ACIS-S	1228	12.1	1999-09-04
ACIS-I	5005	44.5	2005-04-13
ACIS-I	7692	5.0	2007-05-07
ACIS-S	**15186**	**89.9**	**2014-01-19**
ACIS-S	**16564**	**44.5**	**2014-01-22**
ACIS-S	**16565**	**20.8**	**2014-01-24**

5.4 Spatially-resolved ICM Redshift Measurements

In this section, we investigate the dynamics of the ICM in the center of the cluster with spatially resolved X-ray redshift measurements. There are numerous observations of A2142 from XMM and *Chandra*. Since spatial resolution is crucial in this work, we focus on the *Chandra* data. In the *Chandra* data archive, we find seven observations available, as listed in Table 5.3. For X-ray redshift measurements, we only select the three most recent observations taken with ACIS-S to minimize possible systematic errors deriving from different calibrations. The total exposure time is 155.1 ks after data processing. After examining the stacked image, we select a circle of $\sim$3 arcmin for our spatially resolved spectral analysis. The total number of net counts in the 0.5–10 keV energy band within this region is $\sim 10^6$.

Similarly to Liu et al. (2016) [196], we apply the Contour Binning technique [313] to separate the cluster field of view into independent regions based on the surface brightness contours. In order to acquire a more reliable redshift measurement in each region, we adopt a threshold of signal-to-noise ratio S/N larger than that in [196]. We separate the circle of 3 arcmin around the cluster center into 26 regions with S/N larger than 200. Figure 5.9 shows the map of

Table 5.4. X-ray Fitting Results.

Region ID	X-ray redshift	Region ID	X-ray redshift
00	$0.0834^{+0.0007}_{-0.0007}$	13	$0.0906^{+0.0051}_{-0.0031}$
01	$0.0911^{+0.0015}_{-0.0017}$	14	$0.0862^{+0.0022}_{-0.0049}$
02	$0.0862^{+0.0075}_{-0.0082}$	15	$0.0849^{+0.0015}_{-0.0004}$
03	$0.0911^{+0.0011}_{-0.0013}$	16	$0.0972^{+0.0020}_{-0.0085}$
04	$0.0872^{+0.0025}_{-0.0001}$	17	$0.0892^{+0.0032}_{-0.0007}$
05	$0.0866^{+0.0019}_{-0.0025}$	18	$0.0954^{+0.0040}_{-0.0023}$
06	$0.0877^{+0.0055}_{-0.0054}$	19	$0.0845^{+0.0008}_{-0.0022}$
07	$0.0898^{+0.0184}_{-0.0194}$	20	$0.0920^{+0.0016}_{-0.0034}$
08	$0.0876^{+0.0073}_{-0.0054}$	21	$0.0852^{+0.0032}_{-0.0016}$
09	$0.0879^{+0.0015}_{-0.0013}$	22	$0.0913^{+0.0016}_{-0.0017}$
10	$0.0862^{+0.0016}_{-0.0013}$	23	$0.0897^{+0.0035}_{-0.0033}$
11	$0.0879^{+0.0055}_{-0.0041}$	24	$0.0876^{+0.0011}_{-0.0015}$
12	$0.0873^{+0.0011}_{-0.0020}$	25	$0.0931^{+0.0030}_{-0.0029}$

these regions.

The spectra are fitted with *Xspec* v12.9.1 [9] in the 0.5–10 keV band. Background spectrum is generated using the “blank sky" script. To model the X-ray emission from a projected region, we use the double-`apec` thermal plasma emission model [345]. The double-temperature thermal model is helpful to reduce the possible bias in the measurement of the iron line centroid due to the presence of unnoticed thermal components along the line of sight [195]. Galactic absorption is described by the model `tbabs` [399]. The ICM temperature, the metallicity, the redshift, and the normalization are all set unconstrained at the same time. The redshifts of the two components in the model are always linked. Considering the large parameter space to explore, for the fitting we adopt a Monte Carlo Markov Chain (MCMC) method. The chain is generated by the Goodman-Weare algorithm [163], with 10 walkers, 10^4 burn-in steps and the total length of 10^6 steps. After the fitting, chains are top-hat filtered according to the following ranges: temperature from 0.1 keV to 25 keV, metallicity from 0.001 to 2, and redshift from 0.05 to 0.15. The best fit parameters and their uncertainties are estimated from these filtered chains. The best fit results of the regions are listed in Table 5.4.

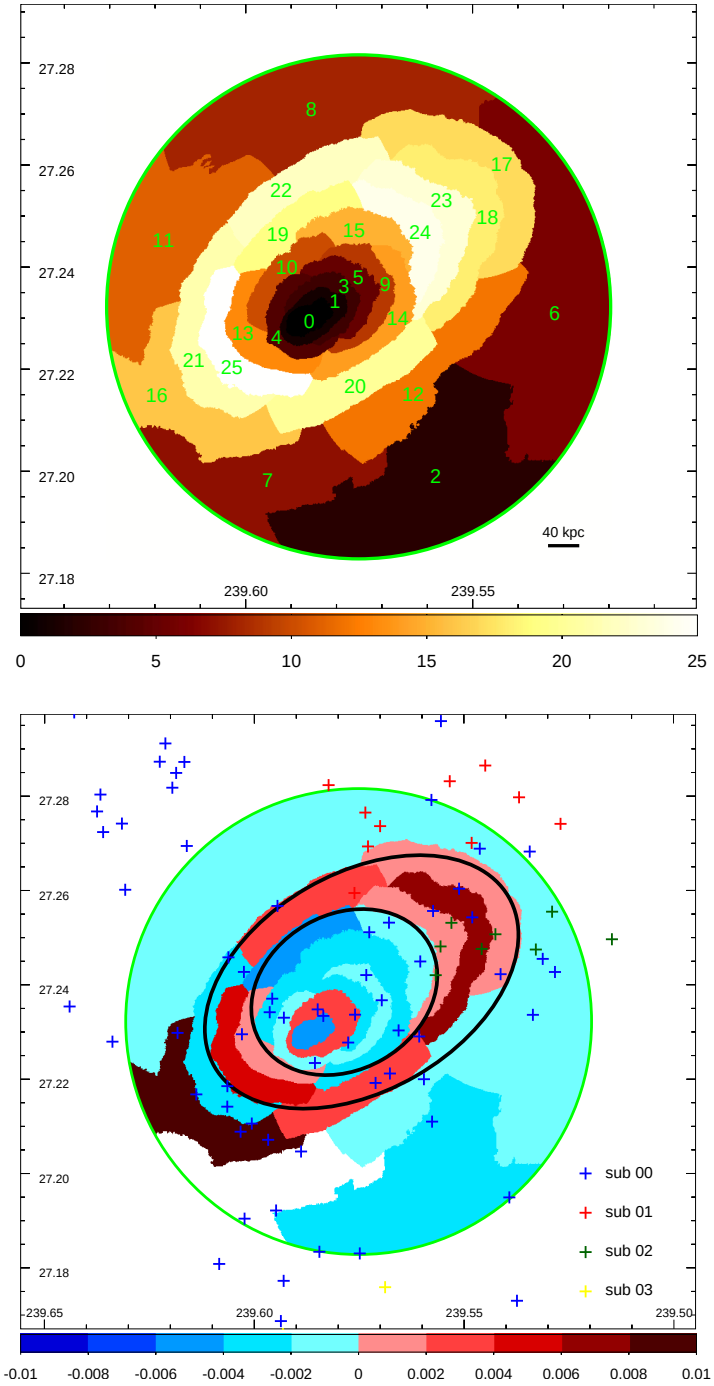

Figure 5.9. Upper: The region map produced on the basis of the surface brightness contours. The color bar denotes the serial number of the regions and has no physical meaning. Lower: Redshift map of A2142. The color bar indicates the redshift difference with respect to the average X-ray redshift $z_{\rm X} = 0.0889 \pm 0.0009$. The black ellipses roughly mark the elliptical annulus with redshift larger than the surroundings.

We present our results in the form of a redshift map, shown in Figure 5.9. Region 7 has a redshift uncertainty larger than 0.01 and is masked from the map. The most prominent feature emerging from the redshift map is that seven regions form an elliptical annulus, marked with the two black ellipses in Figure 5.9, with a mean redshift larger than its surrounding regions. Specifically, its redshift is 0.0916 ± 0.0011. The velocity difference between the annulus and the cluster average is therefore 810 ± 330 km s^{-1}. The emerging of this high-redshift annulus appears to be consistent with the scenario where the ICM is sloshing due to one or more perturbations. However, the limited spatial resolution of the map implies that we can only derive rough estimates of both the size and the redshift of the annulus.

Additionally, we note that the cluster core is surrounded by another high redshift annulus with redshift 0.0911 ± 0.0010. The velocity difference between this annulus and the cluster average is 660 ± 300kms^{-1}. A possible interpration of this feature is a small scale sloshing, that generates a 'wave'-like motion of the ICM. Alternatively, this feature could be the signature of the rotation of the cool core, which is an event also suggested by the spiral-like structures observed in other clusters [181]. Clearly, the projection effects and the large systematic uncertainties in the X-ray redshift measurements require deeper observations with the next generation X-ray bolometers to pin down the appropriate scenario.

5.5 Weak lensing data and analysis

A2142 is among the seven nearby merging clusters targeted by the Subaru weak-lensing analysis of [259], who performed a detailed comparison of the weak-lensing mass distribution with the X-ray brightness and cluster galaxy distributions. [381] conducted a combined weak-lensing and Sunyaev-Zel'dovich effect analysis of A2142, along with three other X-ray luminous clusters targeted by the 7-element AMiBA project [152] to determine the hot gas fractions in the clusters in combination with X-ray temperatures. The Umetsu et al. (2009) [381] weak-lensing analysis of A2142 is based on the same Subaru images as in Okabe et al. (2008) [259], but their improved method of selecting blue+red background galaxies in $g'R_{\rm C}$ color-magnitude space increased the size of the

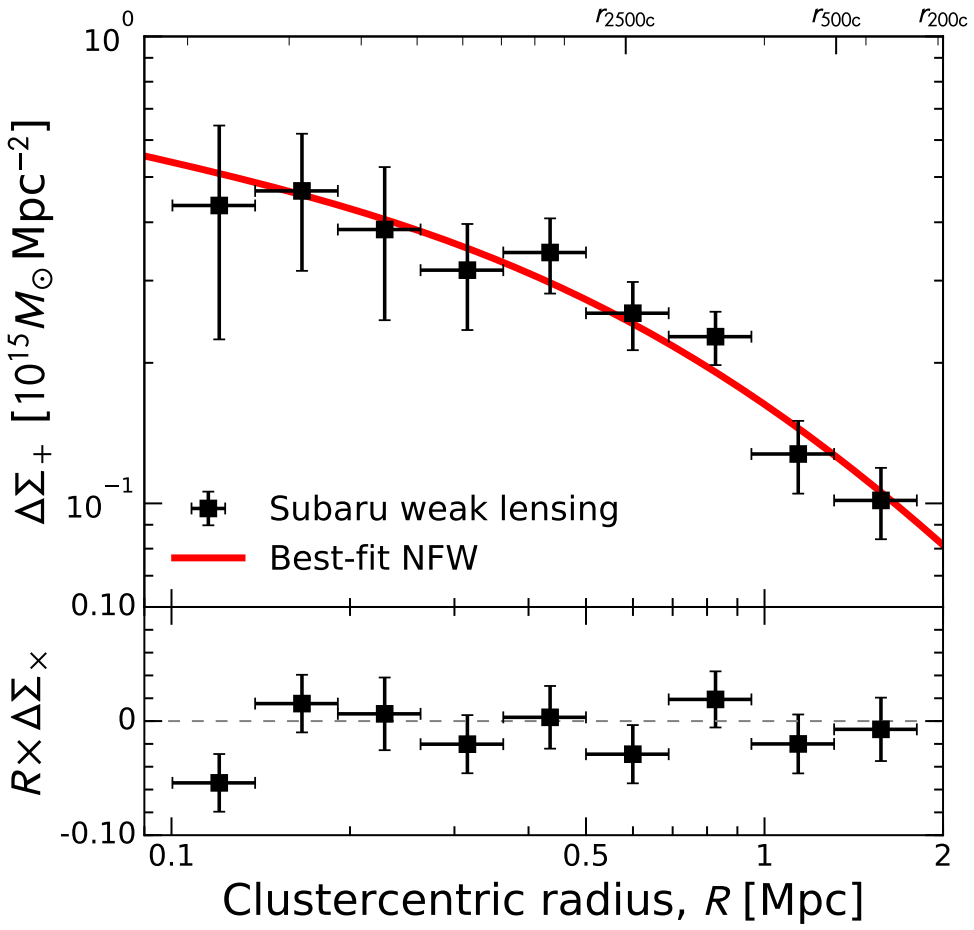

Figure 5.10. Tangential reduced shear profile (upper panel, black squares) of A2142 derived from our Subaru/Suprime-Cam weak-lensing observations, shown in units of projected mass density. The thick-solid (red) line corresponds to the best-fit NFW profile. The lower panel shows the 45° rotated × component, which is consistent with a null signal within 2σ at all cluster radii.

background sample by a factor of 4 relative to that of Okabe et al. (2008) [259]. With the improved background selection, Umetsu et al. (2009) [381] obtained a virial mass estimate of $M_{\rm vir} = 15.2^{+3.1}_{-2.3} \times 10^{14} M_\odot$ and a concentration of $c_{\rm vir} = 5.5 \pm 1.1$ (see their Table 4) from tangential shear fitting assuming a spherical Navarro–Frenk–White (NFW) halo [249].

Here we revisit the weak-lensing properties of A2142 by performing a weak-lensing analysis using our most recent shape measurement pipelines employed by the CLASH collaboration [382] and the LoCuSS collaboration

[258]. We analyze the Subaru/Suprime-Cam $g'R_{\rm C}$ images reduced by Okabe et al. (2008) [259], and apply the same color-magnitude cuts as presented in Umetsu et al. (2009) [381] to select background galaxies. We use the Subaru $R_{\rm C}$-band images for the shape measurement, as done in previous work. Briefly summarizing, the key common feature in our shape measurement pipelines is that only those galaxies detected with sufficiently high significance are used to model the isotropic point-spread-function correction as a function of object size and magnitude [382, 258]. For each galaxy, we apply a shear calibration factor, $g \to g/0.95$, to account for the residual correction estimated using simulated Subaru/Suprime-Cam images [382, 258]. All galaxies with usable shape measurements are then matched with those in the blue+red background samples. Our conservative selection criteria yield a mean surface number density of $n_{\rm g} \simeq 25\,{\rm galaxies\,arcmin^{-2}}$ for the weak-lensing-matched background catalog, compared to $n_{\rm g} \simeq 30\,{\rm galaxies\,arcmin^{-2}}$ found by Umetsu et al. (2009) [381]. We checked that our results from the two different pipelines [382, 258] are robust and entirely consistent with each other.

In Figure 5.10 we show the tangential reduced shear profile in units of projected mass density, $\Delta\Sigma_+(R) = \Sigma_{\rm c} g_+(R)$, with $\Sigma_{\rm c} \simeq 5.5 \times 10^{15} M_\odot\,{\rm Mpc^{-2}}$ the critical surface mass density for lensing and $g_+(R)$ the azimuthally averaged reduced tangential shear as a function of cluster-centric radius R. We fit the $\Delta\Sigma_+(R)$ profile with a spherical NFW halo using log-uniform priors for $M_{200{\rm c}}$ and $c_{200{\rm c}}$ in the range $0.1 < M_{200{\rm c}}/(10^{15} M_\odot\, h^{-1}) < 10$ and $0.1 < c_{200{\rm c}} < 10$, where $h \equiv H_0/(100\,{\rm km\ s^{-1}\,Mpc^{-1}}) = 0.704$. The error analysis includes the contribution from cosmic noise due to the uncorrelated large scale structure projected along the line of sight [153], as well as galaxy shape noise and measurement errors. The mass and concentration parameters are constrained as $M_{200{\rm c}} = (13.0 \pm 2.7) \times 10^{14} M_\odot$ and $c_{200{\rm c}} = 4.1 \pm 0.8$, or $M_{\rm vir} = (16.1 \pm 3.7) \times 10^{14} M_\odot$ and $c_{\rm vir} = 5.5 \pm 1.1$, in good agreement with the results of Umetsu et al. (2009) [381]. The uncertainties are slightly larger than those estimated by Umetsu et al. (2009) [381], who did not account for the cosmic noise contribution.

The mass estimated with the weak lensing analysis is consistent with the mass profile estimated with the caustic method, based on the amplitude of the caustics in the redshift diagram (Figure 5.5). The caustic method estimates the

radius $r_{200} = 2.15$ Mpc and the mass within r_{200}, $M_{200} = (11.5 \pm 3.7) \times 10^{14} M_{\odot}$. This agreement confirms the results of Geller et al. (2013) [121], who show that, for a sample of 19 clusters, the caustic and weak lensing masses within r_{200} agree to within $\sim 30\%$, similarly to the early results of Diaferio et al. (2005) [75].

In Figure 5.11, we show the weak-lensing mass map of A2142. The mass map is smoothed with a Gaussian of FWHM $= 1'.5$. The mass map exhibits an extended structure elongated along the northwest-southeast direction, consistent with the direction of elongation of the X-ray emission. We compare the mass map with the previous map reconstructed from the old shape catalog [259]. Since the number density of background galaxies for this analysis is slightly lower than that of the previous analysis, the Gaussian FWHM used for the map is $1'.5$, larger than that for the old map ($1'.0$). Okabe et al. (2008) [259] found the main peak at $\sim 11\sigma$ and a possible substructure at $\sim 3\sigma$ in the northwest region. The noise level was computed with the theoretical estimations from the number density and the variance of ellipticity. Here, we find the main peak at $\sim 10\sigma$ and the northwest substructure at $\sim 3.3\sigma$. The noise is computed by the bootstrap re-sampling with 3000 realizations using random ellipticity catalog in order to conservatively evaluate a spatially-dependent noise level caused by sparse galaxy distributions. Although the techniques are revised from the previous study, the overall mass distributions are similar to each other. In this paper, we compare the new map with the distributions of the substructures determined by the dynamical method.

5.6 Combined analysis and discussion

In this section, we combine the results of the above analyses to attempt to draw a scenario of the internal structure and dynamics of A2142. We also compare our results with the previous results by Owers et al. [263] and Einasto et al. [90], who use different methods to detect substructures in A2142.

We first compare the optical substructures identified with the σ-plateau algorithm with the ICM redshift map, as shown in Figure 5.9. The ICM redshift map only covers the region within 3 arcmin from the cluster center, so Figure 5.9 only shows the substructures sub00 to sub03 identified with

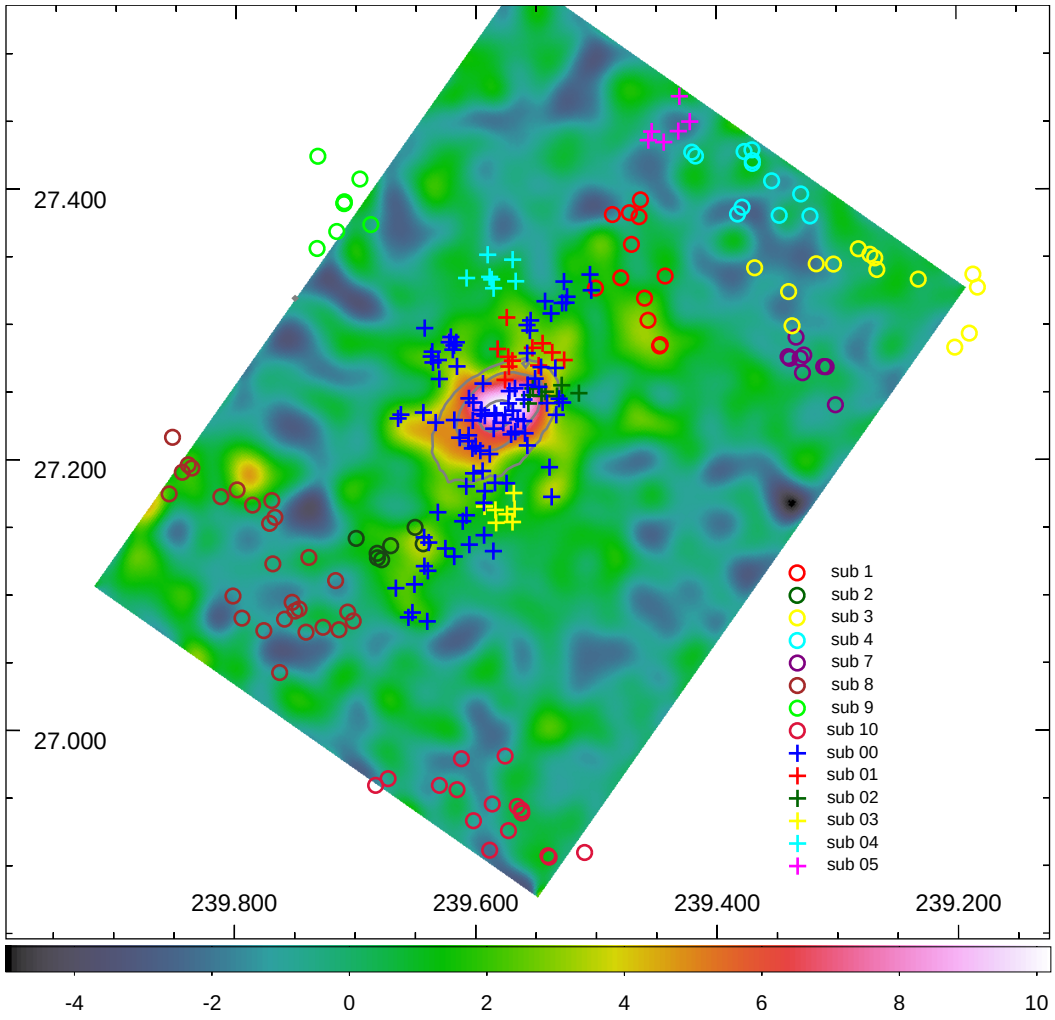

Figure 5.11. The weak-lensing mass map superimposed with the substructures identified with the σ-plateau algorithm. The color code shows the weak-lensing signal-to-noise ratio, namely the surface mass density in units of the 1σ reconstruction error.

the third threshold trimming the binary tree of A2142. Figure 5.9 does not show any clear correlation between the redshift and spatial distributions of the optical substructures and the ICM distribution and redshift. This result suggests that the dynamics of the ICM in this region have decoupled from the dynamics of the galaxies. This behaviour is not unexpected in merging systems, because galaxies behave like collisionless components, unlike the ICM.

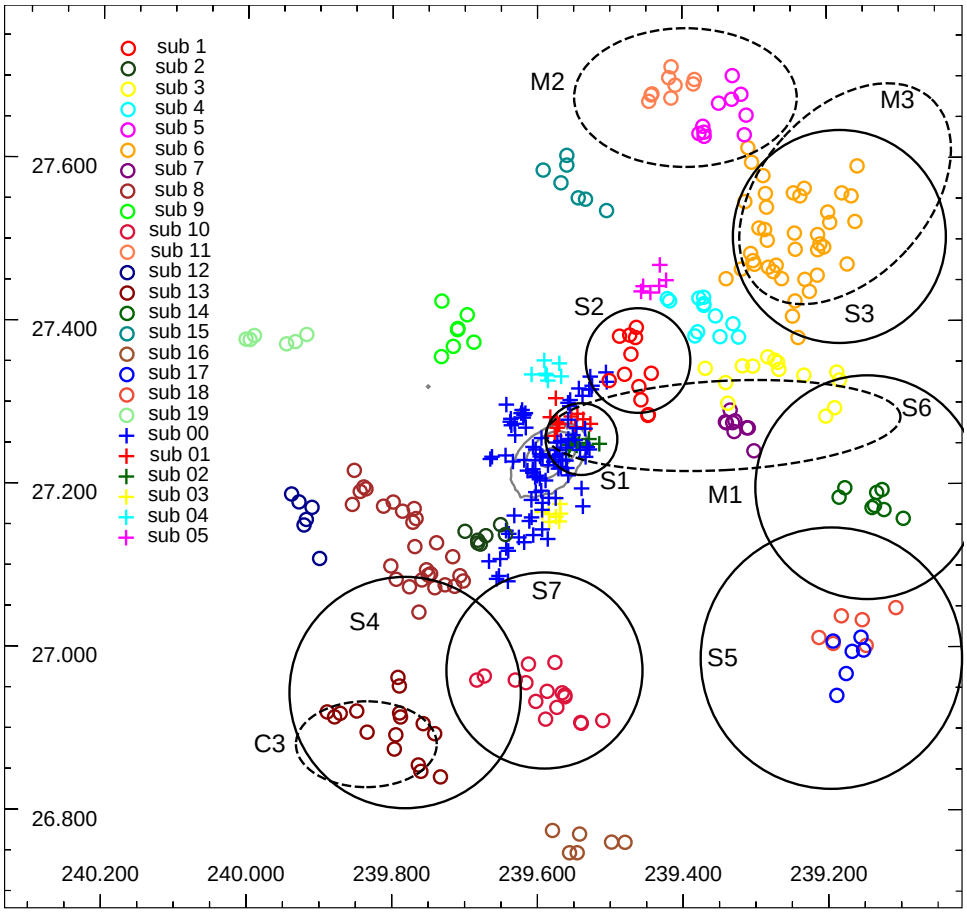

Figure 5.12. Substructures identified with the σ-plateau algorithm and with other methods in the literature. S1–S7 shown as black circles show the location and size of the substructures identified with the κ-test by Owers et al. [263]. The dashed ellipses show the approximate location and size of the structures identified by Einasto et al. [90].

In Figure 5.11, we superimpose the substructures identified by the σ-plateau algorithm on the weak-lensing mass map. Figure 5.11 shows that the shape of the main halo of the mass map and the distribution of the member galaxies of the cluster core sub00 are consistent with each other. Moreover, the $\sim 3.3\sigma$ excess in the weak-lensing signal, located $\sim 7'$–$8'$ northwest of the cluster center, coincides with sub1. This match supports the result of Okabe et al. (2008) [259], who found that this northwest mass substructure is associated with a slight excess of galaxies in the color-magnitude relation of the A2142

galaxies, lying $\sim 5'$ ahead of the northwest edge of the central X-ray core: we confirm that 6 out of the 12 members of sub1 do indeed belong to this group of galaxies identified by Okabe et al. (2008) [259]. Finally, we also find marginally significant excesses in the weak-lensing map that coincide with sub04, sub01, and sub2. These results demonstrate that our σ-plateau substructure identification algorithm can efficiently detect structures that are around the detection limit of the weak-lensing signal.

Figure 5.12 compares the substructures identified with the σ-plateau algorithm with the substructures identified in previous work. Owers et al. (2011) [263] detect 7 substructures, S1–S7, from the projected galaxy surface density distribution and a κ-test on the local kinematics of the galaxies, where the κ-test identifies kinematic substructures by comparing the local velocity distribution to the global velocity distribution [55]. Open circles in Figure 5.12 show the location and size of the substructures identified by Owers et al. (2011) [263], according to their Figure 12.

Einasto et al. (2017) [90] identify four substructures, M1–M3 and C3, by analysing the position and velocities of member galaxies with the *mclust* package, which is based on the analysis of a finite mixture of distributions, in which each mixture component corresponds to a different subgroup. To provide a qualitative impression of the location and size of these structures we plot four ellipses in Figure 5.12, according to the information that can be inferred by eye from Figure 4 and 6 of Einasto et al. (2017) [90].

We can see that sub1 overlaps S2 of Owers et al. (2011) [263], which is consistent with the most obvious DS substructure (see Figure 5.8). Sub5 and sub11 coincide with substructure M2 in Einasto et al. (2017) [90]. Our most prominent substructure sub6 on the northwest coincides with S3 and M3; sub6 is also clearly detected by the DS analysis (Figure 5.8). Sub7 lies within M1; we note that the rest of the galaxies associated to M1 by Einasto et al. (2017) [90] are identified as substructure members by neither Owers et al. (2011) [263] nor our σ-plateau algorithm. Sub10 overlaps S7. Sub13 overlaps S4 and the component C3 of Einasto et al. (2017) [90] (see their Figure 4). Sub17 and sub18 overlap S5 and also appear as clumps of the DS analysis.

All the remaining substructures, except sub8, that are identified by the σ-plateau algorithm and do not have a correspondence with substructures

from previous analyses, have 14 members at most, indicating that either the catalogues used in previous analysis did not contain enough galaxies or these structures, if they are not chance alignment of unrelated galaxies, are too poor to be reliably identified by other methods. We conclude that, overall, this comparison shows a remarkably agreement between the different substructure identifications.

As shown in Sect. 5.4, sub9 in the northeast of the cluster is identified by both the DS method and the σ-plateau algorithm. The circles associated to the galaxies according to the DS method in that region of the sky (Figure 5.8) have both red and blue colors: most of the red circles are members of sub9, whereas the blue circles, that have redshift smaller than the sub9 redshift, are not members of sub9. The X-ray images from both XMM-Newton [86] and *Chandra* [87] show the presence of a faint gas component associated to this structure. For this X-ray emitting gas, [86, 87] determine an average temperature of $\sim$1.4 keV, appropriate for a system with total mass of $\sim 5.1 \times 10^{13}\ M_{\odot}$ [388]. According to the analysis of Munari et al. [246, 247], this mass is consistent with the mass suggested by the velocity dispersion of 310 km s^{-1} that we measure for the members of the optical substructure. Figure 5.13 shows an optical image of sub9, with the open white circles indicating its members according to the σ-plateau algorithm. We also indicate the five galaxies, G1–G5, associated by Eckert et al. [86, 87] to the clump of hot gas. Our analysis confirms that G3, that we name BG5 in section 5.3.1, G4 and G5 are members of sub9. On the contrary, G1 and G2 are not members: in fact, G1 and G2 have a velocity 1700 km s^{-1} smaller and 1130 km s^{-1} larger, respectively, than the mean redshift of sub9. The redshift of sub9 – $z = 0.09459$ – is significantly larger than the average redshift of the cluster – $z = 0.08982$ – and shows that this system is falling into the cluster at large speed.

We conclude that the optical substructure sub9 and the faint X-ray clump originate from the same group that is currently falling into the cluster: the ram pressure of the ICM acting on the group gas, but not on its galaxy members, is a plausible explanation for the displacement on the sky between the galaxies and the X-ray emission.

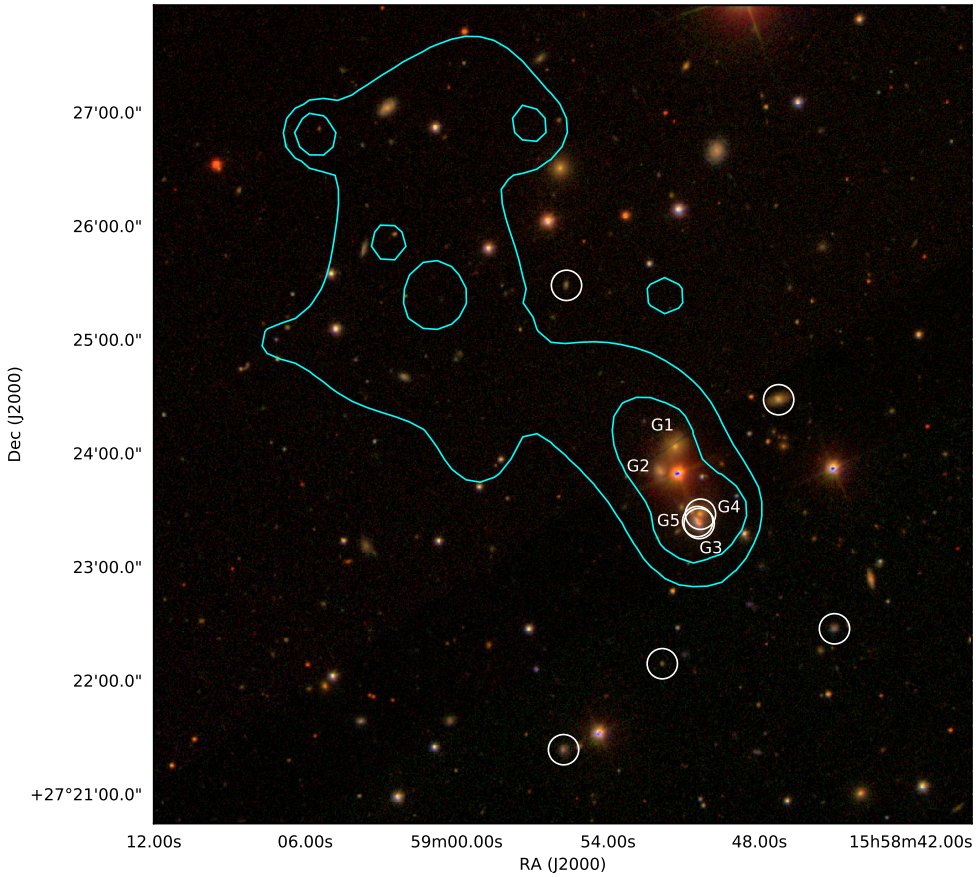

Figure 5.13. The zoomed-in image of the substructure sub9. The SDSS RGB image converted from i, r, g-band is superimposed with the X-ray contours of the gas; the white circles are the members of sub9 according to the σ-plateau algorithm. Five galaxies in the image are labeled G1–G5 as in Eckert et al. (2017) [87]. G3 and G4 are confirmed to be members of sub9.

5.7 Conclusions

We investigate the dynamics of A2142 by comparing the properties of the substructures in the galaxy distribution, the line-of-sight velocity field of the ICM derived from the spatially-resolved X-ray spectroscopy, and the weak-lensing mass distribution. Our main results are as follows:

- Based on a new and extended catalog of spectroscopic redshifts within ~ 3.5 Mpc from the cluster center, we identify a number of substructures with the σ-plateau algorithm. The distribution of the substructures appears consistent with results obtained with other methods, including

the DS method, the κ-test and the *mclust* algorithm.

- Most substructures have a number of galaxy members ~ 10 (see Table 5.2), indicating that there is no sign of recent or ongoing major mergers and suggesting a scenario where the cold fronts observed in A2142 in X-rays originate from core sloshing induced by minor mergers.

- In the northeast outskirts, the galaxy substructure sub9 matches a falling gas clump observed in X-rays; the slight displacement between the positions of the galaxies and the gas might be due to ram pressure on the hot gas.

- The shape of the central substructure sub00 is consistent with the projected weak lensing mass map. Several substructures also coincide with the weak-lensing mass excesses.

- With spatially-resolved X-ray spectroscopy based on *Chandra* data, we measure the line-of-sight velocity distribution of the ICM within ~ 0.35 Mpc from the cluster center. We find an annulus near the X-ray cold fronts with redshift significantly larger than the surroundings, corresponding to a velocity $810 \pm 330\,\mathrm{km\ s^{-1}}$ larger than the cluster mean velocity. We also find that the core is surrounded by high redshift gas, with a velocity $660 \pm 300\,\mathrm{km\ s^{-1}}$ larger than the cluster redshift. The features we observe in the X-ray redshift map appear to be consistent with the core-sloshing scenario suggested in previous work.

Deeper photometric and spectroscopic observations of the field can clearly provide more detailed and solid results. The spatially resolved X-ray redshift measurements will improve by advanced future X-ray bolometers. In particular, with the X-ray IFU on board, the Advanced Telescope for High-ENergy Astrophysics (*Athena*) will remarkably extend the application of this method. Moreover, a more precise weak lensing measurement of the projected mass distribution will be of great help to confirm the relation between the total mass distribution and the galaxy substructures we find here.

Acknowledgments

We thank the anonymous referee whose comments substantially improved the presentation of our results. We thank Dominique Eckert, Sabrina de Grandi, and Maria Chiara Rossetti for the results of XMM-Newton and their helpful comments. We sincerely thank Margaret Geller for her insightful suggestions. This work was supported by the National Natural Science Foundation of China under Grants Nos. 11403002, the Fundamental Research Funds for the Central Universities and Scientific Research Foundation of Beijing Normal University. AD and HY acknowledge partial support from the grant of the Italian Ministry of Education, University and Research (MIUR) (L. 232/2016) "ECCELLENZA1822_D206 - Dipartimento di Eccellenza 2018-2022 Fisica" awarded to the Dept. of Physics of the University of Torino. AD also acknowledges partial support from the INFN Grant InDark. P.T. is supported by the Recruitment Program of High-end Foreign Experts and he gratefully acknowledges hospitality of Beijing Normal University. K.U. acknowledges support from the Academia Sinica Investigator Award and from the Ministry of Science and Technology of Taiwan (grant MOST 103- 2628-M-001-003-MY3).

Chapter 6

Testing the rotation scenario in galaxy cluster Abell 2107

Ang Liu[1,2,3] and Paolo Tozzi[1]

1. INAF - Osservatorio Astrofisico di Arcetri, Firenze, Italy

2. Department of Physics, Sapienza University of Rome, Rome, Italy

3. Department of Physics, University of Rome Tor Vergata, Rome, Italy

(Monthly Notices of the Royal Astronomical Society, Volume 485, Page 3909.)

Abstract

We search for global rotation of the intracluster medium (ICM) in the galaxy cluster Abell 2107, where previous studies have detected rotational motion in the member galaxies with a high significance level. By fitting the centroid of the iron K_α line complex at 6.7–6.9 keV rest frame in *Chandra* ACIS-I spectra, we identify the possible rotation axis with the line that maximizes the difference between the emission-weighted spectroscopic redshift measured in the two halves defined by the line itself. Then, we measure the emission-weighted redshift in linear regions parallel to the preferred rotation axis, and find a significant gradient as a function of the projected distance from the rotation axis, compatible with a rotation pattern with maximum tangential velocity $\mathtt{v}_{\rm max} = 1380 \pm 600$ km/s at a radius $\lambda_0 \sim 160$ kpc. This result, if interpreted in the framework of hydrostatic equilibrium, as suggested by the

regular morphology of Abell 2107, would imply a large mass correction of the order of $\Delta M = (6 \pm 4) \times 10^{13} M_{\odot}$ at ~ 160 kpc, which is incompatible with the cluster morphology itself. A more conservative interpretation may be provided by an unnoticed off-center, head-on collision between two comparable halos. Our analysis confirms the peculiar dynamical nature of the otherwise regular cluster Abell 2107, but is not able to resolve the rotation vs merger scenario, a science case that can be addressed by the next-generation X-ray facilities carrying X-ray bolometers onboard.

6.1 Introduction

Galaxy clusters are the largest virialized structures in the Universe, and have been largely used to map the growth of cosmic structures through cosmic ages, and, ultimately, to constrain cosmological models [34, 1] and modified gravity models [331, 242]. The key quantity is the virialized mass, which is often computed under the assumptions of spherical symmetry, isotropic velocity distribution of the member galaxies, and hydrostatic equilibrium of the X-ray emitting intracluster medium (ICM). However, despite virialization is considered a fair assumption, substantiated by numerical simulations [177], it is now commonly accepted that it is not completely satisfied in several cases, as suggested by in-depth analysis of hydrodynamical numerical studies [28] and by the increasing claims of dynamical substructures and bulk motions observed in massive clusters [130, 267, 196]. In addition to the presence of bulk motions involving significant amount of the cluster mass, another aspect that can significantly affect mass estimates is the presence of global rotation, a possibility which is often ignored when applying the classic mass-weighting methods to galaxy clusters. In dynamical studies the possible presence of global rotation is almost always neglected, with the exception of few numerical works [184, 25, 15]. From the observational point of view, there are several ongoing projects aiming at quantifying the impact of bulk motions, particularly associated with mergers in the external regions of clusters [125], and, in addition, detailed works have been devoted to the non thermal pressure contribution from the combination of turbulence and bulk motions, in which rotation can be considered a particular case, despite not explicitly treated [88].

A fundamental issue concerns the observational difficulty in disentangling asymmetric bulk motions, due to the presence of substructures with anisotropic velocity distribution associated with multiple off-centered mergers or continuous accretion of matter along filaments, from a global rotation. In other words, it is almost impossible to distinguish two overlapping clusters from one rotating cluster [253], if not by tracing the rotation curve with high spatial resolution. In the optical band, these studies are practically limited by the sparse and discrete sampling of the velocity along the line-of-sight, due to the limited number of member galaxies. To date, the number of redshifts available in single clusters can reach a maximum of a thousand cluster members only for a few, well known targets [301, 297]. Due to these difficulties, dynamical studies in the optical band, based on spectroscopic redshift distribution of the member galaxies, are mostly focused on the infall of smaller halos in the outskirts, or galaxies flowing along filamentary structures that are observed to connect the cluster to the mildly non-linear large scale structures of the Universe.

Although very few systematic studies of global rotation have been done, it was possible to show that a minority of clusters do show global rotation not associated with recent mergers, on the basis of spectroscopic samples from SDSS and 2dFGRS [157]. Other studies on cluster rotation have been focused to several specific targets. Apart from a few suggestions of cluster rotation from velocity gradients [166], SC0316-44 was the first cluster for which a claim of rotation was made on the basis of the analysis of only 15 member galaxies [220]. Abell 2107 (hereafter A2107) has been claimed to show spatial correlations in the galaxy velocities, consistent with rotation, in a study by Oegerle et al. (1992) [253], based on the redshifts of 68 member galaxies. However, the pure rotation model does not account for the peculiar velocity of its brightest cluster galaxy (BCG) of ~ 270 km/s with respect to the bulk of the cluster. Eventually, a more in-depth analysis confirmed the rotation of A2107 [166], with the strongest evidence for rotation being the consistent positional angle of the velocity gradient for consecutive galaxy subsamples. Recently, a few systematic studies, using SDSS DR 9 and DR10 spectroscopic data and new algorithms, found rotation in a significant but vastly different fraction of their samples, depending on the sample selection [373, 374, 205]. If confirmed, a robust assessment of a widespread global rotation and the associated amount

of rotational support across the cluster population, would allow one to include this contribution to the well known effects of turbulence and disordered bulk motions, and therefore to alleviate the bias affecting masses measured through classic hydrostatic equilibrium. Pushing further ahead with this study, we also remark that a statistical treatment of rotation among clusters of galaxies can be used to constrain the origin and growth of angular momentum in cosmic structures at cluster scales.

Another observational window potentially relevant to measure the inner dynamical structure of clusters, including rotation, is provided by the X-ray emission from the ICM. This technique has the advantage of tracing the continuous distribution of collisional matter constituted by the dominant baryonic component in clusters. Bulk motions in the ICM can be detected by measuring the spatial distribution of its emission-weighted redshift, and hence radial velocity, in limited regions. This is done by fitting the position of the prominent iron K_α line at 6.7–6.9 keV in the ICM X-ray spectrum. These measurements, however, require high spectral and spatial resolutions at the same time, due to the expected patchy distribution of bulk motions. The tight requirement on spatial resolution limits these studies to the use of CCD data, which, in turn, implies a poor spectral resolution. Given this limitation, the measurement of the centroid of the most prominent emission line complex in CCD spectra provides the most accurate spatially-resolved measurement for the ICM redshift, and the associated statistical error. The uncertainty on the redshift σ_z strongly depends on the strength of the signal, on the modelization of the thermal structure of the ICM, and on calibration issues, and typically is found in the range $0.002 < \sigma_z < 0.01$ for bright, nearby clusters and groups observed with *Chandra*. We refer the reader to [404] for a discussion on the accuracy on the global ICM redshift and to [195, 196] for the accuracy in spatially resolved analysis of the ICM. Therefore, with a typical uncertainty on ICM velocity in nearby clusters in the range $c \times \sigma_z/(1+z) \sim 500 - 2000$ km/s, the search of bulk motions provided positive results only in a few clusters with highly disturbed dynamical status [267, 196], including the remarkable case of the Bullet Cluster, where supersonic bulk motion has been identified along the line of sight and perpendicularly to the merger axis [195]. In general, a direct comparison of bulk motions along the line of sight in the galaxy members

and in the ICM, shows that it is hard to associate galaxies and ICM motions, as we discussed also in Liu et al. (2018) [194] (see also Chapter 5). This is due to the different dynamical evolution of merger and infall in collisionless (dark matter and galaxies) and collisional (ICM) components, which appear to become spatially decoupled within one dynamical time, as we can directly witness in the plane of the sky in the case of the so called bullet-like clusters. In any case, global rotation, if any, is expected to be characterized by velocities significantly lower than the typical velocity dispersion in clusters, which makes it very hard to blindly search for global rotation of the ICM using the available spectral resolution of CCD X-ray imagers that can at best identify velocity differences of ~ 1000 km/s or larger, as previously mentioned. As a matter of fact, the study of ICM bulk motions will be always limited to a few cases until the advent of X-ray bolometers, which will be on board of XRISM and Athena [138]. In the case of XRISM, the low angular resolution of the order of $\sim 1'$ will enable study of bulk motions only in nearby clusters, since the signal from the ICM in distant clusters will be smeared out. On the other hand, the $5 - 10$ arcsec angular resolution of the bolometer onboard Athena [22] is expected to perform to the point of revolutionizing the study of ICM bulk motions. Currently, the launch of XRISM is planned for the year 2021 [1], while Athena is expected to be launched around the year 2031 [2]. This impasse in the study of ICM dynamics follows the dramatic loss of the Hitomi satellite [364], which was anyhow able to provide a high-spectral resolution view of the Perseus cluster, showing the effects of turbulence and bulk motions in its core [150].

In this context, no firm detection of global rotation in the ICM has been reported so far, but a fair number of numerical studies have been devoted to the investigation of the effects of major, off-centered mergers and continuous/minor merger infall from filaments on ICM rotation [24, 16]. The only chance to test observationally ICM rotation is to focus on some extreme case, where the effects of rotation are maximum. In this work, we make a first attempt to find a signature of rotation in the ICM, by targeting A2107, that is, to our knowledge, the best candidate for such a study. A2107 is a massive, cool core cluster

[1] See https://heasarc.gsfc.nasa.gov/docs/xrism/

[2] See https://www.the-athena-x-ray-observatory.eu/

at redshift $z = 0.0412$ [254], with an estimated mass $M_{500} = 1.49 \times 10^{14} M_{\odot}$ [275], and a global (i.e., including the cool core emission) temperature of ~ 4 keV within $\sim 0.3 r_{500}$ [112]. This cluster, in addition to the historical claims of rotation previously mentioned, is also included among the clusters with significant rotation in the recent study of [205], and confirmed by the recent study of Song et al. (2018) [347], who found a 3.8σ signal of rotation based on the analysis of 285 member galaxies within $R < 20'$. The corresponding rotation velocity is 380–440 km/s at $20'$, therefore slightly below the best spectral resolution expected for CCD data. Despite this, we aim at exploiting the archival *Chandra* observation of A2107 to search for global ICM rotation and compare it to the optical results.

The paper is organized as follows. In Section 6.2, we briefly describe the expected signatures of ICM rotation in the X-ray band in the simplest, idealized cases. In Section 6.3, we describe data reduction and analysis. In Section 6.4, we describe the measurement of global rotation, and present the results. In Section 6.5, after commenting on the constraints of possible systematics in our measurements, we discuss the rotation versus merger scenario on the basis of our findings and mention possible extensions of our study. Finally, our conclusions are summarized in Section 6.6. Throughout this paper, we adopt the seven-year WMAP cosmology ($\Omega_{\Lambda} = 0.73$, $\Omega_m = 0.27$, and $H_0 = 70.4$ km s^{-1} Mpc^{-1} [176]. We note, however, that our results have a negligible dependence on the adopted cosmology. Quoted error bars correspond to a 1 σ confidence level, unless noted otherwise.

6.2 ICM rotation: expected signatures in X-rays

In this section we briefly discuss the expected signature of ICM rotation in the X-ray band, assuming cylindrical rotation with no dependence along the rotation axis. We assume a dependence of the rotation velocity on the distance λ from the rotation axis of the kind

$$\mathtt{v}(\lambda) = \mathtt{v}_0 \frac{\lambda/\lambda_0}{(1+\lambda/\lambda_0)^2} \,. \tag{6.1}$$

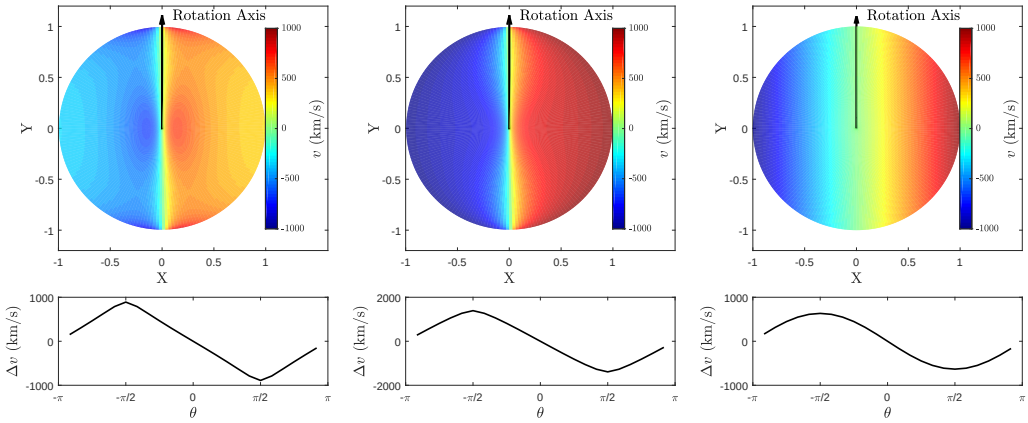

Figure 6.1. Left panel: projected velocity map observed in a cluster rotating with a differential velocity curve according to Equation (6.5), where $c = 5$, $c_{\mathrm{v}} = 10$, and $\mathrm{v}_{\mathrm{max}} = 1000$ km/s, where $\mathrm{v}_{\mathrm{max}} = \mathrm{v}(\lambda_0) = \mathrm{v}_0/4$ as follows from Equation (6.1). Middle and right panels: same as the left panel, but for rotation with a constant velocity of 1000 km/s, and a rigid body rotation with Ω=1000km/s/r_{vir}, respectively. In the lower panels, we plot the average velocity difference between the two semicircles defined by the dividing line, as a function of the angle θ ($\theta = \pi/2$ when the dividing line overlaps with the rotation axis).

This rotation curve is introduced in Bianconi et al. (2013) [24] as representative of a set of plausible rotation patterns in the ICM, as opposed to simpler but less physically motivated cases like rigid-body rotation (constant angular velocity) or flat rotation curve (a steep rise followed by a constant velocity). Here we do not make any attempt to connect the assumed rotation to the hydrostatic distribution of the ICM, which clearly would depend on the rotation pattern, and on the stability of the ICM that can be affected by turbulence due to a strong radial gradient in the tangential velocity. Therefore, we naively consider rotation in an almost spherically symmetric ICM distribution, which is unphysical. However, this is a good approximation to the case of A2107, which shows a regular morphology with small eccentricity, as we will discuss in Section 5.

To compute the map of the velocity along the line of sight, we need to include the effects of projection in the optically thin ICM distribution, and convolve the emission at each position with the corresponding emission weight. Clearly, the presence of different velocities projected along each line of sight

results in both a broadening of the line and a shift of the line centroid. The first effect [407] is not discussed here, since it is below the capability of CCD spectra, while the shift of the line centroid is potentially detectable, at least in the most prominent 6.7–6.9 keV emission line complex from the K_α lines of hydrogen- and helium-like iron. To compute the emission-weighted shift at each position on the plane of the sky, we need to assume a 3D density distribution of the ICM. The average ICM velocity (or redshift shift with respect to the global cluster redshift) along each line of sight is thus weighted by the emissivity, which, in turn, is given by the electron density squared $n_{\rm e}^2$ multiplied by the cooling function $\Lambda(T, Z)$. The dependence of the emission weight on temperature and metallicity is relevant when both quantities rapidly vary with the radius, which typically occurs in cool cores. For simplicity, here we consider only the case of a smooth, isothermal ICM distribution with uniform metallicity described by a single β-model [47], with an emission weight proportional simply to $n_{\rm e}^2$.

Each line of sight sees the contribution of different rotation velocities corresponding to different distances from the rotation axis, and each contribution is weighted by $n_{\rm e}^2$. Therefore, the resulting projected velocity map depends on the ratio of the two scale length: the core radius r_c of the β-model distribution of the ICM, and the scale length λ_0 of the velocity curve. The detailed derivation of the projected line of sight velocity map is provided in the Appendix. An example with the rotation axis lying in the plane of the sky, is shown in Figure 6.1, where all the quantities are expressed in terms of the virial radius $r_{\rm vir}$. The relevant parameters are therefore the concentration of the ICM 3D density distribution, defined as $c = r_{\rm vir}/r_{\rm c}$, and the concentration of the velocity curve, defined as $c_{\rm v} = r_{\rm vir}/\lambda_0$. In the left panel of Figure 6.1, the β parameter is set to 2/3, while the concentration parameters c and $c_{\rm v}$ are put equal to 5 and 10, respectively. For example, this implies, for a virial radius of 1.5 Mpc, a core radius $r_{\rm c} = 300$ kpc, and a velocity scale of $\lambda_0 = 150$ kpc, similar to the model adopted in Bianconi et al. (2013) [24]. For the sake of comparison, we show also the projected map in the case of a flat rotation and a rigid-body rotation (central and right panel, respectively). In all the cases the maximum velocity is set to $\mathtt{v}_{\rm max} = 1000$ km/s. In the case of a rotation profile described by Equation (6.1), the velocity reaches its maximum for $\lambda = \lambda_0$, and corresponds to $\mathtt{v}_{\rm max} = \mathtt{v}_0/4$.

In the left panel of Figure 6.1, the projected velocity map shows a peculiar shape that reflects the combined effects of the spherical ICM distribution and the cylindrical rotation pattern. This pattern can be, in principle, identified in high resolution redshift maps. However, given the poor spectral resolution and the need to extract spectra from large regions to increase the S/N, we can simply assume a constant projected velocity along lines parallel to the rotation axis. The rotation axis can be efficiently identified from simple observables, such as the average emission-weighted projected velocity in opposing semicircles. In the lower panels of Figure 6.1 we show the difference in the projected velocity averaged in each half of the cluster as a function of the angle θ (defined as in Section 4, with $\theta = \pi/2$ when the dividing line overlaps with the rotation axis).

From these examples we conclude that a simple analysis of CCD spectra with high S/N can identify the rotation axis, the maximum velocity and the scale length of the rotation curve, as long as the maximum velocity difference is comparable or larger than the spectral resolution of CCD data. This simple modelization does not take into account the flattening of the ICM distribution due to the rotation itself [24], nor, obviously, the presence of disordered bulk motions across the ICM, which can in principle overlap with the rotation pattern. Therefore, in the following we assume that rotation, if present, occurs around an axis in the plane of the sky, and that there are no significant bulk motions. We will consequently proceed in two steps: first, we identify the rotation axis by maximizing the velocity difference between semicircles as a function of the angle of the dividing line; then, we measure the velocity in stripes parallel to the preferred rotation axis previously identified. Finally, we fit the observed rotation curve with Equation (6.1) to derive the best-fit values of $\mathtt{v}_0$ and λ_0.

6.3 Data reduction and analysis

A2107 was observed with *Chandra* ACIS-I in VFAINT mode on September 7, 2004 for a total exposure time of 35.4 ks (ObsID 4960). The data are reduced with `CIAO` 4.10, using the most updated *Chandra* Calibration Database at the time of writing (CALDB 4.7.8). Unresolved sources within the ICM are

identified with `wavdetect`, checked visually and eventually removed. The cluster appears as a strong, extended source centered on the aimpoint, and covering a significant fraction of each of the four CCDs of ACIS-I (see Figure 6.2). The extraction radius we use to search for rotation is $\sim 5'$, corresponding to ∼240 kpc. This roughly corresponds to $\sim 0.3 r_{500}$, where the radius $r_{500} = 0.796$ Mpc has been estimated in Piffaretti et al. (2011) [275] using the scaling relation between luminosity L_{500} and mass M_{500}. This radius has been chosen in order to maximize the S/N, and it includes a total of 6×10^4 net counts in the 0.5–7 keV band. Since the ICM emission is spread across the entire ACIS-I field of view, the background spectrum is extracted from the 'blank sky' files with the `blanksky` script.

The X-ray spectral analysis is performed with `Xspec` v12.9.1 [8]. A double `apec` thermal plasma emission model [345] is used to fit the ICM spectra. Galactic absorption is described by the model `tbabs` [399], where the Galactic HI column density is set to the value measured in Kalberla et al. (2005) [165], which, at the position of A2107, is $n_{\rm H} = 4.46 \times 10^{20}$ cm^{-2}. During the fit, the temperature, metallicity and normalization of the two thermal components are left free, while the redshift is unique for both. The use of a double `apec` model is required to avoid possible bias associated with the presence of multiple temperatures, which may reflect in a slight but relevant change of the centroid of the line emission complex if the spectral model is forced to have a single temperature. We also check that the use of the 2–7 keV band, as opposed to the full 0.5–7 keV band, gives consistent results on the redshift. Finally, since the measurement of $n_{\rm H}$ often has large uncertain and low spatial resolution, for example Starling et al. (2013) [351] reports $n_{\rm H} = 5.35 \times 10^{20}$cm^{-2} at the position of A2107, we also repeated the fits leaving the value of $n_{\rm H}$ free to vary, and find values ranging from 5.0 to 11.0×10^{20} cm^{-2} when analyzing spectra extracted in annular bins at different radii. We do not consider this as a reliable indication for a larger value for $n_{\rm H}$, mostly because the use of two `apec` models at different temperature increases the degeneracy with the Galactic absorption. Our main concern here is that leaving free the $n_{\rm H}$ parameter does not change significantly the best-fit redshift. To summarize, this strategy allows us to keep under control the effects of colder gas and the complex interplay of different metallicity values at different temperatures, following the prescription discussed

Table 6.1. The *Chandra* data used in this work. Redshift values refer to optical estimates from the NASA/IPAC Extragalactic Database (NED). In the fourth column we list the total exposure times after data reduction.

Cluster	z	*Chandra* ObsID	Exptime (ks)
A2107	0.041	4960	35.4
A2029	0.077	4977	77.1
A1689	0.183	5004,6930,7289,7701	175.9

in Liu et al. (2015) [195].

We also reduce the data of other two clusters observed with *Chandra*, selected in order to have a comparable data quality: A2029 and A1689. These two targets do not have reported claims of rotation, and are considered relaxed clusters with regular morphology. We use these two targets as a basic control sample to test our strategy in searching and characterizing global rotation. In particular, we check whether a spurious rotation signature may appear as a result of our assumption. Clearly, a much larger control sample would be required to assess the statistical significance of a particular rotation measurement. This goes beyond the goal of this study. All the *Chandra* data used in this work, the ObsID and the total exposure time after data reduction are listed in Table 6.1.

6.4 Measurement of global rotation

To identify and quantify global rotation in our sources, we follow the two-step strategy described in Section 2. First, we identify the preferred axis of rotation, defined as the projected line that maximizes the velocity difference measured between the two semicircles. In practice, as shown in Figure 6.2 we divide the cluster into two semicircles A and A', with orientations θ and $\theta - \pi$ where θ is the angle from north counterclockwise to the vertical axis of semicircle A. We perform our spectral analysis of the total emission extracted from the regions A and A', and, in particular, we measure the best-fit redshift. This value corresponds to the emission-weighted average redshift of all the ICM components observed along the line of sight in the selected region.

The measurement of ICM redshift and the assessment of its uncertainty

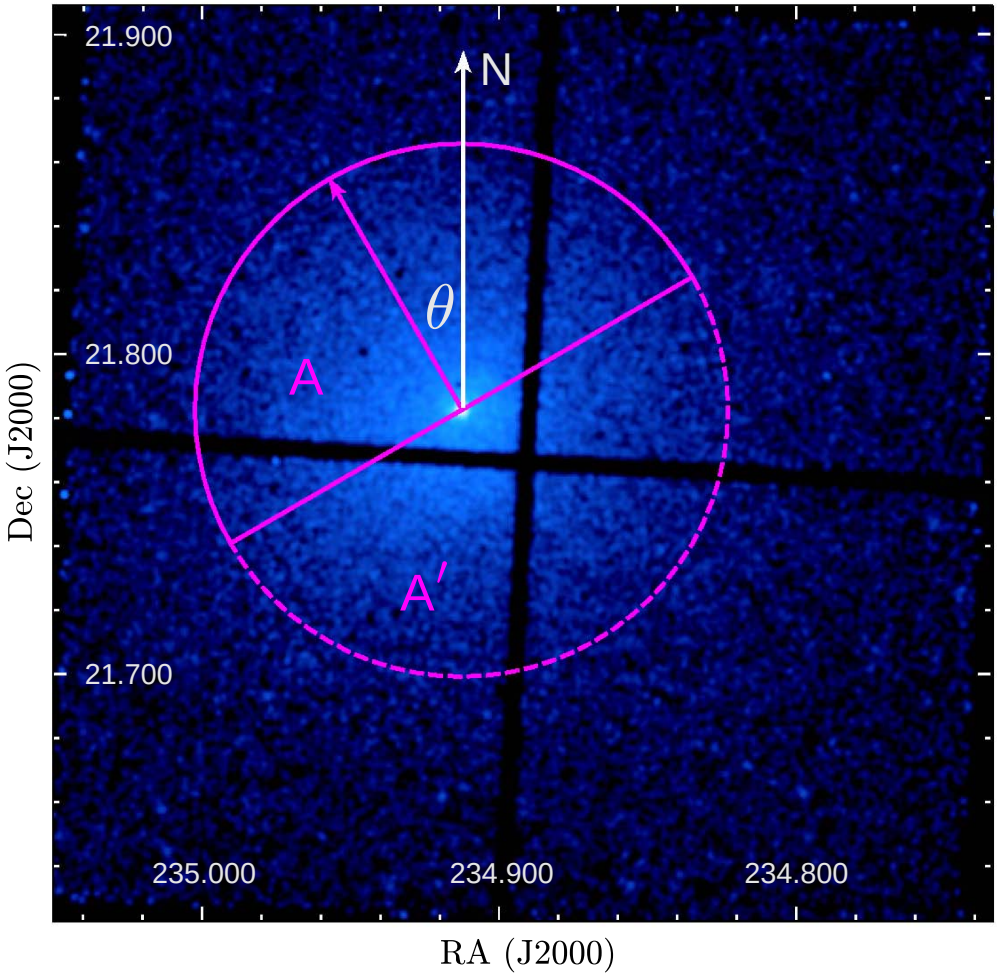

Figure 6.2. *Chandra* X-ray image of A2107 in the 0.5–7 keV energy range. We show the extraction regions and the definition of the position angle θ used to measure the projected velocity difference between semicircles and identify the preferred rotation axis. In the example shown in the figure, the axis (magenta arrow) with an orientation $\theta = 30°$ divides the cluster into the two semicircles A and A′.

have been described and applied in [195, 196] and [194]. From the difference of the two redshifts, we obtain the velocity difference between the two regions as $\Delta \mathrm{v} = \mathrm{v}_A - \mathrm{v}_{A'} = c \times (z_A - z_{A'})/(1 + z_{\mathrm{cl}})$, where z_{cl} is the cluster redshift $z = 0.0412$ [254]. We repeat the measurement as a function of θ and sample $\Delta \mathrm{v}$ as a function of θ in the range $-\pi < \theta < \pi$. The $\Delta \mathrm{v} - \theta$ plot is therefore made

Table 6.2. The best fit parameters of the rotation curves corresponding to different radii.

Radius	$\Delta \mathtt{v}_{\rm max}$ (km/s)	$\theta_{\rm max}$
0–$0.3r_{500}$	3230 ± 590	$-137 \pm 13°$
0–$0.1r_{500}$	3050 ± 680	$-99 \pm 16°$
0.1–$0.3r_{500}$	3950 ± 1170	$-169 \pm 16°$

of points that are highly correlated, since nearby points come from spectral fits of overlapping regions. The resulting curve is then fitted with the function $\Delta \mathtt{v} = \Delta \mathtt{v}_{\rm max} \cdot \cos(\theta - \theta_{\rm max})$, where $\theta_{\rm max}$ corresponds to the maximum velocity difference. The $\Delta \mathtt{v} - \theta$ plot and the best fit function are shown in Figure 6.3. The best fit parameters of the curve, obtained by a simple χ^2 fit, are $\Delta \mathtt{v}_{\rm max} = 3230 \pm 590$ km/s, and $\theta_{\rm max} = -137 \pm 13°$, where the 1 σ error bars are obtained by marginalizing with respect to the other parameter. This result by itself is not a probe of rotation, since a periodic curve is always obtained in any cluster with this method, simply because of noise, or because of the presence of some bulk motion in a particular region of the cluster. Clearly, a value of $\Delta \mathtt{v}_{\rm max}$ significantly higher than zero constitutes a strong indication that the dynamical properties of the ICM are far from being consistent with the usual hydrostatic, no-rotation scenario.

A large uncertainty on the rotation axis may suggest that the shape of the curve is not in agreement with that expected from coherent rotation. To investigate this aspect, we repeat the same measurement using semi-annuli rather than semicircles, in order to search for rotation in shells. In Figure 6.4 we show the rotation curves obtained with the same method but in different radial ranges, namely $r < 0.1r_{500}$ and $0.1r_{500} < r < 0.3r_{500}$. The best fit parameters of the rotation curves corresponding to different radii are listed in Table 6.2. We find that the two measurements of $\theta_{\rm max}$ obtained at different radii are inconsistent with each other at more than 3 σ, showing that a complex, non-cylindrical rotation pattern may be more adequate to describe the results. This may well be a hint for the presence of asymmetric bulk motions, however the data quality is not high enough to further investigate this possibility. Therefore, in the following we will assume $\theta_{\rm max}^{\rm ICM} = -137 \pm 13°$.

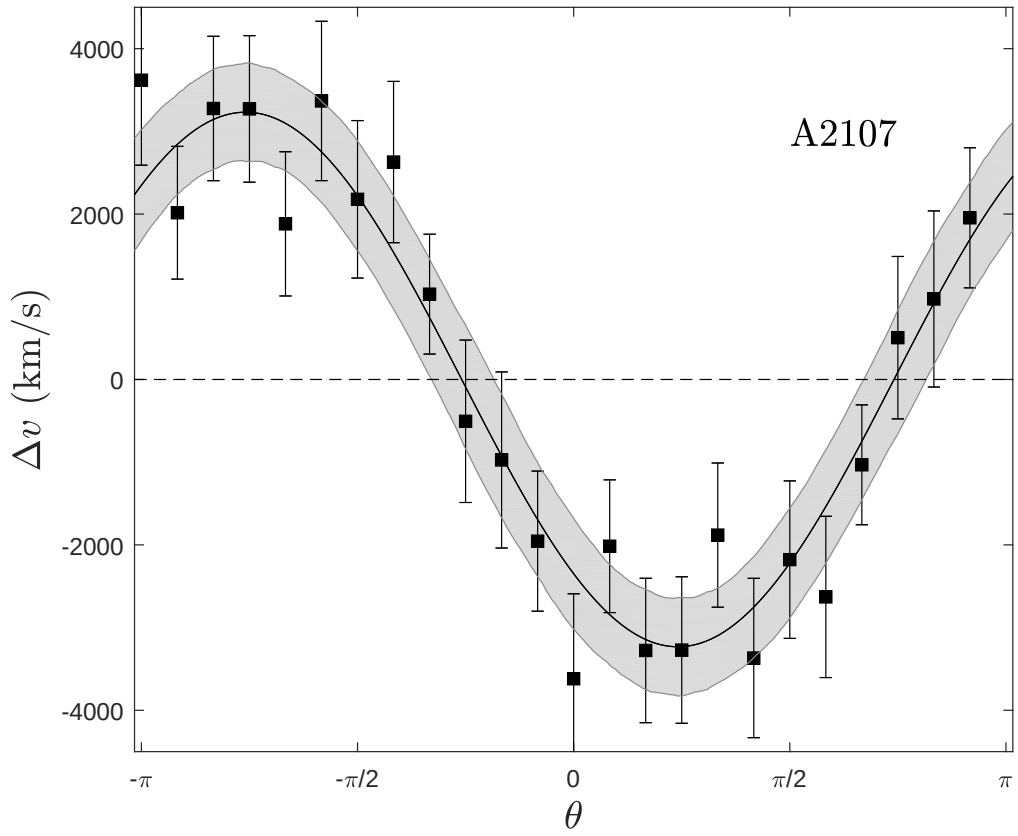

Figure 6.3. The $\Delta \mathrm{v} - \theta$ plot of A2107 measured in steps of $\Delta\theta = 15°$. The angle θ ranges from -180° to 180°, increasing counterclockwise from north ($\theta = 0°$) to east ($\theta = 90°$), and decreasing clockwise from north to west ($\theta = -90°$). Error bars correspond to 1 σ uncertainty.

After identifying the preferred rotation axis of the ICM and its uncertainty, we build the rotation curve by slicing the ICM into a number of independent linear regions parallel to the rotation axis. The average projected redshift is measured in each of these slices, whose size is chosen in order to have at least 10^4 net counts in the 0.5–7 keV band in each, and therefore a reasonable statistical error on the redshift. We identify four regions, where we compute the velocity difference with respect to the global redshift of the ICM, which is measured to be $z_X = 0.0393 \pm 0.0014$ by fitting the spectrum of the global emission within $5'$. Incidentally, we note that the X-ray redshift is slightly more than 1σ lower than the optical redshift value $z_o = 0.0412$. This difference

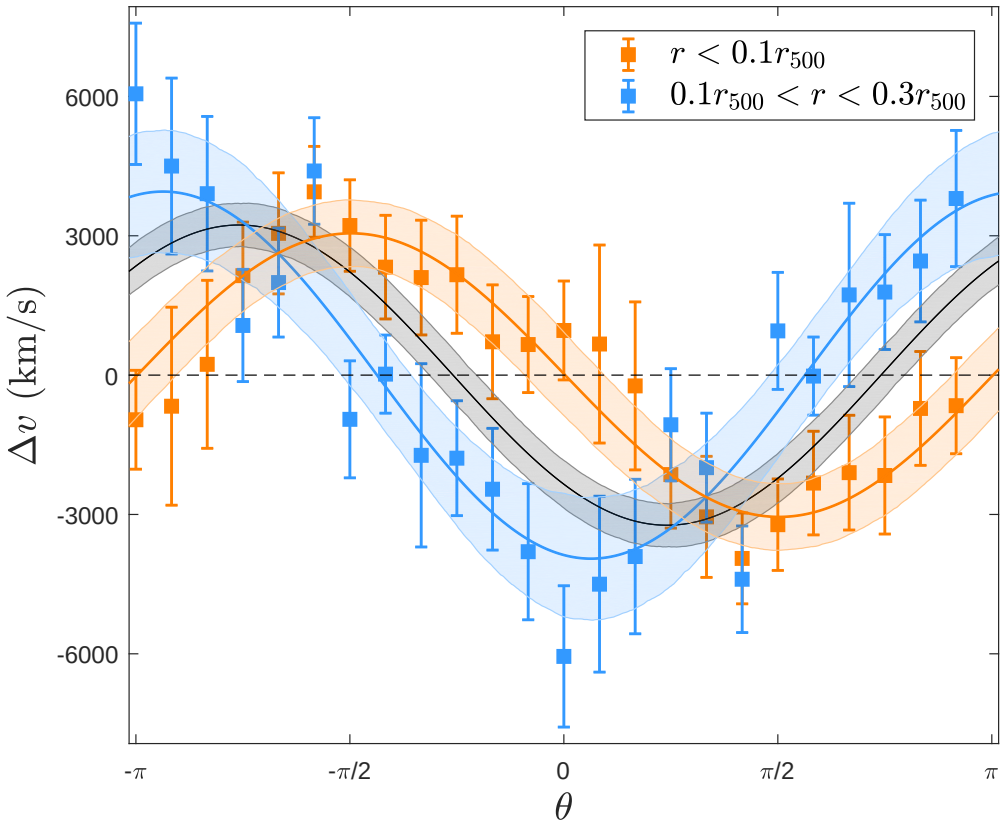

Figure 6.4. The velocity difference in A2107 measured across the rotation axis identified by θ at two different radial ranges. The black line shows the best-fit curve in Figure 6.3.

is not statistically significant, however it may be the hint of a disturbed ICM dynamics, possibly decoupled from the dynamics of the collisionless mass components (galaxies and dark matter), as may happen during mergers [194]. Moreover, the X-ray redshift we measure here is based on a smaller region of $5'$ radius, with respect to the $20'$ radius considered by Oegerle et al. [253, 254] to compute the average optical redshift.

We can now compute the velocity of each slice as $\mathrm{v}_i = c \times (z_i - z_X)/(1 + z_X)$ where i is the index of the slice. The result is shown in Figure 6.5. If we fit these four points with the same rotation curve described in Section 2, we find $\mathrm{v}_0 = 5500 \pm 2400$ km/s, corresponding to $\mathrm{v}_{\mathrm{max}} = 1380 \pm 600$, and $\lambda_0 = 165 \pm 110$ kpc. The χ^2 value of the fit is below unity because of the large error bars

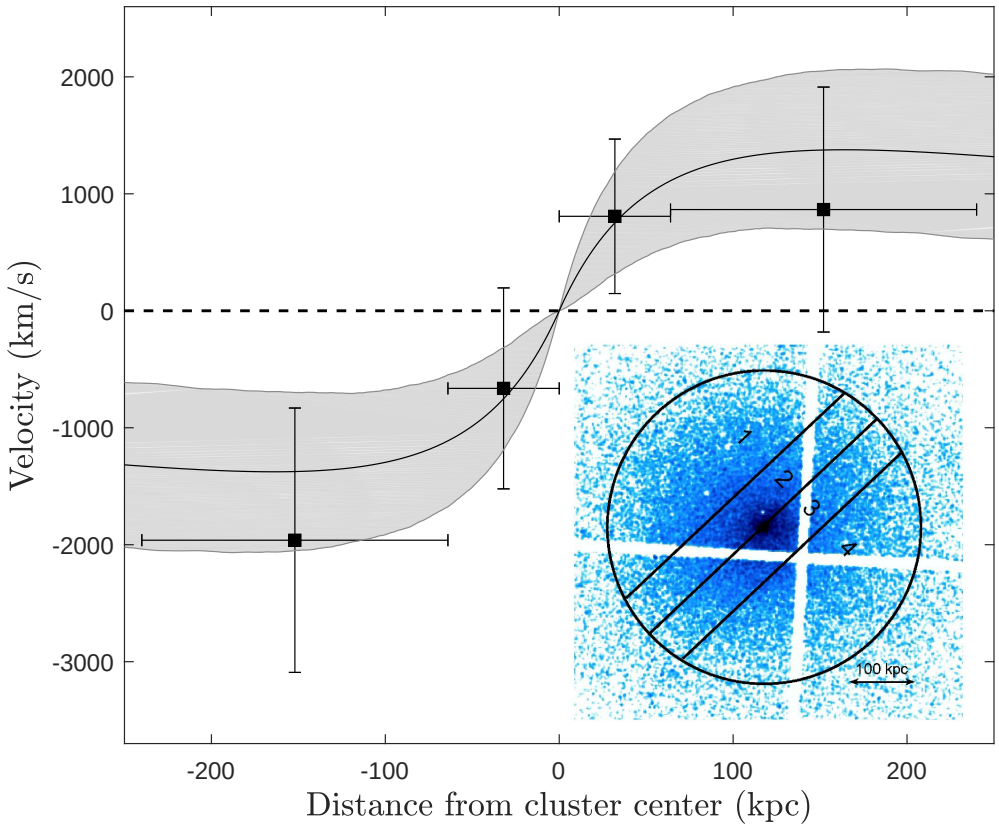

Figure 6.5. Velocity gradient across the slices parallel to the rotation axis defined in Figure 6.4. The solid line shows the best-fit function and the shaded area shows the 1 σ confidence interval.

($\chi^2 = 0.48$), while the χ^2 value for no rotation is 5.79, which corresponds to rejection at a 95% level for 3 degrees of freedom.

We repeat the same analysis on the two relaxed clusters A2029 and A1689, where no significant rotation is expected. In Figure 6.6, we show the $\Delta v - \theta$ curves of these two clusters, where we do not find signatures of rotation. As already noticed, formally a rotation axis can be found for both clusters, but with large uncertainty, and on the basis of a non-significant maximum redshift difference. We proceed with the measurement of the rotation curve, slicing the clusters parallel to the rotation axis. The rotation curves are shown in the right panel of Figure 6.6. Both profiles are consistent with no rotation. Assuming no rotation in these two clusters results in χ^2 of 1.02 and 1.56 with

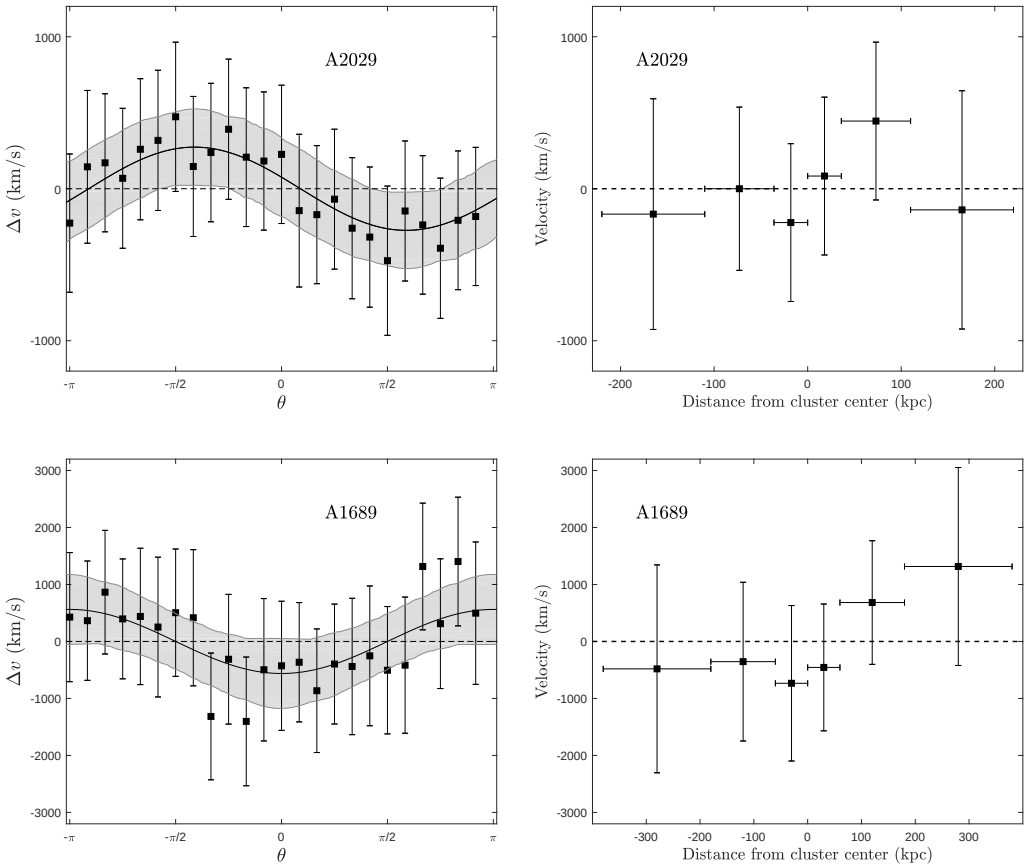

Figure 6.6. Results for the control sample A2029 and A1689. *Left*: Δv-θ curves. *Right*: Velocity gradient along the slices parallel to the rotation axis defined by the Δv-θ curve.

5 degrees of freedom. Clearly, we cannot exclude the presence of rotation in these clusters on the basis of our data, but we exclude a rotation signature with the same significance found for A2107.

We conclude that our spectral analysis of the ICM is consistent with a rotation reaching a maximum velocity of 1000–2000 km/s at a radius between 100 and 300 kpc. The velocity difference between two sides of the cluster is significant at more than 2σ. We also find a null result in two regular clusters, showing that there are no obvious systematic effects in our analysis strategy that can mimic the presence of rotation, providing thus support to the capability of our analysis in finding velocity difference across the ICM.

6.5 Discussion

Before discussing the implications of our findings, we rapidly review possible systematics that may affect our results. Uncertainties on the best-fit redshift values due to calibration issues and fluctuation of the gain of CCDs as a function of the epoch of observation have been discussed by us in detail by Liu et al. [195, 196]. In this work, we only use a single observation, so the time variation of CCD is negligible. Calibration may also change as a function of the position on the CCD. We perform a quick check by computing the position of the Au Lα and Ni Kα fluorescent lines in the spectra obtained from the extraction regions used in our analysis and from the corners of the CCD. Within the statistical limits due to the modest exposure time we are not able to find any significant difference in the centroid of the lines in difference places. Despite we are not able to firmly rule out the presence of some gain variation across the CCD, we are nevertheless able to estimate its impact to be less than the current statistical error on our redshift measurements. We also refer to the extensive investigation on calibration issues on redshift measurement with *Chandra* presented in Liu et al. (2015) [195], where we constrained these effects to be at maximum a 5–10% of the typical statistical error, and therefore not relevant to our conclusions.

We also explore the impact of the uncertainty of background modelization on the redshift measurement. Because the background spectrum we used is generated from the *Chandra* 'blank-sky' files, its normalization in the hard energy range may not be appropriate for our observation. We conservatively consider a 10% maximum variation in the normalization of the background spectrum, and verify that this reflects in a fluctuation in redshift of the order of $\sim$5%, which is well below the statistical error, confirming that the redshift gradient shown in Figure 6.5 is robust against uncertainties in the background modelization.

We then compare our results with the rotation identified by the spectroscopy of the member galaxies in Song et al. (2018) [347]. In this work, the orientations of the maximum velocity are measured in 3 different bins: $0' \leq r < 20'$, $20' \leq r < 35'$, and $35' \leq r < 60'$. Since the extraction radius in our X-ray analysis is only $5'$, we compare our result with that of the [$0'$–$20'$] optical bin.

We find that the rotation axis are significantly different, with $\theta^{\rm gal}_{\rm max} = 7 \pm 14^{\circ}$, and $\theta^{\rm ICM}_{\rm max} = -137 \pm 13^{\circ}$, with the corresponding momentum vectors pointing almost in opposite directions. In Figure 6.7, where the X-ray surface brightness contours from *Chandra* are overlaied to the optical image of A2107 from the Sloan Digital Sky Survey, we also show the preferred rotation axis from the optical and X-ray data. Despite we are comparing rotation velocities estimated at different scales, we are surprised to find a rotation axis with a direction completely different from the optical one. It is not surprising, however, to observe the ICM dynamically decoupled from the galaxies, as we discussed in Chapert 5. Still, in the case of global rotation, there are no obvious reasons why we should not observe a consistent rotation axis in the optical and in the X-ray. Incidentally, if we consider the $20'$–$35'$ radial bin in Song et al. (2018) [347] with $\theta_{\rm max} = -150 \pm 36^{\circ}$, we find that the rotation axis of the galaxies and of the ICM are consistent within the statistical errors. Clearly, this may well be just a coincidence, and our findings seem to suggest that the velocity pattern is probably not uniform, and that the galaxies and ICM do not share the same projected velocity across the cluster.

Another critical aspect is the effect on the total mass measurement implied by the temperature profile and the measured rotation. The total mass without considering rotation is computed via the hydrostatic equation:

$$\frac{\nabla P}{\rho} = -\nabla\Phi = -\frac{GM(r)}{r^2}, \tag{6.2}$$

where ρ, P and Φ denote the gas density, pressure, and the total gravitational potential, respectively. Inserting $P = nk_{\rm B}T = \rho_{\rm g}k_{\rm B}T/(\mu m_{\rm p})$, the total mass within r is:

$$M(r) = -\frac{k_{\rm B}T(r)r}{G\mu m_{\rm p}}\left(\frac{d{\rm ln}\rho_{\rm g}(r)}{d{\rm ln}r} + \frac{d{\rm ln}T(r)}{d{\rm ln}r}\right). \tag{6.3}$$

We measure the deprojected temperature and density profiles using 8 and 20 bins, respectively, with the routine DSDEPROJ [314]. We then fit the temperature profile with the model proposed by Vikhlinin et al. (2006) [388], and the density profile with a single β model. The deprojected temperature and density profiles are shown in Figure 6.8. The best fit functions are used to compute the logarithmic slopes in Equation (6.3). The hydrostatic mass profile is shown in Figure 6.9. With very large uncertainties in the outskirts,

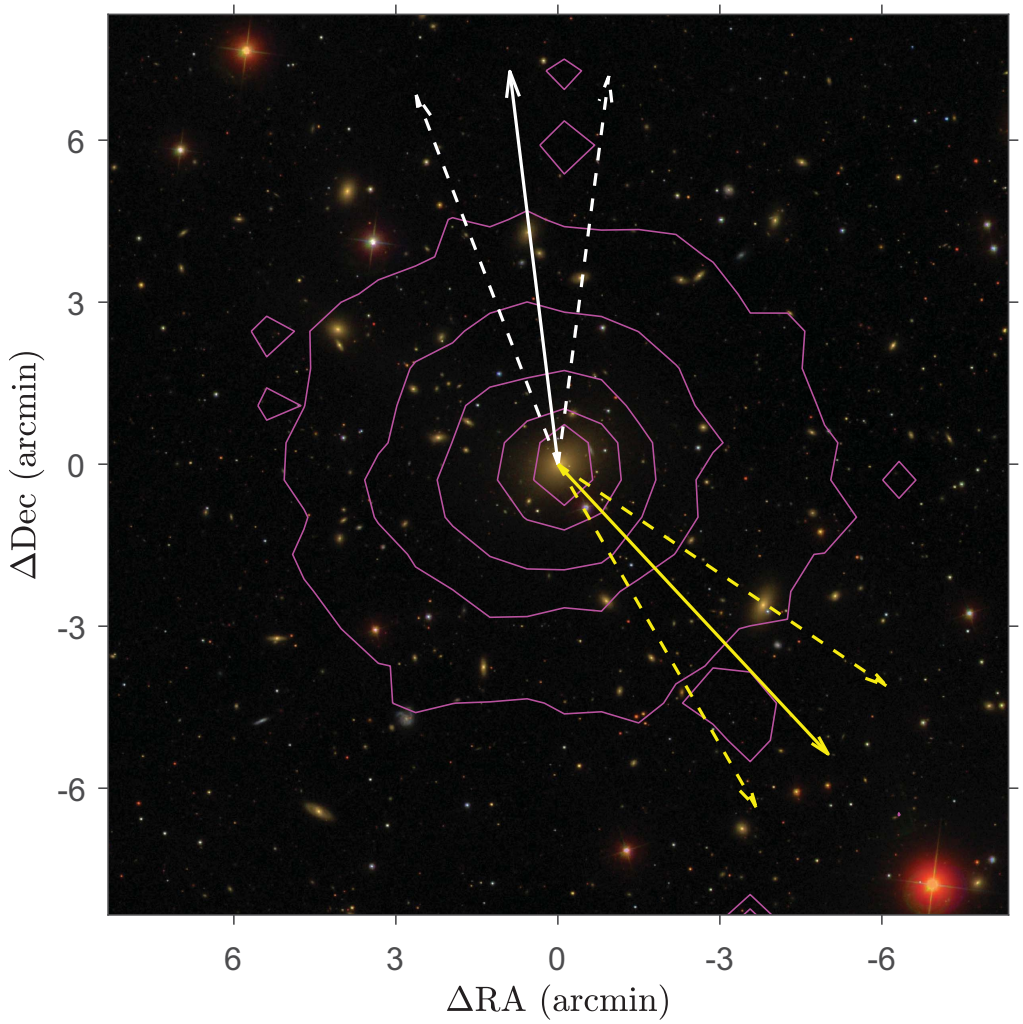

Figure 6.7. SDSS RGB image of A2107 obtained from g, r, i band images. Magenta contours correspond to isophotes in the *Chandra* X-ray image. White and yellow arrows mark the preferred direction of rotation of the member galaxies within 0–20′ [347] and of the ICM, respectively. Dashed arrows show the 1 σ uncertainty on the angle of the rotation axis.

we measure a value of $(4.5 \pm 1.4) \times 10^{13}\, M_{\odot}$ at $r = 200$ kpc, in agreement with the mass profile obtained from the galaxy velocity dispersion by Kalinkov et al. (2005) [166].

If we consider hydrostatic equilibrium in presence of rotation, we are assuming that rotational motions do not affect motions along the radial direction.

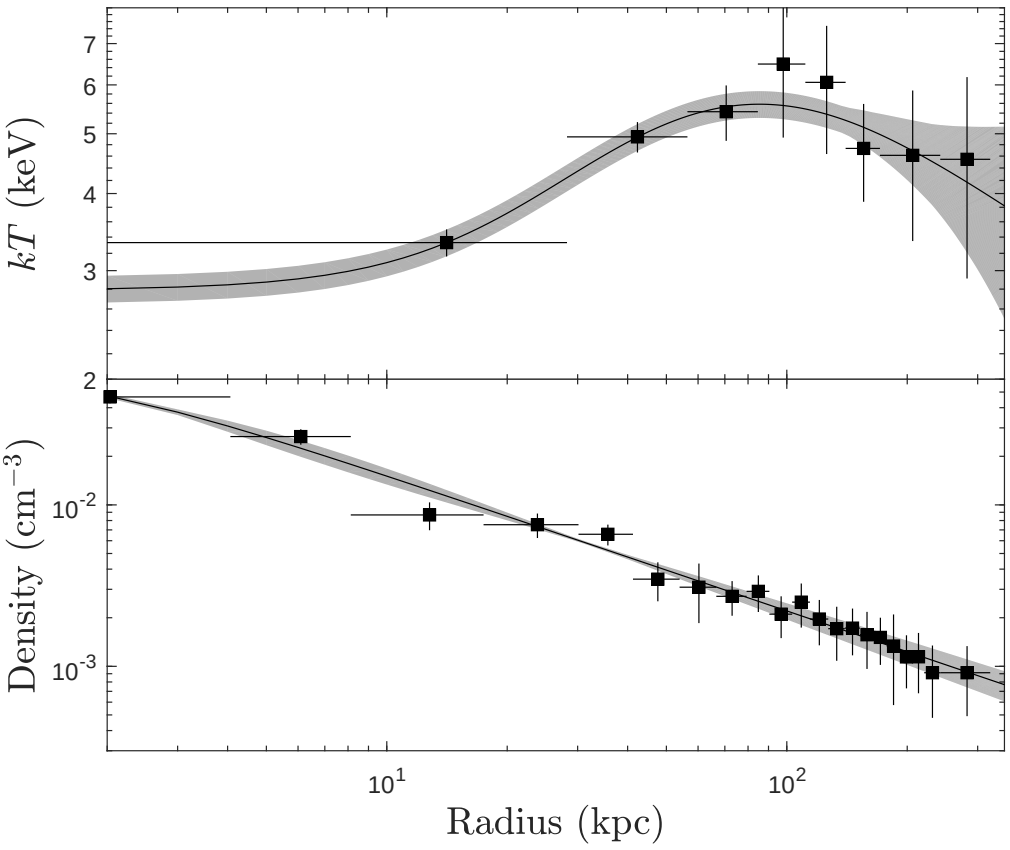

Figure 6.8. Deprojected temperature (upper panel) and density (lower panel) profiles of A2107.

Therefore, we should consider a term proportional to $(\mathrm{v}^2/\lambda)_{\mathrm{rad}}$ in Equation (6.3), which is the projection of the centripetal force on the radial direction at each point. A self consistent treatment can be found in Bianconi et al. (2013) [24]. Here we do not make any attempt to solve for the ellipsoidal mass distribution implied by the presence of rotation and hydrostatic equilibrium. However, we can compute the mass term along the direction perpendicular to the rotation axis, that, at the radius λ_0 corresponds to a correction of $\sim 6 \times 10^{13} M_{\odot}$. From Figure 6.9 it is possible to verify that this correction term is comparable, if not larger, to the hydrostatic mass computed in the assumption of no rotation at the same radius. This clearly shows that the spherical symmetry is inconsistent with such a large rotation. On the other hand, given the large uncertainties, if we consider the 2σ lower limit to the

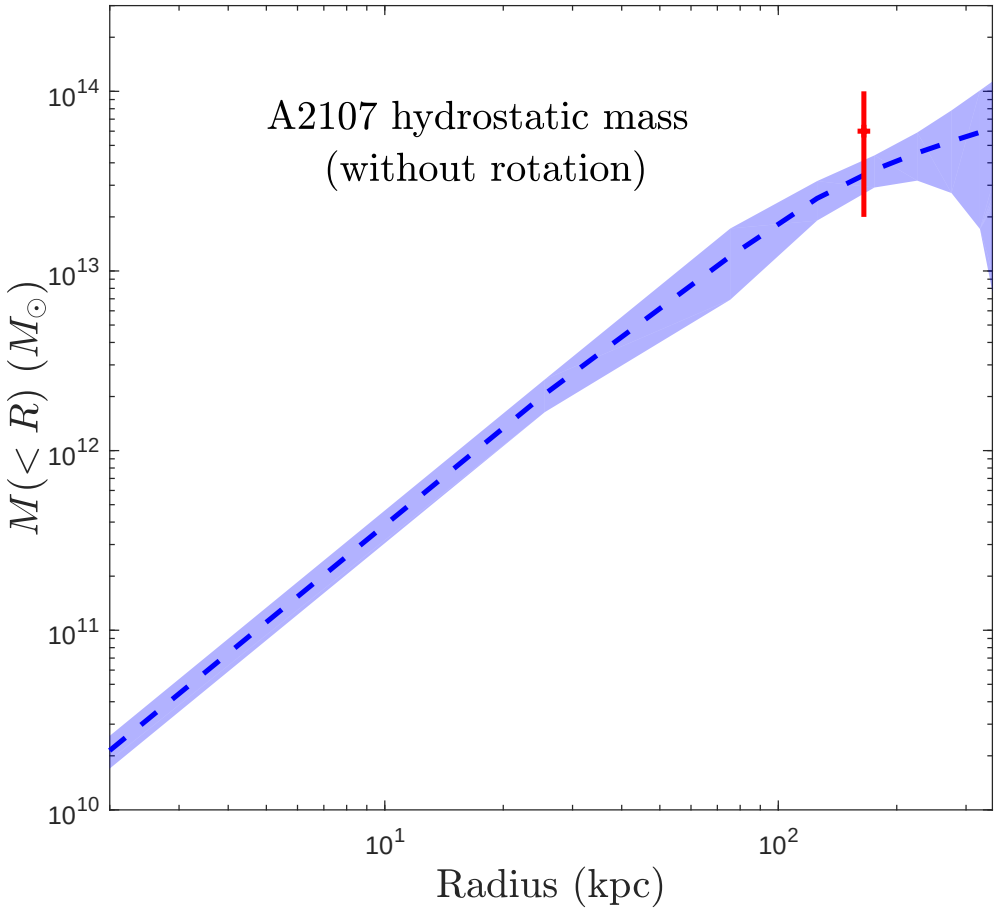

Figure 6.9. The hydrostatic mass profile of A2107 (without including the effect of global rotation) with 1 σ uncertainty computed with bootstrapping shown as a shadowed area. The cross is the approximated mass-correction term due to rotation along the $z = 0$ plane at $\lambda_0 = 160$ kpc.

mass term due to rotation, we find a correction of the order of a few $10^{12} M_\odot$, which corresponds to $\sim 10\%$ of the hydrostatic mass at the same radius, in better agreement with the cluster morphology.

The best-fit value of $\mathrm{v}_{\mathrm{max}}$ is therefore at variance with the regular and round isophotes of the surface brightness of A2107, that can be appreciated in Figure 6.7. We fit the X-ray surface brightness distribution with a 2-D elliptical β model, and get an ellipticity of 0.097, indicating an almost round morphology, that, as shown, may be reconciled with the measured rotation

only when assuming values lower by $\sim 2\sigma$ with respect to the best fit.

If we relax the hypothesis of hydrostatic equilibrium, we can consider a major merger scenario as opposed to rotation. This scenario is suggested by the measurement of an exceptionally high velocity of the BCG relative to the bulk of the galaxy population of ~ 270 km/s [253]. For some reason, however, this possible major merger along the line of sight is not observed in the galaxy distribution nor is associated with any disturbed morphology in the X-ray image. In addition, the BCG is still perfectly centered on the cool core within a few arcsec, as shown in Figure 6.7. On the other hand, the BCG is not active both in X-ray and in radio, an occurrence that, particularly in the radio, should be observed in the majority of cool cores [357]. A possible solution may be provided by an ongoing major merger along the line of sight in its early stages, when the ICM is already significantly decoupled from the bulk of the galaxy, including the BCG, and the cool core is still visible but is not 'active' anymore (in the sense that it does not feed the AGN in the BCG).

To summarize, the results obtained in this work do not allow us to conclude unambiguously that the ICM in A2107 is rotating to some degree. In particular, it is almost impossible with CCD data to distinguish a genuine rotation from disordered and asymmetric bulk motion, or from a major merger along the line of sight. Increasing the depth of the observation may help in reducing the statistical error on the measured redshift, an improvement that can be better achieved with CCD data from XMM-Newton, which has a significantly larger effective area with respect to *Chandra* and therefore it performs more efficiently in observations where high angular resolution is not mandatory. A better redshift map, in principle, can provide an unambiguous view of a rotation pattern. In particular, it will be possible to determine whether the rotation signature is due to a smooth pattern across the entire ICM distribution, or it is merely an effect of one or more mergers, with a patchy redshift map. However, spectral analysis of CCD data would improve rather slowly with increasing exposures, and therefore would require a large investment of observing time.

Another possible strategy is the observation with gratings at constrained angles. In this last case, the rotation (or the asymmetric bulk motion) should show up more clearly as a shift in the emission lines in the direction perpendicular to the dispersion, which should be aligned to the rotation axis. We

remark that A2107 has the advantage of a relatively low temperature, so that several emission lines can be visible in the energy range probed by gratings. At the time of writing, we have submitted an XMM proposal to exploit the EPIC CCD and the RGS onboard XMM-Newton, asking for an angle-constrained observation to maximize the chance to identify the rotation curve in the RGS spectrum. A real breakthrough in the study of the distribution of angular momentum at cluster scale, may be achieved in the next future only with the advent of X-ray bolometers, or, possibly, with better SZ data [58].

6.6 Conclusions

In this work we define a strategy to search for signatures of X-ray cluster rotation in CCD data, on the basis of a simple rotation model. We report the measurement of a possible rotation in the ICM of the cluster A2107, obtained through a spatially resolved measurement of the redshift inferred from the centroid of the iron emission line complex at 6.7 and 6.9 keV in *Chandra* ACIS-I spectra. We identify a preferred rotation axis, and find a significant velocity gradient compatible with a rotation pattern with maximum tangential velocity $\mathtt{v}_{\rm max} = 1380 \pm 600$ km/s at a radius $\lambda_0 \sim 160$ kpc.

If confirmed, this would be the first detection of ICM rotation. Although this work has been stimulated by the previous claims of rotation in A2107 obtained by Manolopoulou et al. (2017) [205] and Song et al. (2018) [347] on the basis of optical spectra of the member galaxies, our results differ both in the direction of the preferred rotation axis, and in the amplitude of the rotation curve. In particular, the high velocity associated with the ICM rotation in our data would be in conflict with the assumption of hydrostatic equilibrium and with the morphology of the cluster. We argue that an unnoticed off-center major merger along the line of sight can be an alternative explanation of the dynamical status of A2107. Therefore, our analysis confirms the peculiar dynamical nature of the otherwise regular cluster A2107, but is not able to provide a definitive answer to the rotation versus merger scenario. We argue that a discrimination among these two scenarios should wait for the next-generation X-ray facilities carrying X-ray bolometers onboard, while some improvements can still be made with further CCD data and angle-constrained

grating spectra, preferably with XMM-Newton. The measurement of ICM rotation is potentially relevant for investigation of the distribution of angular momentum at cluster scale, which is still a debated aspect of the gravitational growth of cosmic structures. Therefore, any insight that can be obtained on the basis of current X-ray facilities in the next years, particularly before XRISM, due to launch in the early 2020s, would be extremely useful to refine the analysis strategy in this field.

Acknowledgements

We thank the anonymous referee for a detailed and constructive report. We acknowledge financial contribution from the agreement ASI-INAF n.2017-14-H.0.

6.7 Appendix: Projected velocity map of ICM with a generic rotation curve

To compute the projected velocity map for a generic rotation curve in a spherical ICM, we need to convolve a cylindrical rotation curve with a spherical distribution of ICM density. As noted in Section 2, we do not solve for a self-consistent hydrostatic and rotating ICM distribution in a fixed dark matter potential well, so we simply assume the case of a spherical symmetry for the ICM distribution despite its rotation. This assumption can be considered a fair description only when the rotational support is a minor correction to the pressure support at each radius. Our treatment here is meant only to give us a guideline on how to design the analysis strategy to recover the rotation curve.

The projected velocity is measured from the redshift of the iron complex emission line, which, at any position on the sky, is the emission-weighted value of the centroid of the lines emitted by each ICM component intercepted by the line of sight. To compute the emission-weighted quantity along the line of sight, we consider a cylindrical reference system with the z axis pointing towards the observer, while the rotation axis is one of the two axis on the plane of the sky. With this choice, the transformation from spherical coordinate r,

θ and ϕ (to describe the ICM properties) to the cylindrical coordinates ρ, θ and z (to describe the projected redshift map) assume the convenient form $\rho = r\sin\phi$, $\theta = \theta$ and $z = r\cos\phi$

We consider a generic rotation curve that depends only on the distance from the rotation axis λ, and it is characterized by an overall normalization and a scale length λ_0. The velocity perpendicular to the vector $\hat{\lambda}$ is thus $\mathtt{v}(\mathtt{v}_0, \lambda, \lambda_0)$.

The distance from the rotation axis reads

$$\lambda = \sqrt{(\rho \times \cos\theta)^2 + z^2}\,. \tag{6.4}$$

The velocity projected along the line of sight is therefore $\mathtt{v}_{\rm los} = \mathtt{v}(\mathtt{v}_0, \lambda, \lambda_0) \times \cos\alpha$, where α is the angle between the velocity vector and the line of sight. We can show that we also have $\cos\alpha = \rho\cos\theta/\lambda$. If we use a generic weighting function $W(\rho, \theta, z)$, we can express the observed $\mathtt{v}_{\rm los}$ as

$$\mathtt{v}_{\rm los}(\rho, \theta) = \frac{\int W(\rho, \theta, z) \cdot \mathtt{v}(\mathtt{v}_0, \lambda, \lambda_0) \cdot \frac{\rho\cos\theta}{\lambda}\, dz}{\int W(\rho, \theta, z) dz} \tag{6.5}$$

where λ depends on ρ, θ and z through Equation (6.4), and the integral is performed over the range $-\sqrt{R_{\rm v}^2 - \rho^2} < z < \sqrt{R_{\rm v}^2 - \rho^2}$, with $R_{\rm v}$ being the virial radius. For example, if we assume the velocity curve described in Section 6.2, an isothermal ICM with a uniform metallicity, and a single β model for the ICM 3D density distribution, with $\beta = 2/3$ for simplicity, we obtain the following expression:

$$\mathtt{v}_{\rm los}(\rho, \theta) = \mathtt{v}_0 c_{\rm v} \rho\cos\theta \frac{\int_{-\sqrt{1-\rho^2}}^{\sqrt{1-\rho^2}} \frac{dz}{(1+c^2(\rho^2+z^2))^2 (1+c_{\rm v}\sqrt{\rho^2\cos^2\theta + z^2})^2}}{\int_{-\sqrt{1-\rho^2}}^{\sqrt{1-\rho^2}} \frac{dz}{(1+c^2(\rho^2+z^2))^2}} \tag{6.6}$$

where the two parameters describing the scale length are defined as $c = R_{\rm v}/R_c$ and $c_{\rm v} = R_{\rm v}/\lambda_0$, and the variables ρ and z have been rescaled by the virial radius $R_{\rm v}$, and therefore range in the interval $(0, 1)$. This formula is valid for a rotation axis on the plane of the sky and it has been used to generate the velocity map in the left panel of Figure 6.1. Maps with different rotation curves can be obtained simply by substituting the curve function $\mathtt{v}(\mathtt{v}_0, \lambda, \lambda_0)$.

Chapter 7

Future perspectives

In this Chapter I will outline the current perspective to continue my scientific research along the lines discussed in this Thesis. I will focus both on the next and the far future, drawing a path that connects the use of current facilities with the future major X-ray missions, possibly bridging a gap of several years when no major new X-ray facilities are expected, that is a matter of concern for a large part of the X-ray astronomical community.

Archival studies

As the two main X-ray observatories, *Chandra* and XMM, have both been operating for 20 years, X-ray astronomy, particularly the study of ICM physics, is reaching a critical point. On one hand, the huge amount of archived data is a valuable legacy and provides a great opportunity to systematically explore the nature of ICM with a sample size of $few \times 10^2$–10^3 clusters, up to redshift 1 and beyond. On the other hand, since *Chandra* is rapidly losing efficiency in the soft band, it is almost impossible to perform high-angular resolution observations on newly discovered high-z clusters in the next decade (for example in the SZ, or in the radio band).

My future line of research is built upon this situation. Clearly, the systematic use of the X-ray archives is a key ingredient to continue my research on the evolution of the chemical enrichment of the ICM. Although the redshift space at $z > 1$ will be hardly filled with more than a handful of sources, there is a lot of investigation strategies that can be successfully applied to the medium- and low-z clusters.

Another direction towards a comprehensive approach, is to frame the

current knowledge of ICM chemical evolution into a more general framework, with the aim of drawing the chemical evolution of the entire population of galaxy clusters, and to connect it to the global chemical evolution of the Universe. As shown in this Thesis, a key point in this framework is a better constraint on the total iron mass in clusters, for which a key ingredient is the abundance and distribution of iron in cluster outskirts (1–2 r_{500}). It is often assumed that a plateau is sufficient to describe the iron distribution at large radii. However, while only a few relevant works have been done in this respect, more quantitative assessment is needed to confirm this assumption. The archived data of XMM-Newton and Suzaku, and , at some level, also the data of the eROSITA mission, which is just beginning the operations at the time of writing, will be essential in this work.

Use of current X-ray facilities and GO projects

One of the most promising extensions of my work is the link between the enrichment studies of the ICM performed in this Thesis (especially the properties of the iron peak and the central iron drop) to the cycle of baryons in the core of galaxy clusters. This includes the feedback processes in cool cores, the formation and evolution of the central BCG, and also the properties of the intracluster light, which also contributes at some level to the formation of the iron peak.

However, the progressive decrease of the effective area of *Chandra* in the soft band due to the contamination of the ACIS detector, which is a dramatic loss for X-ray astronomy, makes it hard to collect photons below 1 keV which are clearly key to study the colder gas components in the core of clusters. In this perspective, the main instrument to investigate the physics of the ICM is XMM-Newton, thanks to its much greater capability of collecting photons. Unfortunately, the HEW of about 15 arcsec is well below the requirement to image and resolve the details of the ICM at the scale of few kpc in medium- and high-z clusters that, as we know, are relevant to understand the details of feedback. Nevertheless, there is still a large space to explore with XMM in low and medium-z clusters.

Another aspect that can be successfully investigated with XMM-Newton, is the ICM dynamics. Once again, the *Chandra* resolution that have been

key to my previous works on ICM dynamics, is severely reduced due to the dearth of effective area, and XMM-Newton becomes a key instrument thanks to the high S/N. The medium angular resolution of XMM-Newton that is still sufficient to spatially resolve dynamic structures in low-z clusters. For example, The combination of EPIC and RGS data is expected to unveil the puzzling dynamical status of the 'rotating' cluster Abell 2107, possibly confirming for the first time the presence of a coherent rotation in the ICM, which would open up the systematic study of the initial distribution of angular momentum at cluster scale, and provide pivotal constraints to the hierarchical evolution of cosmic structures.

Future missions and long-term plan

In the long term, measuring line-of-sight motions of the ICM with X-ray CCD data is a relatively new area with a large potential in the future, provided that the systematic uncertainty due to calibration issues can be reduced to a few hundred km/s (at the time of writing this thesis, Sanders et al. [319] propose a new technique to calibrate the energy scale of EPIC-pn using the fluorescent instrumental background lines, and refine the energy scale to better than 150 km/s). On the other hand, the observations of *Hitomi* on Perseus have proved the powerful ability of X-ray calorimeters in constraining the line of sight velocity of ICM to an accuracy of a few tens of km/s. Despite the untimely loss of *Hitomi*, its successor, XRISM, which will be launched in early 2020s, and Athena, in the far future (Athena is scheduled to be launched in early 2030s), and possibly also the NASA mission Lynx, which is actually proposed as a major NASA mission, will for sure revolutionize our knowledge of the ICM dynamics.

X-ray calorimeters will also be key to search for the cold gas in the cool cores of massive clusters. With a spectral resolution of few eV, despite the poor angular resolution, the observation with bolometers will allow one to identify the presence of residual cooling flow down to a level of $\sim 10 M_{\odot}$/yr or lower, which should be more common than the elusive major cooling flow, and currently at the limit of detectability of XMM-Newton even with large exposures in bright clusters.

A major problem with the future is, nevertheless, constituted by the lack

of a sensitive mission able to expand the parameter space at high redshift. The all sky survey by eROSITA will be a major improvement upon the most recent X-ray all-sky survey, which dates back to ROSAT. However, the poor angular resolution (slightly worse than that of XMM-Newton at the aimpoint) hampers severely the capability of detecting small size (few tens of arcsec) extended sources, not only because of the low S/N, but mostly because of the confusion with the overwhelming population of unresolved sources (AGN and star forming galaxies). This implies that the number of well studied X-ray clusters will remain limited to a few tens of sources. Needless to say, any evolutionary study on the properties of clusters would strongly benefit from an increased X-ray cluster sample. The lack of a dedicated, sensitive survey mission, in the form of a Wide Field X-ray Telescope surveying at least half of the sky, would be, in my view, one of the major issues that will affect the future of X-ray astronomy. As a term of comparison, such a mission would be the equivalent of the impact that Sloan Digital Sky Survey (started 20 years ago) had on optical astrophysics. In this respect, I foresee part of my scientific work to be in support of such a mission, as a necessary tool to bring to completion a systematic and comprehensive study of the chemical and thermodynamical properties of the ICM across cosmic epochs.

Bibliography

[1] Allen, S. W., Evrard, A. E., and Mantz, A. B. Cosmological Parameters from Observations of Galaxy Clusters. *ARA&A*, **49** (2011), 409. arXiv:1103.4829, doi:10.1146/annurev-astro-081710-102514.

[2] Anders, E. and Grevesse, N. Abundances of the elements - Meteoritic and solar. *GeoCoA*, **53** (1989), 197. doi:10.1016/0016-7037(89)90286-X.

[3] Anderson, M. E., Bregman, J. N., Butler, S. C., and Mullis, C. R. Redshift Evolution in the Iron Abundance of the Intracluster Medium. *ApJ*, **698** (2009), 317. arXiv:0904.1007, doi:10.1088/0004-637X/698/1/317.

[4] Andrade-Santos, F., et al. The Fraction of Cool-core Clusters in X-Ray versus SZ Samples Using Chandra Observations. *ApJ*, **843** (2017), 76. arXiv:1703.08690, doi:10.3847/1538-4357/aa7461.

[5] Andreon, S. The enrichment history of the intracluster medium: a Bayesian approach. *A&A*, **546** (2012), A6. arXiv:1209.0565, doi:10.1051/0004-6361/201219194.

[6] Arimoto, N. and Yoshii, Y. Chemical and photometric properties of a galactic wind model for elliptical galaxies. *A&A*, **173** (1987), 23.

[7] Arnaud, K. A. A catalog(ue) of cooling flows. In *NATO ASIC Proc. 229: Cooling Flows in Clusters and Galaxies* (edited by A. C. Fabian), pp. 31–40 (1988).

[8] Arnaud, K. A. XSPEC: The First Ten Years. In *Astronomical Data Analysis Software and Systems V* (edited by G. H. Jacoby and J. Barnes),

vol. 101 of *Astronomical Society of the Pacific Conference Series*, p. 17 (1996).

[9] Arnaud, K. A. XSPEC: The First Ten Years. In *Astronomical Data Analysis Software and Systems V* (edited by G. H. Jacoby and J. Barnes), vol. 101 of *Astronomical Society of the Pacific Conference Series*, p. 17 (1996).

[10] Arnaud, M. and Raymond, J. Iron ionization and recombination rates and ionization equilibrium. *ApJ*, **398** (1992), 394. doi:10.1086/171864.

[11] Ascasibar, Y. and Markevitch, M. The Origin of Cold Fronts in the Cores of Relaxed Galaxy Clusters. *ApJ*, **650** (2006), 102. arXiv:astro-ph/0603246, doi:10.1086/506508.

[12] Asplund, M., Grevesse, N., Sauval, A. J., and Scott, P. The Chemical Composition of the Sun. *ARA&A*, **47** (2009), 481. arXiv:0909.0948, doi:10.1146/annurev.astro.46.060407.145222.

[13] Baldi, A., Ettori, S., Mazzotta, P., Tozzi, P., and Borgani, S. A Chandra Archival Study of the Temperature and Metal Abundance Profiles in Hot Galaxy Clusters at 0.1 ˜ z ˜ 0.3. *ApJ*, **666** (2007), 835. arXiv:0705.3865, doi:10.1086/520505.

[14] Baldi, A., Ettori, S., Molendi, S., Balestra, I., Gastaldello, F., and Tozzi, P. An XMM-Newton spatially-resolved study of metal abundance evolution in distant galaxy clusters. *A&A*, **537** (2012), A142. arXiv:1111.4337, doi:10.1051/0004-6361/201117836.

[15] Baldi, A. S., De Petris, M., Sembolini, F., Yepes, G., Cui, W., and Lamagna, L. Kinetic Sunyaev-Zel'dovich effect in rotating galaxy clusters from MUSIC simulations. *MNRAS*, **479** (2018), 4028. arXiv:1805.07142, doi:10.1093/mnras/sty1722.

[16] Baldi, A. S., De Petris, M., Sembolini, F., Yepes, G., Lamagna, L., and Rasia, E. On the coherent rotation of diffuse matter in numerical simulations of clusters of galaxies. *MNRAS*, **465** (2017), 2584. arXiv:1606.02148, doi:10.1093/mnras/stw2858.

[17] Balestra, I., Tozzi, P., Ettori, S., Rosati, P., Borgani, S., Mainieri, V., Norman, C., and Viola, M. Tracing the evolution in the iron content of the intra-cluster medium. *A&A*, **462** (2007), 429. arXiv:astro-ph/0609664, doi:10.1051/0004-6361:20065568.

[18] Balucinska-Church, M. and McCammon, D. Photoelectric Absorption Cross Sections with Variable Abundances. *ApJ*, **400** (1992), 699. doi:10.1086/172032.

[19] Barcons, X., Nandra, K., Barret, D., den Herder, J.-W., Fabian, A. C., Piro, L., Watson, M. G., and the Athena Team. Athena: the X-ray observatory to study the hot and energetic Universe. In *Journal of Physics Conference Series*, vol. 610 of *Journal of Physics Conference Series*, p. 012008 (2015). doi:10.1088/1742-6596/610/1/012008.

[20] Barret, D., et al. The Hot and Energetic Universe: The X-ray Integral Field Unit (X-IFU) for Athena+. *arXiv e-prints*, (2013). arXiv:1308.6784.

[21] Barret, D., et al. The Athena X-ray Integral Field Unit (X-IFU). In *Space Telescopes and Instrumentation 2016: Ultraviolet to Gamma Ray*, vol. 9905 of *Proc. SPIE*, p. 99052F (2016). arXiv:1608.08105, doi:10.1117/12.2232432.

[22] Barret, D., et al. The ATHENA X-ray Integral Field Unit (X-IFU). In *Space Telescopes and Instrumentation 2018: Ultraviolet to Gamma Ray*, vol. 10699 of *Society of Photo-Optical Instrumentation Engineers (SPIE) Conference Series*, p. 106991G (2018). arXiv:1807.06092, doi:10.1117/12.2312409.

[23] Bartalucci, I., Arnaud, M., Pratt, G. W., Démoclès, J., van der Burg, R. F. J., and Mazzotta, P. Resolving galaxy cluster gas properties at z

1 with XMM-Newton and Chandra. *A&A*, **598** (2017), A61. arXiv:1610.01899, doi:10.1051/0004-6361/201629509.

[24] Bianconi, M., Ettori, S., and Nipoti, C. Gas rotation in galaxy clusters: signatures and detectability in X-rays. *MNRAS*, **434** (2013), 1565. arXiv:1305.5519, doi:10.1093/mnras/stt1112.

[25] Biffi, V., Dolag, K., and Böhringer, H. Velocity structure diagnostics of simulated galaxy clusters. *MNRAS*, **413** (2011), 573. arXiv:1012.1606, doi:10.1111/j.1365-2966.2010.18153.x.

[26] Biffi, V., Mernier, F., and Medvedev, P. Enrichment of the Hot Intracluster Medium: Numerical Simulations. *SSRv*, **214** (2018), 123. arXiv:1811.01955, doi:10.1007/s11214-018-0557-7.

[27] Biffi, V., Planelles, S., Borgani, S., Rasia, E., Murante, G., Fabjan, D., and Gaspari, M. The origin of ICM enrichment in the outskirts of present-day galaxy clusters from cosmological hydrodynamical simulations. *MNRAS*, **476** (2018), 2689. arXiv:1801.05425, doi:10.1093/mnras/sty363.

[28] Biffi, V., et al. On the Nature of Hydrostatic Equilibrium in Galaxy Clusters. *ApJ*, **827** (2016), 112. arXiv:1606.02293, doi:10.3847/0004-637X/827/2/112.

[29] Böhringer, H. and Hensler, G. Metallicity-dependence of radiative cooling in optically thin, hot plasmas. *A&A*, **215** (1989), 147.

[30] Böhringer, H., Matsushita, K., Churazov, E., Finoguenov, A., and Ikebe, Y. Implications of the central metal abundance peak in cooling core clusters of galaxies. *A&A*, **416** (2004), L21. doi:10.1051/0004-6361:20040047.

[31] Böhringer, H. and Morfill, G. E. On the dynamical role of cosmic rays in cooling flows in clusters of galaxies. *ApJ*, **330** (1988), 609. doi:10.1086/166497.

[32] Böhringer, H. and Werner, N. X-ray spectroscopy of galaxy clusters: studying astrophysical processes in the largest celestial laboratories. *A&A Rv*, **18** (2010), 127. doi:10.1007/s00159-009-0023-3.

[33] Böhringer, H., et al. The representative XMM-Newton cluster structure survey (REXCESS) of an X-ray luminosity selected galaxy cluster sample. *A&A*, **469** (2007), 363. arXiv:astro-ph/0703553, doi:10.1051/0004-6361:20066740.

[34] Borgani, S., Fabjan, D., Tornatore, L., Schindler, S., Dolag, K., and Diaferio, A. The Chemical Enrichment of the ICM from Hydrodynamical Simulations. *SSRv*, **134** (2008), 379. arXiv:0801.1062, doi:10.1007/s11214-008-9322-7.

[35] Branduardi-Raymont, G., Fabricant, D., Feigelson, E., Gorenstein, P., Grindlay, J., Soltan, A., and Zamorani, G. Soft X-ray images of the central region of the Perseus cluster. *ApJ*, **248** (1981), 55. doi:10.1086/159129.

[36] Brown, S. and Rudnick, L. Diffuse radio emission in/around the Coma cluster: beyond simple accretion. *MNRAS*, **412** (2011), 2. arXiv:1009.4258, doi:10.1111/j.1365-2966.2010.17738.x.

[37] Brüggen, M., Roediger, E., Lovisari, L., Dupke, R., Ghizzardi, S., Machacek, M. E., and Kraft, R. P. Gas sloshing, cold fronts, Kelvin–Helmholtz instabilities and the merger history of the cluster of galaxies Abell 496. *Monthly Notices of the Royal Astronomical Society*, **420** (2012), 3632. Available from: https://doi.org/10.1111/j.1365-2966.2011.20287.x, arXiv:http://oup.prod.sis.lan/mnras/article-pdf/420/4/3632/2975288/mnras0420-3632.pdf, doi:10.1111/j.1365-2966.2011.20287.x.

[38] Buote, D. A. X-ray evidence for multiphase hot gas with nearly solar Fe abundances in the brightest groups of galaxies. *MNRAS*, **311** (2000), 176. arXiv:astro-ph/9903278, doi:10.1046/j.1365-8711.2000.03046.x.

[39] Buote, D. A., Lewis, A. D., Brighenti, F., and Mathews, W. G. XMM-Newton and Chandra Observations of the Galaxy Group NGC 5044. II. Metal Abundances and Supernova Fraction. *ApJ*, **595** (2003), 151. arXiv:astro-ph/0303054, doi:10.1086/377256.

[40] Buote, D. A. and Tsai, J. C. Quantifying the Morphologies and Dynamical Evolution of Galaxy Clusters. I. The Method. *ApJ*, **452** (1995), 522. arXiv:astro-ph/9502002, doi:10.1086/176326.

[41] Buote, D. A. and Tsai, J. C. Quantifying the Morphologies and Dynamical Evolution of Galaxy Clusters. II. Application to a Sample of ROSAT Clusters. *ApJ*, **458** (1996), 27. arXiv:astro-ph/9504046, doi:10.1086/176790.

[42] Byram, E. T., Chubb, T. A., and Friedman, H. Cosmic X-ray Sources, Galactic and Extragalactic. *Science*, **152** (1966), 66. doi:10.1126/science.152.3718.66.

[43] Caminha, G. B., et al. A refined mass distribution of the cluster MACS J0416.1-2403 from a new large set of spectroscopic multiply lensed sources. *A&A*, **600** (2017), A90. arXiv:1607.03462, doi:10.1051/0004-6361/201629297.

[44] Cash, W. Parameter estimation in astronomy through application of the likelihood ratio. *ApJ*, **228** (1979), 939. doi:10.1086/156922.

[45] Cassano, R., Ettori, S., Giacintucci, S., Brunetti, G., Markevitch, M., Venturi, T., and Gitti, M. On the Connection Between Giant Radio Halos and Cluster Mergers. *ApJL*, **721** (2010), L82. arXiv:1008.3624, doi:10.1088/2041-8205/721/2/L82.

[46] Cavagnolo, K. W., Donahue, M., Voit, G. M., and Sun, M. Intracluster Medium Entropy Profiles for a Chandra Archival Sample of Galaxy Clusters. *ApJS*, **182** (2009), 12. arXiv:0902.1802, doi:10.1088/0067-0049/182/1/12.

[47] Cavaliere, A. and Fusco-Femiano, R. X-rays from hot plasma in clusters of galaxies. *A&A*, **49** (1976), 137.

[48] Cavaliere, A. and Fusco-Femiano, R. The Distribution of Hot Gas in Clusters of Galaxies. *A&A*, **70** (1978), 677.

[49] Chieffi, A. and Limongi, M. Explosive Yields of Massive Stars from Z = 0 to Z = Z_{solar}. *ApJ*, **608** (2004), 405. arXiv:astro-ph/0402625, doi:10.1086/392523.

[50] Churazov, E., Forman, W., Jones, C., and Böhringer, H. XMM-Newton Observations of the Perseus Cluster. I. The Temperature and Surface Brightness Structure. *ApJ*, **590** (2003), 225. arXiv:astro-ph/0301482, doi:10.1086/374923.

[51] Churazov, E., Ruszkowski, M., and Schekochihin, A. Powering of cool filaments in cluster cores by buoyant bubbles - I. Qualitative model. *MNRAS*, **436** (2013), 526. arXiv:1304.3168, doi:10.1093/mnras/stt1594.

[52] Clarke, T. E., Blanton, E. L., and Sarazin, C. L. The Complex Cooling Core of A2029: Radio and X-Ray Interactions. *ApJ*, **616** (2004), 178. arXiv:astro-ph/0408068, doi:10.1086/424911.

[53] Clausius, R. Xvi. on a mechanical theorem applicable to heat. *The London, Edinburgh, and Dublin Philosophical Magazine and Journal of Science*, **40** (1870), 122. Available from: https://doi.org/10.1080/14786447008640370, arXiv:https://doi.org/10.1080/14786447008640370, doi:10.1080/14786447008640370.

[54] Cole, S., et al. The 2dF Galaxy Redshift Survey: power-spectrum analysis of the final data set and cosmological implications. *MNRAS*, **362** (2005), 505. arXiv:astro-ph/0501174, doi:10.1111/j.1365-2966.2005.09318.x.

[55] Colless, M. and Dunn, A. M. Structure and Dynamics of the Coma Cluster. *ApJ*, **458** (1996), 435. arXiv:astro-ph/9508070, doi:10.1086/176827.

[56] Colless, M., et al. The 2dF Galaxy Redshift Survey: spectra and redshifts. *MNRAS*, **328** (2001), 1039. arXiv:astro-ph/0106498, doi:10.1046/j.1365-8711.2001.04902.x.

[57] Colless, M., et al. The 2dF Galaxy Redshift Survey: Final Data Release. *arXiv Astrophysics e-prints*, (2003). arXiv:astro-ph/0306581.

[58] Cooray, A. and Chen, X. Kinetic Sunyaev-Zeldovich Effect from Halo Rotation. *ApJ*, **573** (2002), 43. arXiv:astro-ph/0107544, doi:10.1086/340582.

[59] Cora, S. A. Metal enrichment of the intracluster medium: a three-dimensional picture of chemical and dynamical properties. *MNRAS*, **368** (2006), 1540. arXiv:astro-ph/0603270, doi:10.1111/j.1365-2966.2006.10271.x.

[60] Cora, S. A., Tornatore, L., Tozzi, P., and Dolag, K. On the dynamical origin of the ICM metallicity evolution. *MNRAS*, **386** (2008), 96. arXiv:0802.0975, doi:10.1111/j.1365-2966.2008.13068.x.

[61] Cox, D. P. and Daltabuit, E. Radiative Cooling of a Low-Density Plasma. *ApJ*, **167** (1971), 113. doi:10.1086/151009.

[62] Cox, D. P. and Tucker, W. H. Ionization Equilibrium and Radiative Cooling of a Low-Density Plasma. *ApJ*, **157** (1969), 1157. doi:10.1086/150144.

[63] Croston, J. H., Arnaud, M., Pointecouteau, E., and Pratt, G. W. An improved deprojection and PSF-deconvolution technique for galaxy-cluster X-ray surface-brightness profiles. *A&A*, **459** (2006), 1007. arXiv:astro-ph/0608700, doi:10.1051/0004-6361:20065795.

[64] Davé, R. The galaxy stellar mass-star formation rate relation: evidence for an evolving stellar initial mass function? *MNRAS*, **385** (2008), 147. arXiv:0710.0381, doi:10.1111/j.1365-2966.2008.12866.x.

[65] De Grandi, S., Ettori, S., Longhetti, M., and Molendi, S. On the iron content in rich nearby clusters of galaxies. *A&A*, **419** (2004), 7. arXiv:astro-ph/0310828, doi:10.1051/0004-6361:20034228.

[66] De Grandi, S. and Molendi, S. Metallicity Gradients in X-Ray Clusters of Galaxies. *ApJ*, **551** (2001), 153. arXiv:astro-ph/0012232, doi:10.1086/320098.

[67] De Grandi, S. and Molendi, S. Metal abundances in the cool cores of galaxy clusters. *A&A*, **508** (2009), 565. arXiv:0909.1224, doi:10.1051/0004-6361/200912745.

[68] De Grandi, S., Santos, J. S., Nonino, M., Molendi, S., Tozzi, P., Rossetti, M., Fritz, A., and Rosati, P. On the Fe abundance peak formation in cool-core clusters of galaxies: hints from cluster WARPJ1415.1+3612 at z = 1.03. *A&A*, **567** (2014), A102. arXiv:1406.2224, doi:10.1051/0004-6361/201423928.

[69] de Plaa, J. The origin of the chemical elements in cluster cores. *AN*, **334** (2013), 416. arXiv:1210.1093, doi:10.1002/asna.201211870.

[70] de Plaa, J., Kaastra, J. S., Tamura, T., Pointecouteau, E., Mendez, M., and Peterson, J. R. X-ray spectroscopy on Abell 478 with XMM-Newton. *A&A*, **423** (2004), 49. arXiv:astro-ph/0405307, doi:10.1051/0004-6361:20047170.

[71] den Hartog, R. and Katgert, P. On the dynamics of the cores of galaxy clusters. *MNRAS*, **279** (1996), 349. doi:10.1093/mnras/279.2.349.

[72] Deshev, B., et al. Galaxy evolution in merging clusters: The passive core of the "Train Wreck" cluster of galaxies, <ASTROBJ>A 520</ASTROBJ>. *A&A*, **607** (2017), A131. arXiv:1707.03208, doi:10.1051/0004-6361/201731235.

[73] Diaferio, A. Mass estimation in the outer regions of galaxy clusters. *MNRAS*, **309** (1999), 610. arXiv:astro-ph/9906331, doi:10.1046/j.1365-8711.1999.02864.x.

[74] Diaferio, A. and Geller, M. J. Infall Regions of Galaxy Clusters. *ApJ*, **481** (1997), 633. arXiv:astro-ph/9701034.

[75] Diaferio, A., Geller, M. J., and Rines, K. J. Caustic and Weak-Lensing Estimators of Galaxy Cluster Masses. *ApJL*, **628** (2005), L97. arXiv:astro-ph/0506560, doi:10.1086/432880.

[76] Domainko, W., Gitti, M., Schindler, S., and Kapferer, W. Feedback from intra-cluster supernovae on the ICM in cooling flow galaxy clusters. *A&A*, **425** (2004), L21. arXiv:arXiv:astro-ph/0405493, doi:10.1051/0004-6361:20040178.

[77] Dressler, A. and Shectman, S. A. Evidence for substructure in rich clusters of galaxies from radial-velocity measurements. *AJ*, **95** (1988), 985. doi:10.1086/114694.

[78] Dupke, R. A. and Bregman, J. N. Detection of Bulk Motions in the Intracluster Medium of the Centaurus Cluster. *ApJ*, **562** (2001), 266. arXiv:astro-ph/0106030, doi:10.1086/323433.

[79] Dupke, R. A. and Bregman, J. N. Velocity Gradients in the Intracluster Gas of the Perseus Cluster. *ApJ*, **547** (2001), 705. arXiv:astro-ph/0009429, doi:10.1086/318393.

[80] Dupke, R. A. and Bregman, J. N. Constraints on Intracluster Gas Bulk Motions in Clusters of Galaxies with ASCA. *ApJS*, **161** (2005), 224. arXiv:astro-ph/0506360, doi:10.1086/433185.

[81] Dupke, R. A. and Bregman, J. N. Direct Measurements of Gas Bulk Flows in the Intracluster Medium of the Centaurus Cluster with the Chandra Satellite. *ApJ*, **639** (2006), 781. arXiv:astro-ph/0512045, doi:10.1086/499343.

[82] Dupke, R. A., Mirabal, N., Bregman, J. N., and Evrard, A. E. The Merger in Abell 576: A Line-of-Sight Bullet Cluster? *ApJ*, **668** (2007), 781. arXiv:0706.1073, doi:10.1086/520708.

[83] Dwarakanath, K. S., van Gorkom, J. H., and Owen, F. N. A VLA search for neutral hydrogen in cooling flow clusters. *ApJ*, **432** (1994), 469. doi:10.1086/174586.

[84] Eckert, D., Molendi, S., and Paltani, S. The cool-core bias in X-ray galaxy cluster samples. I. Method and application to HIFLUGCS. *A&A*, **526** (2011), A79. arXiv:1011.3302, doi:10.1051/0004-6361/201015856.

[85] Eckert, D., Roncarelli, M., Ettori, S., Molendi, S., Vazza, F., Gastaldello, F., and Rossetti, M. Gas clumping in galaxy clusters. *MNRAS*, **447** (2015), 2198. arXiv:1310.8389, doi:10.1093/mnras/stu2590.

[86] Eckert, D., et al. The stripping of a galaxy group diving into the massive cluster A2142. *A&A*, **570** (2014), A119. arXiv:1408.1394, doi:10.1051/0004-6361/201424259.

[87] Eckert, D., et al. Deep Chandra observations of the stripped galaxy group falling into Abell 2142. *A&A*, **605** (2017), A25. arXiv:1705.05844, doi:10.1051/0004-6361/201730555.

[88] Eckert, D., et al. Non-thermal pressure support in X-COP galaxy clusters. *A&A*, **621** (2019), A40. arXiv:1805.00034, doi:10.1051/0004-6361/201833324.

[89] Edge, A. C. The detection of molecular gas in the central galaxies of cooling flow clusters. *MNRAS*, **328** (2001), 762. arXiv:arXiv:astro-ph/0106225, doi:10.1046/j.1365-8711.2001.04802.x.

[90] Einasto, M., et al. Infalling groups and galaxy transformations in the cluster A2142. *ArXiv e-prints*, (2017). arXiv:1711.07806.

[91] Ettori, S. β-model and cooling flows in X-ray clusters of galaxies. *MNRAS*, **318** (2000), 1041. arXiv:astro-ph/0005224, doi:10.1046/j.1365-8711.2000.03664.x.

[92] Ettori, S., Baldi, A., Balestra, I., Gastaldello, F., Molendi, S., and Tozzi, P. The evolution of the spatially resolved metal abundance in galaxy clusters up to z = 1.4. *A&A*, **578** (2015), A46. arXiv:1504.02107, doi:10.1051/0004-6361/201425470.

[93] Ettori, S., Donnarumma, A., Pointecouteau, E., Reiprich, T. H., Giodini, S., Lovisari, L., and Schmidt, R. W. Mass Profiles of Galaxy Clusters from X-ray Analysis. *SSRv*, **177** (2013), 119. arXiv:1303.3530, doi:10.1007/s11214-013-9976-7.

[94] Ettori, S. and Fabian, A. C. Effects of sedimented helium on the X-ray properties of galaxy clusters. *MNRAS*, **369** (2006), L42. arXiv:astro-ph/0603383, doi:10.1111/j.1745-3933.2006.00170.x.

[95] Fabian, A. C. Cooling Flows in Clusters of Galaxies. *ARA&A*, **32** (1994), 277. doi:10.1146/annurev.aa.32.090194.001425.

[96] Fabian, A. C. Observational Evidence of Active Galactic Nuclei Feedback. *ARA&A*, **50** (2012), 455. arXiv:1204.4114, doi:10.1146/annurev-astro-081811-125521.

[97] Fabian, A. C., Nulsen, P. E. J., and Canizares, C. R. Cooling flows in clusters of galaxies. *Nature*, **310** (1984), 733. doi:10.1038/310733a0.

[98] Fabian, A. C., Nulsen, P. E. J., and Canizares, C. R. Cooling flows in clusters of galaxies. *A&A Rv*, **2** (1991), 191. doi:10.1007/BF00872767.

[99] Fabian, A. C., Sanders, J. S., Allen, S. W., Crawford, C. S., Iwasawa, K., Johnstone, R. M., Schmidt, R. W., and Taylor, G. B. A deep Chandra observation of the Perseus cluster: shocks and ripples. *MNRAS*, **344** (2003), L43. arXiv:astro-ph/0306036, doi:10.1046/j.1365-8711.2003.06902.x.

[100] Fabian, A. C., Sanders, J. S., Taylor, G. B., Allen, S. W., Crawford, C. S., Johnstone, R. M., and Iwasawa, K. A very deep Chandra observation of the Perseus cluster: shocks, ripples and conduction. *MNRAS*, **366** (2006), 417. arXiv:arXiv:astro-ph/0510476, doi:10.1111/j.1365-2966.2005.09896.x.

[101] Fabian, A. C., Zarneck, J. C., Culhane, J. L., Hawkins, F. J., Peacock, A., Pounds, K. A., and Parkinson, J. H. Copernicus X-Ray Observations of NGC 1275 and the Core of the Perseus Cluster. *ApJ*, **189** (1974), L59. doi:10.1086/181464.

[102] Fabricant, D., et al. Hectospec, the MMT's 300 Optical Fiber-Fed Spectrograph. *PASP*, **117** (2005), 1411. arXiv:astro-ph/0508554, doi:10.1086/497385.

[103] Feng, J. L. Dark matter candidates from particle physics and methods of detection. *Annual Review of Astronomy and Astrophysics*, **48** (2010), 495. Available from: https://doi.org/10.1146/annurev-astro-082708-101659, arXiv:https://doi.org/10.1146/annurev-astro-082708-101659, doi:10.1146/annurev-astro-082708-101659.

[104] Feretti, L., Giovannini, G., Govoni, F., and Murgia, M. Clusters of galaxies: observational properties of the diffuse radio emission. *A&A Rv*, **20** (2012), 54. arXiv:1205.1919, doi:10.1007/s00159-012-0054-z.

[105] Fink, M., Kromer, M., Seitenzahl, I. R., Ciaraldi-Schoolmann, F., Röpke, F. K., Sim, S. A., Pakmor, R., Ruiter, A. J., and Hillebrandt, W. Three-dimensional pure deflagration models with nucleosynthesis and synthetic observables for Type Ia supernovae. *MNRAS*, **438** (2014), 1762. arXiv:1308.3257, doi:10.1093/mnras/stt2315.

[106] Finoguenov, A., David, L. P., and Ponman, T. J. An ASCA Study of the Heavy-Element Distribution in Clusters of Galaxies. *ApJ*, **544** (2000), 188. arXiv:astro-ph/9908150, doi:10.1086/317173.

[107] Finoguenov, A. and Ponman, T. J. Constraining the role of Type IA and Type II supernovae in galaxy groups by spatially resolved analysis of ROSAT and ASCA observations. *MNRAS*, **305** (1999), 325. arXiv:astro-ph/9901100, doi:10.1046/j.1365-8711.1999.02403.x.

[108] Foreman-Mackey, D., Hogg, D. W., Lang, D., and Goodman, J. emcee: The MCMC Hammer. *PASP*, **125** (2013), 306. arXiv:1202.3665, doi:10.1086/670067.

[109] Forman, W., Kellogg, E., Gursky, H., Tananbaum, H., and Giacconi, R. Observations of the Extended X-Ray Sources in the

Perseus and Coma Clusters from UHURU. *ApJ*, **178** (1972), 309. doi:10.1086/151791.

[110] Fritz, G., Davidsen, A., Meekins, J. F., and Friedman, H. Discovery of an X-Ray Source in Perseus. *ApJL*, **164** (1971), L81. doi:10.1086/180697.

[111] Fujita, Y., Matsumoto, T., and Wada, K. Strong Turbulence in the Cool Cores of Galaxy Clusters: Can Tsunamis Solve the Cooling Flow Problem? *ApJL*, **612** (2004), L9. arXiv:astro-ph/0407368, doi:10.1086/424483.

[112] Fujita, Y., Sarazin, C. L., and Sivakoff, G. R. Chandra Observations of A 2670 and A 2107: A Comet Galaxy and cDs with Large Peculiar Velocities. *PASJ*, **58** (2006), 131. arXiv:astro-ph/0512308, doi:10.1093/pasj/58.1.131.

[113] Fukazawa, Y., Makishima, K., Tamura, T., Nakazawa, K., Ezawa, H., Ikebe, Y., Kikuchi, K., and Ohashi, T. Statistical properties of metal abundances of the intracluster medium in the central region of clusters. *MNRAS*, **313** (2000), 21. doi:10.1046/j.1365-8711.2000.03204.x.

[114] Garmire, G. P., Bautz, M. W., Ford, P. G., Nousek, J. A., and Ricker, G. R., Jr. Advanced CCD imaging spectrometer (ACIS) instrument on the Chandra X-ray Observatory. In *X-Ray and Gamma-Ray Telescopes and Instruments for Astronomy.* (edited by J. E. Truemper and H. D. Tananbaum), vol. 4851 of *Proc. SPIE*, pp. 28–44 (2003). doi:10.1117/12.461599.

[115] Gaspari, M., Brighenti, F., and Ruszkowski, M. Solving the cooling flow problem through mechanical AGN feedback. *Astronomische Nachrichten*, **334** (2013), 394. arXiv:1209.3305, doi:10.1002/asna.201211865.

[116] Gaspari, M., Melioli, C., Brighenti, F., and D'Ercole, A. The dance of heating and cooling in galaxy clusters: three-dimensional

simulations of self-regulated active galactic nuclei outflows. *MNRAS*, **411** (2011), 349. arXiv:1007.0674, doi:10.1111/j.1365-2966.2010.17688.x.

[117] Gaspari, M., Ruszkowski, M., and Sharma, P. Cause and Effect of Feedback: Multiphase Gas in Cluster Cores Heated by AGN Jets. *ApJ*, **746** (2012), 94. arXiv:1110.6063, doi:10.1088/0004-637X/746/1/94.

[118] Gaspari, M. and Sądowski, A. Unifying the Micro and Macro Properties of AGN Feeding and Feedback. *ApJ*, **837** (2017), 149. arXiv:1701.07030, doi:10.3847/1538-4357/aa61a3.

[119] Gastaldello, F., Ettori, S., Balestra, I., Brighenti, F., Buote, D. A., de Grandi, S., Ghizzardi, S., Gitti, M., and Tozzi, P. Apparent high metallicity in 3-4 keV galaxy clusters: the inverse iron-bias in action in the case of the merging cluster Abell 2028. *A&A*, **522** (2010), A34. arXiv:1006.3255, doi:10.1051/0004-6361/201014279.

[120] Geller, M. J. and Beers, T. C. Substructure within clusters of galaxies. *PASP*, **94** (1982), 421. doi:10.1086/131003.

[121] Geller, M. J., Diaferio, A., Rines, K. J., and Serra, A. L. Measuring the Mass Distribution in Galaxy Clusters. *ApJ*, **764** (2013), 58. arXiv:1209.5675, doi:10.1088/0004-637X/764/1/58.

[122] Geller, M. J., Hwang, H. S., Dell'Antonio, I. P., Zahid, H. J., Kurtz, M. J., and Fabricant, D. G. SHELS: Complete Redshift Surveys of Two Widely Separated Fields. *ApJS*, **224** (2016), 11. arXiv:1603.06885, doi:10.3847/0067-0049/224/1/11.

[123] Geller, M. J., Hwang, H. S., Fabricant, D. G., Kurtz, M. J., Dell'Antonio, I. P., and Zahid, H. J. SHELS: A Complete Galaxy Redshift Survey with R = 20.6. *ApJS*, **213** (2014), 35. arXiv:1405.7704, doi:10.1088/0067-0049/213/2/35.

[124] Gendron-Marsolais, M., et al. Uplift, Feedback, and Buoyancy: Radio Lobe Dynamics in NGC 4472. *ApJ*, **848** (2017), 26. arXiv:1710.04235, doi:10.3847/1538-4357/aa8a6f.

[125] Ghirardini, V., Ettori, S., Eckert, D., Molendi, S., Gastaldello, F., Pointecouteau, E., Hurier, G., and Bourdin, H. The XMM Cluster Outskirts Project (X-COP): Thermodynamic properties of the intracluster medium out to R_{200} in Abell 2319. *A&A*, **614** (2018), A7. arXiv:1708.02954, doi:10.1051/0004-6361/201731748.

[126] Ghizzardi, S., De Grandi, S., and Molendi, S. Metal jumps across sloshing cold fronts: The case of A 496. *AN*, **334** (2013), 422. arXiv:1306.1241, doi:10.1002/asna.201211871.

[127] Ghizzardi, S., De Grandi, S., and Molendi, S. Metal distribution in sloshing galaxy clusters: the case of A496. *A&A*, **570** (2014), A117. arXiv:1407.6814, doi:10.1051/0004-6361/201424016.

[128] Ghizzardi, S., Rossetti, M., and Molendi, S. Cold fronts in galaxy clusters. *A&A*, **516** (2010), A32. arXiv:1003.1051, doi:10.1051/0004-6361/200912496.

[129] Giacconi, R., Murray, S., Gursky, H., Kellogg, E., Schreier, E., and Tananbaum, H. The Uhuru catalog of X-ray sources. *ApJ*, **178** (1972), 281. doi:10.1086/151790.

[130] Girardi, M., Escalera, E., Fadda, D., Giuricin, G., Mardirossian, F., and Mezzetti, M. Optical Substructures in 48 Galaxy Clusters: New Insights from a Multiscale Analysis. *ApJ*, **482** (1997), 41. doi:10.1086/304113.

[131] Girardi, M., et al. CLASH-VLT: Substructure in the galaxy cluster MACS J1206.2-0847 from kinematics of galaxy populations. *A&A*, **579** (2015), A4. arXiv:1503.05607, doi:10.1051/0004-6361/201425599.

[132] Gorenstein, P., Fabricant, D., Topka, K., Harnden, F. R., Jr., and Tucker, W. H. Soft X-ray structure of the Perseus cluster of galaxies. *ApJ*, **224** (1978), 718. doi:10.1086/156421.

[133] Govoni, F., Feretti, L., Giovannini, G., Böhringer, H., Reiprich, T. H., and Murgia, M. Radio and X-ray diffuse emission in six clusters of galaxies. *A&A*, **376** (2001), 803. arXiv:astro-ph/0107275, doi:10.1051/0004-6361:20011016.

[134] Govoni, F., Ferrari, C., Feretti, L., Vacca, V., Murgia, M., Giovannini, G., Perley, R., and Benoist, C. Detection of diffuse radio emission in the galaxy clusters A800, A910, A1550, and CL 1446+26. *A&A*, **545** (2012), A74. arXiv:1207.2915, doi:10.1051/0004-6361/201219151.

[135] Grevesse, N. and Sauval, A. J. Standard Solar Composition. *SSRv*, **85** (1998), 161. doi:10.1023/A:1005161325181.

[136] Grillo, C., et al. CLASH-VLT: Insights on the Mass Substructures in the Frontier Fields Cluster MACS J0416.1-2403 through Accurate Strong Lens Modeling. *ApJ*, **800** (2015), 38. arXiv:1407.7866, doi:10.1088/0004-637X/800/1/38.

[137] Gronenschild, E. H. B. M. and Mewe, R. Calculated X-radiation from optically thin plasmas. III - Abundance effects on continuum emission. *A&AS*, **32** (1978), 283.

[138] Guainazzi, M. and Tashiro, M. S. The Hot Universe with XRISM and Athena. *ArXiv e-prints*, (2018). arXiv:1807.06903.

[139] Guennou, L., et al. Structure and substructure analysis of DAFT/FADA galaxy clusters in the [0.4-0.9] redshift range. *A&A*, **561** (2014), A112. arXiv:1311.6922, doi:10.1051/0004-6361/201321208.

[140] Guerras, E., Dai, X., Steele, S., Liu, A., Kochanek, C. S., Chartas, G., Morgan, C. W., and Chen, B. Extended X-Ray Monitoring of Gravitational Lenses with Chandra and Joint Constraints on X-Ray Emission Regions. *ApJ*, **836** (2017), 206. arXiv:1609.05192, doi:10.3847/1538-4357/aa5728.

[141] Gursky, H., Kellogg, E., Murray, S., Leong, C., Tananbaum, H., and Giacconi, R. A Strong X-Ray Source in the Coma Cluster Observed by UHURU. *ApJL*, **167** (1971), L81. doi:10.1086/180765.

[142] Gursky, H., Kellogg, E. M., Leong, C., Tananbaum, H., and Giacconi, R. Detection of X-Rays from the Seyfert Galaxies NGC 1275 and NGC 4151 by the UHURU Satellite. *ApJL*, **165** (1971), L43. doi:10.1086/180713.

[143] Gursky, H., Solinger, A., Kellogg, E. M., Murray, S., Tananbaum, H., Giacconi, R., and Cavaliere, A. X-Ray Emission from Rich Clusters of Galaxies. *ApJL*, **173** (1972), L99. doi:10.1086/180926.

[144] Gutierrez, K. and Krawczynski, H. The Off-Axis Galaxy Cluster Merger A115. *ApJ*, **619** (2005), 161. arXiv:astro-ph/0312454, doi:10.1086/426420.

[145] Heinz, S., Brüggen, M., Young, A., and Levesque, E. The answer is blowing in the wind: simulating the interaction of jets with dynamic cluster atmospheres. *MNRAS*, **373** (2006), L65. arXiv:astro-ph/0606664, doi:10.1111/j.1745-3933.2006.00243.x.

[146] Helmken, H., Delvaille, J. P., Epstein, A., Geller, M. J., Schnopper, H. W., and Jernigan, J. G. Compact and diffuse X-ray sources in the core of the Perseus cluster /Abell 426/. *ApJ*, **221** (1978), L43. doi:10.1086/182661.

[147] Henriksen, M. J. and Mushotzky, R. F. The physical implications of an isothermal model for the hot intracluster medium. *ApJ*, **292** (1985), 441. doi:10.1086/163172.

[148] Hillebrandt, W. and Niemeyer, J. C. Type IA Supernova Explosion Models. *ARA&A*, **38** (2000), 191. arXiv:astro-ph/0006305, doi:10.1146/annurev.astro.38.1.191.

[149] Hillel, S. and Soker, N. Heating the intracluster medium by jet-inflated bubbles. *MNRAS*, **455** (2016), 2139. arXiv:1504.04846, doi:10.1093/mnras/stv2483.

[150] Hitomi Collaboration, et al. The quiescent intracluster medium in the core of the Perseus cluster. *Nature*, **535** (2016), 117. arXiv:1607.04487, doi:10.1038/nature18627.

[151] Hitomi Collaboration, et al. Measurements of resonant scattering in the Perseus Cluster core with Hitomi SXS. *PASJ*, **70** (2018), 10. arXiv:1710.04648, doi:10.1093/pasj/psx127.

[152] Ho, P. T. P., et al. The Yuan-Tseh Lee Array for Microwave Background Anisotropy. *ApJ*, **694** (2009), 1610. arXiv:0810.1871, doi:10.1088/0004-637X/694/2/1610.

[153] Hoekstra, H. How well can we determine cluster mass profiles from weak lensing? *MNRAS*, **339** (2003), 1155. arXiv:astro-ph/0208351, doi:10.1046/j.1365-8711.2003.06264.x.

[154] Howell, D. A. Type Ia supernovae as stellar endpoints and cosmological tools. *Nature Communications*, **2** (2011), 350. doi:10.1038/ncomms1344.

[155] Hudson, D. S., Mittal, R., Reiprich, T. H., Nulsen, P. E. J., Andernach, H., and Sarazin, C. L. What is a cool-core cluster? a detailed analysis of the cores of the X-ray flux-limited HIFLUGCS cluster sample. *A&A*, **513** (2010), A37. arXiv:0911.0409, doi:10.1051/0004-6361/200912377.

[156] Hwang, H. S., Geller, M. J., Diaferio, A., Rines, K. J., and Zahid, H. J. Comparing Dense Galaxy Cluster Redshift Surveys with Weak-lensing Maps. *ApJ*, **797** (2014), 106. arXiv:1410.3883, doi:10.1088/0004-637X/797/2/106.

[157] Hwang, H. S. and Lee, M. G. Searching for Rotating Galaxy Clusters in SDSS and 2dFGRS. *ApJ*, **662** (2007), 236. arXiv:astro-ph/0702184, doi:10.1086/514328.

[158] Iani, E., et al. Inquiring into the nature of the Abell 2667 Brightest Cluster Galaxy: physical properties from MUSE. *MNRAS*, (2019), 1551. arXiv:1906.04744, doi:10.1093/mnras/stz1631.

[159] Ichinohe, Y., Simionescu, A., Werner, N., and Takahashi, T. An azimuthally resolved study of the cold front in Abell 3667. *MNRAS*, **467** (2017), 3662. arXiv:1702.01026, doi:10.1093/mnras/stx280.

[160] Ivezic, Z., Connolly, A. J., VanderPlas, J. T., and Gray, A. *Statistics, Data Mining, and Machine Learning in Astronomy: A Practical Python Guide for the Analysis of Survey Data*. Princeton University Press, Princeton, NJ, USA (2014). ISBN 0691151687, 9780691151687.

[161] Iwamoto, K., Brachwitz, F., Nomoto, K., Kishimoto, N., Umeda, H., Hix, W. R., and Thielemann, F.-K. Nucleosynthesis in Chandrasekhar Mass Models for Type IA Supernovae and Constraints on Progenitor Systems and Burning-Front Propagation. *ApJS*, **125** (1999), 439. arXiv:astro-ph/0002337, doi:10.1086/313278.

[162] Johnstone, R. M., Allen, S. W., Fabian, A. C., and Sanders, J. S. Chandra observations of Abell 2199. *MNRAS*, **336** (2002), 299. arXiv:astro-ph/0202071, doi:10.1046/j.1365-8711.2002.05743.x.

[163] Jonathan Goodman, J. W. Ensemble samplers with affine invariance. *Communications in Applied Mathematics and Computational Science*, **5** (2010), 65.

[164] Kaastra, J. S., et al. Spatially resolved X-ray spectroscopy of cooling clusters of galaxies. *A&A*, **413** (2004), 415. arXiv:astro-ph/0309763, doi:10.1051/0004-6361:20031512.

[165] Kalberla, P. M. W., Burton, W. B., Hartmann, D., Arnal, E. M., Bajaja, E., Morras, R., and Pöppel, W. G. L. The Leiden/Argentine/Bonn (LAB) Survey of Galactic HI. Final data release of the combined LDS and IAR surveys with improved stray-radiation corrections. *A&A*, **440** (2005), 775. arXiv:astro-ph/0504140, doi:10.1051/0004-6361:20041864.

[166] Kalinkov, M., Valchanov, T., Valtchanov, I., Kuneva, I., and Dissanska, M. Rotation of the cluster of galaxies A2107. *MNRAS*, **359**

(2005), 1491. arXiv:astro-ph/0505091, doi:10.1111/j.1365-2966.2005.09008.x.

[167] Karzas, W. J. and Latter, R. Electron Radiative Transitions in a Coulomb Field. *ApJS*, **6** (1961), 167. doi:10.1086/190063.

[168] Kauffmann, G. Hierarchical clustering and the Butcher-Oemler effect. *MNRAS*, **274** (1995), 153. arXiv:astro-ph/9404051, doi:10.1093/mnras/274.1.153.

[169] Kelley, R. L., et al. The Astro-H high resolution soft x-ray spectrometer. In *Space Telescopes and Instrumentation 2016: Ultraviolet to Gamma Ray*, vol. 9905 of *Proc. SPIE*, p. 99050V (2016). doi:10.1117/12.2232509.

[170] Kellogg, E., Baldwin, J. R., and Koch, D. Studies of cluster X-ray sources, energy spectra for the Perseus, Virgo, and Coma clusters. *ApJ*, **199** (1975), 299. doi:10.1086/153692.

[171] King, I. The structure of star clusters. I. an empirical density law. *AJ*, **67** (1962), 471. doi:10.1086/108756.

[172] King, I. R. The structure of star clusters. III. Some simple dynamical models. *AJ*, **71** (1966), 64. doi:10.1086/109857.

[173] Kirkpatrick, C. C., Gitti, M., Cavagnolo, K. W., McNamara, B. R., David, L. P., Nulsen, P. E. J., and Wise, M. W. Direct Evidence for Outflow of Metal-Enriched Gas Along the Radio Jets of Hydra A. *ApJL*, **707** (2009), L69. arXiv:0909.2252, doi:10.1088/0004-637X/707/1/L69.

[174] Kirkpatrick, C. C., McNamara, B. R., and Cavagnolo, K. W. Anisotropic Metal-enriched Outflows Driven by Active Galactic Nuclei in Clusters of Galaxies. *ApJL*, **731** (2011), L23. arXiv:1103.0793, doi:10.1088/2041-8205/731/2/L23.

[175] Kitayama, T., et al. ASTRO-H White Paper - Clusters of Galaxies and Related Science. *arXiv e-prints*, (2014). arXiv:1412.1176.

[176] Komatsu, E., et al. Seven-year Wilkinson Microwave Anisotropy Probe (WMAP) Observations: Cosmological Interpretation. *ApJS*, **192** (2011), 18. arXiv:1001.4538, doi:10.1088/0067-0049/192/2/18.

[177] Kravtsov, A. V. and Borgani, S. Formation of Galaxy Clusters. *ARA&A*, **50** (2012), 353. arXiv:1205.5556, doi:10.1146/annurev-astro-081811-125502.

[178] Kravtsov, A. V., Nagai, D., and Vikhlinin, A. A. Effects of Cooling and Star Formation on the Baryon Fractions in Clusters. *ApJ*, **625** (2005), 588. arXiv:astro-ph/0501227, doi:10.1086/429796.

[179] Kurtz, M. J. and Mink, D. J. RVSAO 2.0: Digital Redshifts and Radial Velocities. *PASP*, **110** (1998), 934. arXiv:astro-ph/9803252, doi:10.1086/316207.

[180] Lacey, C. and Cole, S. Merger rates in hierarchical models of galaxy formation. *MNRAS*, **262** (1993), 627. doi:10.1093/mnras/262.3.627.

[181] Laganá, T. F., Andrade-Santos, F., and Lima Neto, G. B. Spiral-like structure at the centre of nearby clusters of galaxies. *A&A*, **511** (2010), A15. arXiv:0911.3785, doi:10.1051/0004-6361/200913180.

[182] Lakhchaura, K., Mernier, F., and Werner, N. Possible depletion of metals into dust grains in the core of the Centaurus cluster of galaxies. *A&A*, **623** (2019), A17. arXiv:1812.00121, doi:10.1051/0004-6361/201834755.

[183] Landau, L. D. and Lifshitz, E. M. *Fluid mechanics* (1959).

[184] Lau, E. T., Kravtsov, A. V., and Nagai, D. Residual Gas Motions in the Intracluster Medium and Bias in Hydrostatic Measurements of Mass Profiles of Clusters. *ApJ*, **705** (2009), 1129. arXiv:0903.4895, doi:10.1088/0004-637X/705/2/1129.

[185] Lea, S. M., Silk, J., Kellogg, E., and Murray, S. Thermal-Bremsstrahlung Interpretation of Cluster X-Ray Sources. *ApJ*, **184** (1973), L105. doi:10.1086/181300.

[186] Leccardi, A. and Molendi, S. Radial metallicity profiles for a large sample of galaxy clusters observed with XMM-Newton. *A&A*, **487** (2008), 461. arXiv:0806.1445, doi:10.1051/0004-6361:200810113.

[187] Leccardi, A., Rossetti, M., and Molendi, S. Thermo-dynamic and chemical properties of the intra-cluster medium. *A&A*, **510** (2010), A82. arXiv:0910.4894, doi:10.1051/0004-6361/200913094.

[188] Li, Y. and Bryan, G. L. Simulating the Cooling Flow of Cool-core Clusters. *ApJ*, **747** (2012), 26. arXiv:1112.2701, doi:10.1088/0004-637X/747/1/26.

[189] Liddle, A. *An Introduction to Modern Cosmology, Second Edition* (2003).

[190] Lin, Y.-T., Stanford, S. A., Eisenhardt, P. R. M., Vikhlinin, A., Maughan, B. J., and Kravtsov, A. Baryon Content of Massive Galaxy Clusters at z = 0-0.6. *ApJL*, **745** (2012), L3. arXiv:1112.1705, doi:10.1088/2041-8205/745/1/L3.

[191] Liu, A. and Tozzi, P. Testing the rotation versus merger scenario in the galaxy cluster Abell 2107. *MNRAS*, **485** (2019), 3909. arXiv:1903.03858, doi:10.1093/mnras/stz713.

[192] Liu, A., Tozzi, P., Yu, H., De Grandi, S., and Ettori, S. Spatial distribution of metals in the ICM: evolution of the iron excess in relaxed galaxy clusters. *MNRAS*, **481** (2018), 361. arXiv:1808.06742, doi:10.1093/mnras/sty2294.

[193] Liu, A. and Yu, H. Review of X-ray cool-core clusters of galaxies. *Progress in Astronomy*, **32** (2014), 71.

[194] Liu, A., Yu, H., Diaferio, A., Tozzi, P., Hwang, H. S., Umetsu, K., Okabe, N., and Yang, L.-L. Inside a Beehive: The Multiple Merging Processes in the Galaxy Cluster Abell 2142. *ApJ*, **863** (2018), 102. arXiv:1806.10864, doi:10.3847/1538-4357/aad090.

[195] Liu, A., Yu, H., Tozzi, P., and Zhu, Z.-H. A Method to Search for Bulk Motions in the ICM with Chandra CCD Spectra: Application to the Bullet Cluster. *ApJ*, **809** (2015), 27. arXiv:1508.04879, doi:10.1088/0004-637X/809/1/27.

[196] Liu, A., Yu, H., Tozzi, P., and Zhu, Z.-H. Searching for Bulk Motions in the Intracluster Medium of Massive, Merging Clusters with Chandra CCD Data. *ApJ*, **821** (2016), 29. arXiv:1602.07704, doi:10.3847/0004-637X/821/1/29.

[197] Liu, A., Zhai, M., and Tozzi, P. On the origin of central abundance drops in the intracluster medium of galaxy groups and clusters. *MNRAS*, **485** (2019), 1651. arXiv:1902.07661, doi:10.1093/mnras/stz533.

[198] Lopes, P. A. A., Trevisan, M., Laganá, T. F., Durret, F., Ribeiro, A. L. B., and Rembold, S. B. Optical substructure and BCG offsets of Sunyaev-Zel'dovich and X-ray-selected galaxy clusters. *MNRAS*, **478** (2018), 5473. arXiv:1805.09631, doi:10.1093/mnras/sty1374.

[199] Lovisari, L. and Reiprich, T. H. The non-uniformity of galaxy cluster metallicity profiles. *MNRAS*, **483** (2019), 540. arXiv:1811.05987, doi:10.1093/mnras/sty3130.

[200] Lovisari, L., et al. X-Ray Morphological Analysis of the Planck ESZ Clusters. *ApJ*, **846** (2017), 51. arXiv:1708.02590, doi:10.3847/1538-4357/aa855f.

[201] Macquorn Rankine, W. J. On the Thermodynamic Theory of Waves of Finite Longitudinal Disturbance. *Philosophical Transactions of the Royal Society of London Series I*, **160** (1870), 277.

[202] Madau, P. and Dickinson, M. Cosmic Star-Formation History. *ARA&A*, **52** (2014), 415. arXiv:1403.0007, doi:10.1146/annurev-astro-081811-125615.

[203] Maeda, K., Röpke, F. K., Fink, M., Hillebrandt, W., Travaglio, C., and Thielemann, F.-K. Nucleosynthesis in Two-

Dimensional Delayed Detonation Models of Type Ia Supernova Explosions. *ApJ*, **712** (2010), 624. arXiv:1002.2153, doi:10.1088/0004-637X/712/1/624.

[204] Mann, A. W. and Ebeling, H. X-ray-optical classification of cluster mergers and the evolution of the cluster merger fraction. *MNRAS*, **420** (2012), 2120. arXiv:1111.2396, doi:10.1111/j.1365-2966.2011.20170.x.

[205] Manolopoulou, M. and Plionis, M. Galaxy cluster's rotation. *MNRAS*, **465** (2017), 2616. arXiv:1604.06256, doi:10.1093/mnras/stw2870.

[206] Mantz, A. B., Allen, S. W., Morris, R. G., Schmidt, R. W., von der Linden, A., and Urban, O. Cosmology and astrophysics from relaxed galaxy clusters - I. Sample selection. *MNRAS*, **449** (2015), 199. arXiv:1502.06020, doi:10.1093/mnras/stv219.

[207] Mantz, A. B., Allen, S. W., Morris, R. G., Simionescu, A., Urban, O., Werner, N., and Zhuravleva, I. The metallicity of the intracluster medium over cosmic time: further evidence for early enrichment. *MNRAS*, **472** (2017), 2877. arXiv:1706.01476, doi:10.1093/mnras/stx2200.

[208] Mantz, A. B., et al. The XXL Survey: XVII. X-ray and Sunyaev-Zel'dovich Properties of the Redshift 2.0 Galaxy Cluster XLSSC 122. *ArXiv:1703.08221*, (2017). arXiv:1703.08221.

[209] Mantz, A. B., et al. The XXL Survey. XVII. X-ray and Sunyaev-Zel'dovich properties of the redshift 2.0 galaxy cluster XLSSC 122. *A&A*, **620** (2018), A2. arXiv:1703.08221, doi:10.1051/0004-6361/201630096.

[210] Maoz, D. and Graur, O. Star formation, supernovae, iron, and alpha: consistent cosmic and Galactic histories. *ArXiv:1703.04540*, (2017). arXiv:1703.04540.

[211] Maoz, D. and Mannucci, F. Type-Ia Supernova Rates and the Progenitor Problem: A Review. *PASA*, **29** (2012), 447. arXiv:1111.4492, doi:10.1071/AS11052.

[212] Maoz, D., Mannucci, F., and Nelemans, G. Observational Clues to the Progenitors of Type Ia Supernovae. *ARA&A*, **52** (2014), 107. arXiv:1312.0628, doi:10.1146/annurev-astro-082812-141031.

[213] Markevitch, M. On the discrepancy between Chandra and XMM temperature profiles for A1835. *arXiv e-prints*, (2002), arXiv:0205333. arXiv:arXiv:0205333.

[214] Markevitch, M., Gonzalez, A. H., David, L., Vikhlinin, A., Murray, S., Forman, W., Jones, C., and Tucker, W. A Textbook Example of a Bow Shock in the Merging Galaxy Cluster 1E 0657-56. *ApJL*, **567** (2002), L27. arXiv:arXiv:astro-ph/0110468, doi:10.1086/339619.

[215] Markevitch, M., Govoni, F., Brunetti, G., and Jerius, D. Bow Shock and Radio Halo in the Merging Cluster A520. *ApJ*, **627** (2005), 733. arXiv:astro-ph/0412451, doi:10.1086/430695.

[216] Markevitch, M., Sarazin, C. L., and Vikhlinin, A. Physics of the Merging Clusters Cygnus A, A3667, and A2065. *ApJ*, **521** (1999), 526. arXiv:astro-ph/9812005, doi:10.1086/307598.

[217] Markevitch, M. and Vikhlinin, A. Shocks and cold fronts in galaxy clusters. *PhR*, **443** (2007), 1. arXiv:astro-ph/0701821, doi:10.1016/j.physrep.2007.01.001.

[218] Markevitch, M., Vikhlinin, A., and Mazzotta, P. Nonhydrostatic Gas in the Core of the Relaxed Galaxy Cluster A1795. *ApJL*, **562** (2001), L153. arXiv:astro-ph/0108520, doi:10.1086/337973.

[219] Markevitch, M., et al. Chandra observation of abell 2142: Survival of dense subcluster cores in a merger. *The Astrophysical Journal*, **541** (2000), 542. Available from: http://stacks.iop.org/0004-637X/541/i=2/a=542.

[220] Materne, J. and Hopp, U. The cluster of galaxies SC0316-44 - Does it rotate? *A&A*, **124** (1983), L13.

[221] Matsushita, K., Finoguenov, A., and Böhringer, H. XMM observation of M 87. II. Abundance structure of the interstellar and intergalactic medium. *A&A*, **401** (2003), 443. arXiv:astro-ph/0212069, doi:10.1051/0004-6361:20021791.

[222] Matsushita, K., Sakuma, E., Sasaki, T., Sato, K., and Simionescu, A. Metal-mass-to-light Ratios of the Perseus Cluster Out to the Virial Radius. *ApJ*, **764** (2013), 147. arXiv:1301.0655, doi:10.1088/0004-637X/764/2/147.

[223] Maughan, B. J., Jones, C., Forman, W., and Van Speybroeck, L. Images, Structural Properties, and Metal Abundances of Galaxy Clusters Observed with Chandra ACIS-I at 0.1 z 1.3. *ApJS*, **174** (2008), 117-135. arXiv:astro-ph/0703156, doi:10.1086/521225.

[224] Mazzali, P. A., Röpke, F. K., Benetti, S., and Hillebrandt, W. A Common Explosion Mechanism for Type Ia Supernovae. *Science*, **315** (2007), 825. arXiv:astro-ph/0702351, doi:10.1126/science.1136259.

[225] Mazzotta, P., Markevitch, M., Vikhlinin, A., Forman, W. R., David, L. P., and van Speybroeck, L. Chandra Observation of RX J1720.1+2638: a Nearly Relaxed Cluster with a Fast-moving Core? *ApJ*, **555** (2001), 205. arXiv:astro-ph/0102291, doi:10.1086/321484.

[226] McDonald, M., et al. The Growth of Cool Cores and Evolution of Cooling Properties in a Sample of 83 Galaxy Clusters at 0.3 < z < 1.2 Selected from the SPT-SZ Survey. *ApJ*, **774** (2013), 23. arXiv:1305.2915, doi:10.1088/0004-637X/774/1/23.

[227] McDonald, M., et al. The Evolution of the Intracluster Medium Metallicity in Sunyaev Zeldovich-selected Galaxy Clusters at 0 z 1.5. *ApJ*, **826** (2016), 124. arXiv:1603.03035, doi:10.3847/0004-637X/826/2/124.

[228] McDonald, M., et al. A Detailed Study of the Most Relaxed SPT-Selected Galaxy Clusters: Cool Core and Central Galaxy Properties. *ArXiv e-prints*, (2018). arXiv:1809.09104.

[229] McNamara, B. R. and Nulsen, P. E. J. Heating Hot Atmospheres with Active Galactic Nuclei. *ARA&A*, **45** (2007), 117. arXiv:0709.2152, doi:10.1146/annurev.astro.45.051806.110625.

[230] McNamara, B. R. and O'Connell, R. W. Star formation in cooling flows in clusters of galaxies. *AJ*, **98** (1989), 2018. doi:10.1086/115275.

[231] Meekins, J. F., Fritz, G., Chubb, T. A., and Friedman, H. Physical Sciences: X-rays from the Coma Cluster of Galaxies. *Nature*, **231** (1971), 107. doi:10.1038/231107a0.

[232] Mernier, F., Werner, N., Bagchi, J., Simionescu, A., Böhringer, H., Allen, S. W., and Jacob, J. Magnetic fields and extraordinarily bright radio emission in the X-ray faint galaxy group MRC 0116 + 111. *MNRAS*, **486** (2019), 5430. arXiv:1902.09560, doi:10.1093/mnras/stz1228.

[233] Mernier, F., Werner, N., Lakhchaura, K., de Plaa, J., Gu, L., Kaastra, J. S., Mao, J., Simionescu, A., and Urdampilleta, I. How do atomic code uncertainties affect abundance measurements in the intracluster medium? *Astron. Nachr.*, **00** (2019), arXiv:1911.09684. arXiv:1911.09684.

[234] Mernier, F., et al. Origin of central abundances in the hot intracluster medium. II. Chemical enrichment and supernova yield models. *A&A*, **595** (2016), A126. arXiv:1608.03888, doi:10.1051/0004-6361/201628765.

[235] Mernier, F., et al. Radial metal abundance profiles in the intra-cluster medium of cool-core galaxy clusters, groups, and ellipticals. *A&A*, **603** (2017), A80. arXiv:1703.01183, doi:10.1051/0004-6361/201630075.

[236] Mernier, F., et al. Enrichment of the Hot Intracluster Medium: Observations. *SSRv*, **214** (2018), 129. arXiv:1811.01967, doi:10.1007/s11214-018-0565-7.

[237] Mewe, R. and Gronenschild, E. H. B. M. Calculated X-radiation from optically thin plasmas. IV - Atomic data and rate coefficients for spectra in the range 1-270 A. *A&AS*, **45** (1981), 11.

[238] Mewe, R., Gronenschild, E. H. B. M., and van den Oord, G. H. J. Calculated X-radiation from optically thin plasmas. V. *A&AS*, **62** (1985), 197.

[239] Million, E. T., Allen, S. W., Werner, N., and Taylor, G. B. Ram-pressure stripping of the cool core of the Ophiuchus Cluster. *MNRAS*, **405** (2010), 1624. arXiv:0910.0025, doi:10.1111/j.1365-2966.2010.16596.x.

[240] Million, E. T., Werner, N., Simionescu, A., and Allen, S. W. Core-collapse supernova enrichment in the core of the Virgo cluster. *MNRAS*, **418** (2011), 2744. arXiv:1108.4434, doi:10.1111/j.1365-2966.2011.19664.x.

[241] Mink, D. J., Wyatt, W. F., Caldwell, N., Conroy, M. A., Furesz, G., and Tokarz, S. P. Automating Reduction of Multifiber Spectra from the MMT Hectospec and Hectochelle. In *Astronomical Data Analysis Software and Systems XVI* (edited by R. A. Shaw, F. Hill, and D. J. Bell), vol. 376 of *Astronomical Society of the Pacific Conference Series*, p. 249 (2007).

[242] Mitchell, M. A., He, J.-h., Arnold, C., and Li, B. A general framework to test gravity using galaxy clusters - I. Modelling the dynamical mass of haloes in f(R) gravity. *MNRAS*, **477** (2018), 1133. arXiv:1802.02165, doi:10.1093/mnras/sty636.

[243] Mitchell, R. J., Culhane, J. L., Davison, P. J. N., and Ives, J. C. Ariel 5 observations of the X-ray spectrum of the Perseus Cluster. *MNRAS*, **175** (1976), 29P. doi:10.1093/mnras/175.1.29P.

[244] Molendi, S., Eckert, D., De Grandi, S., Ettori, S., Gastaldello, F., Ghizzardi, S., Pratt, G. W., and Rossetti, M. A critical assessment of the metal content of the intracluster medium. *A&A*, **586** (2016), A32. arXiv:1511.05428, doi:10.1051/0004-6361/201527356.

[245] Molendi, S. and Pizzolato, F. Is the Gas in Cooling Flows Multiphase? *ApJ*, **560** (2001), 194. arXiv:arXiv:astro-ph/0106552, doi:10.1086/322387.

[246] Munari, E., Biviano, A., Borgani, S., Murante, G., and Fabjan, D. The relation between velocity dispersion and mass in simulated clusters of galaxies: dependence on the tracer and the baryonic physics. *MNRAS*, **430** (2013), 2638. arXiv:1301.1682, doi:10.1093/mnras/stt049.

[247] Munari, E., Biviano, A., and Mamon, G. A. Mass, velocity anisotropy, and pseudo phase-space density profiles of Abell 2142. *A&A*, **566** (2014), A68. arXiv:1311.1210, doi:10.1051/0004-6361/201322450.

[248] Mushotzky, R. F. and Loewenstein, M. Lack of Evolution in the Iron Abundance in Clusters of Galaxies and Implications for the Global Star Formation Rate at High Redshift. *ApJL*, **481** (1997), L63. arXiv:astro-ph/9702149, doi:10.1086/310651.

[249] Navarro, J. F., Frenk, C. S., and White, S. D. M. The Structure of Cold Dark Matter Halos. *ApJ*, **462** (1996), 563. arXiv:astro-ph/9508025, doi:10.1086/177173.

[250] Nomoto, K., Kobayashi, C., and Tominaga, N. Nucleosynthesis in Stars and the Chemical Enrichment of Galaxies. *ARA&A*, **51** (2013), 457. doi:10.1146/annurev-astro-082812-140956.

[251] Nomoto, K. and Leung, S.-C. Single Degenerate Models for Type Ia Supernovae: Progenitor's Evolution and Nucleosynthesis Yields. *SSRv*, **214** (2018), 67. arXiv:1805.10811, doi:10.1007/s11214-018-0499-0.

[252] Nomoto, K., Tominaga, N., Umeda, H., Kobayashi, C., and Maeda, K. Nucleosynthesis yields of core-collapse supernovae and hypernovae, and galactic chemical evolution. *Nuclear Physics A*, **777** (2006), 424. arXiv:astro-ph/0605725, doi:10.1016/j.nuclphysa.2006.05.008.

[253] Oegerle, W. R. and Hill, J. M. Structure, rotation, and the peculiar velocity cD galaxy in Abell 2107. *AJ*, **104** (1992), 2078. doi:10.1086/116383.

[254] Oegerle, W. R. and Hill, J. M. Dynamics of cD Clusters of Galaxies. IV. Conclusion of a Survey of 25 Abell Clusters. *AJ*, **122** (2001), 2858. doi:10.1086/323536.

[255] Oegerle, W. R., Hill, J. M., and Fitchett, M. J. Observations of High Dispersion Clusters of Galaxies: Constraints on Cold Dark Matter. *AJ*, **110** (1995), 32. doi:10.1086/117495.

[256] O'Hara, T. B., Mohr, J. J., Bialek, J. J., and Evrard, A. E. Effects of Mergers and Core Structure on the Bulk Properties of Nearby Galaxy Clusters. *ApJ*, **639** (2006), 64. arXiv:astro-ph/0510064, doi:10.1086/499327.

[257] Okabe, N., Futamase, T., Kajisawa, M., and Kuroshima, R. Subaru Weak-lensing Survey of Dark Matter Subhalos in the Coma Cluster: Subhalo Mass Function and Statistical Properties. *ApJ*, **784** (2014), 90. arXiv:1304.2399, doi:10.1088/0004-637X/784/2/90.

[258] Okabe, N. and Smith, G. P. LoCuSS: weak-lensing mass calibration of galaxy clusters. *MNRAS*, **461** (2016), 3794. arXiv:1507.04493, doi:10.1093/mnras/stw1539.

[259] Okabe, N. and Umetsu, K. Subaru Weak Lensing Study of Seven Merging Clusters: Distributions of Mass and Baryons. *PASJ*, **60** (2008), 345. arXiv:astro-ph/0702649, doi:10.1093/pasj/60.2.345.

[260] O'Sullivan, E., David, L. P., and Vrtilek, J. M. The impact of sloshing on the intragroup medium and old radio lobe of NGC 5044.

MNRAS, **437** (2014), 730. arXiv:1310.2163, doi:10.1093/mnras/stt1926.

[261] O'Sullivan, E., Giacintucci, S., David, L. P., Vrtilek, J. M., and Raychaudhury, S. A deep Chandra observation of the poor cluster AWM 4 - II. The role of the radio jets in enriching the intracluster medium. *MNRAS*, **411** (2011), 1833. arXiv:1010.0610, doi:10.1111/j.1365-2966.2010.17812.x.

[262] Ota, N. and Yoshida, H. Search for gas bulk motions in eight nearby clusters of galaxies with Suzaku. *PASJ*, **68** (2016), S19. arXiv:1511.07904, doi:10.1093/pasj/psv128.

[263] Owers, M. S., Nulsen, P. E. J., and Couch, W. J. Minor Merger-induced Cold Fronts in Abell 2142 and RXJ1720.1+2638. *ApJ*, **741** (2011), 122. arXiv:1109.5692, doi:10.1088/0004-637X/741/2/122.

[264] Panagoulia, E. K., Fabian, A. C., and Sanders, J. S. Searching for the missing iron mass in the core of the Centaurus cluster. *MNRAS*, **433** (2013), 3290. arXiv:1305.7046, doi:10.1093/mnras/stt969.

[265] Panagoulia, E. K., Sanders, J. S., and Fabian, A. C. A volume-limited sample of X-ray galaxy groups and clusters - III. Central abundance drops. *MNRAS*, **447** (2015), 417. arXiv:1411.6040, doi:10.1093/mnras/stu2469.

[266] Parekh, V., Durret, F., Padmanabh, P., and Pandge, M. B. A hot X-ray filament associated with A3017 galaxy cluster. *MNRAS*, **470** (2017), 3742. arXiv:1705.07344, doi:10.1093/mnras/stx1457.

[267] Parekh, V., van der Heyden, K., Ferrari, C., Angus, G., and Holwerda, B. Morphology parameters: substructure identification in X-ray galaxy clusters. *A&A*, **575** (2015), A127. arXiv:1411.6525, doi:10.1051/0004-6361/201424123.

[268] Peacock, J. A. *Cosmological Physics* (1999).

[269] Peebles, P. J. E. *Principles of Physical Cosmology* (1993).

[270] Penzias, A. A. and Wilson, R. W. A Measurement of Excess Antenna Temperature at 4080 Mc/s. *ApJ*, **142** (1965), 419. doi:10.1086/148307.

[271] Peres, C. B., Fabian, A. C., Edge, A. C., Allen, S. W., Johnstone, R. M., and White, D. A. A ROSAT study of the cores of clusters of galaxies - I. Cooling flows in an X-ray flux-limited sample. *MNRAS*, **298** (1998), 416. arXiv:arXiv:astro-ph/9805122, doi:10.1046/j.1365-8711.1998.01624.x.

[272] Perlmutter, S., et al. Measurements of Ω and Λ from 42 High-Redshift Supernovae. *ApJ*, **517** (1999), 565. arXiv:astro-ph/9812133, doi:10.1086/307221.

[273] Peterson, J. R. and Fabian, A. C. X-ray spectroscopy of cooling clusters. *PhR*, **427** (2006), 1. arXiv:astro-ph/0512549, doi:10.1016/j.physrep.2005.12.007.

[274] Peterson, J. R., Paerels, F. B. S., Kaastra, J. S., Arnaud, M., Reiprich, T. H., Fabian, A. C., Mushotzky, R. F., Jernigan, J. G., and Sakelliou, I. X-ray imaging-spectroscopy of Abell 1835. *A&A*, **365** (2001), L104. arXiv:arXiv:astro-ph/0010658, doi:10.1051/0004-6361:20000021.

[275] Piffaretti, R., Arnaud, M., Pratt, G. W., Pointecouteau, E., and Melin, J.-B. The MCXC: a meta-catalogue of x-ray detected clusters of galaxies. *A&A*, **534** (2011), A109. arXiv:1007.1916, doi:10.1051/0004-6361/201015377.

[276] Piffaretti, R., Jetzer, P., Kaastra, J. S., and Tamura, T. Temperature and entropy profiles of nearby cooling flow clusters observed with XMM-Newton. *A&A*, **433** (2005), 101. arXiv:arXiv:astro-ph/0412233, doi:10.1051/0004-6361:20041888.

[277] Pinkney, J., Roettiger, K., Burns, J. O., and Bird, C. M. Evaluation of Statistical Tests for Substructure in Clusters of Galaxies. *ApJS*, **104** (1996), 1. doi:10.1086/192290.

[278] Pinto, C., Sanders, J. S., Werner, N., de Plaa, J., Fabian, A. C., Zhang, Y.-Y., Kaastra, J. S., Finoguenov, A., and Ahoranta, J. Chemical Enrichment RGS cluster Sample (CHEERS): Constraints on turbulence. *A&A*, **575** (2015), A38. arXiv:1501.01069, doi:10.1051/0004-6361/201425278.

[279] Planck Collaboration, et al. Planck early results. VIII. The all-sky early Sunyaev-Zeldovich cluster sample. *A&A*, **536** (2011), A8. arXiv:1101.2024, doi:10.1051/0004-6361/201116459.

[280] Planck Collaboration, et al. Planck 2013 results. XXIX. The Planck catalogue of Sunyaev-Zeldovich sources. *A&A*, **571** (2014), A29. arXiv:1303.5089, doi:10.1051/0004-6361/201321523.

[281] Planck Collaboration, et al. Planck 2013 results. XXXII. The updated Planck catalogue of Sunyaev-Zeldovich sources. *A&A*, **581** (2015), A14. arXiv:1502.00543, doi:10.1051/0004-6361/201525787.

[282] Planck Collaboration, et al. Planck 2015 results. XIII. Cosmological parameters. *A&A*, **594** (2016), A13. arXiv:1502.01589, doi:10.1051/0004-6361/201525830.

[283] Planelles, S., Borgani, S., Fabjan, D., Killedar, M., Murante, G., Granato, G. L., Ragone-Figueroa, C., and Dolag, K. On the role of AGN feedback on the thermal and chemodynamical properties of the hot intracluster medium. *MNRAS*, **438** (2014), 195. arXiv:1311.0818, doi:10.1093/mnras/stt2141.

[284] Pointecouteau, E. and Silk, J. New constraints on modified Newtonian dynamics from galaxy clusters. *MNRAS*, **364** (2005), 654. arXiv:astro-ph/0505017, doi:10.1111/j.1365-2966.2005.09590.x.

[285] Ponman, T. J., Cannon, D. B., and Navarro, J. F. The thermal imprint of galaxy formation on X-ray clusters. *Nature*, **397** (1999), 135. arXiv:astro-ph/9810359, doi:10.1038/16410.

[286] Porter, T. A., Johnson, R. P., and Graham, P. W. Dark matter searches with astroparticle data. *Annual Review*

of Astronomy and Astrophysics, **49** (2011), 155. Available from: https://doi.org/10.1146/annurev-astro-081710-102528, arXiv: https://doi.org/10.1146/annurev-astro-081710-102528, doi:10.1146/annurev-astro-081710-102528.

[287] Pratt, G. W., Croston, J. H., Arnaud, M., and Böhringer, H. Galaxy cluster X-ray luminosity scaling relations from a representative local sample (REXCESS). *A&A*, **498** (2009), 361. arXiv:0809.3784, doi:10.1051/0004-6361/200810994.

[288] Predehl, P. eROSITA on SRG. *Astronomische Nachrichten*, **338** (2017), 159. doi:10.1002/asna.201713324.

[289] Presotto, V., et al. Intracluster light properties in the CLASH-VLT cluster MACS J1206.2-0847. *A&A*, **565** (2014), A126. arXiv:1403.4979, doi:10.1051/0004-6361/201323251.

[290] Rajpurohit, K., et al. Deep VLA Observations of the Cluster 1RXS J0603.3+4214 in the Frequency Range of 12 GHz. *ApJ*, **852** (2018), 65. arXiv:1712.01327, doi:10.3847/1538-4357/aa9f13.

[291] Rasmussen, J. and Ponman, T. J. Temperature and abundance profiles of hot gas in galaxy groups - I. Results and statistical analysis. *MNRAS*, **380** (2007), 1554. arXiv:0707.0717, doi:10.1111/j.1365-2966.2007.12191.x.

[292] Raymond, J. C. and Smith, B. W. Soft X-ray spectrum of a hot plasma. *ApJS*, **35** (1977), 419. doi:10.1086/190486.

[293] Rebusco, P., Churazov, E., Böhringer, H., and Forman, W. Impact of stochastic gas motions on galaxy cluster abundance profiles. *MNRAS*, **359** (2005), 1041. arXiv:astro-ph/0501141, doi:10.1111/j.1365-2966.2005.08965.x.

[294] Reichardt, C. L., et al. Galaxy Clusters Discovered via the Sunyaev-Zel'dovich Effect in the First 720 Square Degrees of the South Pole Telescope Survey. *ApJ*, **763** (2013), 127. arXiv:1203.5775, doi:10.1088/0004-637X/763/2/127.

[295] Renzini, A. Iron as a Tracer in Galaxy Clusters and Groups. *ApJ*, **488** (1997), 35. arXiv:astro-ph/9706083, doi:10.1086/304696.

[296] Riess, A. G., et al. Observational Evidence from Supernovae for an Accelerating Universe and a Cosmological Constant. *AJ*, **116** (1998), 1009. arXiv:astro-ph/9805201, doi:10.1086/300499.

[297] Rines, K. J., Geller, M. J., Diaferio, A., and Hwang, H. S. HeCS-SZ: The Hectospec Survey of Sunyaev-Zeldovich-selected Clusters. *ApJ*, **819** (2016), 63. arXiv:1507.08289, doi:10.3847/0004-637X/819/1/63.

[298] Riseley, C. J., Scaife, A. M. M., Wise, M. W., and Clarke, A. O. Diffuse radio emission in MACS J0025.4-1222: the effect of a major merger on bulk separation of ICM components. *A&A*, **597** (2017), A96. arXiv:1611.01273, doi:10.1051/0004-6361/201629530.

[299] Roediger, E., Brüggen, M., Rebusco, P., Böhringer, H., and Churazov, E. Metal mixing by buoyant bubbles in galaxy clusters. *MNRAS*, **375** (2007), 15. arXiv:astro-ph/0611531, doi:10.1111/j.1365-2966.2006.11300.x.

[300] Romeo, A. D., Sommer-Larsen, J., Portinari, L., and Antonuccio-Delogu, V. Simulating galaxy clusters - I. Thermal and chemical properties of the intracluster medium. *MNRAS*, **371** (2006), 548. arXiv:astro-ph/0509504, doi:10.1111/j.1365-2966.2006.10735.x.

[301] Rosati, P., Balestra, I., Grillo, C., Mercurio, A., Nonino, M., Biviano, A., Girardi, M., Vanzella, E., and Clash-VLT Team. CLASH-VLT: A VIMOS Large Programme to Map the Dark Matter Mass Distribution in Galaxy Clusters and Probe Distant Lensed Galaxies. *The Messenger*, **158** (2014), 48.

[302] Rosati, P., Borgani, S., and Norman, C. The Evolution of X-ray Clusters of Galaxies. *ARA&A*, **40** (2002), 539. arXiv:astro-ph/0209035, doi:10.1146/annurev.astro.40.120401.150547.

[303] Rosati, P., et al. Multi-wavelength study of XMMU J2235.3-2557: the most massive galaxy cluster at z 1. *A&A*, **508** (2009), 583. arXiv:0910.1716, doi:10.1051/0004-6361/200913099.

[304] Rossetti, M., Eckert, D., De Grandi, S., Gastaldello, F., Ghizzardi, S., Roediger, E., and Molendi, S. Abell 2142 at large scales: An extreme case for sloshing? *A&A*, **556** (2013), A44. arXiv:1305.2420, doi:10.1051/0004-6361/201321319.

[305] Rossetti, M., Gastaldello, F., Eckert, D., Della Torre, M., Pantiri, G., Cazzoletti, P., and Molendi, S. The cool-core state of Planck SZ-selected clusters versus X-ray-selected samples: evidence for cool-core bias. *MNRAS*, **468** (2017), 1917. arXiv:1702.06961, doi:10.1093/mnras/stx493.

[306] Rossetti, M., Gastaldello, F., Ferioli, G., Bersanelli, M., De Grandi, S., Eckert, D., Ghizzardi, S., Maino, D., and Molendi, S. Measuring the dynamical state of Planck SZ-selected clusters: X-ray peak - BCG offset. *MNRAS*, **457** (2016), 4515. arXiv:1512.00410, doi:10.1093/mnras/stw265.

[307] Russell, H. R., Sanders, J. S., and Fabian, A. C. Direct X-ray spectral deprojection of galaxy clusters. *MNRAS*, **390** (2008), 1207. arXiv:0808.2371, doi:10.1111/j.1365-2966.2008.13823.x.

[308] Russell, H. R., Sanders, J. S., Fabian, A. C., Baum, S. A., Donahue, M., Edge, A. C., McNamara, B. R., and O'Dea, C. P. Chandra observation of two shock fronts in the merging galaxy cluster Abell 2146. *MNRAS*, **406** (2010), 1721. arXiv:1004.1559, doi:10.1111/j.1365-2966.2010.16822.x.

[309] Russell, H. R., et al. Shock fronts, electron-ion equilibration and intracluster medium transport processes in the merging cluster Abell 2146. *MNRAS*, **423** (2012), 236. arXiv:1202.5320, doi:10.1111/j.1365-2966.2012.20808.x.

[310] Rybicki, G. B. and Lightman, A. P. *Radiative Processes in Astrophysics* (1986).

[311] Salpeter, E. E. The Luminosity Function and Stellar Evolution. *ApJ*, **121** (1955), 161. doi:10.1086/145971.

[312] Sanders, J. S. and Fabian, A. C. Spatially resolved X-ray spectroscopy of the core of the Centaurus cluster. *MNRAS*, **331** (2002), 273. arXiv:astro-ph/0109336, doi:10.1046/j.1365-8711.2002.05211.x.

[313] Sanders, J. S. and Fabian, A. C. Resonance scattering, absorption and off-centre abundance peaks in clusters of galaxies. *MNRAS*, **370** (2006), 63. arXiv:astro-ph/0604575, doi:10.1111/j.1365-2966.2006.10497.x.

[314] Sanders, J. S. and Fabian, A. C. A deeper X-ray study of the core of the Perseus galaxy cluster: the power of sound waves and the distribution of metals and cosmic rays. *MNRAS*, **381** (2007), 1381. arXiv:0705.2712, doi:10.1111/j.1365-2966.2007.12347.x.

[315] Sanders, J. S. and Fabian, A. C. Revealing O VII from stacked X-ray grating spectra of clusters, groups and elliptical galaxies. *MNRAS*, **412** (2011), L35. arXiv:1012.0235, doi:10.1111/j.1745-3933.2010.01000.x.

[316] Sanders, J. S., Fabian, A. C., Russell, H. R., Walker, S. A., and Blundell, K. M. Detecting edges in the X-ray surface brightness of galaxy clusters. *MNRAS*, **460** (2016), 1898. arXiv:1605.02911, doi:10.1093/mnras/stw1119.

[317] Sanders, J. S., Fabian, A. C., and Taylor, G. B. A Chandra observation of the disturbed cluster core of Abell 2204. *MNRAS*, **356** (2005), 1022. arXiv:astro-ph/0406094, doi:10.1111/j.1365-2966.2004.08526.x.

[318] Sanders, J. S., Fabian, A. C., and Taylor, G. B. Feedback through multiple outbursts in the cluster 2A 0335+096. *MNRAS*, **396** (2009), 1449. arXiv:0904.1374, doi:10.1111/j.1365-2966.2009.14892.x.

[319] Sanders, J. S., et al. Measuring bulk flows of the intracluster medium in the Perseus and Coma galaxy clusters using XMM-Newton. *arXiv e-prints*, (2019), arXiv:1911.13108. arXiv:1911.13108.

[320] Sanders, R. H. Clusters of galaxies with modified Newtonian dynamics. *MNRAS*, **342** (2003), 901. arXiv:astro-ph/0212293, doi:10.1046/j.1365-8711.2003.06596.x.

[321] Sanders, R. H. and McGaugh, S. S. Modified newtonian dynamics as an alternative to dark matter. *Annual Review of Astronomy and Astrophysics*, **40** (2002), 263. Available from: https://doi.org/10.1146/annurev.astro.40.060401.093923, arXiv:https://doi.org/10.1146/annurev.astro.40.060401.093923, doi:10.1146/annurev.astro.40.060401.093923.

[322] Sanderson, A. J. R., O'Sullivan, E., and Ponman, T. J. A statistically selected Chandra sample of 20 galaxy clusters - II. Gas properties and cool core/non-cool core bimodality. *MNRAS*, **395** (2009), 764. arXiv:0902.1747, doi:10.1111/j.1365-2966.2009.14613.x.

[323] Sanderson, A. J. R., Ponman, T. J., and O'Sullivan, E. A statistically selected Chandra sample of 20 galaxy clusters - I. Temperature and cooling time profiles. *MNRAS*, **372** (2006), 1496. arXiv:arXiv:astro-ph/0608423, doi:10.1111/j.1365-2966.2006.10956.x.

[324] Santos, J. S., Rosati, P., Tozzi, P., Böhringer, H., Ettori, S., and Bignamini, A. Searching for cool core clusters at high redshift. *A&A*, **483** (2008), 35. arXiv:0802.1445, doi:10.1051/0004-6361:20078815.

[325] Santos, J. S., Tozzi, P., Rosati, P., and Böhringer, H. The evolution of cool-core clusters. *A&A*, **521** (2010), A64. arXiv:1008.0754, doi:10.1051/0004-6361/201015208.

[326] Santos, J. S., Tozzi, P., Rosati, P., Nonino, M., and Giovannini, G. Deep Chandra observation of the galaxy cluster WARPJ1415.1+3612 at z =1 . An evolved cool-core cluster at high

redshift. *A&A*, **539** (2012), A105. arXiv:1111.3642, doi:10.1051/0004-6361/201118162.

[327] Sarazin, C. L. *X-ray emission from clusters of galaxies* (1988).

[328] Sato, K., Matsushita, K., Ishisaki, Y., Yamasaki, N. Y., Ishida, M., Sasaki, S., and Ohashi, T. Suzaku Observations of AWM 7 Cluster of Galaxies: Temperatures, Abundances, and Bulk Motions. *PASJ*, **60** (2008), 333. arXiv:0707.4342.

[329] Sato, K., Tokoi, K., Matsushita, K., Ishisaki, Y., Yamasaki, N. Y., Ishida, M., and Ohashi, T. Type Ia and II Supernovae Contributions to Metal Enrichment in the Intracluster Medium Observed with Suzaku. *ApJL*, **667** (2007), L41. arXiv:0708.0263, doi:10.1086/522031.

[330] Sato, T., Matsushita, K., Ota, N., Sato, K., Nakazawa, K., and Sarazin, C. L. Suzaku Observations of Iron K-Lines from the Intracluster Medium of the Coma Cluster. *PASJ*, **63** (2011), 991. arXiv:1109.0154, doi:10.1093/pasj/63.sp3.S991.

[331] Schmidt, F., Vikhlinin, A., and Hu, W. Cluster constraints on f(R) gravity. *PhRvD*, **80** (2009), 083505. arXiv:0908.2457, doi:10.1103/PhysRevD.80.083505.

[332] SDSS Collaboration, Albareti, F. D., Allende Prieto, C., Almeida, A., Anders, F., and et al. The Thirteenth Data Release of the Sloan Digital Sky Survey: First Spectroscopic Data from the SDSS-IV Survey MApping Nearby Galaxies at Apache Point Observatory. *ArXiv e-prints*, (2016). arXiv:1608.02013.

[333] Seitenzahl, I. R., et al. Three-dimensional delayed-detonation models with nucleosynthesis for Type Ia supernovae. *MNRAS*, **429** (2013), 1156. arXiv:1211.3015, doi:10.1093/mnras/sts402.

[334] Serlemitsos, P. J., Smith, B. W., Boldt, E. A., Holt, S. S., and Swank, J. H. X-radiation from clusters of galaxies - Spectral evidence for a hot evolved gas. *ApJL*, **211** (1977), L63. doi:10.1086/182342.

[335] Serna, A. and Gerbal, D. Dynamical search for substructures in galaxy clusters. A hierarchical clustering method. *A&A*, **309** (1996), 65. Available from: http://adsabs.harvard.edu/abs/1996A%26A...309..65S, arXiv:astro-ph/9509080.

[336] Serra, A. L. and Diaferio, A. Identification of Members in the Central and Outer Regions of Galaxy Clusters. *ApJ*, **768** (2013), 116. arXiv:1211.3669, doi:10.1088/0004-637X/768/2/116.

[337] Serra, A. L., Diaferio, A., Murante, G., and Borgani, S. Measuring the escape velocity and mass profiles of galaxy clusters beyond their virial radius. *MNRAS*, **412** (2011), 800. arXiv:1011.0372, doi:10.1111/j.1365-2966.2010.17946.x.

[338] Sijacki, D., Springel, V., Di Matteo, T., and Hernquist, L. A unified model for AGN feedback in cosmological simulations of structure formation. *MNRAS*, **380** (2007), 877. arXiv:0705.2238, doi:10.1111/j.1365-2966.2007.12153.x.

[339] Simionescu, A., Werner, N., Böhringer, H., Kaastra, J. S., Finoguenov, A., Brüggen, M., and Nulsen, P. E. J. Chemical enrichment in the cluster of galaxies Hydra A. *A&A*, **493** (2009), 409. arXiv:0809.2613, doi:10.1051/0004-6361:200810225.

[340] Simionescu, A., Werner, N., Forman, W. R., Miller, E. D., Takei, Y., Böhringer, H., Churazov, E., and Nulsen, P. E. J. Metal transport by gas sloshing in M87. *MNRAS*, **405** (2010), 91. arXiv:1002.0395, doi:10.1111/j.1365-2966.2010.16450.x.

[341] Simionescu, A., Werner, N., Mantz, A., Allen, S. W., and Urban, O. Witnessing the growth of the nearest galaxy cluster: thermodynamics of the Virgo Cluster outskirts. *MNRAS*, **469** (2017), 1476. arXiv:1704.01236, doi:10.1093/mnras/stx919.

[342] Simionescu, A., Werner, N., Urban, O., Allen, S. W., Ichinohe, Y., and Zhuravleva, I. A Uniform Contribution of Core-collapse and Type Ia Supernovae to the Chemical Enrichment Pat-

tern in the Outskirts of the Virgo Cluster. *ApJL*, **811** (2015), L25. arXiv:1506.06164, doi:10.1088/2041-8205/811/2/L25.

[343] Simionescu, A., et al. Constraints on the chemical enrichment history of the Perseus Cluster of galaxies from high-resolution X-ray spectroscopy. *MNRAS*, **483** (2019), 1701. arXiv:1806.00932, doi:10.1093/mnras/sty3220.

[344] Smartt, S. J. Progenitors of Core-Collapse Supernovae. *ARA&A*, **47** (2009), 63. arXiv:0908.0700, doi:10.1146/annurev-astro-082708-101737.

[345] Smith, R. K., Brickhouse, N. S., Liedahl, D. A., and Raymond, J. C. Collisional Plasma Models with APEC/APED: Emission-Line Diagnostics of Hydrogen-like and Helium-like Ions. *ApJL*, **556** (2001), L91. arXiv:astro-ph/0106478, doi:10.1086/322992.

[346] Smoot, G. F., et al. Structure in the COBE differential microwave radiometer first-year maps. *ApJL*, **396** (1992), L1. doi:10.1086/186504.

[347] Song, H., Hwang, H. S., Park, C., Smith, R., and Einasto, M. A Redshift Survey of the Nearby Galaxy Cluster A2107: Global Rotation of the Cluster and Its Connection to Large-scale Structures in the Universe. *ApJ*, **869** (2018), 124. arXiv:1810.11985, doi:10.3847/1538-4357/aaed27.

[348] Song, H., Hwang, H. S., Park, C., and Tamura, T. A Redshift Survey of the Nearby Galaxy Cluster Abell 2199: Comparison of the Spatial and Kinematic Distributions of Galaxies with the Intracluster Medium. *ApJ*, **842** (2017), 88. arXiv:1705.04232, doi:10.3847/1538-4357/aa72dc.

[349] Springel, V. The cosmological simulation code GADGET-2. *MNRAS*, **364** (2005), 1105. arXiv:astro-ph/0505010, doi:10.1111/j.1365-2966.2005.09655.x.

[350] Staniszewski, Z., et al. Galaxy Clusters Discovered with a Sunyaev-Zel'dovich Effect Survey. *ApJ*, **701** (2009), 32. arXiv:0810.1578, doi:10.1088/0004-637X/701/1/32.

[351] Starling, R. L. C., Willingale, R., Tanvir, N. R., Scott, A. E., Wiersema, K., O'Brien, P. T., Levan, A. J., and Stewart, G. C. X-ray absorption evolution in gamma-ray bursts: intergalactic medium or evolutionary signature of their host galaxies. *MNRAS*, **431** (2013), 3159. arXiv:1303.0844, doi:10.1093/mnras/stt400.

[352] Stewart, G. C., Fabian, A. C., Nulsen, P. E. J., and Canizares, C. R. The mass profile and gas content of M87. *ApJ*, **278** (1984), 536. doi:10.1086/161820.

[353] Strüder, L., et al. The European Photon Imaging Camera on XMM-Newton: The pn-CCD camera. *A&A*, **365** (2001), L18. doi:10.1051/0004-6361:20000066.

[354] Sugawara, C., Takizawa, M., and Nakazawa, K. Suzaku Observation of the Radio Halo Cluster Abell 2319: Gas Dynamics and Hard X-Ray Properties. *PASJ*, **61** (2009), 1293. arXiv:0909.1358, doi:10.1093/pasj/61.6.1293.

[355] Suginohara, T. and Ostriker, J. P. The Effect of Cooling on the Density Profile of Hot Gas in Clusters of Galaxies: Is Additional Physics Needed? *ApJ*, **507** (1998), 16. arXiv:astro-ph/9803318, doi:10.1086/306326.

[356] Sukhbold, T., Ertl, T., Woosley, S. E., Brown, J. M., and Janka, H.-T. Core-collapse Supernovae from 9 to 120 Solar Masses Based on Neutrino-powered Explosions. *ApJ*, **821** (2016), 38. arXiv:1510.04643, doi:10.3847/0004-637X/821/1/38.

[357] Sun, M. Every BCG with a Strong Radio Agn has an X-Ray Cool Core: Is the Cool Core-Noncool Core Dichotomy Too Simple? *ApJ*, **704** (2009), 1586. arXiv:0904.2006, doi:10.1088/0004-637X/704/2/1586.

[358] Sun, M., Voit, G. M., Donahue, M., Jones, C., Forman, W., and Vikhlinin, A. Chandra Studies of the X-Ray Gas Properties of Galaxy Groups. *ApJ*, **693** (2009), 1142. arXiv:0805.2320, doi:10.1088/0004-637X/693/2/1142.

[359] Sunyaev, R. A. and Zeldovich, Y. B. The Spectrum of Primordial Radiation, its Distortions and their Significance. *CoASP*, **2** (1970), 66.

[360] Sunyaev, R. A. and Zeldovich, Y. B. The Observations of Relic Radiation as a Test of the Nature of X-Ray Radiation from the Clusters of Galaxies. *CoASP*, **4** (1972), 173.

[361] Sutherland, R. S. and Dopita, M. A. Cooling functions for low-density astrophysical plasmas. *ApJS*, **88** (1993), 253. doi:10.1086/191823.

[362] Takahashi, T., Mitsuda, K., Kelley, R., Fabian, A., Mushotzky, R., Ohashi, T., Petre, R., and on behalf of the ASTRO-H Science Working Group. ASTRO-H White Paper - Introduction. *arXiv e-prints*, (2014). arXiv:1412.2351.

[363] Takahashi, T., et al. The ASTRO-H X-ray astronomy satellite. In *Space Telescopes and Instrumentation 2014: Ultraviolet to Gamma Ray*, vol. 9144 of *Proc. SPIE*, p. 914425 (2014). arXiv:1412.1356, doi:10.1117/12.2055681.

[364] Takahashi, T., et al. Hitomi (ASTRO-H) X-ray Astronomy Satellite. *Journal of Astronomical Telescopes, Instruments, and Systems*, **4** (2018), 021402. doi:10.1117/1.JATIS.4.2.021402.

[365] Tamura, T., Kaastra, J. S., den Herder, J. W. A., Bleeker, J. A. M., and Peterson, J. R. Elemental abundances in the intracluster medium as observed with XMM-Newton. *A&A*, **420** (2004), 135. arXiv:astro-ph/0403058, doi:10.1051/0004-6361:20040103.

[366] Tamura, T., et al. X-ray Spectroscopy of the Core of the Perseus Cluster with Suzaku: Elemental Abundances in the Intracluster Medium.

ApJL, **705** (2009), L62. arXiv:0909.5003, doi:10.1088/0004-637X/705/1/L62.

[367] Tamura, T., et al. Gas Bulk Motion in the Perseus Cluster Measured with Suzaku. *ApJ*, **782** (2014), 38. arXiv:1312.4526, doi:10.1088/0004-637X/782/1/38.

[368] Tananbaum, H., Gursky, H., Kellogg, E. M., Levinson, R., Schreier, E., and Giacconi, R. Discovery of a Periodic Pulsating Binary X-Ray Source in Hercules from UHURU. *ApJL*, **174** (1972), L143. doi:10.1086/180968.

[369] Tchernin, C., et al. The XMM Cluster Outskirts Project (X-COP): Physical conditions of Abell 2142 up to the virial radius. *A&A*, **595** (2016), A42. arXiv:1606.05657, doi:10.1051/0004-6361/201628183.

[370] Thölken, S., Lovisari, L., Reiprich, T. H., and Hasenbusch, J. X-ray analysis of the galaxy group UGC 03957 beyond R_{200} with Suzaku. *A&A*, **592** (2016), A37. arXiv:1603.05255, doi:10.1051/0004-6361/201527608.

[371] Tittley, E. R. and Henriksen, M. Cluster Mergers, Core Oscillations, and Cold Fronts. *ApJ*, **618** (2005), 227. arXiv:astro-ph/0409177, doi:10.1086/425952.

[372] Tornatore, L., Borgani, S., Matteucci, F., Recchi, S., and Tozzi, P. Simulating the metal enrichment of the intracluster medium. *MNRAS*, **349** (2004), L19. arXiv:astro-ph/0401576, doi:10.1111/j.1365-2966.2004.07689.x.

[373] Tovmassian, H. M. The Rotation of Galaxy Clusters. *Astrophysics*, **58** (2015), 328. arXiv:1510.03489, doi:10.1007/s10511-015-9387-4.

[374] Tovmassian, H. M. The Rotation of Groups of Galaxies. *Astrophysics*, **58** (2015), 471. doi:10.1007/s10511-015-9400-y.

[375] Tozzi, P. and Norman, C. The Evolution of X-Ray Clusters and the Entropy of the Intracluster Medium. *ApJ*, **546** (2001), 63. arXiv:astro-ph/0003289, doi:10.1086/318237.

[376] Tozzi, P., Rosati, P., Ettori, S., Borgani, S., Mainieri, V., and Norman, C. Iron Abundance in the Intracluster Medium at High Redshift. *ApJ*, **593** (2003), 705. arXiv:astro-ph/0305223, doi:10.1086/376731.

[377] Tozzi, P., Santos, J. S., Nonino, M., Rosati, P., Borgani, S., Sartoris, B., Altieri, B., and Sanchez-Portal, M. Chandra and optical/IR observations of CXO J1415.2+3610, a massive, newly discovered galaxy cluster at z ˜ 1.5. *A&A*, **551** (2013), A45. arXiv:1212.2560, doi:10.1051/0004-6361/201220637.

[378] Tozzi, P., et al. Chandra Deep Observation of XDCP J0044.0-2033, a Massive Galaxy Cluster at z 1.5. *ApJ*, **799** (2015), 93. arXiv:1412.5200, doi:10.1088/0004-637X/799/1/93.

[379] Turner, M. J. L., et al. The European Photon Imaging Camera on XMM-Newton: The MOS cameras : The MOS cameras. *A&A*, **365** (2001), L27. arXiv:astro-ph/0011498, doi:10.1051/0004-6361:20000087.

[380] Ueda, S., Ichinohe, Y., Kitayama, T., and Umetsu, K. Line-of-Sight Gas Sloshing in the Cool Core of Abell 907. *ApJ*, **871** (2019), 207. arXiv:1812.07835, doi:10.3847/1538-4357/aafa19.

[381] Umetsu, K., et al. Mass and Hot Baryons in Massive Galaxy Clusters from Subaru Weak-Lensing and AMiBA Sunyaev-Zel'Dovich Effect Observations. *ApJ*, **694** (2009), 1643. arXiv:0810.0969, doi:10.1088/0004-637X/694/2/1643.

[382] Umetsu, K., et al. CLASH: Weak-lensing Shear-and-magnification Analysis of 20 Galaxy Clusters. *ApJ*, **795** (2014), 163. arXiv:1404.1375, doi:10.1088/0004-637X/795/2/163.

[383] Urban, O., Werner, N., Allen, S. W., Simionescu, A., and Mantz, A. A uniform metallicity in the outskirts of massive, nearby galaxy clusters. *MNRAS*, **470** (2017), 4583. arXiv:1706.01567, doi:10.1093/mnras/stx1542.

[384] Urdampilleta, I., Mernier, F., Kaastra, J. S., Simionescu, A., de Plaa, J., Kara, S., and Ercan, E. N. Iron abundance distribution in the hot gas of merging galaxy clusters. *A&A*, **629** (2019), A31. arXiv:1906.08067, doi:10.1051/0004-6361/201935452.

[385] Vanderlinde, K., et al. Galaxy Clusters Selected with the Sunyaev-Zel'dovich Effect from 2008 South Pole Telescope Observations. *ApJ*, **722** (2010), 1180. arXiv:1003.0003, doi:10.1088/0004-637X/722/2/1180.

[386] Venturi, T., et al. The two-component giant radio halo in the galaxy cluster Abell 2142. *A&A*, **603** (2017), A125. arXiv:1703.06802, doi:10.1051/0004-6361/201630014.

[387] Vikhlinin, A., Burenin, R., Forman, W. R., Jones, C., Hornstrup, A., Murray, S. S., and Quintana, H. Lack of Cooling Flow Clusters at z $>$ 0.5. In *Heating versus Cooling in Galaxies and Clusters of Galaxies* (edited by H. Böhringer, G. W. Pratt, A. Finoguenov, and P. Schuecker), p. 48 (2007). arXiv:arXiv:astro-ph/0611438, doi:10.1007/978-3-540-73484-0_9.

[388] Vikhlinin, A., Kravtsov, A., Forman, W., Jones, C., Markevitch, M., Murray, S. S., and Van Speybroeck, L. Chandra Sample of Nearby Relaxed Galaxy Clusters: Mass, Gas Fraction, and Mass-Temperature Relation. *ApJ*, **640** (2006), 691. arXiv:astro-ph/0507092, doi:10.1086/500288.

[389] Vikhlinin, A., Markevitch, M., and Murray, S. S. A Moving Cold Front in the Intergalactic Medium of A3667. *ApJ*, **551** (2001), 160. arXiv:astro-ph/0008496, doi:10.1086/320078.

[390] Vikhlinin, A., Markevitch, M., Murray, S. S., Jones, C., Forman, W., and Van Speybroeck, L. Chandra Temperature Profiles for a Sample of Nearby Relaxed Galaxy Clusters. *ApJ*, **628** (2005), 655. arXiv:arXiv:astro-ph/0412306, doi:10.1086/431142.

[391] Vikhlinin, A., et al. Chandra Cluster Cosmology Project. II. Samples and X-Ray Data Reduction. *ApJ*, **692** (2009), 1033. arXiv:0805.2207, doi:10.1088/0004-637X/692/2/1033.

[392] Voit, G. M. and Donahue, M. The Fate of Stellar Mass Loss in Central Cluster Galaxies. *ApJL*, **738** (2011), L24. arXiv:1108.2068, doi:10.1088/2041-8205/738/2/L24.

[393] Wen, Z. L. and Han, J. L. Substructure and dynamical state of 2092 rich clusters of galaxies derived from photometric data. *MNRAS*, **436** (2013), 275. arXiv:1307.0568, doi:10.1093/mnras/stt1581.

[394] Werner, N., de Plaa, J., Kaastra, J. S., Vink, J., Bleeker, J. A. M., Tamura, T., Peterson, J. R., and Verbunt, F. XMM-Newton spectroscopy of the cluster of galaxies 2A 0335+096. *A&A*, **449** (2006), 475. arXiv:astro-ph/0512401, doi:10.1051/0004-6361:20053868.

[395] Werner, N., Durret, F., Ohashi, T., Schindler, S., and Wiersma, R. P. C. Observations of Metals in the Intra-Cluster Medium. *SSRv*, **134** (2008), 337. arXiv:0801.1052, doi:10.1007/s11214-008-9320-9.

[396] Werner, N., Urban, O., Simionescu, A., and Allen, S. W. A uniform metal distribution in the intergalactic medium of the Perseus cluster of galaxies. *Nature*, **502** (2013), 656. arXiv:1310.7948, doi:10.1038/nature12646.

[397] Werner, N., et al. Deep Chandra observation and numerical studies of the nearest cluster cold front in the sky. *MNRAS*, **455** (2016), 846. arXiv:1506.06429, doi:10.1093/mnras/stv2358.

[398] Willingale, R., Starling, R. L. C., Beardmore, A. P., Tanvir, N. R., and O'Brien, P. T. Calibration of X-ray absorption in our Galaxy. *MNRAS*, **431** (2013), 394. arXiv:1303.0843, doi:10.1093/mnras/stt175.

[399] Wilms, J., Allen, A., and McCray, R. On the Absorption of X-Rays in the Interstellar Medium. *ApJ*, **542** (2000), 914. arXiv:astro-ph/0008425, doi:10.1086/317016.

[400] Wolter, H. Spiegelsysteme streifenden Einfalls als abbildende Optiken für Röntgenstrahlen. *Annalen der Physik*, **445** (1952), 94. doi:10.1002/andp.19524450108.

[401] Yahil, A. and Vidal, N. V. The Velocity Distribution of Galaxies in Clusters. *ApJ*, **214** (1977), 347. doi:10.1086/155257.

[402] Yang, L., Tozzi, P., Yu, H., Lusso, E., Gaspari, M., Gilli, R., Nardini, E., and Risaliti, G. X-Ray Properties of AGN in Brightest Cluster Galaxies. I. A Systematic Study of the Chandra Archive in the 0.2 z 0.3 and 0.55 z 0.75 Redshift Range. *ApJ*, **859** (2018), 65. arXiv:1804.08633, doi:10.3847/1538-4357/aabfd7.

[403] Yu, H., Serra, A. L., Diaferio, A., and Baldi, M. Identification of Galaxy Cluster Substructures with the Caustic Method. *ApJ*, **810** (2015), 37. arXiv:1503.08823, doi:10.1088/0004-637X/810/1/37.

[404] Yu, H., Tozzi, P., Borgani, S., Rosati, P., and Zhu, Z.-H. Measuring redshifts using X-ray spectroscopy of galaxy clusters: results from Chandra data and future prospects. *A&A*, **529** (2011), A65. arXiv:1102.2089, doi:10.1051/0004-6361/201016236.

[405] Zarattini, S., et al. Fossil group origins. VII. Galaxy substructures in fossil systems. *A&A*, **586** (2016), A63. arXiv:1511.02854, doi:10.1051/0004-6361/201527175.

[406] Zhang, C., Churazov, E., Forman, W. R., and Jones, C. Stand-off distance of bow shocks in galaxy clusters as proxy for Mach number. *MNRAS*, **482** (2019), 20. arXiv:1808.02885, doi:10.1093/mnras/sty2501.

[407] Zhuravleva, I., Churazov, E., Kravtsov, A., and Sunyaev, R. Constraints on the ICM velocity power spectrum from the X-ray

lines width and shift. *MNRAS*, **422** (2012), 2712. arXiv:1203.1057, doi:10.1111/j.1365-2966.2012.20844.x.

[408] Zwicky, F. Die Rotverschiebung von extragalaktischen Nebeln. *Helvetica Physica Acta*, **6** (1933), 110.

[409] Zwicky, F. On the Masses of Nebulae and of Clusters of Nebulae. *ApJ*, **86** (1937), 217. doi:10.1086/143864.

Acknowledgments

The work presented in this thesis could not have been finished without the help of my supervisor, Dr. Paolo Tozzi. I have benefited a lot from the guidance of Paolo since 2013, when I was a Master student at Beijing Normal University. His extensive experience and acute insight have been so important to me, and have prevented me many times from making mistakes or going into wrong directions in research. He is always ready to give me advice and assistance on many aspects, from the reduction and analysis of X-ray data, to the writing of a scientific article or an observing proposal. It is his great effort that has helped me grow from a young student who has no experience of performing independent research, to who I am today. I owe my greatest appreciation to Paolo.

I would like to thank my collaborators, Dr. Stefano Ettori, Piero Rosati, Sabrina De Grandi, Fabio Gastaldello, Ciro Pinto, Colin Norman, Meng Zhai, Edoardo Iani, Giulia Rodighiero, Gabriel Caminha, Roberto Gilli, Eros Vanzella, Antonaldo Diaferio, Ho Seong Hwang, Keiichi Umetsu, and Nobuhiro Okabe, for your great help in my research during PhD. I have learned so much from the collaborations and discussions with you. Your generous assistance and constructive comments and ideas are essential to the work in this thesis, and will also be of great importance to my future career.

I am very grateful to Elena Amato, Guido Risaliti, Giovanni Cresci, Anna Gallazzi, Crescenzo Tortora, Simone Bianchi, Leslie Hunt, and everyone in Arcetri Astrophysical Observatory who have helped me in my course works and research. I also thank Pasquale Mazzotta, Fernanda Lupinacci, Roberto Capuzzo Dolcetta and Paolo de Bernardis in Rome, for their assistance to me during the past three years.

I would like to thank my supervisor in the University of Oklahoma, Dr.

Xinyu Dai, for your guidance and support to me. It is such a pity that I was not able to finish the PhD in OU, but I really enjoy the time working with you. Your creativity, your deep and extensive knowledge over a wide scope of research fields, and your enthusiasm on astrophysical research, have all deeply impressed me, and made a great impact on my career and also my personality. I also would like to thank Eduardo Guerras, John Wisniewski, and everyone in OU who have helped me in my course works and research. The time in OU has been a precious memory in my life.

I would like to thank my supervisor in Beijing Normal University, Dr. Zonghong Zhu, for your support since 2011 when I was an undergraduate student. I view you as a life mentor, not only because you are a great scientist, but your personality has deeply impacted my career and life.

Finally, I would like to thank my family for the love and support for all these years.

Publication list

- On the origin of central abundance drops in the intracluster medium of galaxy groups and clusters

  Ang Liu, Meng Zhai, Paolo Tozzi

  2019, MNRAS, 485, 1651 (this thesis, Chapter 3) [197]

- Testing the rotation versus merger scenario in the galaxy cluster Abell 2107

  Ang Liu, Paolo Tozzi

  2019, MNRAS, 485, 3909 (this thesis, Chapter 6) [191]

- Spatial distribution of metals in the ICM: evolution of the iron excess in relaxed galaxy clusters

  Ang Liu, Paolo Tozzi, Heng Yu, Sabrina De Grandi, Stefano Ettori

  2018, MNRAS, 481, 361 (this thesis, Chapter 2) [192]

- Inside a beehive: the multiple merging processes in the galaxy cluster Abell 2142

  Ang Liu, Heng Yu, Antonaldo Diaferio, Paolo Tozzi, Ho Seong Hwang, Keiichi Umetsu, Nobuhiro Okabe, Lilan Yang

  2018, ApJ, 863, 102 (this thesis, Chapter 5) [194]

- Searching for bulk motions in the intracluster medium of massive, merging clusters with Chandra CCD data

  Ang Liu, Heng Yu, Paolo Tozzi, Zonghong Zhu

  2016, ApJ, 821, 29 [196]

- A method to search for bulk motions in the ICM with Chandra CCD spectra: application to the Bullet cluster

  Ang Liu, Heng Yu, Paolo Tozzi, Zonghong Zhu

  2015, ApJ, 809, 27 [195]

- Chemical evolution of galaxy clusters: dissecting the iron mass budget of the intracluster medium

  Ang Liu, Paolo Tozzi, Stefano Ettori, Sabrina De Grandi, Fabio Gastaldello, Piero Rosati, Colin Norman

  A&A submitted. (this thesis, Chapter 4)

- Identification and properties of the host galaxy of X-ray and radio sources in MUSE-HUDF

  Ang Liu, Paolo Tozzi, Gabriel B. Caminha, Piero Rosati, et al.

  In prep.

- Review of X-ray cool-core clusters of galaxies

  Ang Liu, Heng Yu

  2014, Progress in Astronomy, 32, 1 [193]

- Extended X-ray monitoring of gravitational lenses with Chandra and joint constraints on X-ray emission regions

  Eduardo Guerras, Xinyu Dai, Shaun Steele, **Ang Liu**, Christopher S. Kochanek, George Chartas, Christopher W. Morgan, Bin Chen

  2017, ApJ, 836, 206 [140]

- Inquiring into the nature of the Abell 2667 Brightest Cluster Galaxy: physical properties from MUSE

  Edoardo Iani, ..., **Ang Liu**, et al.

  2019, MNRAS, 487, 5593 [158]

- The Local Group analogues in Λ cold dark matter cosmological simulations

Meng Zhai, Qi Guo, Gang Zhao, Qing Gu, **Ang Liu**

ApJ accepted.